TU Delft

Delft University of Technology

Document Version
Final published version

Citation (APA)
Bensason, D. Y. (2025). *The Wakes of Novel Vertical-Axis Wind Turbines: An Experimental Study*. [Dissertation (TU Delft), Delft University of Technology]. https://doi.org/10.4233/uuid:4f6be931-8bd0-4f72-adf9-b81a8fa8705c

Important note
To cite this publication, please use the final published version (if applicable).
Please check the document version above.

Copyright
In case the licence states “Dutch Copyright Act (Article 25fa)”, this publication was made available Green Open Access via the TU Delft Institutional Repository pursuant to Dutch Copyright Act (Article 25fa, the Taverne amendment). This provision does not affect copyright ownership.
Unless copyright is transferred by contract or statute, it remains with the copyright holder.

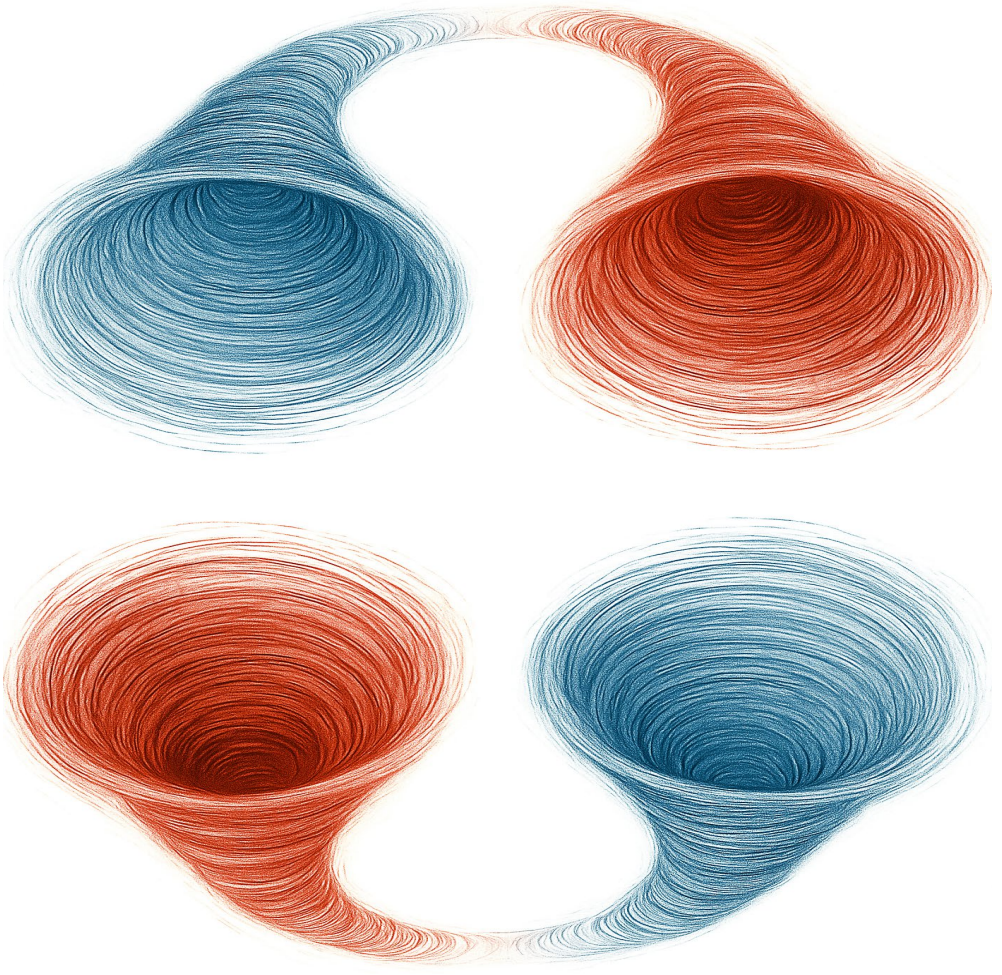
Sharing and reuse
Other than for strictly personal use, it is not permitted to download, forward or distribute the text or part of it, without the consent of the author(s) and/or copyright holder(s), unless the work is under an open content license such as Creative Commons.

Takedown policy
Please contact us and provide details if you believe this document breaches copyrights.
We will remove access to the work immediately and investigate your claim.

This work is downloaded from Delft University of Technology.

The Wakes of Novel Vertical-Axis Wind Turbines

An Experimental Study



David Yefim Bensason

The wakes of novel vertical-axis wind turbines

Propositions

accompanying the dissertation

The wakes of novel vertical-axis wind turbines

by

David Yefim Bensason

1. Blade pitch offers a mechanically simple method to achieve an enhanced wake recovery for VAWTs. [This thesis].
2. Leveraging the aerodynamic potential of turbine frames enables new strategies for wake control and farm-level optimization. [This thesis]
3. Active wake recovery methods like the helix recreate what VAWTs intrinsically accomplish—ironically mimicking the very 'complex aerodynamics' often criticized in them.
4. Mitigating the climate crisis must rely more on policy reform rather than technological innovation.
5. Without the COVID-19 pandemic, remote and hybrid work models would have remained stalled by outdated corporate norms.
6. The climate crisis must be treated as the global emergency it is — with even more urgency, resources, and cooperation than seen during the COVID-19 pandemic.
7. The conference name TORQUE should stand for "Traveling Overseas Repeatedly: Questionable Use of Emissions".
8. Long-distance overnight trains in Europe must be made significantly more affordable and accessible if they are to serve as a real alternative to air travel.
9. Equations should be excluded from scientific presentations unless their physical meaning is clearly explained.
10. Motorsport is less a sport, and more an engineering showcase disguised as competition.

These propositions are regarded as opposable and defendable, and have been approved as such by the promotor Dr. A. Sciacchitano.

The wakes of novel vertical-axis wind turbines

Dissertation

for the purpose of obtaining the degree of doctor
at Delft University of Technology,
by the authority of the Rector Magnificus, prof. dr. ir. T.H.J.J. van der Hagen,
chair of the Board for Doctorates,
to be defended publicly on Monday 17 November 2025 at 10:00 o'clock

by

David Yefim BENSASON

Master of Engineering in Mechanical Engineering,
University of Bath, United Kingdom,
born in Houston, TX, United States.

this dissertation has been approved by the candidate's promotors

Promotor: Prof. Dr. Ir. C.J. Simao Ferreira
Promotor: Dr. A. Sciacchitano

Composition of the doctoral committee:

Rector Magnificus,	chairperson
Prof. Dr. Ir. C.J. Simao Ferreira,	Delft University of Technology
Dr. A. Sciacchitano,	Delft University of Technology
Independent members:	
Prof.dr.ir. J.W. van Wingerden,	Delft University of Technology
Prof.dr. J. Carroll,	University of Strathclyde
Prof.dr. T. Griffith,	University of Texas at Dallas
Dr. K. Mulleners,	École Polytechnique Fédérale de Lausanne
Non-independent members:	
Dr.ir. D.A.M. De Tavernier,	Delft University of Technology
Reserve member:	
Prof.dr. F. Scarano,	Delft University of Technology

This research was partially funded by the European Union's Horizon 2020 research and innovation program under grant agreement No. 101007135.

TU Delft Delft University of Technology

X-ROTOR

Funded by the Horizon 2020 Framework Programme of the European Union

Keywords: Vertical-axis wind turbines, X-Rotor, Mutli-rotor systems, wakes, wind tunnel, particle image velocimetry
Printed by: Proefschriftspecialist
Front & Back: Artistic rendering of vortex pair generated by AI and post-processed.

The author set this thesis in LaTeX using the Libertinus and Inconsolata fonts.

ISBN 978-94-6384-858-9

An electronic version of this dissertation is available at
http://repository.tudelft.nl/.

Contents

Summary ix

Samenvatting xi

Acknowledgments xv

I Prologue 1

1 Introduction 3
- 1.1 The need for renewable energy . . . 4
- 1.2 Offshore wind energy . . . 4
- 1.3 Vertical-axis wind turbines . . . 7
- 1.4 Multi-rotor systems . . . 8
- 1.5 This thesis: objectives and research questions . . . 9
- 1.6 Thesis Outline . . . 10

2 State of the art: wind turbine wake aerodynamics 13
- 2.1 The case for VAWTs . . . 14
- 2.2 VAWT Aerodynamics . . . 15
  - 2.2.1 VAWT wakes . . . 15
  - 2.2.2 Unsteady effects . . . 18
- 2.3 Application of VAWTs in wind farms . . . 21
- 2.4 Wake control for HAWTs . . . 22
  - 2.4.1 Wake steering techniques . . . 22
  - 2.4.2 A de-coupled wake steering approach . . . 23
  - 2.4.3 Wake mixing techniques . . . 25
- 2.5 Wake control for VAWTs . . . 26
- 2.6 The X-Rotor VAWT . . . 29
  - 2.6.1 Cost benefits . . . 31
  - 2.6.2 Primary rotor . . . 31
  - 2.6.3 Secondary rotor and control . . . 33
  - 2.6.4 Other studies on the X-Rotor . . . 35
- 2.7 Multi-rotor Systems . . . 35
  - 2.7.1 MRS wakes . . . 36
  - 2.7.2 Wake steering for MRS . . . 37

3 Methodology: experimental techniques for wake measurements 39
- 3.1 Introduction . . . 40
- 3.2 Working principle of particle image velocimetry . . . 40
- 3.3 Stereoscopic particle image velocimetry . . . 41

3.4 Volumetric particle tracking velocimetry . . . 42
3.4.1 Examples of 3D wake measurements for VAWTs . . . 43

II H-type VAWT wind farm 45

4 Experimental demonstration of a high-density VAWT wind farm 47
4.1 Introduction . . . 48
4.2 Working principle of the vortex-generator mode . . . 49
4.3 Experimental methods . . . 53
4.3.1 Wind tunnel . . . 53
4.3.2 Wind turbine model . . . 53
4.3.3 Flow measurement system . . . 55
4.3.4 Case overview . . . 56
4.3.5 Flow measurement uncertainty . . . 57
4.4 Results . . . 59
4.4.1 Rotor thrust performance . . . 59
4.4.2 Streamwise vorticity system . . . 60
4.4.3 Wake topology . . . 63
4.4.4 Wake recovery . . . 65
4.4.5 Available power . . . 70
4.4.6 Surface momentum flux . . . 72
4.5 Conclusions . . . 80

III The X-Rotor vertical-axis wind turbine 83

5 Experimental characterization of the X-Rotor wake within the volume of rotation 85
5.1 Introduction . . . 86
5.2 Methods . . . 86
5.2.1 Wind tunnel and turbine model . . . 86
5.2.2 Flow measurement systems . . . 87
5.2.3 Flow measurement uncertainty . . . 88
5.2.4 Case description . . . 89
5.3 Results . . . 89
5.3.1 Phase-locked flow fields at $\theta = 90^\circ$ . . . 89
5.3.2 Flow field variation with phase . . . 90
5.3.3 Spatial evolution of the wake . . . 92
5.4 Conclusions . . . 94

6 The impact of blade-tip mounted rotors on the X-Rotor vertical-axis wind turbine 95
6.1 Introduction . . . 96
6.2 Methods . . . 96
6.2.1 Secondary rotor design and operating conditions . . . 96
6.2.2 Flow measurement system . . . 98
6.2.3 Measurement cases . . . 99

6.3 Results . . . 100
6.3.1 The wake of the secondary rotor . . . 100
6.3.2 The aerodynamic gearbox principle . . . 102
6.3.3 Wake comparison: secondary rotor & baseline . . . 102
6.3.4 Tip-vortex trajectory . . . 105
6.3.5 Vortex circulation . . . 107
6.3.6 Mixing and energy flux . . . 109
6.4 Conclusions . . . 111

7 The near wake deformation of the X-Rotor with pitched blades 113
7.1 Introduction . . . 114
7.2 Wake re-energization mechanism . . . 114
7.3 Methods . . . 116
7.3.1 Wind tunnel and X-Rotor model . . . 116
7.3.2 Flow measurement system . . . 116
7.3.3 Case overview . . . 118
7.3.4 Numerical demonstration of rotor load distribution . . . 118
7.3.5 Uncertainty in flowfield analysis . . . 121
7.4 Results . . . 123
7.4.1 Velocity fields . . . 123
7.4.2 Verification of the vorticity system . . . 124
7.4.3 Phase-locked flow fluctuations . . . 129
7.4.4 Kinetic energy flux . . . 131
7.5 Conclusions . . . 134

8 The full wake topology of the X-Rotor with the fixed-pitch wake recovery strategy 135
8.1 Introduction . . . 136
8.2 Background on vortex-generator wake control . . . 136
8.3 Methods . . . 138
8.3.1 Wind tunnel and turbine model . . . 138
8.3.2 Flow measurement system . . . 140
8.3.3 Measurement cases . . . 141
8.3.4 Measurement uncertainty . . . 142
8.4 Results . . . 143
8.4.1 Wake topology . . . 143
8.4.2 Available power . . . 146
8.4.3 Vortex system validation . . . 148
8.4.4 The role of the dominant CVP . . . 150
8.4.5 Mean kinetic energy replenishment . . . 155
8.5 Conclusions . . . 161

IV The multi-rotor system 163

9 Wake re-energization of a VAWT-based multi-rotor system 165
9.1 Introduction . . . 166
9.2 De-coupled lift-induced recovery . . . 169

9.3 Methodology . . . 171
9.3.1 MRS model . . . 171
9.3.2 High-lifting wings . . . 171
9.3.3 Flow measurement technique . . . 174
9.3.4 Measurement cases . . . 175
9.4 Results . . . 177
9.4.1 Wake topology . . . 177
9.4.2 Vortex circulation . . . 180
9.4.3 Available power . . . 184
9.4.4 Momentum recovery process . . . 186
9.4.5 Kinetic energy flux . . . 187
9.5 Conclusions . . . 192

V Conclusions and outlook **195**

10 Conclusion **197**
10.1 Key findings . . . 198
10.2 Outlook and recommendations . . . 201
10.2.1 VAWT wind farms . . . 201
10.2.2 The X-Rotor VAWT . . . 202
10.2.3 MRS . . . 203

VI Appendices **205**

A In relation to Chapter 4 **207**
A.1 Sub-volume size . . . 207
A.2 Vorticity fields . . . 208
A.3 Turbulent kinetic energy . . . 210

B In relation to Chapter 7 **213**
B.1 Airfoil polar . . . 213
B.2 Isometric view of velocity and vorticity fields . . . 214

C In relation to Chapter 8 **219**
C.1 Curve fitted vorticity distributions . . . 219

D In relation to Chapter 9 **221**
D.1 Wing-tip vortex circulation convergence . . . 221
D.2 Fitted vortex distribution . . . 222

Bibliography **225**

Curriculum Vitæ **239**

List of Publications **241**

Summary

Offshore wind energy has gained prominence due to its favorable wind resources, turbine scaling potential, and vast installation areas. However, wake losses caused by closely spaced wind turbines remain a significant challenge, reducing overall wind farm efficiency. This thesis explores the application of vertical-axis wind turbines (VAWTs) geometries for maximizing energy density through passive wake recovery techniques. In addition to traditional Darrieus-type VAWTs, the efficacy of passive wake control techniques for novel multi-rotor systems (MRS), namely the X-Rotor and block design concepts, is assessed through experimental studies and proof-of-concept demonstrations.

The thesis begins with a large-scale experimental investigation into the wake dynamics of a high-energy-density VAWT wind farm, providing the first comprehensive dataset of three-dimensional, time-averaged flowfield measurements. A dense grid of nine H-type VAWTs with fixed spacing was analyzed, exploring a passive wake control strategy known as the "vortex generator" mode, where blade pitch is modified to accelerate wake re-energization. Two pitch configurations were tested: positive (pitched-in) and negative (pitched-out). The positive pitch case exhibited significant momentum influx from above and below the rotor, along with lateral wake deflection. In contrast, the negative pitch case induced upwash while injecting high-momentum flow from the sides. Wake recovery was quantified by assessing available power, showing a maximum of 72.4% recovery three diameters downstream in the positive pitch case, 6.4 times higher than the baseline. The negative pitch case reached a 53% recovery four diameters downstream, a 2.1-fold improvement over the baseline. These findings highlight the potential of passive wake control strategies to enhance wind farm energy density.

The X-Rotor introduces an innovative design featuring an X-shaped VAWT, referred to as the "primary rotor," and blade-tip-mounted HAWTs, known as the "secondary rotors." This design employs an "aerodynamic gearbox" mechanism, where the primary rotor extracts mechanical power while the secondary rotors drive electrical generators at the blade tips. This thesis presents the first experimental wake measurements of the X-Rotor, revealing that its wake remains concentrated within its projected frontal area, shaped by the coned blades. The shed vorticity follows an elliptical pattern, inducing cross-flow components along the height. This dataset provides a baseline for evaluating the secondary rotors' impact on wake evolution near the bottom blade tips and demonstrating the aerodynamic gearbox mechanism.

When the secondary rotor experiences peak load, turbulent mixing intensifies. However, as it progresses through the upwind half of the cycle, its load decreases due to yawing out of the flow while the primary rotor blade load increases, resulting in a dominant and coherent tip-vortex structure. The secondary rotors enhance tip vortex diffusion, reducing in-plane velocity gradients at the rotor's edge and within its rotation volume. The baseline case showed ten times higher advective contributions to kinetic energy flux due to coherent vortical structures, whereas the secondary rotors increased turbulence-driven contributions

nearly 30-fold. Despite enhanced tip-vortex diffusion, circulation remains largely conserved compared to baseline measurements.

The primary rotor wake was measured up to six diameters downstream to assess the efficacy of the "vortex generator" control strategy. Like the H-type rotor, the X-Rotor exhibited intrinsic asymmetry favoring the windward side, with trailing vortices moving upward and inward, causing lateral wake contraction near the blade tips. Spanwise variations in wake fluctuations were observed, likely due to differences in shed vorticity along the coned blade span. Both "vortex generator" modes demonstrated wake recovery mechanisms similar to the H-type rotor. However, unlike the straight-bladed case, the X-Rotor lacked a symmetric counter-rotating vortex pair between the upper and lower blade tips. The absence of an opposing vortex pair from the lower blade tips, combined with the complexity of a root vortex, resulted in a distinct wake topology. Despite these differences, available power in the wake was consistently higher across all measurement planes when using the "vortex generator" strategy. The positive pitch configuration increased power by up to 117% at two diameters downstream, compared to a 74% increase for the negative pitch case.

Finally, the thesis presents the first experimental investigation into a de-coupled wake steering strategy for a VAWT-based MRS, evaluating its near-wake dynamics. This study explored external lift-generating devices for wake recovery and steering. Consistent with previous numerical and experimental studies on MRS, individual rotor wakes remained distinct in the near wake. High-speed flow pockets were observed between rotors in both baseline and wing-equipped cases. With wings, induced cross flow of the wake was significant, with upwash exceeding 20% of freestream velocity near the top wing and approximately 10% in the remaining actuator area, compared to a maximum of 3% in the baseline case. Available power in the wake increased by a factor of 1.4 at two diameters downstream when using the wings.

An analysis of momentum exchange highlighted similarities to the negative pitch case of the "vortex generator mode" for isolated VAWTs. The dominant wingtip vortices generated substantial wake-upwash, expelling low-momentum flow from above the rotor while injecting high-momentum flow from the sides. The line-integrated flux of streamwise kinetic energy increased by a factor of 10.5 at the top of the actuator plane and 1.6 at the edges compared to the baseline case. These findings offer a promising proof-of-concept for integrating passive wake control strategies into MRS designs, advancing the potential for high-energy-density offshore wind farms.

To summarize, this thesis contributes to the understanding of wake dynamics and passive wake recovery strategies in VAWT-based offshore wind farms. It provides the first large-scale experimental dataset of wake recovery in a high-energy-density VAWT farm, introduces novel X-Rotor wake dynamics, and explores de-coupled wake steering strategies. These findings offer valuable insights for optimizing wind farm performance and enhancing offshore wind energy in constrained environments.

Samenvatting

Offshore windenergie is steeds relevanter geworden door gunstige windomstandigheden, de schaalbaarheid van turbines en de beschikbaarheid van uitgestrekte installatieruimte. Echter, wake (windschaduw) verliezen veroorzaakt door dicht bij elkaar geplaatste windturbines blijven een aanzienlijke uitdaging, waardoor de algehele efficiëntie van windparken afneemt. Dit proefschrift onderzoekt de toepassing van verticale-aswindturbines (VAWT's) om de energiedichtheid te maximaliseren via passieve technieken voor wake-herstel. Naast traditionele Darrieus-type VAWT's wordt de effectiviteit van passieve wakecontrole-technieken voor nieuwe multi-rotor systemen (MRS), namelijk de X-Rotor en blokontwerpconcepten, beoordeeld door middel van experimentele studies en proof-of-concept demonstraties.

Het proefschrift begint met een grootschalig experimenteel onderzoek naar de wakedynamica van een VAWT-windpark met hoge energiedichtheid, waarbij de eerste uitgebreide dataset van driedimensionale, tijdsgemiddelde stromingsveldmetingen wordt gepresenteerd. Een dicht raster van negen H-type VAWT's met vaste afstand werd geanalyseerd, waarbij een passieve wakecontrole-strategie onderzocht die bekendstaat als de 'vortex generator'-modus, waarbij de bladstand wordt aangepast om de herenergetisering van de wake te versnellen. Twee configuraties werden getest: positief (blad naar binnen gericht) en negatief (blad naar buiten gericht). In de positieve configuratie trad aanzienlijke momentuminstroom van boven en onder de rotor op, samen met laterale wake-afbuiging. Daarentegen veroorzaakte de negatieve configuratie opwaartse stroming terwijl hoog-momentumstroming vanaf de zijkanten werd geïnjecteerd. Wake-herstel werd gekwantificeerd door het beschikbare vermogen te beoordelen: maximaal 72,4% herstel drie diameters stroomafwaarts in de positieve configuratie, 6,4 keer hoger dan de basislijn. De negatieve configuratie bereikte 53% herstel vier diameters stroomafwaarts, een verbetering van 2,1 keer ten opzichte van de basislijn. Deze bevindingen benadrukken het potentieel van passieve wakecontrole-strategieën om de energiedichtheid van windparken te verhogen.

De X-Rotor introduceert een innovatief ontwerp met een X-vormige VAWT, de "primaire rotor", en op de bladpunten gemonteerde HAWT's, de "secundaire rotoren". Dit ontwerp maakt gebruik van een äerodynamische versnellingsbak-mechanisme, waarbij de primaire rotor mechanisch vermogen onttrekt terwijl de secundaire rotoren elektriciteit opwekken aan de bladpunten. Dit proefschrift presenteert de eerste experimentele wake-metingen van de X-Rotor en toont aan dat zijn wake geconcentreerd blijft binnen het geprojecteerde frontale oppervlak, gevormd door de conische bladen. De afgeworpen wervels volgen een elliptisch patroon en veroorzaken dwarsstromingscomponenten langs de hoogte. Deze dataset biedt een referentie om de invloed van de secundaire rotoren op de wake-ontwikkeling nabij de onderste bladpunten te evalueren en het concept van de aerodynamische versnellingsbak aan te tonen. Wanneer de secundaire rotor piekbelasting ervaart, neemt de turbulente menging toe. Naarmate hij door de loefzijde van de cyclus beweegt, neemt de belasting echter af door het uit de stroming draaien, terwijl de blad-

belasting van de primaire rotor toeneemt. Dit resulteert in een dominante en coherente tipwervelstructuur. De secundaire rotoren bevorderen de diffusie van tipwervels, waardoor de snelheidsgradiënten in het vlak bij de rotor-rand en binnen het rotatievolume afnemen. De basislijn toonde tien keer hogere advectieve bijdragen aan de kinetische energiestroom door coherente wervelstructuren, terwijl de secundaire rotoren de door turbulentie aangedreven bijdragen bijna 30 keer vergrootten. Ondanks de versterkte tipwerveldiffusie bleef de circulatie grotendeels behouden ten opzichte van de basislijnmetingen.

De wake van de primaire rotor werd tot zes diameters stroomafwaarts gemeten om de effectiviteit van de "vortex generator-strategie te beoordelen. Net als de H-type rotor vertoonde de X-Rotor intrinsieke asymmetrie ten gunste van de loefzijde, waarbij naslepende wervels omhoog en naar binnen bewogen en laterale wake-contractie nabij de bladpunten veroorzaakten. Variaties in wake-fluctuaties over de spanwijdte werden waargenomen, waarschijnlijk door verschillen in afgeworpen wervels langs de conische bladspanwijdte. Beide "vortex generator-modi lieten wake-herstelmechanismen zien die vergelijkbaar waren met de H-type rotor. In tegenstelling tot het rechte-blad geval ontbrak de X-Rotor echter een symmetrisch tegenrotatie-wervelpaar tussen de bovenste en onderste bladpunten. Het ontbreken van een tegengesteld wervelpaar van de onderste bladpunten, gecombineerd met de complexiteit van een wortelwervel, resulteerde in een onderscheidende wake-topologie. Ondanks deze verschillen was het beschikbare vermogen in de wake consequent hoger over alle meetvlakken bij gebruik van de "vortex generator-strategie. De positieve configuratie verhoogde het vermogen met maximaal 117% op twee diameters stroomafwaarts, vergeleken met 74% voor de negatieve configuratie.

Ten slotte presenteert het proefschrift het eerste experimentele onderzoek naar een ontkoppelde wake-stuurstrategie voor een VAWT-gebaseerd MRS, waarbij de nabij-wake-dynamica wordt geëvalueerd. Deze studie onderzocht externe liftgenererende apparaten voor wake-herstel en -sturing. In overeenstemming met eerdere numerieke en experimentele studies van MRS bleven de individuele rotorwakes duidelijk gescheiden in de nabij-wake. In zowel de basislijn- als de vleugeluitgeruste gevallen werden hogesnelheidsstromingszones tussen rotoren waargenomen. Met vleugels was de geïnduceerde dwarsstroming van de wake aanzienlijk: opwaartse stroming bedroeg meer dan 20% van de vrije-stroom-snelheid nabij de bovenste vleugel en ongeveer 10% in de resterende actuatorzone, vergeleken met maximaal 3% in de basislijn. Het beschikbare vermogen in de wake nam met een factor 1,4 toe op twee diameters stroomafwaarts bij gebruik van de vleugels.

Een analyse van de momentumuitwisseling toonde overeenkomsten met de negatieve configuratie van de "vortex generator-modus voor geïsoleerde VAWT's. De dominante vleugeltipwervels genereerden substantiële wake-opwaartse stroming, waarbij laag-momentumstroming van boven de rotor werd verdreven en hoog-momentumstroming vanaf de zijkanten werd geïnjecteerd. De lijn-geïntegreerde flux van stroomafwaartse kinetische energie nam toe met een factor 10,5 aan de bovenkant van het actuatorvlak en 1,6 aan de randen vergeleken met de basislijn. Deze bevindingen vormen een veelbelovende proof-of-concept voor de integratie van passieve wakecontrole-strategieën in MRS-ontwerpen, en vergroten het potentieel voor offshore windparken met hoge energiedichtheid.

Samenvattend draagt dit proefschrift bij aan het begrip van wake-dynamica en passieve wake-herstelstrategieën in VAWT-gebaseerde offshore windparken. Het levert de eerste grootschalige experimentele dataset van wake-herstel in een VAWT-park met hoge ener-

giedichtheid, introduceert nieuwe X-Rotor wake-dynamica en onderzoekt ontkoppelde wake-stuurstrategieën. Deze bevindingen bieden waardevolle inzichten voor het optimaliseren van windparkprestaties en het verbeteren van de offshore windenergieopbrengst in beperkte omgevingen.

Thank you to Jelle Poland for the translation

Acknowledgments

This thesis and the defense that it accompanies mark the end of my journey as a PhD candidate and my time in the Netherlands. You know how people say time flies when you have fun? At the start of my journey at TU Delft, I figured this saying would not apply, given the stigma behind the pursuit of a PhD. However, sitting here in my cozy office, on the scenic 9th floor of the AE building overlooking the beautiful canal, appreciating my Lego Star Wars and Naruto figurines, staring at Adhyanth, who once again seems to be losing at online chess, I cannot help but realize that these four years have blown past too quickly. Furthermore, although I vividly remember stressful periods, whether related to late nights in the lab, troubleshooting software, or frustrations with writing, I cannot help but reminisce about the silver lining that weaves through it all.

I would like to take this opportunity to thank those who have made the accomplishment of the PhD possible. First and foremost, I would like to acknowledge those who made the PhD experience as enjoyable as it was, namely my colleagues, many of whom I consider lifelong friends.

Rishi, I am eternally grateful for all of the laughs we have shared during countless nights of watching shows, playing games, and drinking chai! Without your humor, this entire experience would have been infinitely more dull. I will forever be grateful to you for putting me on Naruto. Erik, I cannot express enough how much I value your friendship and its importance during my PhD! The time spent with you doing sports and watching shows over airfryer meals could be considered the foundation of this thesis. I am also blessed to have found someone with a comparable passion for Star Wars and sci-fi as me. Deepali, you were always up for having a good laugh. I cherish all the insightful debates we had and for introducing me to CrossFit! You were always unwavering in your support, and it is one of your qualities I appreciate the most! Jelle, your ability to keep any conversation calm and objective is a trait that I greatly admire. I could always rely on you to take my side on any issue, and I was always excited to hear about your latest trip! Oriol, a big gracias to you! My frequent visits to your office to discuss matters unrelated to work were essential to completing my PhD. I will always remember our trekking trip in the Rockies! Adhyanth, we started this PhD journey together and even had the joy to work on the same project with you. This journey would not have been the same without your kindness and criticality, whether discussing work-related topics or other subjects (such as TV shows).

While I don't have the space (this thesis is already too long) to shout out all of the people who have shaped this experience explicitly, I would still like to thank the following people: Likhita, Abhuday, Simone, Abhratej, Ricardo, Matteo, Ali, Guanqun, Mehtab, Clem, Mihir, Jingna, Rention, Shantanu, George, Hauyan, Helena, Dylan, Kiran, Shyam. You have all played a large part in the process and the Team Cusine gang would have not been the same without you.

Next, I would like to thank my academic supervisors. Carlos, outside our discussions about technical aspects of the research, I always felt I could approach you regarding advice

on topics outside of work, be it career ambitions or personal interests. I particularly enjoyed our discussions regarding sci-fi novels and TV shows, specifically Star Wars. You don't often come by others who have read the Thrawn Trilogy and are not embarrassed to nerd out about it. Your guidance and unwavering support during the PhD were critical to its timely completion, and I am eternally grateful for that.

Andrea, I have learned a great deal from you! I appreciate all of the time you have taken to explain complex topics to me, as well as all of your support during the wind tunnel campaigns. Your workload increased significantly within the final year of my PhD, yet you always found the time to meet with me. This PhD would not have been as successful without you, nor my time as enjoyable as it was in Delft without your guidance. I look forward to the day you visit Zurich so we can catchup!

Of course, a big thank you to those who made all of the experiments possible: Dennis Bruikman, Frits Donker Duyvis, Stefan Bernardy, Peter Duyndam, Eddy van den Bos, Henk-Jan Siemer, and Gert-Jan Berends. Without you, the weeks in the wind tunnel would not have run as smoothly!

To my parents (mama and papa). I am eternally grateful to you for your support not only during the PhD but also through every stage of my life. Though I am not sure whether you fully understood what my research was about, I know you have always wanted the best for me. I love you very much! To my brother, I greatly appreciate your support during the PhD, and you are always hearing me out and taking my side on things. Not only concerning the bs at work, but on other matters as well. I feel that we grew closer over these four years, with more frequent phone calls and visits. I hope we continue improving our squash game when I return home for good. Love you man!

Finally, I dedicate this last paragraph to Ilaria. You have been supportive of me throughout the entirety of my PhD, and it would not have been as enjoyable without you! You are my venting buddy and are always able to put things in perspective with your statements, such as "Does anyone actually care?" or "I mean, will anyone actually read it?". But all jokes aside, your support and encouragement are a large reason why this time of my life will be so memorable. I can't wait for the next stage of our lives together, as we will finally be in the same place! I love you!!

David Bensason
Delft, October 2025

I

Prologue

1

Introduction

1

1.1 The need for renewable energy

Global warming stands as one of the most pressing challenges of our time. As population growth, industrialization, and the electrification of various sectors continue to drive up global energy demand, the urgent need to reduce greenhouse gas emissions and mitigate climate change has made the transition to sustainable energy sources a priority. While the Paris Agreement aims to limit global temperature rise to a 1.5°C, studies suggest that this threshold could be surpassed by 2035 without immediate intervention [1]. Hence, a net-zero emission scenario by 2050 has been proposed by the International Energy Agency [2]. Of the many renewable energy sources, wind energy plays a vital role in the green energy transition, with a global installed capacity of 906 GW by the end of 2022 [3]. However, to realize the net-zero scenario, a global wind energy capacity of 2.75 TW is required by 2030. Hence, to support the required growth and to maximize the potential of wind power, research must focus on improving the efficiency, reliability, and productivity of wind energy technologies.

1.2 Offshore wind energy

In recent years, research and deployment of offshore wind energy have gained traction, with an increase of 10.8GW of installed capacity worldwide [3] in 2023, yielding a total of 75.2GW. This is a 24% increase in added capacity compared to the year 2022. Several factors make offshore wind a more attractive option compared to onshore wind and drive its development, namely: (i) the favorable wind resource, (ii) the potential for rotor upscaling, and (iii) the availability of large surface areas for wind farms [4]. These factors directly influence the power output of a wind turbine, which can be expressed by the equation:

$$P = C_P 0.5 \rho U_\infty^3 A, \tag{1.1}$$

where C_P is the power coefficient, ρ is the fluid density, U_∞ is the inflow speed, and A is the frontal area of the rotor.

Offshore wind turbines benefit from consistently high wind speeds (U_∞) and reduced turbulence levels, contributing to higher capacity factors, defined as the ratio of actual to maximum possible energy output over time [5]. These conditions are partly attributed to a lower surface roughness than onshore conditions. Surface roughness refers to the variation in the terrain (like forests, hills, and buildings) that obstructs wind flow and slows it down. Additionally, the lower turbulence gives rise to a thinner wind shear (defined as the boundary of slow-moving flow close to a surface), yielding an earlier transition to high-speed flows from the surface compared to onshore conditions [6].

Rotor up-scaling refers to the growth of the rotor diameter and hence frontal area (A), hub heights, and reported rated power. In general, up-scaling is driven by the objective of attaining higher capacity factors, which can be realized through two major design features [7]. One option is to reduce the specific power of the rotor (defined as the ratio between the rated power and swept area) by increasing the swept area of the rotor. The second is exposing the rotor to higher wind speeds, often realized by constructing taller towers. Furthermore, there is a potential reduction in operational expenditures (OPEX) for farms with larger turbines, which is a driver of the formulation of energy cost [8]. Up-scaling has benefits towards the capital expenditures (CAPEX) as well, where reductions in the balance

of systems costs (cables, electrical infrastructure) are reduced with increased turbine rating [9]. Put simply, a farm with a fixed capacity would require fewer rotors if larger, reducing the overall infrastructure costs. Further impacts of variables such as component life and idle/downtime are active areas of research [10].

The final factor is the available surface area for wind farms when moving offshore [6]. Larger areas enable more installed capacity and more efficient layouts. Additionally, offshore wind farms have increasingly adopted a clustered arrangement, driven by economic, operational, and maintenance advantages associated with closely spaced turbines [9, 11]. In some cases, the clustering approach is necessary to fit the most lucrative offshore conditions, which involve optimal wind resources, shallow waters for fixed-bottom designs, and minimal social and political constraints.

Despite the aforementioned advantages, several challenges still hinder its development. These extend into several aspects of wind farm design, from environmental and sociopolitical implications to operational considerations. However, in this thesis, the topic of interest is associated with the drawbacks of wind turbine clustering. While clustering offers operational benefits, field, experimental, and numerical studies have shown that densely packed turbines often suffer performance penalties due to wake losses, resulting in reduced overall wind farm efficiency [12] and reductions in the theoretical capacity factors. Wind turbine wakes are defined as regions of low kinetic energy downstream of the rotor, which is a by-product of the extracted mechanical power of the turbine from the wind and is visualized in Figure 1.1. The extent of these losses is largely influenced by the farm layout and local atmospheric conditions. Field studies of offshore wind farms have reported losses ranging from 10% to 23%, depending on turbine spacing (ranging from 4D to 12D), wind resource, and farm size [13].

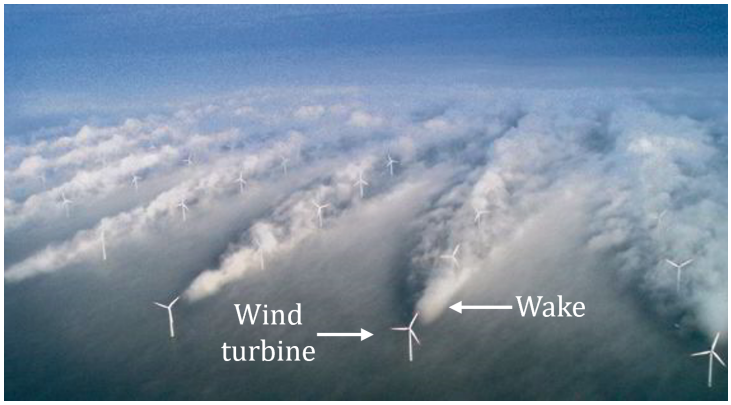


Figure 1.1: Image of the Horns Rev 1 offshore wind farm in Denmark (Courtesy: Vattenfall. Photographer is Christian Steiness).

This raises the question: why not space the turbines farther apart to reduce these losses? As discussed, concerning the benefits of turbine clustering, increasing the spacing (i.e., the size of the farm) would lead to an increase in internal wind farm grid infrastructure [14]. Furthermore, the full potential of the available power in a given offshore space will not be utilized. Finally, although offshore wind farms benefit larger farm areas, the available

1

space for economically lucrative wind farms is not unlimited. In a recent work by [15], the North Sea was used as a case study to see if the European energy demand could be met with just offshore energy. In this hypothetical case, a 100-turbine wind farm of 15MW machines and fixed spacing of 9D was erected across all locations in the North Sea. The resulting Levelized Cost of Energy (LCoE) was evaluated and revealed that viable areas where the LCoE fell around 5-10 €cents/kWh concentrated around water depths up to 45m and increased when moving away from the shorelines, reaching values as high as 20 €cents/kWh in water depths of around 90m. This study was extended for a hypothetical case where the entire North Sea (including water depths of 45m and lower) was covered using 15MW turbines with a spacing of 8D, achieving the European energy demand of approximately 3500 TWh/year. Although this is a promising prospect for offshore wind development, there are limitations and assumptions to this exercise, namely the simplified wake model, subsequent wake loss, as well as the neglect of existing wind farms and other constraints on the available area.

An overview of the offshore wind farm project development in the North Sea is shown in Figure 1.2. As evidenced by the amount of annotation, a large majority of the area along the coasts of the Netherlands, Denmark, Germany, and the UK is already populated by commissioned projects or those at different stages of construction. Meanwhile, regions with larger depths requiring more expensive floating solutions, such as the area east of Edinburgh, are marked as development zones or in the concept planning stage. Hence, limited offshore space is already becoming a challenge and has shed light on yet another hindrance to offshore wind development, namely cluster wakes [16, 17].

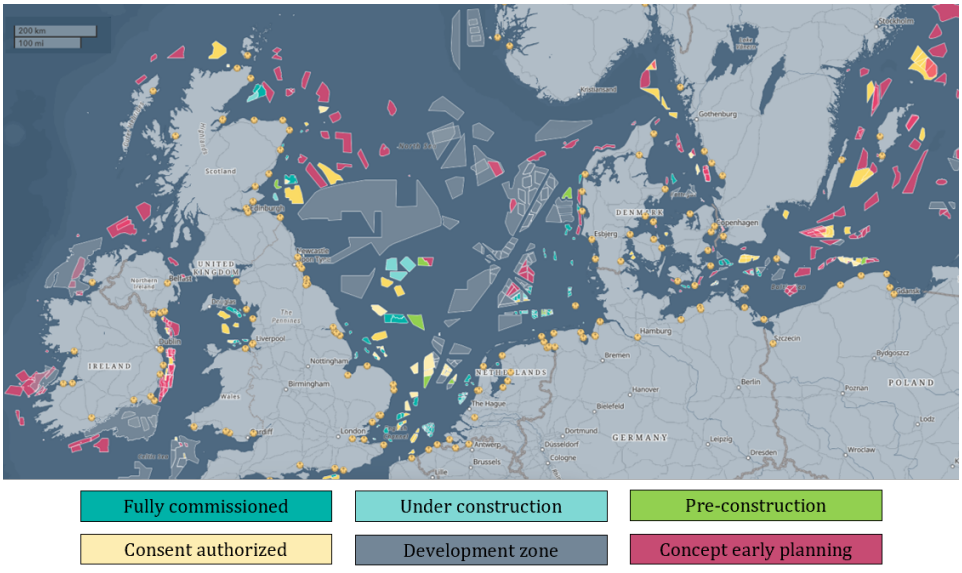


Figure 1.2: Planned and realized wind farms in the North Sea, taken from `www.4coffshore.com` in 2024. A scale is provided on the top left of the map, and a legend describing the nature of the illustrated offshore installations is provided.

Hence, on the one hand, offshore wind farm rotor arrangements should be as dense as

possible for economic and operational reasons, while spaced enough to reduce wake losses within the farm. Given the limited area, it is not feasible to have wind farms occupy large amounts of area. Energy density is a standard metric for a wind farm to quantify the energy production of the entire farm in watts (W) per unit area it occupies (m^2). It is desirable to maximize when considering an offshore installation. Hence, one can either increase the energy production of the farm as a whole or decrease the occupied space encaptured by the farm (spacing between rotors). The latter option is one that is commonly done to its fullest extent when considering the siting conditions of a farm and is limited by wake losses. Hence, the former is the most lucrative research direction, namely, the study of increasing energy production in a farm in a given area.

Several methods to achieve this have been studied for conventional HAWTs and often fall under the category of wake steering, which is defined as the intentional deflection of a wind turbine's wake. The popular methods of wake steering, their underlying physics, and reported efficacy will be discussed in more detail in Chapter 2. However, in this thesis, the option of using an alternative turbine geometry, namely the vertical-axis wind turbine (VAWT), to reduce wind farm wake losses and energy density will be investigated. Furthermore, novel turbine concepts that have been developed in the context of increasing offshore wind farm efficiency that incorporate VAWTs will be considered.

1.3 Vertical-axis wind turbines

Vertical-axis wind turbines can be split into two main categories, namely lift-driven and drag-driven. Several geometries exist for each, and two representative concepts are shown in Figure 1.3. For the lift-driven concept, the H-type Darrieus wind turbine is shown, in this case, the field turbine of Agile Wind TM. For the drag-driven, the Savonius rotor is shown, in this case, an elaborate flower design belonging to Flower Turbines TM. In general, the lift-driven rotor is the most common design for large-scale applications as it has a higher efficiency than its drag-driven counterpart [18]. Nonetheless, Savonius rotors have gained popularity in urban applications due to their high performance at lower wind speeds and reduced sound emission [19]. Furthermore, recent research has explored hybrid VAWT configurations that take advantage of the self-starting and performance benefits of Savonius Darrieus VAWTs, respectively [20]. However, as this thesis focuses on large-scale installations for wind farms, the lift-driven H-type Darrieus VAWT is used as the baseline. This is also the most common test subject for wind tunnel and numerical studies to investigate the fundamental aerodynamics of VAWTs, as will be discussed in Chapter 2.

Unlike the extended wake lengths typically observed with horizontal-axis wind turbines (HAWTs), vertical-axis wind turbines (VAWTs) exhibit a natural acceleration in wake recovery, with kinetic energy replenishment occurring within up to 6 rotor diameters (6D) [21]. Although VAWTs generally show lower power performance, studies on closely spaced, co-rotating, and counter-rotating configurations have revealed a significant performance boost due to favorable fluid interactions between the turbines [22, 23]. These findings have sparked increased interest in investigating the three-dimensional wakes of VAWTs. A comprehensive overview of VAWT wake aerodynamics, both on a rotor and farm scale, will be described in Chapter 2.

This intrinsically higher rate of wake recovery compared to VAWTs makes them ideal

1

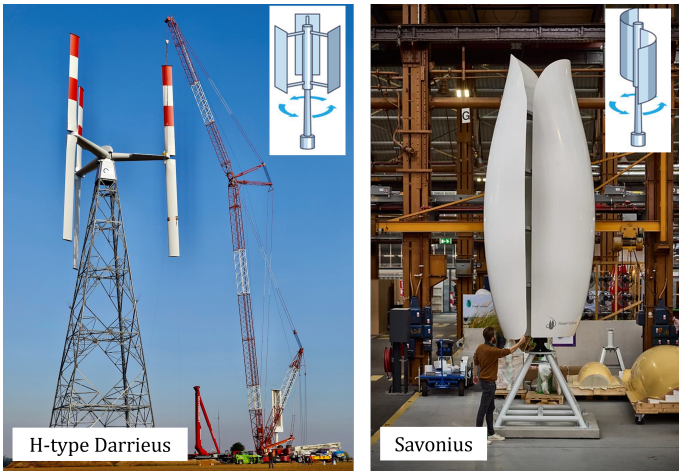


Figure 1.3: Different VAWT configurations. (Left) The lift-driven H-type Darrieus configuration (`https://www.agilewindpower.com/en/media`) and (Right) the drag-drive Savonius configuration. A schematic of the rotation direction of simplified geometries of the respective concepts is provided on the top right of each.

candidates for high-density arrangements [24], and has hence revived the wind energy communities' interest in this technology. In addition to the intrinsic wake recovery, a novel wake re-energization method using a blade pitch has been introduced in a recent study by [25], which has the potential to increase the energy density of a farm even further, hereinafter referred to as the "vortex generator" mode.

Another avenue of interest considered in this thesis is the concept of multi-rotor systems that have the potential to increase the energy densities of farms.

1.4 Multi-rotor systems

Multi-rotor systems (MRS) offer a compelling alternative to the current trend of HAWT up-scaling. Rather than relying on a single large rotor, the MRS employs multiple smaller rotors, providing a new approach to large-scale wind energy capture. This design leverages the benefits of up-scaling, leading to lower costs and reduced weight compared to traditional HAWTs [26]. A subset of innovative MRS designs is shown in Figure 1.4. The X-Rotor includes a VAWT-based primary rotor (lift-driven) with blade-tip mounted secondary rotors (HAWTs). The 4R-V29 demonstrator is a HAWT-based MRS, which includes four individual rotors fastened to a central tower. Some MRS include a distinctive feature, which is the universal support frame, which allows for a block design approach, as shown on the bottom row of Figure 1.4. On the left and right are a HAWT and VAWT MRS block design, respectively. While the idea of HAWT-based MRS is not novel, the application of VAWTs in the design is. Recent studies on VAWT-based MRS have shown significant potential, delivering power performance comparable to large HAWTs while improving Operations and Maintenance (O&M) efficiency [27]. Additionally, in the context of wake re-energization, block-designed MRS have a unique potential and flexibility concerning the design of their support structure. Cross-flow loading and, subsequently, wake steering

can be achieved by integrating external de-coupled lift-generating devices into the frame, as detailed in Chapter 2.

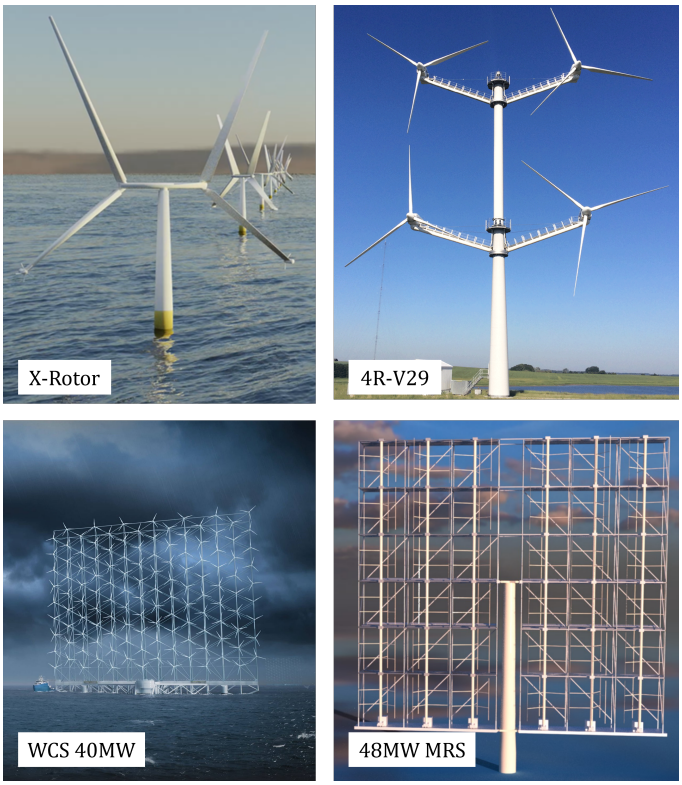


Figure 1.4: Different MRS concepts (Top Left) The X-Rotor VAWT [28], (Top Right) The Vestas multi-rotor demonstrator 4R-V29 located on Riso Campus, Denmark, adapted from [29], (Bottom Left) the 40MW Windcatcher System (WCS) introduced by Wind Catching (TM) `https://www.windcatching.com/technology`. (Bottom Right) the 48MW MRS VAWT-based block design [27, 30] (actually a render from BSC project).

1.5 This thesis: objectives and research questions

The potential for VAWTs, namely the Darrieus concept, towards increasing the energy density of farms has been established and thoroughly investigated experimentally and numerically, as will be described in Chapter 2. However, despite the promise of these innovative concepts, there remains a limited understanding of rotor-level wake aerodynamics. Furthermore, their potential and synergy with both existing and novel wake re-energization methods, such as the "vortex generator" mode and external lifting devices, have not yet been explored. Of these, the X-Rotor and VAWT-based MRS are of particular interest as they include VAWT features and, hence, have the potential for the application of high-energy density wind farms.

This dissertation advances the state-of-the-art VAWT technology by providing experimental studies and proof of concepts of novel VAWT-based MRS systems, both on an

1

isolated rotor wake level as well as in their application for wind farms using a de-coupled wake steering method.

The overall research questions are:

1. What is the wake re-energization process of a high-energy density VAWT wind farm, and how is it modified when using established wake control strategies?
2. What are the driving mechanisms that characterize the wake of the X-Rotor vertical axis wind turbine?
3. How does the addition of de-coupled cross-flow generating devices impact the near wake of a VAWT-based multi-rotor system (MRS)?

1.6 Thesis Outline

The dissertation is organized according to the rotor geometries and topics, namely the H-type Darrieus VAWT, X-Rotor VAWT, and MRS block design. An overview of the workflow is shown in Figure 1.5.

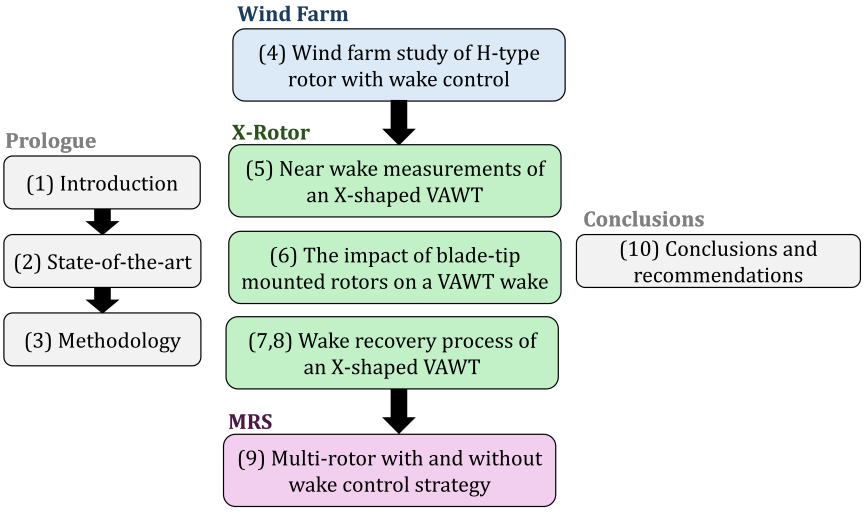


Figure 1.5: Flowchart of the thesis structure.

- Prologue: Following an overview of the thesis topic in Chapter 1, a comprehensive background of topics pertinent to this thesis is presented in Chapter 2. This includes an overview of VAWT and HAWT wake aerodynamics, as well as farm-scale wake re-energization methods for both concepts. Furthermore, an overview of the state-of-the-art of the novel MRS technologies is provided. Finally, a description of the experimental methods used in this thesis is provided in Chapter 3. This includes an overview of the flow measurement techniques used in the dissertation.

- Wind farm: An experimental demonstration of a lab-scaled high-energy density VAWT wind farm is discussed in Chapter 4. This study provides the first set of 3D-resolved wake measurements of a scaled VAWT farm with and without "vortex generator" wake control. The chapter addresses research question **RQ1**.
- X-Rotor: Research question **RQ2** is addressed through several chapters that provide the first experimental measurements of the X-Rotor wake. The wake within the volume of rotation of the primary rotor is presented in Chapter 5. Next, the impact of the blade-tip mounted secondary rotors on the wake is studied in Chapter 6. Finally, the passive "vortex generator" mode for wake recovery is applied to the X-Rotor to study the near and far wake of the primary rotor in Chapters 7 and 8.
- MRS: Whilst the "vortex generator" technique for the VAWTs is a coupled strategy, an MRS offers the potential of de-coupled energization technique. Lab-scale measurements of the near wake of a VAWT-based MRS are presented in Chapter 9 with and without de-coupled wake recovery devices. These findings address **RQ3**.
- Conclusions: Finally, the conclusions and recommendations based on the presented work are discussed in Chapter 10. An outlook of the research topics is also presented.

2

State of the art: wind turbine wake aerodynamics

The following chapter provides a more detailed overview of vertical-axis and multi-rotor wake aerodynamics, as well as their similarities and differences to traditional horizontal-axis technology. The relevance of VAWT technology is discussed in Section 2.1. An overview of VAWT wake aerodynamics is provided in Section 2.2 before highlighting their relevance for wind farm applications in Section 2.3. Next, wake control techniques are discussed for HAWTs and VAWTs in Section 2.4 and Section 2.5, respectively. Finally, an overview of the research regarding the novel X-Rotor and block design MRS is presented in Section 2.6 and Section 2.7, respectively.

2.1 The case for VAWTs

As discussed in Chapter 1, VAWTs are a distinct class of wind energy systems characterized by their vertical rotor orientation. While HAWTs dominate the industry, VAWTs offer unique advantages that make them suitable for specific applications, but they also come with certain limitations, which are mainly related to the same core cause, namely, the complex 3D aerodynamics. Unlike traditional horizontal-axis wind turbines, a VAWT blade experiences cyclically varying inflow conditions and, hence, effective angles of attack. This, in turn, leads to cyclically varying blade loads and various unsteady flow phenomena, which are elucidated in Section 2.2.2 depending on the operating conditions of the rotor, as well as a cyclic torque response. Both of these results have detrimental effects on the structural soundness of a VAWT, leading to increased fatigue and premature failure [31, 32]. These disadvantages led to a stagnation of VAWT development and research in the early 80s, with limited understanding and low-order aerodynamic modeling techniques that could capture the full three-dimensionality of the cylindrical actuation surface. Meanwhile, the commercial success of HAWT technology skewed the research efforts.

Despite this, research in VAWT technology has increased in recent years, given its potential favorable application to offshore wind energy solutions. A deeper understanding of the three-dimensionality of the wake, as well as rotor loading, has yielded the necessary tools for the development of control techniques that can minimize undesirable load fluctuations while maintaining or even increasing rotor performance [33].

The advantageous features of VAWTs are summarized in Figure 2.1, with the key points:

1. **Omni-directionality**: This translates to a simpler and cheaper mechanical design with no need for a yawing mechanism.

2. **Potential cost reductions**: Along with eliminating the need for a yawing mechanism, VAWTs offer a simpler design with untapered and untwisted blades, reducing overall material costs [34]. Furthermore, heavy components, such as the gearbox and drivetrain, can be positioned at the tower's base—or even submerged in the water for offshore applications [35]. These benefits also ease the challenges with floater design with upscaling rotors for offshore applications [36].

3. **Faster wake recovery**: This is a critical advantage of VAWTs compared to HAWTs, which makes them particularly suited for offshore applications [37, 38]. A more detailed description of the VAWT wake and its affinity for wind farm applications is provided in the subsequent sections Section 2.2 and Section 2.3, respectively.

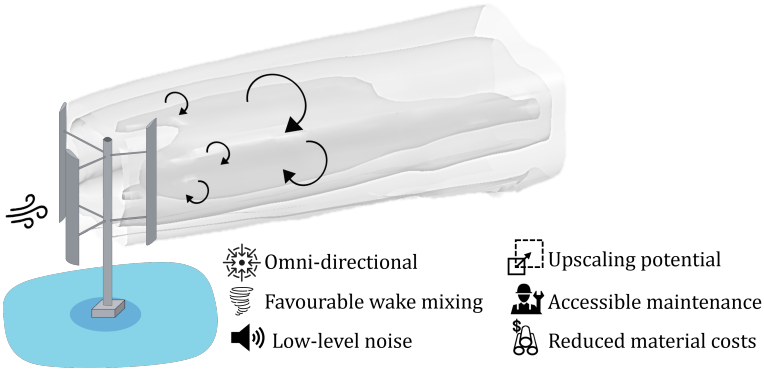


Figure 2.1: Schematic representation of an offshore three-bladed VAWT wake. The main advantages of a VAWT are listed with their respective icons.

2.2 VAWT Aerodynamics

2.2.1 VAWT wakes

The wake topology of VAWTs has been extensively studied in the literature, both through experimental and numerical techniques, and is directly related to blade loading. For brevity, only work conducted on H-type Darrieus VAWTs will be discussed. A top-view schematic of a 2D blade section of a VAWT is shown in Figure 2.2. The lift (L) and drag (D) forces act perpendicular and parallel to the relative incoming velocity (V_{rel}). The projected normal (F_N) and tangential loads (F_T) act perpendicular to the inflow angle (ψ), which is the sum of the angle of attack (α) and pitch angle (θ_p). The upwind (U), downwind (D), windward (W), and leeward (L) passage of the blade corresponds to the azimuth ranges $0^\circ < \theta < 180^\circ$, $180^\circ < \theta < 360^\circ$, $270^\circ < \theta < 90^\circ$, and $90^\circ < \theta < 270^\circ$, respectively. The angle of attack of the blade reaches higher magnitudes in the upwind half of the cycle and flips from positive to negative once entering the downwind half. The normal load dominates the net force on the blade and follows a profile and direction similar to the angle of attack variation.

On the right of Figure 2.2, the main vortical structures associated with a VAWT are shown via simulated results from [39]. The cyclic variation in the blade's effective inflow velocity and angle of attack results in a constant variation in the bound circulation of the blade and hence translates to an ongoing shedding of vorticity along the blade, as labeled. Furthermore, given the finite length of the blades, trailing tip vortices are shed from the top and bottom with equal and opposite strength, in accordance with Helmholtz's theorem. As the blade loading is not symmetric between the windward and leeward passage, the structures are not equal in magnitude about the symmetry plane $y/D = 0$. Similarly, the shed vorticity is a product of the constantly changing bound circulation in time about the blade, with strengths proportional to the instantaneous blade loading.

The near and far-wake of a VAWT was experimentally characterized by [41] using Particle Image Velocimetry (PIV) measurements. The analysis focused on the asymmetry in the flowfield between the upwind and downwind halves of the cycle, stemming from the azimuthally-dependent load distribution of the rotor. Special attention was allocated to the tip-vortex trajectories and interactions as a function of the radial location in the wake. The

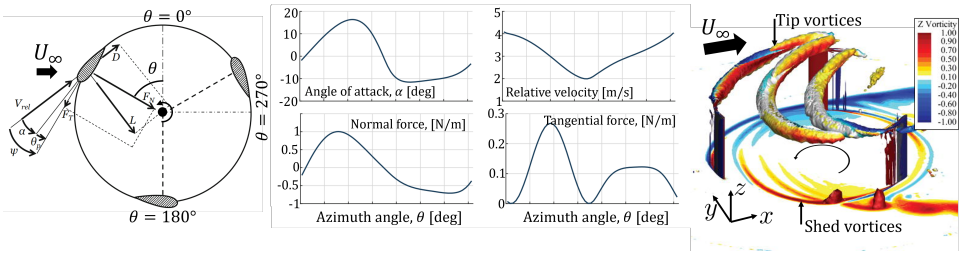


Figure 2.2: (Left) Top-view schematic relevant forces acting on a 2D-blade element, taken from [40]. (Middle) Simulated results from [40] of the operational conditions of a 2D-blade element at a tip-speed ratio $\lambda = 3.0$ as a function of the azimuth angle θ. These include the angle of attack, relative velocity, blade normal force, and blade tangential force. (Right) Simulated results from [39] showing the isosurfaces using the Lambda-2 vortex criterion of a 3-bladed VAWT. The contours are flooded by the Z vorticity at the mid-span of the rotor. The tip and shed vortices are labeled.

results suggest an upward trajectory of the tip vortices generated in the upwind half of the rotor cycle near the edges of the rotor. Meanwhile, the tip-vortex structure generated upwind and downwind convects downwards near the center of the rotor. Although these experimental results shed light on the wake dynamics of VAWT, making them a common source for numerical model validation [42], their results lack cross-stream measurements of the wake topology and a discussion of the re-energization process.

A comparison between the wake re-energization processes of a HAWT and VAWT is numerically investigated by [38]. The results confirm the importance of simulating the 3D effects related to the tip-vortices of a VAWT as they contribute significantly towards the re-energization of the near-wake. Contours of the vorticity structures and time-averaged wake are shown in Figure 2.3. When considering the time-averaged and fluctuating components of the URANS equation in the streamwise direction, it becomes clear that while the VAWT has significant amounts of advective flux of mean kinetic energy in the near wake ($x/D \leq 3$), the HAWT relies on the turbulent energization process, which takes effect once the coherent vortical structures in the near-wake break down ($x/D \geq 4$). The subsequent impact on the cross-section averaged streamwise energy flux was computed, demonstrating a systematically favorable recovery of the VAWT compared to the HAWT by a factor of 3 at $x/D = 4$, as shown in Figure 2.4. This accelerated wake recovery confirms the potential of VAWTs for high-energy-density wind farm applications, discussed in further detail in Section 2.3. The importance of the tip-vortices on the wake recovery of a VAWT was experimentally confirmed by [37], who investigated the wake topology of VAWT submerged in a scaled atmospheric boundary layer. The analysis focuses on re-energization by considering the advective and turbulent flux contributions towards kinetic energy replenishment, highlighting the dominant role of the trailing vortices in the near wake towards the injection of high-momentum flow.

Although the aforementioned studies confirm the importance of the trailing vorticity on the wake topology and recovery rate of a VAWT, the link between vortex strength, dynamics, and generation to the turbine performance (loading) has only recently been investigated. The work of [25] provided an explanation between the quadrant-based loading of a VAWT and the subsequent vorticity system, shown via a flowchart in Figure 2.5. By

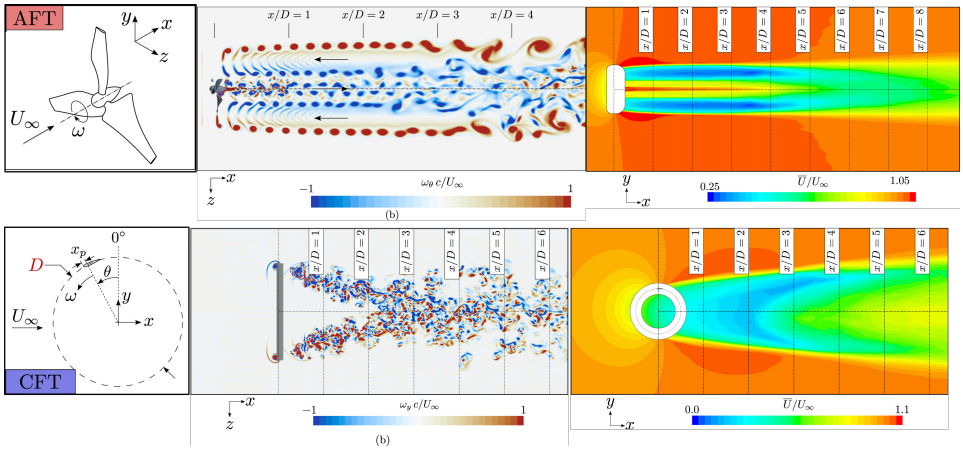


Figure 2.3: Out-of-plane vorticity and time-averaged streamwise velocity contours for the HAWT (axial flow turbine AFT) and VAWT (cross-flow turbine CFT) at the symmetry plane $z/D = 0$. The white areas correspond to regions where the average flowfield is not available due to the moving mesh. The results are obtained from [38].

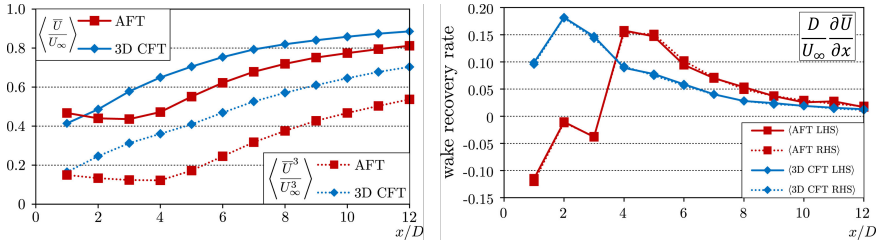


Figure 2.4: (Left) Section-averaged mean streamwise velocity and mean streamwise energy flux for the HAWT (axial flow turbine AFT) and VAWT (cross-flow turbine CFT). (Right) Section-averaged value of the streamwise derivative of the mean streamwise velocity component for the two rotor geometries. The results are obtained from [38].

energizing the trailing vortices generated in select quadrants of the cycle, the induced axial and lateral cross-flows in the wake can increase, resulting in a method for controlling the wake topology and deflection. This technique is described in more detail in Section 2.5 and depends on the assumption of the rotor as an actuator cylinder (AC), conceptualized by [43]. The static cylinder has azimuthally varying loads to present the time-average normal loading of a blade. This link between the AC loading, trailing vorticity, and wake topology was numerically validated by [44]. In this study, a static AC was shown to reproduce the trailing vorticity system of VAWT and demonstrated similar modes of recovery to those reported by [25] based on various relative distributions of loads among the cylinder quadrants. A similar study was conducted by [45], who validated the wake profiles of the AC simulations with experimental results obtained by [46] up to $x/D = 10$.

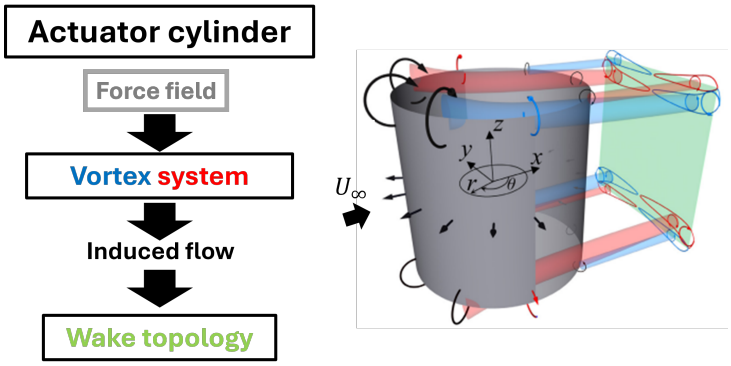


Figure 2.5: Schematic illustration of the trailing vorticity system from [25]. The gray surface represents the idealized actuator cylinder surface, while the red and blue iso-surfaces indicate the trailing vorticity. An arbitrary cross-stream plane in the wake is shown via a green sheet with the intersection points of the aforementioned vorticity structures. To the left, the flowchart describes the mechanism that drives the wake topology of a VAWT.

2.2.2 Unsteady effects

The main unsteady aerodynamic phenomena associated with VAWT aerodynamic modeling have been listed and described in [17] and include dynamic stall, blade-vortex interactions, blade-wake interactions, flow curvature, and dynamic inflow. Here, the former three phenomena are explained as the latter are more critical towards the numerical modeling of VAWT wakes.

Dynamic stall

Dynamic stall is a phenomenon that involves the flow separation of an airfoil undergoing a dynamic motion while also exceeding its stall angle [47], with experimental measurements dating back as far as 1932 [48] when observing sudden lift increases resulting from aircraft wing gust interactions. Furthermore, the occurrence and impact of the dynamic stall have been studied extensively in the context of helicopter aerodynamics [49–51]. The occurrence and severity of dynamic stall are dependent on several operational and geometric parameters, which can influence the mean angle of attack, reduced frequency, Mach number, and location and nature of the laminar-turbulent transition along the blade. A comprehensive overview of studies of these parameters on dynamic stall is provided in [17].

Given the similarity in rotation axis between helicopters and vertical-axis wind turbines, it is no surprise that dynamic stall is a relevant flow phenomenon for vertical-axis wind turbine aerodynamics as well. As the rotational plane and incoming wind direction coincide, the blade's effective flow conditions and subsequent angle of attack vary considerably throughout the blade's cycle. A comprehensive review of basic VAWT aerodynamics is provided in [17]. In general, the main parameters dictating the occurrence and severity of dynamic stall for vertical-axis wind turbines are the operational tip-speed ratio and reduced frequency of the blade [17, 33, 52]. The former dictates whether the blade will exceed the static stall angle, respective onset location, and percentage time spent above the stall limit in the rotor's cycle. Studies have demonstrated the onset of dynamic stall for

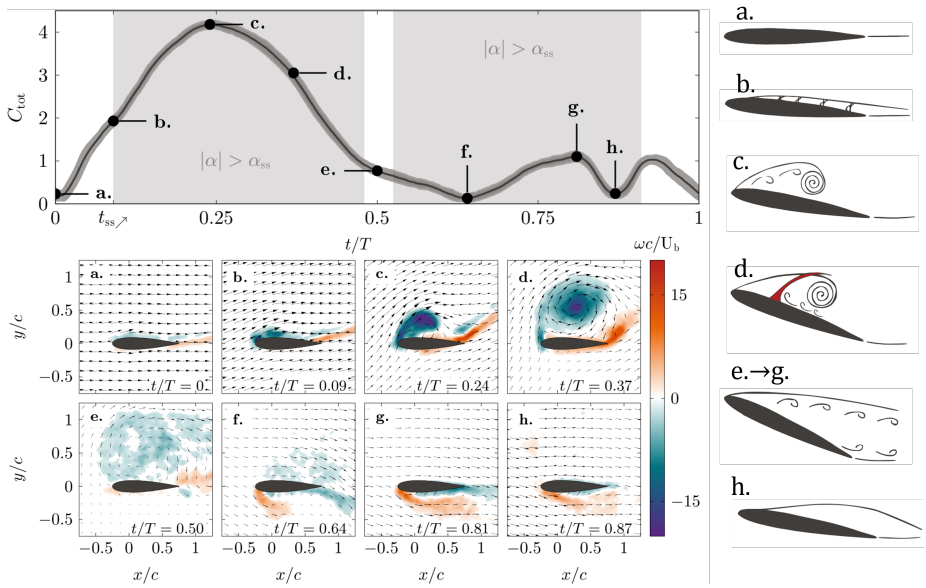


Figure 2.6: (Left) Experimental load and flow measurements at mid-span of a NACA0018 blade undergoing a VAWT cycle at a tip-speed ratio of $\lambda = 1.5$ from [54]. (Right) Schematic of the characteristic dynamics stall stages labeled according to the flow measurements, adapted from [47].

tip-speed ratios $\lambda < 4$ within the upwind passage of the blade, increasing in severity with decreasing tip-speed ratio [52, 53]. Simply operating at higher tip-speed ratios to avoid dynamic stall poses a trade-off in rotor performance, where maximum power coefficients at realistic solidities [0.2 -0.5] coincide with operating tip-speed ratios $\lambda < 4$ [26, 54].

Blade-level experimental flow measurements of a VAWT undergoing dynamic stall at a tip-speed ratio of $\lambda = 1.5$ is shown in Figure 2.6. Additionally, the total load coefficient of the blade (defined as the net of the radial and tangential forces on the blade) as a function of convective time is shown. The corresponding azimuthal positions of the flow measurements along the VAWT cycle are shown along with the idealized schematic of the dynamic stall process. The dynamic stall process for a VAWT blade can be described by six characteristic stages, illustrated in Figure 2.6. First, the blade begins in a state of attached flow (a.), which is the case for the conditions when the effective angle of attack falls below the static stall limit. The onset of flow reversal (b.) is marked by the surpassing of the static stall angle and is followed by a shear layer roll-up (c.). At this stage, the shear layer continues to feed the formation of a large-scale leading-edge vortex, which grows to a critical size. The stall onset (d.) is marked by the separation of the leading-edge vortex from the blade, induced by the entrainment of counter-rotating vorticity from the trailing edge. The vortex is shed into the wake and remains in a fully stalled state (e.). Finally, the flow reattaches (f.) as the blade's effective angle of attack falls below the static stall limit.

The several effects of dynamic stall on vertical-axis wind turbines have been listed by [55], with the main detrimental impacts being the high magnitude fluctuating blade loads, which reduce the fatigue life. Concerns with the periodic release of large-scale vortices

and subsequent blade-vortex interactions (commented on in the following subsection) also affect the noise characteristics.

Blade-vortex and blade-wake interaction

Blade-vortex interactions (BVI) are an intrinsic phenomenon associated with VAWT aerodynamics. They result from two main features, namely the cyclic variation in the blade's effective inflow conditions and the vertical rotation axis. A result highlighting BVI is shown in Figure 2.7. These planar measurements show the out-of-plane vorticity (shed vorticity) at the mid-span of a VAWT. As discussed above, the shed vorticity in the wake is a product of the changing bound circulation of the blade [40]. This is evident by the blue and orange vorticity shed by the blade, closely following the blade's trajectory. The presence of both positive and negative shed vorticity is apparent, stemming from the suction and pressure side, respectively. The orientation of the two (blue above orange and vice versa) flips at azimuth positions $\theta = 0^\circ$ and $\theta = 180^\circ$, where the pressure and suction sides of the blade reverse. The interaction aspect of BVI stems from the VAWT vertical rotational axis, where the blade will interact with the convected shed vorticity in the downwind half. The regions of this interaction are delineated via red rectangles in Figure 2.7. As expected, the interaction of the blade with the shed vorticity leads to cyclic and sudden variations in the effective angle of attack and resulting loads, which is often credited to fatigue and premature failure [20, 54, 56].

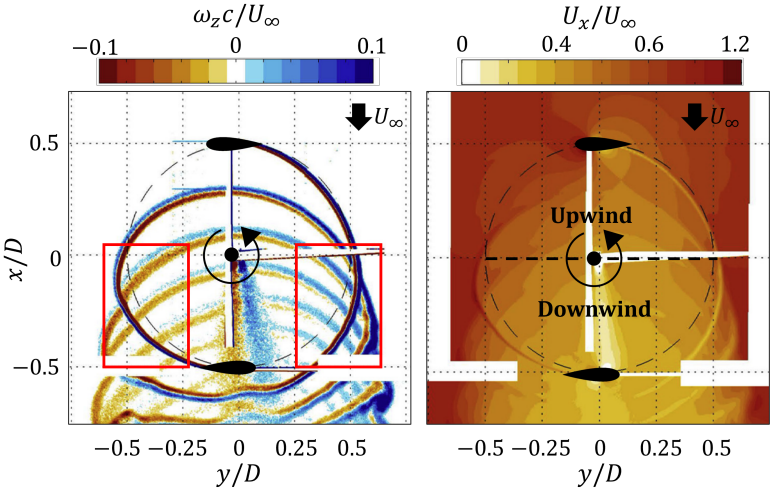


Figure 2.7: Planar-PIV measurements at mid-span of a H-Type VAWT, adapted from [41]. (Left) Shed vorticity contour highlighting the blade-vortex interaction (delineated in a red rectangle), (Right) Streamwise velocity contour highlighting the blade-wake interaction in the downwind passage of the cycle.

Blade-wake interactions (BWI) stem from the same cause as BVI, namely, the vertical rotational axis. As visualized in Figure 2.7, the blade operates in its wake in the downwind half of the cycle due to the convected flow deficit stemming from its upwind passage. As such, the blade encounters unsteady flow conditions in the downwind passage, leading to variations in induced velocity and subsequent loading. Hence, the downwind half of

the cycle intrinsically contributes the least towards the torque (and ultimately power) contribution of the rotor as a whole [56, 57], as seen by the lower blade load in Figure 2.6.

It is worth noting that the severity of BVI and BWI on the loading and wake aerodynamics of the VAWT is strongly dependent on the operational and geometric conditions, namely the solidity and tip-speed ratio [58, 59].

2.3 Application of VAWTs in wind farms

The application of VAWTs for large-scale wind farm deployment has been an active area of research given their favorable wake recovery, as described in Section 2.2. Furthermore, several studies have investigated the effects of closely spaced rotors on their wake and performance, highlighting their potential to enhance performance.

For instance, [60] numerically explored the effects of parameters such as separation distance, tip-speed ratio, and rotation direction, revealing that optimal configurations significantly improve performance in the upwind or downwind blade passages depending on the rotation direction. Complementing these findings, [23] used a 2D vortex panel method to parametrically investigate the interactions between two closely spaced VAWTs with varying tip-speed ratio, solidity, rotational direction, rotor spacing, and wind direction. The results conclude that counter-rotating pairs offer the greatest benefit due to accelerated flow between the rotors. However, these numerical approaches, while insightful, are limited by their 2D nature, as noted by [44], who emphasized the strong 3D effects introduced by VAWTs with low aspect ratios. Experimental work such as [61] has provided 3D insights through particle tracking velocimetry (described in Chapter 3), affirming numerical results about performance gains but limiting conclusions to the near wake (up to $x/D = 2$). To address this gap, [62, 63] measured the far-wake (up to $x/D = 21$) of doublet rotors using a 3-component pressure probe when operating at different rotation direction combinations. The results shed light on the wake deformations resulting from varied rotational directions and the relative contributions of advective and turbulent fluxes towards the streamwise momentum recovery between doublet and single rotor configurations. The authors note that the wake area increases when using a doublet configuration, while the advective and turbulent contributions of the axial flux towards the streamwise momentum recovery increase. This work is extended by [64], who tested the same rotors in a closed test section with varying degrees of inflow turbulence intensity. Previous studies [65, 66] have observed performance increases of isolated rotors with increasing inflow turbulence, credited to the improvements in static and dynamic stall conditions experienced at airfoil level, especially at lower tip-speed ratios. [64] reports a larger increase in performance of an isolated VAWT compared to a doublet with the same inflow turbulence conditions.

In the context of wind farms, the use of closely spaced rotors and clusters has shown promise in increasing power density. [67] numerically analyzed energy replenishment within VAWT farms, comparing staggered and aligned layouts, and found that although turbulent axial flux aids in kinetic energy recovery near the start of the farm, it is often outweighed by advective efflux from farm blockage. By around 15–20 rotor diameters (D) downstream, kinetic energy recovery becomes substantial, particularly with 20D streamwise spacing of rotor clusters. Field experiments conducted by [24] demonstrated that counter-rotating VAWT clusters, despite lower individual turbine performance than horizontal-axis wind turbines (HAWTs), achieve significantly higher power density due to

their ability to be spaced more closely. Measurements by [68, 69] further validated these findings, using ultrasonic anemometers to capture velocity data in clustered and in-line rotor arrangements. Similarly, [70] showed through simulations that clustering boosts individual rotor power generation by up to 10% and increases farm-level power density by a factor of three, emphasizing the efficiency of such configurations.

Laboratory experiments focusing on VAWT arrays provide further insight into rotor-to-rotor interactions and wake dynamics, though they are often constrained by scale and model fidelity. For instance, [71, 72] employed arrays of cylinders with varying heights to simulate flow patterns, but these low-order models excluded critical performance characteristics, such as phase-dependent shed and trailing vorticity strengths and directions. More recently, [73] investigated the wake interactions of two VAWTs with different lateral and streamwise spacing, revealing details about wake superposition and recovery processes. The study extended to include passive pitch adjustments to the rotors, offering potential pathways for improving array performance through wake control strategies. These laboratory studies complement field and numerical findings, contributing to a more comprehensive understanding of VAWT array dynamics.

2.4 Wake control for HAWTs

The wake recovery process for an isolated HAWT has been studied extensively, both experimentally and numerically (see reviews by [74, 75]). In the near wake, where coherent tip and root vortices are identifiable, the entrainment of energy is ascribed to a vertical advection of momentum, accompanied by vortex leapfrogging. However, once these coherent structures break down, the process is mainly governed by turbulent kinetic energy entrainment, leading to phenomena such as wake meandering [75, 76]. Hence, within a wind farm, the main driver of the replenishment of momentum in the wake is governed by the rate of turbulent entrainment of kinetic energy [77].

Wake control strategies for HAWTs have been a popular research topic, addressing the substantial wake losses experienced in wind farms, as discussed in Chapter 1. For simplicity, these are categorized into wake steering and wake mixing techniques. Note that strategies involving the derating of turbines will not be discussed.

2.4.1 Wake steering techniques

The greatest potential for replenishing the kinetic energy in a farm is to entrain high momentum flow from above the rotor layer, as the turbines are often situated close to the sea surface. Wake steering is a heavily researched and applied method for increasing the net performance of a wind plant through the intentional misalignment of selected turbines with the incoming flow direction, often realized through a yaw misalignment of the rotor face with the incoming wind [78]. The "steering" turbine will forfeit some performance efficiency to deflect its wake away from downstream rotors, leading to reported performance increases of the overall wind plant [79, 80]. A demonstration of this technique is shown in Figure 2.8 when applied to an existing onshore array made of six turbines. When applying the wake steering strategy through a yaw misalignment, the overall performance of the array increased by 28%. Although this gain is substantial, the authors acknowledge that this case is unique, given the staggered arrangement of the rotors as well as the dominant wind

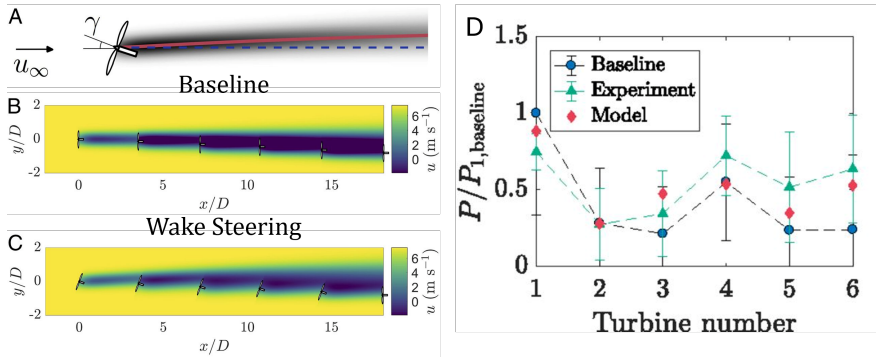


Figure 2.8: (A) Schematic of the wake steering concept using a yaw misalignment γ. The blue dashed and red solid lines indicate the trajectory of the wake (black shaded region) core without and with a yaw misalignment, respectively. Numerical simulations of the wakes for an array of six turbines are shown for (B) the baseline case and (C) the steering case. (D) The power performance of an equivalent array for a case with average inflow speed $U_\infty = 5-6$ m/s. Experimental results using wake steering (green) and the model-predicted recoveries are compared to the baseline performance. The figures and results are obtained from [79].

direction at the site. The potential gains through wake steering depend on factors such as wind resource (wind direction, speed, turbulence, etc.), turbine layout, and intrinsic baseline wake loss [81]. Like yaw control, utilizing the tilt angle to deflect the wake vertically is an extensively studied method for increased wake recovery rate [82, 83].

The underlying driver of enhanced entrainment of kinetic energy in the wake through yaw and tilt misalignment has been attributed to a counter-rotating vortex pair (CVP) generated due to the introduction of a lateral force on the wake [84], which enhance the rate of advective flow re-energizing in the wake, as visualized in Figure 2.9. This phenomenon has been further demonstrated experimentally by [85] for both a yawed and tilted rotor configuration, highlighting the mechanism of wake recovery using the Reynolds averaged Navier-Stokes equation (RANS) terms. In the case of wake steering using yaw misalignment, the influx of high-momentum flow is realized from the sides of the rotor, with the wake being deflected to the side. Tilting the rotor is another wake control strategy that has been investigated and relies on the same underlying physics as the yawed case, with an included vertical force component and CVP, which entrain high momentum flow from above and below the rotor while steering the wake upward or downward. Recent studies [82] have demonstrated the potential of this wake steering technique for large-scale wind farms. Despite the promise of these wake steering strategies, studies have commented on the impact of yaw control on a farm level on the fatigue loading of the turbines. The work by [86] concluded that yawing turbines in a farm that operates at and below rated conditions will increase the fatigue loads overall and become more uniform throughout the farm. Nevertheless, the relative impacts on blade-root and shaft-bending modes are heavily dependent on the wind conditions and frequency of yaw control.

2.4.2 A de-coupled wake steering approach

Wake steering for horizontal-axis wind turbines through yaw control is a coupled method for wake recovery. The mechanism of recovery (i.e., a trailing counter-rotating vortex

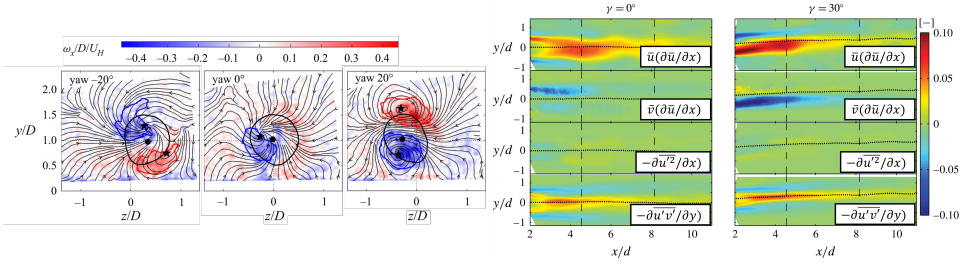


Figure 2.9: (Left) Cross-stream measurements behind a wind-tunnel scaled HAWT showing the dominant CVP at positive and negative yaw angles $\pm 20^\circ$ at $x/D = 3$, adapted from [85]. (Right) Measurements at the symmetry plane of a wind-tunnel scaled HAWT showing the RANS terms in the streamwise direction when yawed, adapted from [84].

pair) is generated via an augmentation of the rotor's operation and, hence, leads to a performance decrease.

These shortcomings have stimulated interest in wake steering and recovery techniques using decoupled methods and external cross-flow generating devices. The work of [87] explored this concept by introducing a "synthetic forcing" in the vertical direction to promote the wake recovery of a modular wind farm using LES. As described in Section 2.2, the vertical entrainment of energy from the boundary layer is a critical feature in the wake recovery process of HAWTs on rotor scale and wind farms. The hypothetical vertical forcing aimed to exploit and increase the vertical flux of momentum and was scaled proportionally to the rotor thrust. The results highlighted the overall increase in vertical mixing, yielding higher flow velocities at the turbine discs, which in turn boosted turbine power output. However, the authors did not propose a physical mechanism to generate such forcing and rather suggested that they could be achieved through conventional techniques such as rotor tilt and yaw. This idea was extended by [88], who investigated the wake recovery of a HAWT with de-coupled cross flow generating devices in the form of NACA 4412 blades. Ten designs for promoting the vertical momentum flux in the wake were considered, as visualized in Figure 2.10. The designs range from single blades located above and below the rotor, cascading elements above and behind the rotor, and curved geometries situated around the circumference of the actuator. The results revealed an increase in available momentum downstream and, subsequently, an increase in total power performance for all cases, varying degrees. Designs such as I, V, and VII were effective at steering the wake but also decreased the upstream turbine performance due to their close proximity to the actuator surface. Meanwhile, designs such as IV, VIII, IX, and X increased the performance of the upstream rotor due to their inadvertent diffuser effect. The authors conclude that designs VI, IX, and X have the most potential. Design VI yields a total power increase on the order of 1.2 while maintaining a simple design. Meanwhile, designs IX and X yield a total power increase on the order of 1.7 but employ curved blade geometries.

Although the aforementioned study highlights the potential of de-coupled wake re-energization devices from a rotor's surface, the simulations had the blades free floating in the computational domain. Hence, they did not suggest any ways to fasten these large-scale blades in orientations so close to the actuation surface. In this thesis, the economic benefits of the MRS are combined with the de-coupled wake re-energization technique by taking

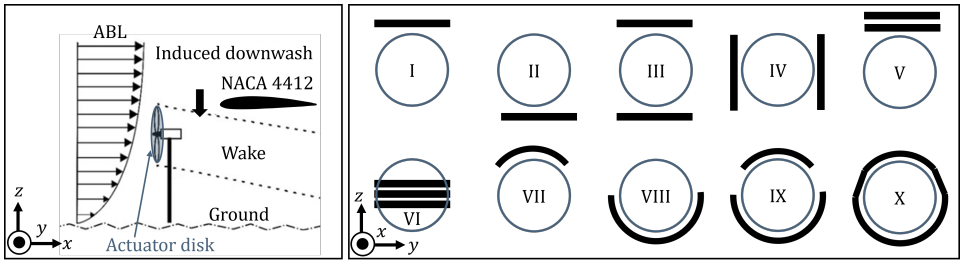


Figure 2.10: Schematic of the design cases for wake deflection via external cross-flow generating devices adapted from [88]. The rotor is modeled using an actuator disk (AD), and the lift-generating devices are modeled as NACA 4412 airfoils. The 10 design cases are visualized from a front view, with the circles representing the AD blade rectangles of the airfoils.

advantage of the supporting frame of an MRS with a block design (Chapter 9).

2.4.3 Wake mixing techniques

Wake steering through yaw and tilt is considered a passive technique, i.e., it requires a steady-state adjustment based on the farm layout, turbine operational settings, and meteorological conditions. However, in recent years, more advanced techniques have been developed to enhance the wake recovery rate of HAWTs via continuous adjustments to the turbine's operation, with the intent of accelerating the mixing processes. This idea was explored by [89] using large-eddy simulations of a wind farm modeled via actuator disks. An optimization approach was applied to maximize the farm performance using both static (constant) and active (time-varying) control of the actuator's induction (and hence thrust) factor. The results concluded that the dynamic induction approach outperforms the static one, with performance gains of up to 19%.

The method of dynamic induction control relies on the cyclic variation of the rotor thrust. For a rotor (one with blades rather than an actuator disk), this can be achieved through collective, cyclic variations in the blade pitch, as shown by [90], coined the pulse technique. This was the first experimental study to apply dynamic induction control for an array of three turbines and reported a 4% in overall performance when the most upwind rotor used periodic pitch variations. A schematic visualization of the wake is shown in Figure 2.11, highlighting the concentrated and localized wake deficit stemming from the pulsing upstream rotor, as well as the overall gain in power compared to the baseline case. Experimental measurements of the wake for a single rotor using cyclic pitch variations were carried out by [91]. The result concluded a significant increase in available power for hypothetical downstream rotors up to a distance of $x/D = 3.5$. Furthermore, visualizations of the tip-vortex development shed light on vortex leapfrogging and breakdown induced by the control technique, highlighting their importance in the wake-mixing process.

Finally, [92] extended the idea of dynamic induction control by considering individual cyclic blade pitch actions and coined the helix approach, due to the helical shape in the wake, as shown in Figure 2.11. Numerical simulations were carried out for a two-turbine wind farm, concluding a 7.5% increase in overall production when using the helix method. An experimental study of the wake of the helix approach was carried out by [93] for a

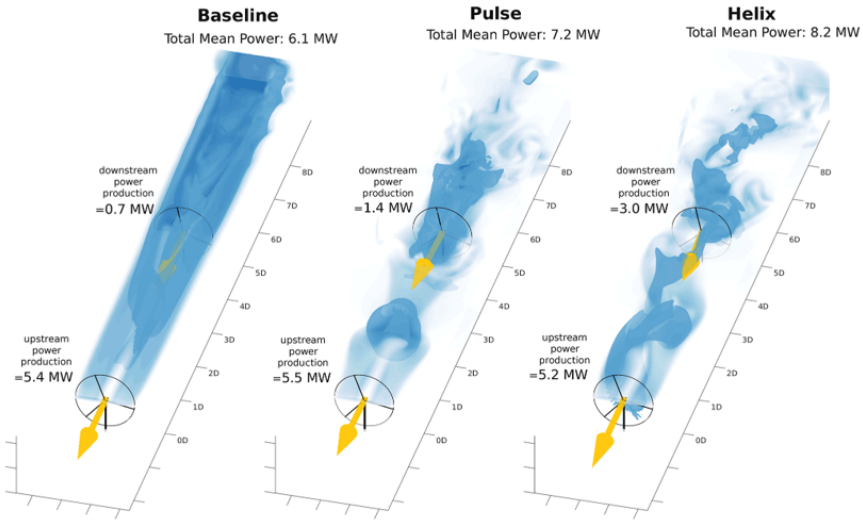


Figure 2.11: Numerical simulation results of the wake for two inline rotors under (left) baseline conditions, (middle) collective periodic induction control (pulse), and (right) individual dynamic induction control (helix). The blue-shaded regions and intensity correspond to the isosurfaces of the velocity. This schematic was obtained from [94].

two-turbine array. The study focused on the wake and tip-vortex evolution, concluding an overall increase in power production range from 8.0% to 15.1% depending on the pitching amplitude and frequency with the helix approach and direction or rotation of the helix.

2.5 Wake control for VAWTs

Given the current market preference for HAWT technology, as well as the intrinsically faster wake recovery potential of VAWTs (discussed in Section 2.2), less literature is available on techniques targeted towards wake steering and re-energization of VAWT wakes. Nonetheless, the few documented techniques rely on the same principles of HAWTs, namely the energization of streamwise vortices that increase the advective flux of MKE in the wake. Unlike HAWTs, the cross-flow feature of VAWTs results in intrinsic shed vorticity in the streamwise direction, with circulation strengths proportional to the bound circulation (and hence blade load) at a given azimuthal position, as described in Section 2.2. The importance of these structures to the wake topology was theorized using an idealized actuator cylinder theory [43] and experimentally validated by [25], with the main working principle highlighted in Figure 2.5. Given the dependence of the wake topology on the induced flow of the trailing vorticity system, the question is: **how can the rotor loading be modified to yield a vorticity system that accelerates the wake recovery through advective fluxes?**

The explored techniques for enhancing the wake recovery of VAWTs answer this question in different ways. [95] performed numerical simulations using an actuator line model of a VAWT with different inclination angles of the blade. A subset of the results

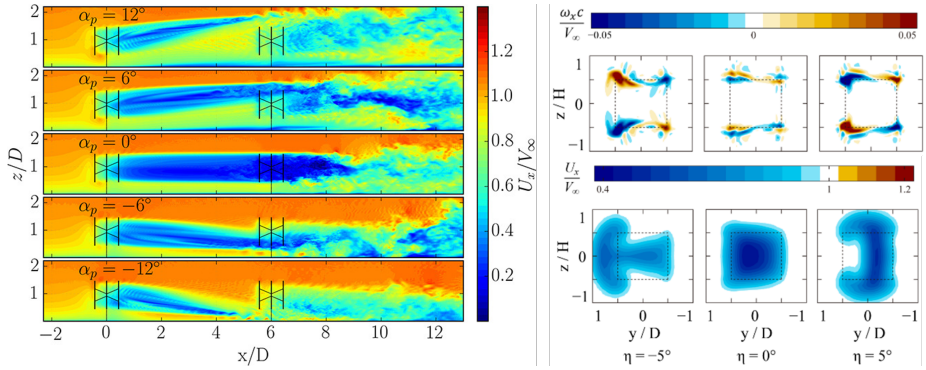


Figure 2.12: (Left) The simulated wake at mid-plane $y/D = 0$ for two VAWTs, with the upwind rotor operating at varying strut pitch angles $-12^\circ \leq \alpha_p \leq 12^\circ$ from [97]. (Right) Simulated streamwise vorticity and wake of a VAWT at a cross-section $x/D = 5$ with varying inclined pitch axis η from [95].

is shown in Figure 2.12. For the baseline case of operation, where no inclination angle is simulated, the trailing vorticity system shows a mixture of positive and negative structures stemming from the blade tips, with no evident dominant structure. However, when a tilt angle is applied, dominant counter-rotating pairs are generated at the blade tips, with seemingly equal and opposite modes between positive and negative tilt. As seen in the panel below, these structures induced significant cross-stream fluxes, leading to distinctive wake topologies. Although the authors quantify the wake recovery rates, they do not elucidate the mechanism of wake recovery (i.e., the role of turbulent and advective flux contributions towards the mean kinetic energy replenishment). Furthermore, they do not discuss the impact of these inclination angles on the azimuthally resolved blade loading and hence miss the critical link between the modified rotor loading and streamwise vorticity system. The work of [96] investigated the impacts of skewed inflow on the blade-level performance of a VAWT through experimental measurements and a numerical free-wake panel method. The results highlight the asymmetry in blade loading along the span of the blade throughout the cycle of the rotor.

The work of [97] achieved wake deflection through the pitching of struts on a VAWT, as shown in Figure 2.12. Two rotors are simulated, with one upwind operating with varying passive pitch adjustments. The results highlight the upward and downward deflection of the wake with growing severity as the magnitude of strut pitch increases. The performance enhancements of the downwind rotor 6D downstream (operating with no pitch adjustment at varying lateral distances) are quantified. For the case where the downwind rotor is inline, a performance enhancement by a factor of 6.4 compared to the non-pitched case is reported with an angle of 10°. Unlike the aforementioned technique, this achieves a modification of the rotor loading without using the blades themselves. However, the contours of the streamwise velocity at different cross-stream locations were not elucidated. Furthermore, no comment was made on the impact of pitch struts on the blade-level performance of the rotor. However, recent work by [98] shed light on the trailing vortex topology of a VAWT with pitched struts using a panel method with a free wake modeling approach. The results highlight the relative strengths of trailing vortex paired energized from the

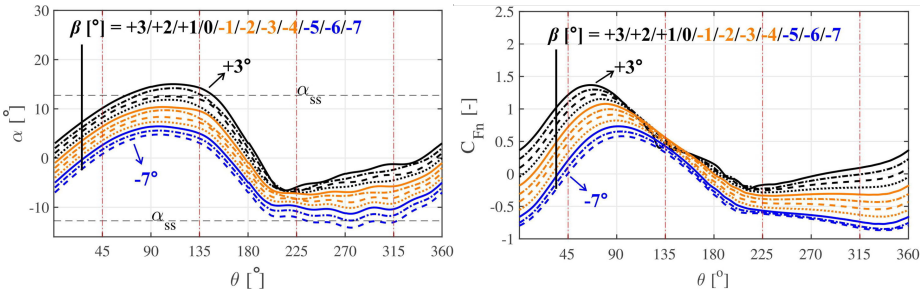


Figure 2.13: Numerical simulation results of a VAWT operating at a tip-speed ratio of $\lambda = 4$ with passive pitch offsets β, obtained from [99]. Three results show the blade-level variation of (left) the effective angle of attack and (right) the normal load coefficient as a function of rotor phase.

connection points between the struts and blades, describing the subsequent modes in which momentum is entrained in the wake (i.e., either from the sides or above the rotor).

The final method, which is of particular interest in this thesis, is a technique that uses blade pitch to accelerate the wake recovery. Numerical results [99] revealing the impact of passive blade pitch offsets on the effective angle of attack throughout one revolution are shown in Figure 2.13, along with the normal load coefficient of the blade. Positive pitch offsets increase the angle of attack magnitudes in the upwind half of the cycle whilst decreasing them in the downwind half, and vice versa for negative pitch angles. This, in turn, modifies the load distribution of the blade throughout its cycle, with normal loads shifting towards the upwind and downwind passage for positive and negative pitch offsets, respectively. Modifying blade-level loading with passive and active blade pitch adjustments has been established in the literature through experimental [56] and numerical [59, 99, 100] investigations, often in the context of developing optimum pitching schemes for maximizing power performance. However, these works do not investigate the subsequent impacts these pitch profiles would have on the trailing vorticity system and subsequent wake topology. Special attention is given to the work of [25], who theorized and experimentally validated the link between blade pitch, rotor loading, trailing vorticity, and, finally, the wake topology. To demonstrate the working principle of this technique, two extreme passive pitch adjustments of $\pm 10^{\circ}$ were tested, with a subset of the results shown in Figure 2.14. The results demonstrate recovery modes similar to those of [95], where a positive pitch ejects the wake laterally, while a negative pitch ejects the wake axially. This technique relies on the redistribution of loads among the different quadrants of a VAWT's cycle, selectively energizing the trailing vorticity structures stemming from each. This method, coined in this thesis as the "vortex generator" mode, is applied to various VAWT geometries in this thesis, with a detailed overview of the working principle provided in Chapter 4. The wake of a VAWT using passive pitch adjustments was numerically validated by [101] using a RANS approach, as well as by [98] using a panel method, shown in Figure 2.14. This work is unique as it combines the techniques of blade (B) and strut (S) pitching, linking the resulting vorticity systems to yet more modes of wake recovery.

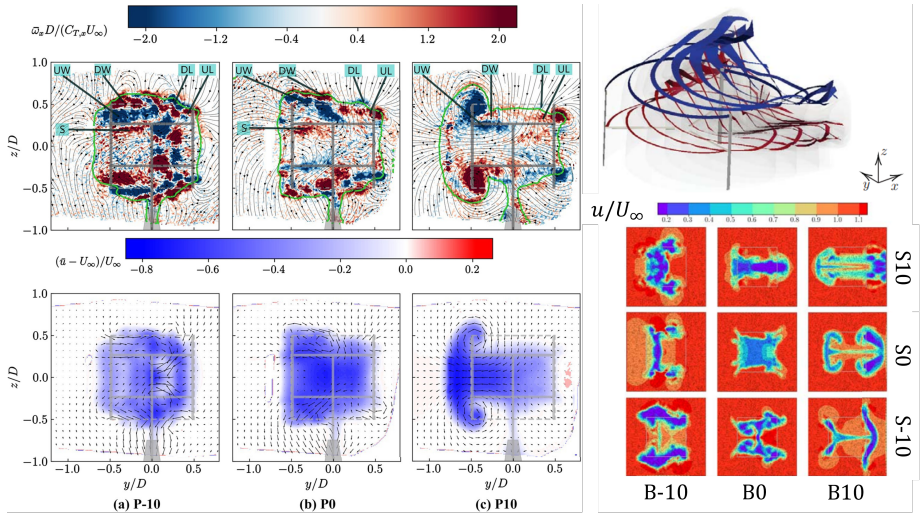


Figure 2.14: (Left) Experimental measurements of vorticity and wake of a VAWT at a cross-section $x/D = 1$ with varying passive pitch adjustments β adapted from [25]. (Right) Simulated streamwise vorticity and wake of a VAWT with varying combinations of passive blade pitch (B) and strut pitch (S) adapted from [98]. The blue and red panels correspond to the streamwise vorticity shed by the blades and struts, respectively.

2.6 The X-Rotor VAWT

The Horizon 2020 European Commission-funded project - X-ROTOR (**X**-Shaped **R**adical **O**ffshore Wind **T**urbine for **O**verall Cost of Energy **R**eduction) - proposes a radical rethink of the traditional vertical-axis wind turbine working principle, visualized in Figure 2.15. The academic and industrial project consortium members (listed in Figure 2.15) have the overall objective to develop an innovative wind turbine design that can address the goal of reducing the cost of energy and improve the scalability of offshore wind turbines. The proposed concept, referred to as the X-Rotor, consists of two main novelties. These are, namely, (i) an X-shaped VAWT, hereinafter referred to as the "primary rotor," and (ii) blade-tip mounted HAWTs, hereinafter referred to as the "secondary rotors."

The working principle of the X-Rotor concept was first introduced in [28]. The design relies on an "aerodynamic gearbox" working principle for electrical power generation, where the primary rotor extracts mechanical power from the wind while the secondary rotors are responsible for driving electrical generators and power take-off (located on the blade tips). As the secondary rotors are located at the blade tips of the primary rotor, they will face a high incident wind speed, namely the vectorial sum of the tip speed of the primary rotor and free stream wind speed. Hence, the secondary rotor can be small while operating at a high rotational frequency. This allows for power take-off to be realized through a direct drive setup, cutting the costs associated with gearboxes or multi-pole generators. Beyond housing the secondary rotors and extracting mechanical power from the wind, the primary rotor is responsible for maintaining the optimum operating condition (speed) for power conversion via active pitchable upper blades. With the absence of a nacelle and the power take-off systems located near sea level (25-30m), O&M cost savings

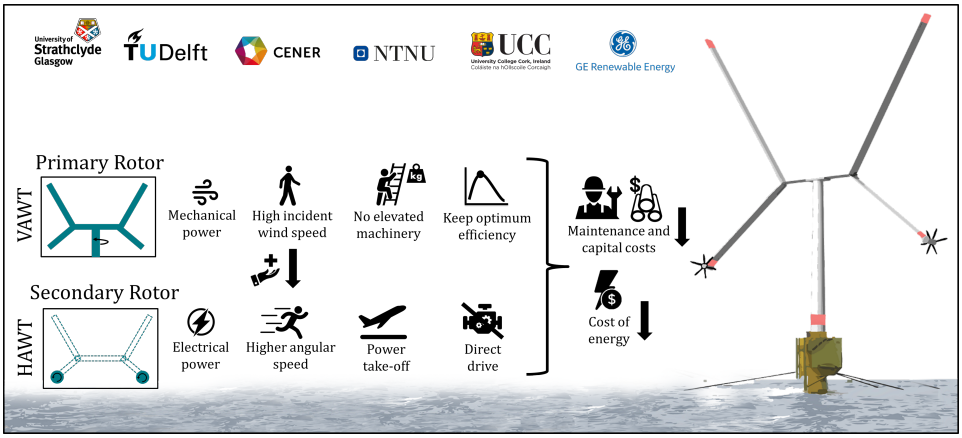


Figure 2.15: An artistic rendering of the X-rotor vertical-axis wind turbine. Note that the spar floater and mooring lines are an idealized representation of the X-rotor in an offshore floating environment and are not part of the design. Furthermore, the blades are untapered for simplicity in this schematic. The project partners of the Horizon 2020 X-ROTOR project are shown at the top. The iconography provides an overview of the working principle of the X-Rotor.

associated with maintenance are expected. The introductory work by [28] highlights the following main benefits of the X-Rotor concept:

1. An LCoE reduction relative to similarly rated wind energy technologies
   (a) Expected capital cost reductions from the omission of a gearbox, multi-pole generator.
   (b) Ease in manufacturing for untwisted primary rotor blades.
   (c) Lower O&M costs without a gearbox and proximity of the secondary rotor generators to the sea level.
2. Application towards floating solutions
   (a) As with other VAWT technologies, the center of gravity is lower, simplifying the floater design.
   (b) Center of thrust and overturning moments
3. Potential for up-scaling
   (a) Modular secondary rotors can be added to help with power take-off.

The paper applies an O&M cost model defined by [102] for a 100 X-Rotor wind farm to capture the benefits of the direct drive feature of the X-Rotor. Compared to existing wind turbine technologies, this preliminary study estimates up to 55% savings in O&M costs, up to 32% in turbine cost and savings, resulting in a CoE saving of up to 26%. It is worth mentioning that these estimates relied on several assumptions regarding the citing conditions, turbine component failure rates, repair times, repair costs, and vessel operating

details. Although some of these inputs were justified using existing data for conventional technologies, the authors acknowledge that more accurate estimates of savings require more detailed modeling of the X-Rotor performance, loads, and overall dimensions.

2.6.1 Cost benefits

More recent estimates of the cost benefits and feasibility of the X-Rotor for offshore applications have been performed by [103]. The study demonstrates that a 100 X-Rotor wind farm achieves O&M cost savings by a factor of 1.4 compared to conventional HAWTs even when the design does not consider detachable modular secondary roots that could be transported onshore for maintenance. Considering this added benefit (more established design), the factor increases to 1.7. These savings are mainly driven by the exemption of components with historically high failure rates (gearboxes), reductions in repair times, and ease of access for the secondary rotors.

This study was then extended by [104] to evaluate the LCoE for a hypothetical offshore wind farm made of 100 5MW X-Rotors. The study used an in-house O&M and power production modeling tool, which has been validated against alternative models and enhanced by studies such as [103]. The studies conclude a 10 - 19% reduction in LCoE of the X-Rotor compared to conventional HAWT technology (with the range depending on the drive-train configuration of the HAWT). CapEx savings range from 5 - 14%, driven by the removal of components such as a gearbox, yaw system, and large generator. The OPEx savings vary between 21 - 45% due to the reduced failure rates without a gearbox and lower heights of components (secondary rotors). These new estimates fall within the ranges predicted by [28]. The author concludes that further savings can still be realized by considering the (i) floating case (which has been shown to be favorable for VAWT technologies), (ii) increased capacity cases, which could be reduced by increasing the number of primary rotor blades and secondary rotors, and (iii) reduced wake losses and increased power densities of VAWT farms.

2.6.2 Primary rotor

The aforementioned works explore the cost savings of the X-Rotor concept and its suitability for the offshore market in the near future. However, several of these studies rely on the overall aerodynamic feasibility of the primary rotor to extract mechanical power from the wind, as well as the associated blade loads. The work of [105] modeled the coned-shaped primary rotor of the X-Rotor concept using a double-multiple stream tube (DMS) model, with the objective of creating a framework for fast aerodynamic computations for controller design. The model was validated against experimental data from the Sandia 17m arced Darrieus VAWT. The model matched the instantaneous and time-averaged blade load measurements to a high degree, as well as power performance at tip-speed ratios in the range of 3 - 6. Next, the DMS model has been compared to the higher fidelity lifting line theory tool CACTUS, demonstrating a high degree of similarity in power performance at tip-speed ratios below 4.

This model was included in a benchmark of numerical models at a range of fidelity by [106]. Low (2DAC actuator cylinder and DMS), medium (QBlade, CACTUS), and high (URANS, PFLOW) fidelity results were compared for the aerodynamic performance of the primary rotor of the X-Rotor concept, shown in Figure 2.16. Additionally, cases with passive

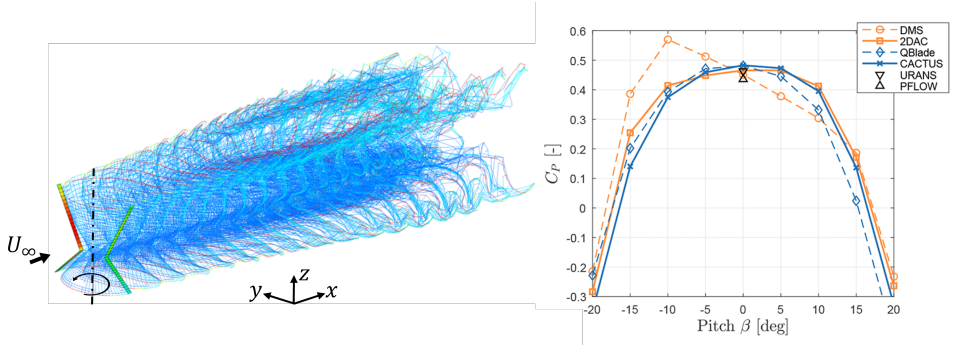


Figure 2.16: Numerical results from the X-Rotor benchmark study of [106] (Left) the X-Rotor blade discretization and vortex lattice system from QBlade simulations (Right) primary rotor power coefficient C_P as a function of passive blade pitch β for several numerical models at a tip-speed ratio of $\lambda = 5$.

pitch adjustments applied to the upper blades were simulated with low and mid-fidelity tools. For the design case (tip-speed ratio $\lambda = 5.0$ and pitch 0), all of the models agree to a very high degree, with a maximum difference of C_P of 0.05. Meanwhile, the low fidelity models under-predict the thrust coefficient C_T by up to 0.1. Furthermore, the low fidelity models deviate from the middle fidelity models for the cases with pitched blades, with differences increasing as the tip-speed ratio increases, credited to the breakdown in the streamtube assumptions for the DMS and 3D effects for the 2DAC, as well as the lack of accounting for the vertical induction imposed by the coned blades of the X-Rotor. The time-resolved vertical induction modeled by the middle fidelity tools was discussed, which further highlighted the increased three-dimensionality of the X-Rotor compared to H-Type designs.

Finally, a recent study by [107] investigated the effect of the blade inclination angle of a vertical-axis wind turbine on performance. The coned blade feature of the X-Rotor was a design choice aimed at increasing the swept area of the primary rotor and hence mechanical power extraction from the wind [28]. A parametric study was performed on design variables such as inclination angle, chord distribution, and blade length using the 2DAC approach, which was validated against higher fidelity models in the work of [106]. The study found that for cases with fixed chord lengths (straight blades), power gains between 10% - 68% compared to equivalent H-type geometries can be achieved, depending on the blade length. However, when considering the maximum blade stresses at the root section and the associated blade volumes, the optimal design will be an H-type rotor (no inclination angle). However, when allowing for varying chord distributions (tapered blades as in the X-Rotor design), the power gains ranged between 10% - 69% whilst satisfying limits on the root bending stress. Furthermore, optimal design reduced rotor torque (used as a proxy for generator size and cost) by 3%-9%. The authors note that this exploratory analysis of blade inclination angle could be improved by performing a more detailed aero-structural analysis, including factors such as fatigue and extreme loading cases in the optimization, as well as the impact of rotor loads on the supporting structure. Furthermore, it is important to consider the limitations of the 2DAC model, namely the lack of dynamic stall modeling (which would be relevant given the varying speed ratio along the inclined blade span) and

the neglection of 3D flow effects stemming from inclined blades, which have been shown by [106] to be of importance for designs such as the X-Rotor.

2.6.3 Secondary rotor and control

The aforementioned studies focus on the aerodynamic modeling of the primary rotor. However, the operating conditions are strictly linked to the desired inflow conditions and performance of the secondary rotors. Although the "aerodynamic gearbox" concept and working principle of the X-Rotor was touched on by [28], an in-depth analysis of the implications of this working principle of the operating conditions and design of the secondary rotors was not discussed. The work of [108] provides a comprehensive overview of the "aerodynamic gearbox" concept and elucidates the maximum achievable conversion efficiency between the primary and secondary rotors through a parametric study.

The principle of the "aerodynamic gearbox" can be summarized by Equation (2.1).

$$\underbrace{\frac{1}{\omega_1}\frac{1}{2}\rho A_1 C_{P1} U_\infty^3}_{\overline{Q_1}} = N R_1 \underbrace{\frac{1}{2}\rho A_2 \overline{C_{T2} U_I^2}}_{\overline{T_2}} \tag{2.1}$$

Subscripts $_1$ and $_2$ correspond to variables for the primary rotor and secondary rotor, respectively. The overline variables denote time averages over one primary rotor revolution. The rotational frequency of the rotors is denoted by ω, ρ is the air density, A is the rotor area, N is the number of secondary rotors, U_∞, and U_I are the freestream and secondary rotor indecent velocities, and C_P and C_T are the power and thrust coefficients, respectively. This balance between the primary rotor torque Q_1 and secondary rotor thrust T_2 defines an equilibrium point where the primary rotor speed is controlled entirely by the thrust on the secondary rotors, which are the only sources of electrical power as the generators are mounted at the blade-tips. Note no counter (retarding) torque is imposed on the primary rotor as the primary rotor shaft is not connected to a generator.

Before proceeding with the parametric study, the design limitations of the secondary rotors are elucidated, which were also touched on by [28]:

1. The tip speed of the secondary rotor should be **low enough** to avoid compressibility effects and excessive acoustic emissions.

2. The rotational frequency should be **high enough** to maintain the feasibility of direct drive without compromising the conversion efficiency in the generator.

These limitations define upper limits in the product of the primary and secondary rotor tip-speed ratios and the secondary rotor radius.

Given the locations of the secondary rotors, they will experience a unique aerodynamic environment. These features have been elucidated by [108] and include:

1. Orbital motion
   (a) A phase-dependent shear profile
   (b) Curved wake
   (c) A phase-dependent yaw offset

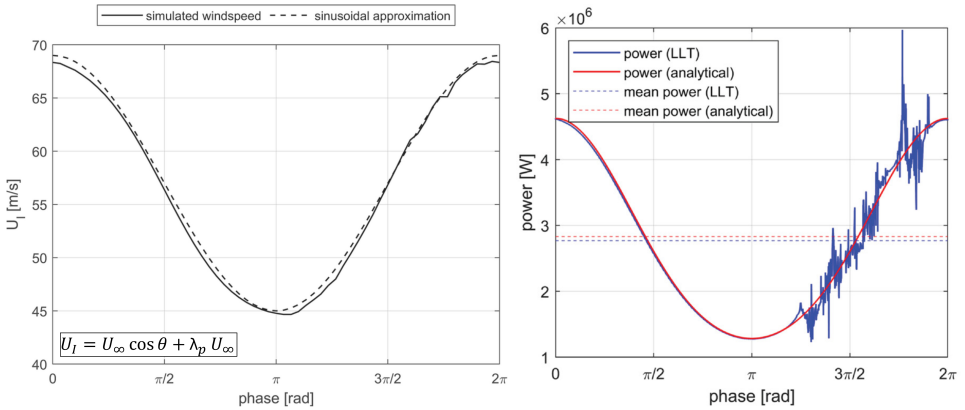


Figure 2.17: Numerical results from [108] (Left) QBlade simulated effective inflow velocity of the secondary rotor U_I versus the sinusoidal approximation, calculated using the expression on the bottom left. (Right) A comparison between the QBlade simulated (LLT) secondary rotor power and prediction using a BEM (Blade Element Momentum) approach (analytical). The dashed lines indicate the cycle-averaged values.

2. Secondary rotor self-wake interaction
3. Coupled effects between the primary and secondary rotors
   (a) Tip-vortex interactions
   (b) Primary rotor wake-dependent inflow on the secondary rotors

Some of these effects are investigated by [108]. First, the analytically derived incident velocity of the secondary rotors (sum of freestream component and primary rotor blade tip speed) is validated. Simulations of the primary rotor wake without the secondary rotors using QBlade are used to evaluate the hypothetical frontal area-averaged normal velocity of a secondary rotor as a function of the primary rotor phase. The two curves show an excellent agreement with minor differences near phases where blade-vortex interactions are expected for the primary rotor, as shown in Figure 2.17. Next, an analytical model was derived using a BEM approach with higher fidelity simulations of an isolated secondary rotor in orbital motion using the lifting line code Qblade. Here, a comparison between the primary rotor phase-dependent power and thrusts shows an excellent agreement in the upwind half of the cycle. However, in the downwind half starting at a phase of around $\theta = 225^\circ$, large fluctuations in the power and thrust of the secondary rotor are evident in the QBlade simulated values, as shown in Figure 2.17. This is due to the self-wake interaction of the secondary rotor, which is not accounted for in the analytical BEM approach. Nonetheless, the cycle-averaged power and thrusts yield differences of 2.2% and 3.1%, respectively.

Although the study by [108] provides a study of secondary rotor design that could achieve the "aerodynamic gearbox" principle of the X-Rotor, the complementary controller design required to maintain the optimum performance at different operating conditions is discussed by [109]. Four modes of operation with different control strategies are defined, namely:

- **Constant rotor speed (Mode 1):** at very low wind speeds.
- **Maximized energy capture (Mode 2):** at intermediate wind speeds.
- **Pre-emptive pitching (Mode 3):** at wind speeds just below the rated wind speed.
- **Constant torque and rotor speed (Mode 4):** at wind speeds above the rated wind speed.

The developed control strategy was tested using a primary rotor phase-resolved non-linear model in Simulink. The results show that the controller can successfully regulate an X-Rotor model with sufficient complexity of dynamic properties across all modes.

2.6.4 Other studies on the X-Rotor

This thesis focuses on the aerodynamics of the X-Rotor primary and secondary rotor wake. Nonetheless, for completeness, an overview of studies concerning other aspects of the X-Rotor design process is provided. Studies regarding the pile design and support structure are provided by [110] and [111], respectively. Furthermore, studies around the direct drive solution and the generator and transformer design for the secondary rotors are provided by [112–114].

2.7 Multi-rotor Systems

The previous sections provided insight into the wake dynamics and state-of-the-art for isolated VAWT rotors. As briefly described in Chapter 1, Multi-Rotor Systems also offer relevant advantages towards high-energy density applications in offshore settings. An MRS is described as a system that includes several smaller rotors mounted on a single support structure. A comprehensive overview of the origins and history of MRS is provided by [26], which dates the first conceptualization to the 1930s by Hermann Honnef. Today, interest in MRS is growing, largely because of their ability to address the challenges associated with scaling up traditional single-rotor turbines, which often lead to substantial increases in both weight and cost, as discussed by [36]. A comprehensive overview of the scaling advantages of MRS is given by [115], which includes reduced blade mass and costs for a matched capacity, reduced rotor-nacelle assembly weight and costs, ease of installation, repair, and transportation of smaller rotors. Other operational benefits have also been hypothesized, which could lower the energy cost, such as the flexibility of operating individual rotors at different speeds, yielding higher average power outputs, or even subsets of rotors while others undergo maintenance. The latter, of course, could lead to imbalanced loads on the structure, which would need to be considered.

In addition to the economic benefits of MRS, several studies have demonstrated the aerodynamic benefits of closely spaced co-planar rotors. The study of [116] compared the flow of a 7-rotor MRS to an equivalent single rotor using numerical simulations, concluding an overall power increase of 3%. The results suggested an acceleration of the flow on the rotor plane induced by cumulative flow blockage, boosting the performance of centrally placed rotors. The aforementioned design case was experimentally validated by [117] via flow measurement in the induction region and wake of an MRS made of actuator disks at varying inter-rotor spacings. The results confirmed a performance increase (measured

streamwise thrust) of the centrally placed rotor, which diminished with increased rotor spacing compared to a single rotor case. Meanwhile, the neighboring rotors along the perimeter demonstrated negligible performance differences. Numerical studies have also confirmed the performance enhancement of closely spaced rotors in wind farm settings. The works of [118, 119] confirmed the performance enhancement of laterally spaced rotors, which increased with higher thrusts and reduced spacings, reaching improvement factors of 1.1. However, the benefits diminish once downstream rotors are accounted for on the farm due to the overall blockage increase.

Despite the many advantages MRS offers, there are also drawbacks. One significant hurdle of multi-rotor designs is the increased complexity of the system. Adding multiple rotors requires a more intricate support frame at the tower top to hold and yaw the assembly, resulting in an additional mass of steel and increased structural load at the top of the tower. This can offset some of the weight savings achieved by the aforementioned rotor-nacelle assembly, potentially adding complexity and cost to the tower design. As highlighted by [26], new challenges arise, such as the design and implementation of a yawing mechanism and structural challenges associated with the drag of large-scale supporting frames. Finally, although the benefits of closely spaced rotors have been investigated, as mentioned above, the aerodynamics of MRS are more complicated when considering the interactions between rotors and the influence of wind shear across the assembly, as highlighted by [115].

2.7.1 MRS wakes

The wakes of such devices is still an active research topic. As described in Chapter 1, wake recovery is critical for achieving the goal of high-energy density wind farms. The work of [120] explored the impact of geometric and operational parameters, such as rotor spacing, number of rotors, and rotational direction, on the wake topology as well as recovery rate when compared to an equivalent single rotor system using large-eddy simulations. The work highlights the transition of localized high velocity-deficit regions behind each rotor in the near-wake of the MRS towards a single combined wake structure in the far-wake. An analysis of the momentum recovery demonstrated an accelerated wake recovery of the MRS in the near-wake before approaching conditions similar to those of the single rotor case upon wake merging. These results are consistent with the study of [121], which highlighted the almost two-fold increase in wake recovery downstream of the MRS compared to the single rotor case. Increasing the rotor spacing yielded lower velocity deficits in the near wake with a delayed approach to the single rotor case. Results by [117] confirm this through experimental measurements of an MRS made of actuator disks. Furthermore, the experimental work of [122] elucidates the physical process that drives the individual rotor wakes to merge. The impact of increasing the number of rotors (while decreasing their size) for the MRS case was twofold. Although the rate of wake recovery of the individual rotors increases with the increasing number of rotors, the transition towards the uniform wake case was accelerated. Varying combinations of rotation direction for the rotors yielded minimal benefits in the wake recovery rate. This is explained by the fact that the augmented swirl motions cannot lead to enhanced momentum entrainment from a wake edge without sacrificing another. Field measurements of the Vestas 4R-V29 MRS demonstrator [29] compared LES and RANS simulated flow in the near and far wake with LiDAR measurements. The results revealed a power performance increase on the order

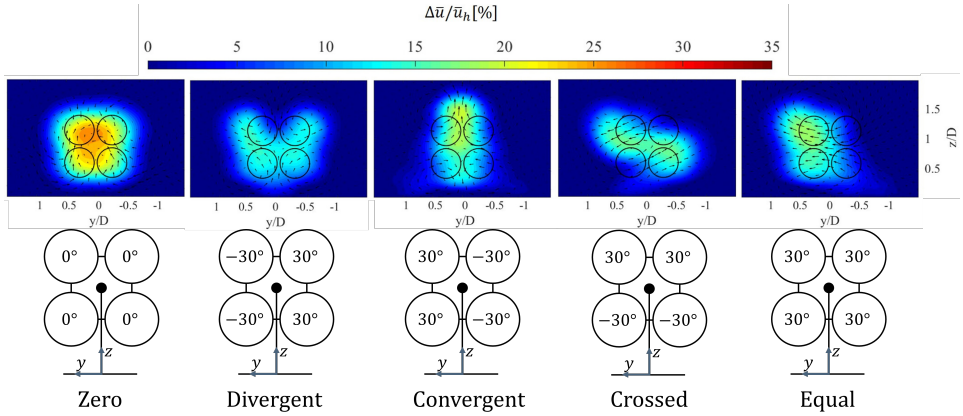


Figure 2.18: Normalized streamwise velocity deficit of a multi-rotor obtained using LES at $x/D = 6$, adapted from [123]. The schematic below each panel shows the respective combination of yaw angles γ for each rotor.

of 2% depending on the inflow conditions compared between an MRS with all four rotors operating versus just one. However, the wake measurements revealed notable differences in the near-wake ($x/D \leq 2$), with the field measurement revealing earlier onsets of wake merging and larger flow deficits compared to the numerical simulations. Meanwhile, in the far wake, the velocity deficit profiles yield a closer match with the numerical results.

2.7.2 Wake steering for MRS

Exploratory investigations have been conducted on the wake steering potential of MRS by introducing yaw control as an extra degree of freedom. The work of [123] investigated the wake steering potential of an MRS with four uniformly spaced rotors with individual yaw control using numerical simulations. A subset of the results using LES are presented in Figure 2.18 for five combinations of yaw operation. Each of the combinations yielded a distinctive mode of wake modulation compared to the baseline case (zero). The divergent and crossed modes of operation resulted in significant wake expansions with lower velocity deficits in the near-wake. Meanwhile, the convergent and equal modes of operation yielded wake contractions and redirection in the vertical and lateral directions, respectively, confirming a large recovery in the far wake. A power analysis highlighted the large increase in available power for a hypothetical downstream rotor, reaching an increase by a factor of 1.3 at $x/D = 7$ compared to the baseline case. However, when considering the total power (i.e., the power of the upstream rotor and potential downstream), the gains of the yawed cases exceeded those of the baseline case only in the near wake (up to $x/D = 5$) before falling below the baseline condition. The authors highlight that the gains in performance in larger wind farm settings would be higher as the benefits of the yawed wake would be experienced beyond the second row of turbines. As in the case for wake steering through yaw misalignment for HAWTs, discussed in Section 2.4.1, the yawed turbine experiences a performance penalty, which in this case is 24% at $\gamma = 30^\circ$.

3

Methodology: experimental techniques for wake measurements

The main experimental techniques used in this dissertation are discussed in this chapter, providing examples of each in the context of vertical-axis wind turbines and wind energy when possible.

3.1 Introduction

Wind tunnel experiments for wake measurements are a common technique due to their repeatability and control over key parameters such as wind speed, turbulence intensity, wind direction, etc. These make the results of wind tunnel campaigns crucial for the validation and development of numerical models, which can be extended toward larger test matrices for wind farm applications. In this chapter, the flow measurement techniques used in the wind tunnel for this thesis, namely Particle Image Velocimetry (PIV), will be introduced, with examples of their applications to wind turbines wake measurements.

3.2 Working principle of particle image velocimetry

PIV is a non-intrusive optical measurement technique used to measure the temporal and spatial evolution of tracer particles in a flow, yielding the final desired product of vector fields. This technique is often used in lab settings where the measurement domain and flow conditions are carefully regulated. The technique can be split into several classifications depending on the number of spatial dimensions measured (classified as D) and the number of components the resulting vector field yields (denoted as C). A simple planar PIV (2D-2C) setup is shown in Figure 3.1 with all of the main features of the setup included.

A PIV setup consists of three main components, namely, seeding, illumination, and imaging. For most applications, tracer particles need to be added to the flow. These can take several forms depending on the medium that is being seeded (liquid or gas) and the desired particle size. A comprehensive overview of the most common seeding techniques is provided by [124]. Next, the seeding must be illuminated in either a discrete plane (planar and stereo-PIV) or volume (tomographic) twice within a known time interval. The two light pulses needed for illumination are at times t_0 and $t_0 + \Delta t$, respectively. Finally, the scattered light resulting from the illumination and seeding has to be recorded by a digital camera.

The subsequent steps for interpreting the recorded images to generate vector fields are calibration, evaluation, and post-processing. The calibration step yields a relationship between the displacement of a particle in a recorded image plane and the displacement of the particle in the flow itself. Typically, an image filtering step is applied within the workflow to account for reflections and optical occlusions when measuring around complex geometries. Next, a cross-correlation-based algorithm is used to determine the average particle displacements within pre-defined integration windows. Finally, post-processing steps are applied to remove possible invalid measurements.

In this thesis, stereoscopic (2D-3C) and tomographic (3D-3C) PIV setups were used, which will be discussed in more detail in Section 3.3 and Section 3.4, respectively. A schematic of the fundamental elements for tomographic PIV is shown in Figure 3.1.

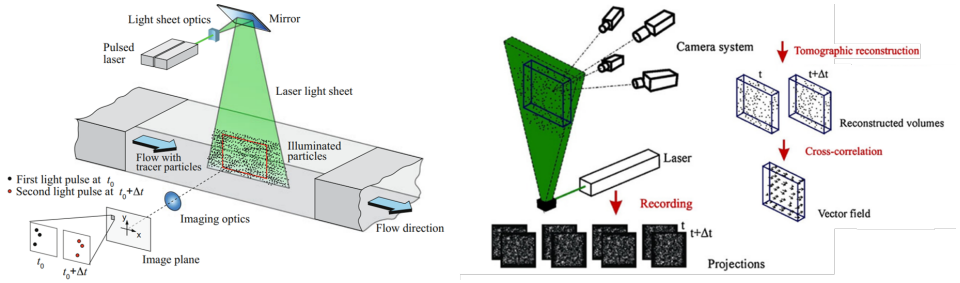


Figure 3.1: Schematic illustrations of example PIV setups. (Left) Planar PIV setup, adapted from [124] (Right) Tomographic PIV setup, adapted from [125].

3.3 Stereoscopic particle image velocimetry

As described in Section 3.2, planar PIV is 2D-2C and does not account for any out-of-plane velocity components. Although 2C would be sufficient for some applications, for highly 3D flows, capturing the out-of-plane velocity component is critical. Stereoscopic PIV is a 2D-3C technique that extends on the baseline principles discussed in Section 3.2. Two cameras are arranged at different viewing angles concerning the measurement plane to allow for "stereoscopic vision," similar to human eyes, and effectively yield the reconstruction of three velocity components on a 2D plane [124].

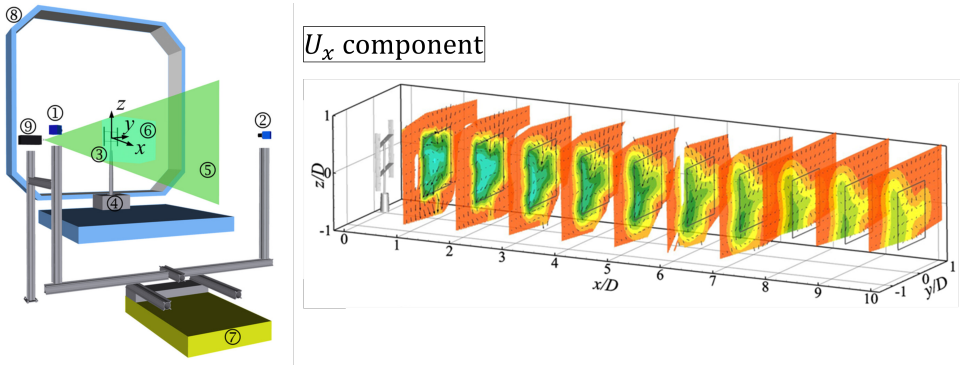


Figure 3.2: Example of a lab-scale stereoscopic PIV experiment of a VAWT wake adapted from [25]. (Left) Rendering of the experimental setup with the main components of the measurement system labeled, including the two cameras (1,2) and laser (9). (Right) Resulting wake measurement in the yz-plane showing the streamwise flow component U_x.

An example of a stereoscopic PIV system for studying a VAWT wake is presented in Figure 3.2. The setup highlights the orientation of the planes in the global reference system, and the presented results show the out-of-plane component. As the wakes of VAWTs are very three-dimensional, it is common for experiments concerning VAWT wakes to be 2D-3C setups.

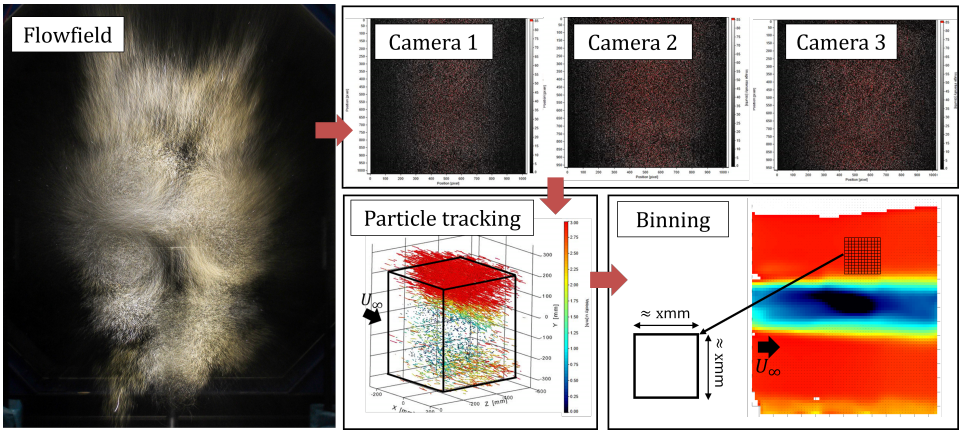


Figure 3.3: Visualization of the main steps for particle tracking velocimetry. Images are recorded at a predefined frequency using three cameras. Then, a 3D triangulation and tracking algorithm is applied to yield time-resolved trajectories of individual particles. Finally, the data can be interpolated and binned onto a Cartesian grid of a predefined resolution.

3.4 Volumetric particle tracking velocimetry

Particle Tracking Velocimetry (PTV) is a Lagrangian measurement technique that tracks individual tracer particles to reconstruct their trajectories in three-dimensional space, providing high-resolution flow field data. An example setup is shown in Figure 3.4 for the study of a HAWT wake [91]. A set of high-speed cameras is used to capture images of Helium-Filled Soap Bubbles (HFSB), which are illuminated by LED flashlights. This system yields time-resolved measurements of flow structures, as seen in Figure 3.4. In addition to this, the system can be used for large-scale measurement applications, as one measurement volume can be in the range of $0.4 \times 0.7 \times 0.7$ m^3 [91]. Combining this system with the traversing bed, as shown in Figure 3.2 (yellow device), would yield an even larger measurement volume.

The main steps of particle tracking velocimetry are visualized in Figure 3.3 using images and data from the wind farm measurement campaign (Chapter 4). The HFSB tracers are illuminated using LED Flashlights at a predefined frequency. A series of three cameras records the HFSB before feeding the data into a particle tracking algorithm. In this thesis, the "Shake-the-box" algorithm is used to generate time-resolved particle tracks [126]. This method involves several steps, including iterative particle reconstruction (IPR) to determine initial 3D particle positions, predictive tracking using a motion model, and an optimization step where particle positions are "shaken" to minimize re-projection errors across multiple camera views. Outliers are removed, and trajectory gaps are bridged to ensure smooth, time-resolved particle tracking. The final refined trajectories provide accurate Lagrangian flow field data. Next, to obtain spatially and temporally averaged data, the tracks are projected and binned onto a Cartesian grid with a predefined resolution.

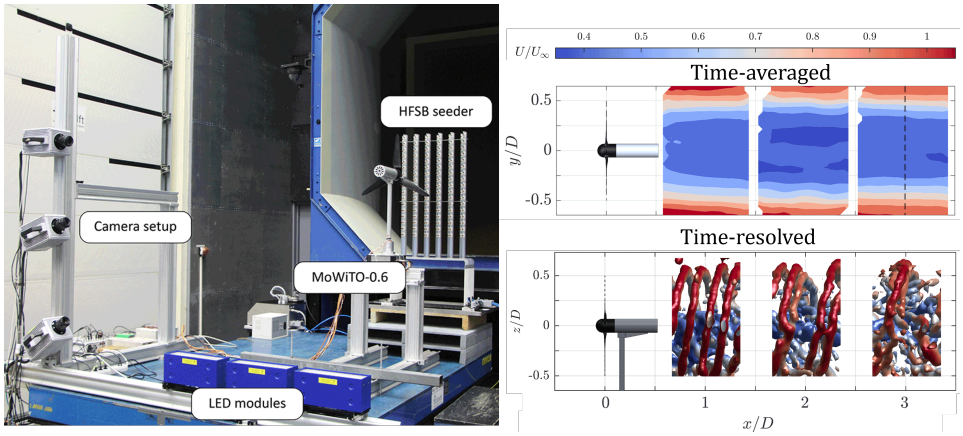


Figure 3.4: Experimental measurement campaign of a HAWT wake in TU Delft's OJF using tomographic measurement setup, adapted from [91]. The experimental setup is shown on the left, and the main components are labeled. On the right, the time-averaged wake at the symmetry plane and a phase-locked result of the blade-tip vortices are presented.

3.4.1 Examples of 3D wake measurements for VAWTs

The stereoscopic PIV measurement technique provides three-dimensional data but is limited to a 2D plane. Given the dominant three-dimensionality of the VAWT wake, which is further attenuated when using the "vortex generator" mode of wake re-energization, having fully spatially resolved 3D data is preferable. The literature on experimental 3D-resolved wakes of VAWTs in wind tunnel settings is limited [61, 127, 128] and is not available for rotors using the aforementioned wake control strategy and for far wake measurements. A subset of some of the 3D wake VAWT measurement campaigns is shown in Figure 3.5. The image on top shows one of the only field experiments that measure the wake of a VAWT [21]. This study is unique as it offers 3D-resolved measurements in the near-wake of a full-scale VAWT under normal operating conditions in realistic (outdoor) conditions, highlighting the dominant CVP in the streamwise direction. The image on the bottom left shows a top-view image of a VAWT in a wind tunnel setting with HFSB as tracers. A subset of the streamwise vorticity results is shown as well, once again highlighting the dominant CVP. This investigation by [61] was extended to two closely spaced rotors in co- and counter-rotating operational conditions, with measurements extending up to two diameters (2D). The image on the bottom right demonstrates the volumetric measurement technique using HFSB to measure the tip region of H-type VAWT [127], with a subset of tip-vortex structures shown.

Although these studies employ 3D measurement techniques, they are limited to the near-wake or even the blade tip region. Furthermore, they do not include the effects of wake re-energization methods on VAWTs. This research gap will be filled in this thesis.

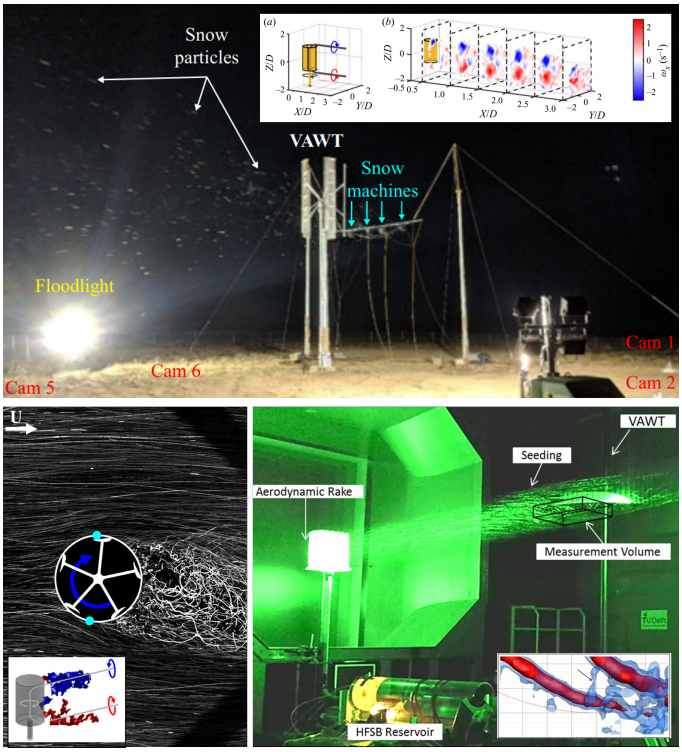


Figure 3.5: Examples of 3D resolved VAWT wake measurements. (Top) Experimental outdoor setup and a subset of streamwise vorticity results of the measurements of the near-wake structure of a full-scale VAWT, adapted from [21]. (Bottom left) Top-view image of HFSB tracers around an H-type VAWT measured in a wind tunnel, with a subset of the results showing the streamwise vorticity structures, adapted from [61]. (Bottom right) Experimental measurements of an H-type VAWT at TU Delft's Open-Jet Facility (OJF) using HFSB as tracers. The setup and subset of the results of phase-locked tip-vortex structures are adapted from [127].

II

H-type VAWT wind farm

4

Experimental demonstration of a high-density VAWT wind farm

The present study extends the idea of the VAWT vortex generator mode for wake recovery on a wind farm scale, where upstream turbines entrain vertical momentum for those downstream. The study provides an experimental wind tunnel demonstration of the passive "vortex generator" control technique applied to an array of nine H-type VAWTs arranged in a grid layout. Volumetric particle tracking velocimetry measures the wake within the simulated wind farm. The results demonstrate the strong dependence of the wake topology of a VAWT on the streamwise vorticity system, which can be effectively modified by pitching the blades and subsequently changing the load distribution of about the different quadrants of a VAWT. An increase in momentum entrainment in the wake is observed for both "vortex generator" modes of operation, highlighting the potential towards the goal of enhanced energy density. Measured increases in available power within the farm reach factors of 6.4 and 2.1 for the pitch-in and out cases, respectively, considering potential rotors directly in line with those upwind.

This chapter is based on **Bensason D.**, Mulay J., Sciacchitano A., Simao Ferreira C. Experimental demonstration of regenerative wind farming using a high-density layout of VAWTs, *Wind Energy Science*, 2025 [129].
The data supporting this study is openly available in the 4TU.ResearchData repository at `https://doi.org/10.4121/7bf33a69-6542-41ee-af6d-3fd621b802e1`.

4.1 Introduction

The shorter wake lengths of VAWTs and affinity for farm-scale applications were discussed in Chapter 2. Furthermore, the promise of the passive wake control technique coined the "vortex generator" for enhanced re-energization was highlighted by [25].

By simplifying the load distribution to an idealized actuator cylinder surface [43], the deformation and deflection of the VAWT wake topology were linked to the distribution of load discretized between the different quadrants of the rotor cycle. By redistributing the load among the upwind, downwind, windward, and leeward quadrants, the strength of the trailing vortical structures shed in the respective quadrants can be increased or decreased, leading to modification of the wake topology. This concept was further developed and confirmed via numerical simulations [44, 130]. An effective method to modify the load cycle of a VAWT is through blade pitch. Experimental results by [56] demonstrated the impact of cyclic and fixed blade pitch motions on the normal load and subsequent thrust vectoring of an H-type VAWT, confirming the augmentation and redistribution of load among the different quadrants of the cycle. Subsequent planar flowfield measurements at the mid-span of the rotor blade at different phases confirmed the normal load distribution with varying pitching schemes [131]. The work of [25, 101] measured the wake of an H-type VAWT using a stereoscopic measurement system at discrete downwind plans ranging up to 10D with different fixed pitch offsets applied to the blades, namely a case where blades are pitched inward (inside the rotor swept volume) and outward. A comprehensive visualization of the wake deformation and deflection as a function of the augmented trailing vorticity was revealed, demonstrating significant gains in available power for potential downstream rotors of up to 150% at 5D. An enhanced advective momentum flux above and below the rotor was observed for the case where the load is shifted towards the upwind half of the blade cycle. In contrast, the lateral advective kinetic energy entrainment is increased when the load is shifted towards the downward half.

Current experimental studies, which are 2D2C or 2D3C, provide limited information on the three-dimensionality of a VAWT wake topology and vortex strength due to the intrinsic limitations of planar measurements. This is further magnified by the use of blade pitching schemes, which rely mainly on the modification of these vortical structures, leading to heavy 3D wake phenomena [44]. The literature on experimental 3D-resolved wakes of VAWTs in wind tunnel settings is limited, as discussed in Chapter 3. Further, the experimental demonstration with a 3D resolved flowfield of the potential of blade pitch towards wake re-energization in a farm setting has not been investigated to date.

The goal of this chapter is to report the 3D-resolved wake measurement results of a wind tunnel-scaled high-energy density wind farm made of VAWTs with and without wake control strategies in a standard grid arrangement. Although staggered as opposed to in-line arrangements have been shown to be superior for optimum farm performance [67, 70], the objective of this work is to highlight the efficacy of the passive blade pitch recovery strategy for the most detrimental conditions for wake losses. The results from this study provide a basis for ongoing and future numerical model validation. The flow fields at the inflow, within, and outflow of the farm are measured using three-dimensional Lagrangian Particle Tracking, focusing on the central column of the farm. This work offers a detailed analysis of the vortical structures in the wind farm and how the wake topology changes when these structures are enhanced. An overview of the working principle of the "vortex generator"

mode of VAWTs and its application towards regenerative wind farming is provided in Section 4.2. The 3D wake measurement technique and wind tunnel simulated wind farm setup are described in Section 4.3. The discussion of the results given in Section 8.4 focuses on the modification of the trailing vorticity system and the subsequent impact on the wake topology. The wake recovery is quantified, and the driving mechanisms for recovery are isolated via the energy budget analysis.

4.2 Working principle of the vortex-generator mode

The working principle of an H-Type VAWT as a vortex generator has been numerically and experimentally explored by [25, 101], in which the link between the wake topology and deflection to the quadrant discretized blade load distribution is evaluated.

The working principle can be best described by simplifying the phase-dependent VAWT blade load as an idealized Actuator Cylinder (AC) that includes radially dependent normal loads, which represent the blade integrated loads [43], as visualized in Figure 4.1. The AC simulated normal loading and wake characteristics for VAWTs have been validated using high-fidelity models and experimental results by [44, 130, 132]. The work of [25] demonstrated that a modification in the idealized load distribution of the AC could lead to enhanced wake deformation and deflection depending on the load distribution between the different quadrants. The load profile of the AC can be modified in several ways, including pitching the struts connecting the blades to the tower [97, 98], inclining the angle of the rotor blade [95], and applying blade pitch [56]. The present work uses the blade pitch method for modifying the idealized AC load. As a proof of concept for using this "vortex generator" mode for a wind tunnel simulated wind farm, fixed-pitch offsets are used (constant applied throughout the entire rotor cycle), as in the work of [25].

A top-view schematic representation of the idealized actuator cylinder load for the "vortex generator" cases is shown in Figure 4.1, adapted from the work of [25], for a rotor rotating counter-clockwise. Three cases are shown: the baseline, where no fixed pitch is applied; the pitch-in case, where the blade is pitched towards the supporting tower; and the pitch-out case, where the blade is pitched away from the rotor volume. The VAWT cycle is discretized in four quadrants, namely the upwind windward UW $0^\circ < \theta < 90^\circ$, upwind leeward UL $90^\circ < \theta < 180^\circ$, downwind leeward DL $180^\circ < \theta < 270^\circ$, and downwind windward DW $270^\circ < \theta < 360^\circ$. The actuator circumference (corresponding to the upper blade-tip trajectory) is color-coded based on the direction of the trailing tip-vortex shed from each quadrant in the inertial frame of reference, with red and blue as anti-clockwise and clockwise, respectively. This cyclic variation in tip-vortex direction is intrinsic to VAWT aerodynamics and is a product of the variation in relative angle of attack and, subsequently, the direction of circulation of the blade-tip vortex [41, 134]. The normal arrows represent the blade-integrated loads. Below each mode, the projected frontal area of the top half of the rotor ($z/D > 0$) (green-shaded region) at a generic downstream plane is shown with the projected intersections of the quadrant-labeled trailing vortical structures. The directions of rotation of these structures are indicated by arrows embedded in the idealized circular vortex intersection. As the inflow is uniformly laminar and no ground effect is included in this study, the wake topology should be symmetric about the symmetry plane $z/D = 0$. Hence, the vortical structures stemming from the bottom blade tips will be equal and opposite to those generated at the top, in accordance with Helmholtz's theorem.

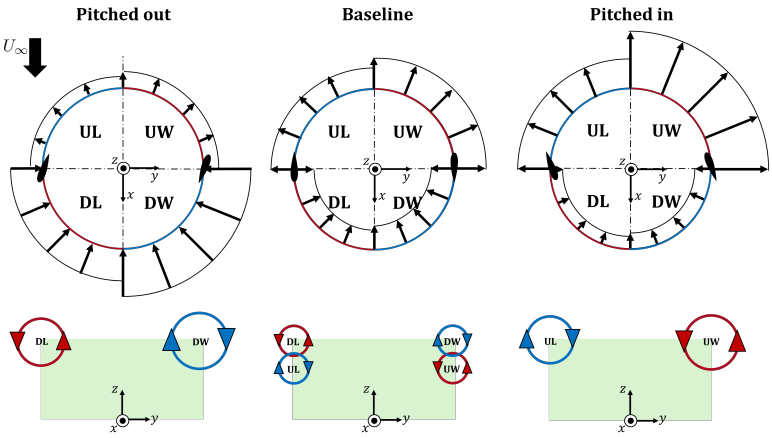


Figure 4.1: Top view schematic of the simplified AC force fields for the three "vortex generator" modes of operations adapted from [25, 133], namely the baseline case (where no pitch is applied), a pitch in case, and pitch out. Blades at a phase position of $\theta = 0^\circ$ are shown at exaggerated sizes and pitch angles to demonstrate the pitching convention. The coordinate systems are shown at the center of the AC, and the rotation direction is anti-clockwise. The quadrants of the idealized AC are labeled as upwind windward UW $0^\circ < \theta < 90^\circ$, upwind leeward UL $90^\circ < \theta < 180^\circ$, downwind leeward DL $180^\circ < \theta < 270^\circ$, and downwind windward DW $270^\circ < \theta < 360^\circ$. The top edges of the rotor cylinder are color-coded based on the direction of rotation in the internal frame of reference of the trailing blade-tip vortices, with red and blue as counter-clockwise and clockwise, respectively. The top half of the rotor's projected frontal area (green) at a generic measurement plane downstream is shown below each mode. The projected dominant quadrant-labeled streamwise vortical structures stemming from the blade tips for each pitch case are shown via circular arrows.

The AC loads shown for a VAWT are simplified to understand the trailing vorticity and subsequent wake topology described in the results that will follow. In reality, the blade load is a result of both the normal and tangential loads, of which the normal is dominant, which varies azimuthally throughout the cycle [56]. Furthermore, under the realistic operating conditions of a VAWT, where unsteady effects are present, such as dynamic stall, turbulence, and dynamic inflow, the load profiles can change significantly. Experimentally acquired blade load profiles as a function of azimuth with variable pitch control are presented by [56] for a straight-bladed VAWT and highlight this non-uniformity. Nonetheless, these schematics are sufficient for describing the impacts of AC load modification on the wake, with each case described as follows:

Baseline case: In the case where no pitch is applied, the AC loading is intrinsically asymmetric. The upwind half of the cycle will experience a higher load than the downwind as the latter involves the blades operating in their own wake [44, 131]. Furthermore, the windward passage of the blade will exhibit larger loads than the leeward due to the higher relative wind speed as the blade moves into the wind. Despite the more favorable load of the upwind quadrants, the trailing vorticity in the near wake of the rotor will exhibit the counter-rotating vortex pairs (CVP) from both halves of the cycle [25, 41, 134]. The aforementioned favorable loading on the windward passage on the blade leads to an intrinsic asymmetry in the wake in favor of the windward side, as shown experimentally by [41, 133].

Pitched in case: When the blades are pitched inward, the load is shifted towards the upwind half, as shown by the increased integrated load magnitude along the upwind quadrants. As a result, the vortical structures generated in the upwind half are energized and become the dominant CVP in the wake, as shown in the projected frontal area, with the less energized pairs stemming from the downwind half charging in direction and merging with the dominant pair, as experimentally demonstrated through phase-locked wake measurements of the near wake of a VAWT by [133]. Once again, the windward side is more energized than the leeward, leading to a stronger UW than the UL vortex, visualized by the difference in vortex size. The impact of this load modification is twofold. Firstly, the domain CVP on the upper tips will induce a significant axial downwash in the wake, with high momentum flow from above the rotor being injected into the volume while the low momentum wake is ejected out laterally. Secondly, given the imbalance in load between the windward and leeward halves of the rotor, a strong lateral force will be imposed on the wake, leading to a lateral deflection of the low momentum flow towards the windward side. The results of [25] have confirmed this mode of operation, highlighting the potential of the enhanced advective momentum transfer between the freestream and wake towards an accelerated wake recovery.

Pitched out case: Finally, when the blade is pitched out, the AC load is shifted toward the downwind half of the cycle. Hence, the rotation directions of the vortical structures shed from the blade tips will be opposite those for the positive pitch case. As in the aforementioned mode of operation, the dominant vortical structures in the wake will lead to a modification in topology, with an induced upwash and downwash in the upper and lower halves, respectively, while high-speed momentum is injected from the sides of the rotor. Meanwhile, the load imbalance between the leeward and windward sides results in a lateral deflection of the wake center towards the leeward side. This mode of operation was also experimentally demonstrated by [25]; however, it showed to have less potential than the pitched-in mode of operation with respect to streamwise momentum recovery, presumably due to the intrinsically lower efficiency in the downwind half of the cycle, as discussed for the baseline case.

A schematic representation of an array of three uniformly spaced inline VAWTs is shown in Figure 4.2 for the three modes of operation. The wake structures at the midplane $y/D = 0$ are represented via gray-shaded areas, with the streamwise velocity profiles at different downstream locations $U_x(x)$ represented via arrows of varying size (magnitude). For this study, the inflow is uniform laminar with speed U_∞ without a ground effect. Hence, the wake structure and re-energization mechanism will be symmetric about the symmetry plane in xy. Additionally, arrows representing advective and turbulent entrainment of kinetic energy in the wake are represented via purple and blue arrows, respectively. The sizes of these arrows reflect the relative magnitude of the contributions in the wake.

For the baseline case, in the near-wake, the wake re-energization is mainly caused by the lateral momentum advection due to the cohesive vortical structures shed in the wake, as included in Figure 4.1 [38]. As the structures diffuse and mix, the wake recovery process will transition towards a turbulent kinetic energy entrainment. With no strong lateral force induced by the rotor load, the wakes of different turbines will continue to superimpose on each other within the farm, growing in size due to the wake expansion.

For the negative pitch case, the advective contribution towards the wake recovery will

significantly increase due to the dominant vortical structures highlighted in Figure 4.1. Given the direction of rotation of the downwind tip-vortex structures, high momentum flow will be injected in the wake from the lateral direction, while the low momentum wake is ejected out above and below the rotor. Hence, the wake will recover more compared to the baseline case, as highlighted by the non-gray shaded regions downstream of the rotor. Meanwhile, the region of flow deficit will grow above and below the rotor compared to the baseline case.

Finally, for the positive pitch case, the streamwise vortical structures injected high momentum flow from above and below the rotor whilst ejecting the low momentum flow laterally outward. Hence, the wake will contract in the axial direction, increasing the availability of high-energy streamwise flow for downstream rotors.

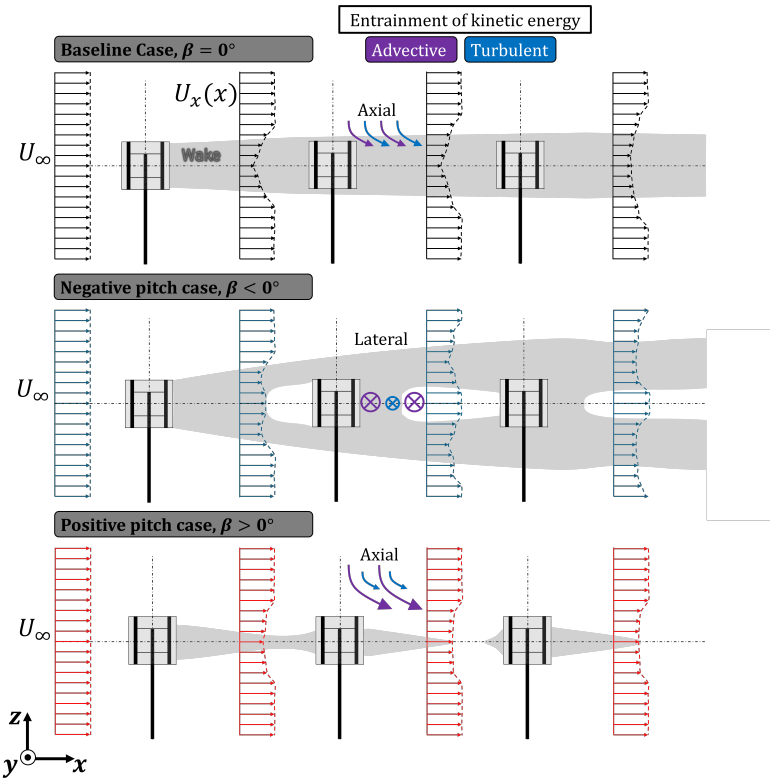


Figure 4.2: Schematic representation of the wake evolution at xz plane ($y/D = 0$) of an array of three uniformly spaced inline VAWTs with laminar-uniform inflow U_∞. The illustration is a simplified adaptation of numerical results obtained by [135]. The gray-shaded region represents simplified wakes, while the white areas show the free stream flow. The profiles of the streamwise velocity $U_x(x)$ within the array for the three pitch cases β are shown in black, blue, and red for the baseline, pitched out, and pitched in cases, respectively. As no ground effect is included in this study, the wake structure and re-energization process will be symmetric about the symmetry plane xy. The advective and turbulent contributions towards the wake recovery for the three modes of operation are portrayed using purple and blue arrows, respectively. The size of the arrows corresponds to the relative contributions of each for the three cases, with the direction labeled above. In this case, the axial corresponds to the directions above and below the rotor (z-axis) and lateral from the sides of the rotor (y-axis).

4.3 Experimental methods

4.3.1 Wind tunnel

The experiments are conducted in the open-jet facility (OJF) of TU Delft's Aerospace Engineering faculty, visualized in Figure 8.2. The tunnel has been used for wake studies of the same VAWT geometry in a single and two-turbine array [25, 73] as well as for other scaled VAWT experiments [41, 131]. The closed-loop wind tunnel has an octagonal outlet of dimension 2.85m × 2.85m with a contraction ratio of 3:1. The jet stream bound shear layer angle and turbulence intensity are reported as 4.7° and 0.5%, respectively [136]. The region of uniform flow extends 6m beyond the tunnel exit, which encompasses the measurement volume for this experiment.

4.3.2 Wind turbine model

The H-type Darrieus VAWT model is designed in-house and is an altered version of the geometry used by [25]. A detailed schematic is provided in Figure 8.3, and illustrated in a wind farm array in Figure 8.2. The rotor geometry is mounted on a rotor shaft with a 10mm diameter and 1100mm height, which runs through a tower. The rotor tower is 700mm tall, made of milled aluminum, and follows a tapered profile with base and tip diameters of 50mm and 25mm, respectively. Further, the tower houses roller bearings at the top and bottom to minimize any deflections of the shaft resulting from imbalances in the rotor. The tower is fastened to an aluminum stand, which connects to an in-house-designed three-component balance. The stand houses a Maxon EC90 260W DC motor, which is controlled via an ESCON 50/5 controller that rotates the rotor shaft at a constant rpm in either a clockwise or anti-clockwise direction. Prior to the wind farm flowfield measurements, the cycle-averaged streamwise and lateral thrust components of the rotor are measured at different tip-speed ratios using the force balance. The force balance has a maximum range of ±50N and a maximum error of $\leq 0.1\%$. Further details of the design are provided by [25].

The rotor geometry consists of two straight untapered blades with a span of S = 300mm fastened to the rotor shaft via two struts separated by 150mm, as shown in Figure 8.3. The struts have an oval-shaped profile with a span, thickness, and chord of 300mm, 4mm, and 30mm, respectively. The blades are made of extruded aluminum with a NACA0012 profile with a chord c = 30mm. The different fixed-pitch adjustments are realized by interchanging modular 3D-printed adapters between the blade and strut at all four connection points, shown in blue in Figure 8.3. The adapters have the same chord and thickness as the struts. In this experiment, the fixed-pitch settings of $\beta = -10^\circ$, 0°, and 10° about the mid-chord are used to allow for a qualitative comparison with the work of [25, 73]. Positive and negative pitch are defined as pitch inward towards the tower and outward, respectively. The rotor diameter is D = 300mm. All components of the rotor are painted black to minimize the reflections during the flow measurement process, described in Section 4.3.3. The rotor solidity is $\sigma = NcS/A = 0.2$, where $N = 2$ is the number of blades and $A = 0.09$ m^2 is the projected frontal area of the rotor. The wind tunnel blockage of a single rotor is 0.011, considering the projected frontal area of the rotor.

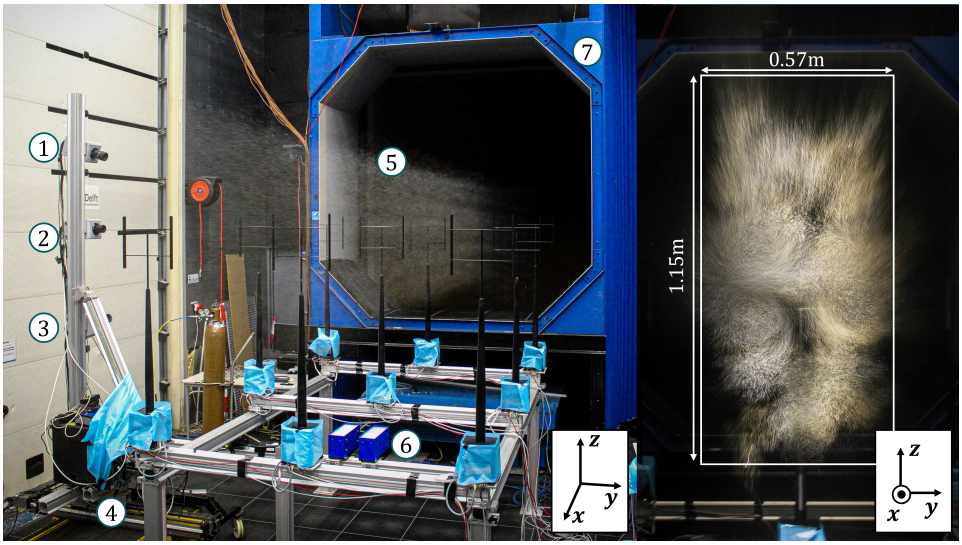


Figure 4.3: Experimental setup in the OJF. (Left) The main components are labeled and defined as follows: ① Camera 1, ② Camera 2, ③ Camera 3, ④ Traversing system, ⑤ HFSB stream tube, ⑥ LEDs, ⑦ OJF outlet. (Right) A close-up image of an illuminated measurement volume with the dimensions of the field of view is marked, showing the deformed stream tube of the HFSB. The coordinate systems for the two panels are shown on the bottom right.

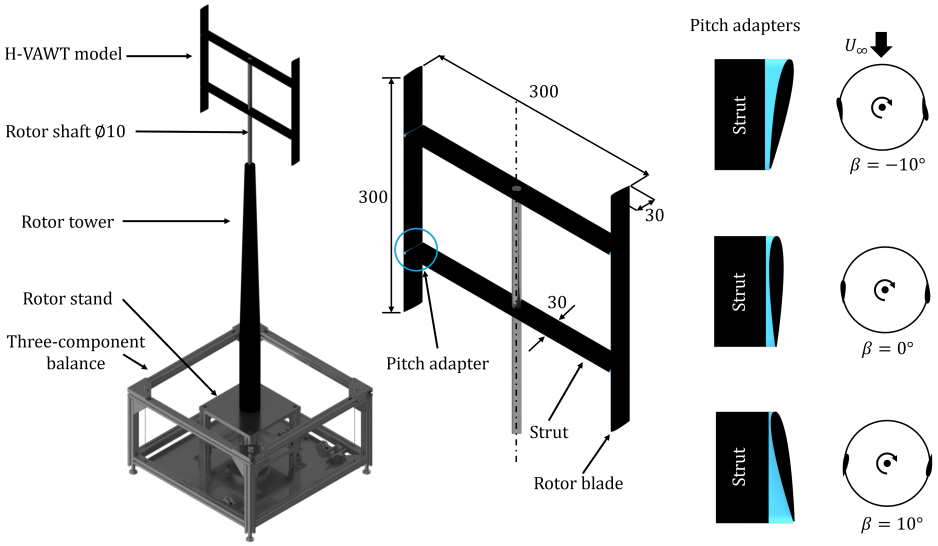


Figure 4.4: (Left) Rendered schematic of the H-type VAWT model mounted on the three-component balance. (Middle) Rendering of the rotor geometry. The turquoise circle outlines one of the pitch adapters situated at the connection point between the blades and struts. (Right) Top-view rendering of the three pitch adapters (turquoise) mounted between the blade and struts, with a pitch towards and away from the tower denoted as positive and negative pitch, respectively. The top-view schematic of the rotor shows exaggerated blade sizes for clarity. The main components of the rotor are labeled, with all dimensions in mm.

4.3.3 Flow measurement system

The velocity fields are obtained through three-dimensional Lagrangian Particle Tracking. Seeding is generated using a rake placed in the settling chamber of the OJF made up of 200 nozzles, each releasing neutrally buoyant helium-filled soap bubbles (HFSB) at a rate of 30,000/sec and an average diameter of 0.4mm [137]. Given the rake dimensions and the contraction ratio of the outlet, the seeded streamtube is approximately 0.57m × 1.2m, as visualized in Figure 8.2. The resulting seeding concentration was, on average, 1 HFSB/cm^3 [127]. The rake has been shown to minimally impact the turbulence intensity of the incoming flow by 0.8% [138]. Given the limited size of the generated stream tube and desired lateral measurement volume, the seeding rake was translated along the width of the tunnel to adequately seed the desired measurement volume, described in Section 4.3.4.

The flow tracers are illuminated from below the farm using LaVision LED Flashlights 300, as shown in Figure 8.2, with a pulse length of 200μs. Images of the illuminated bubbles are recorded using three Photron FASTCAM SA1.1 high-speed cameras (CMOS, 1 MPx, 12 bit, 20 um pixel pitch). Image frames are acquired at a frequency of 500Hz with an image resolution of 1024px × 1024px. Cameras 1, 2, and 3 have mounted lenses of 60mm, 50mm, and 60mm focal length, respectively, with a set numerical aperture of f/22. An individual measurement volume is approximately 0.17m^3, resulting in a digital image resolution of 1.6 px/mm with a magnification factor of M = 0.03. A total of 4600 frames are captured per measurement volume, corresponding to an acquisition time of 9.2s. Given the rotational frequency of the rotor during the wake measurements of ω = 70 rad/s, approximately 102 rotor revolutions are captured. The illumination and imaging are synchronized using a LaVision PTU-X timing device. The cameras and LEDs are mounted rigidly on a traversing bed, visualized in Figure 8.2. This allows for the translation of the measurement volume in the streamwise and lateral directions such that several can be stitched together without the need for re-calibrating the acquisition system, as described in Section 4.3.4.

The acquired frames were processed using LaVisions DaVis 10 software. First, background removal is applied by subtracting a minimum time filter with a kernel of five images. Geometric calibration of the camera positions relative to the measurement domain was performed using a calibration plate, followed by a volume self-calibration using an unperturbed flowfield recording of particles [139]. The residual measurement errors fall below 0.1 pixels for all three cameras. Next, tracer trajectories were evaluated using the Shake-the-Box (STB) algorithm [126]. The number of identified particle tracks per time-step ranges between 8000 and 15,000, depending on the specific measurement volumes in the farm and pitch case, due to the strong deflection of tracers in and out of the field of view. Next, the individual STB volumes measured within the overall farm measurement volume shown in Figure 4.5 are stitched together with the corresponding lateral and streamwise offsets recorded using the traversing system, as described above, yielding a total measurement volume of approximately 5.3m^3. Finally, the binning step involves mapping particle tracks of the fully stitched volume on a Cartesian grid by spatially averaging over smaller cells [140]. In this study, all time stamps are binned together to yield a time-averaged wake measurement. The sub-volume size is 128×128×128 voxels used, where one voxel = 80mm. Given an overlap of 75%, the final grid spacing of the velocity vectors is 19.9mm. A justification of the selected sub-volume size is provided in Appendix A.1, demonstrating its adequacy for capturing the wake scale dynamics in the wind farm.

Pitch case	Description
$\beta = -10^\circ$	The blades of all of the rotors are pitched out
$\beta = 0^\circ$	No fixed pitch is applied to the rotors (baseline)
$\beta = 10^\circ$	The blades of all of the rotors are pitched in

Table 4.1: Overview of the wake recovery strategy test cases

4.3.4 Case overview

The free stream wind speed is constant at U_∞ = 3 m/s. The rotational frequency of all of the rotors is maintained at ω = 70 rad/s, equating to a tip-speed ratio of $\lambda = \omega R/U_\infty$ = 3.5 and diameter-based Reynolds Number of $Re_D = 6.1 \times 10^4$. Previous works have studied the wakes of VAWTs at similar Reynolds numbers [25, 37, 141], concluding that the wake topology is largely Reynolds-insensitive. This corroborates the conclusions drawn by [21], who observed similar wake characteristics between a full-scale VAWT in in-situ conditions and water-channel measurements at a Reynolds number two orders of magnitude lower.

A series of nine identical turbines are arranged in a grid beyond the exit of the OJF, as shown in Figure 8.2 and a top-view schematic in Figure 4.5. The streamwise and lateral spacing between the rows and columns is 5D (1.5m) and 3.18D (0.953m), respectively. The resulting gap between the blades of the peripheral rotors and the projected edge of the outlet is 1.1D. The shear layer of the open jet is reported to increase the turbulence intensity to up to 10% at approximately 0.3D from the outlet edge [136]. Hence, particularly for the positively pitched case, the wakes of the peripheral columns may interact with the shear layer of the jet. While this is a limitation of the experimental facility, the impacts on the wake topology of the central column will be investigated through ongoing numerical validations, discussed in Section 7.5. All rotors operate at the same rotational frequency in the clockwise direction with respect to the incoming flow. The phases of the rotors are not synchronized. The origin of the coordinate system $x = y = z$ =0 is defined as the geometric center of the first rotor in the central column. Note, for the results discussed in Section 8.4, the measured wakes have been mirrored along the $y-$axis as if the rotors rotate counterclockwise for consistency with previous works by [133, 134].

The three modes of operation described in Section 4.2 are used for this experiment. To allow for a qualitative comparison with these previous works by [25], the same fixed-pitch settings of $\beta = -10^\circ, 0^\circ, 10^\circ$ are used. The sign convention is highlighted in Figure 8.3. The case with no wake mixing strategy $\beta = 0^\circ$ will be referred to as the baseline case. The wind farm wake is measured for these three pitch cases independently, where all rotors are pitched by the same amount. Furthermore, the grid spacing between the rotors is kept constant, with no lateral offset spacing between the rotors applied. A description of these three cases is provided in Table 4.1.

As discussed in Section 4.3.3, the full-time-averaged wake of the wind farm is measured by stitching several smaller measurement sub-volumes together using the traversing bed, which has an accuracy of $\pm$ 0.01mm. An example of the boundaries and instantaneous tracked HFSB single measurement sub-volume within the farm domain is shown in Figure 4.5. The overall measurement extent of the volumes at different positions within the farm for the $\beta = 10^\circ$ case is shown in Figure 4.5 via colored lines. The size of the measurement volumes varies between the different farm positions due to the strong wake

deflections experienced for the vortex generator mode cases, leading to frequent areas in the flow void of any HFSB, as shown in Figure 8.2. To account for this, several measurement sub-volumes are captured, accompanied by frequent movement of the seeding rake in the settling chamber, and rigid camera and LED construction are used to distribute tracers more evenly and capture the full wake. The colored lines delineate the overall measurement volume once the individual sub-volumes are stitched together, as discussed in Section 4.3.3. In the inflow of the farm, two sub-volumes are measured. Between the first and second rows, nine sub-volumes are measured. Between the second and third rows, 15 sub-volumes are measured. Finally, in the outflow of the farm, 12 sub-volumes are measured. Note, due to the optical obstructions of the rotors and the nature of the measurement system, the volumes inline with the rotors are omitted from the analysis in Section 8.4. The individual sub-volumes are translated such that there is sufficient overlap between them within a given domain—these range between 0.7D and 1.6D in the streamwise direction and 0.3D and 1D in the lateral direction. The final measurement domain encompasses a total streamwise distance of 17.6D, extending 2D and 5.6D in the inflow of the farm and wake behind the far, respectively. The lateral measurement ranges vary between the different sections of the farm (i.e., inflow, behind the first row, second row, etc.). To measure the inflow of the farm, it was assumed that the induction of the third row did not greatly impact the inflow, and hence, first-row rotors were removed, and the inflow of the second row was measured and assumed to be that of the first row. As described in Section 4.2, to avoid the ground effect, the rotors are on a frame of rigid beams, resulting in a clearance between the ground and bottom blade tip of the rotor of 2.2m (7.3D), as shown in Figure 8.2.

4.3.5 Flow measurement uncertainty

Given the complexity of the measurement system, several sources of uncertainty are evident regarding the quantification of velocity in the wind farm, the most important of which are related to the overall system calibration, particle detection, and triangulation process, the signal-to-noise ratio (SNR) of the recorded images, and the quality of particle tracking and matching.

The overall system calibration and subsequent particle detection are addressed during the camera calibration phase. A geometric calibration is performed, with subsequent volumetric self-calibration [139] on a reduced sample of the particle images to remove any remaining disparities between cameras, resulting in a final pixel accuracy of 0.03px. Given the relatively low image averaged particle seeding density of between $3{\times}10^{-2}$ particles per pixel (ppp), the detection and triangulation of ambiguous particles is minimized [125]. A threshold allowable triangulation error of 1 voxel was used to reduce ghost tracks further and improve the particle reconstruction. Pre-processed images (before background removal using the time filter described in Section 4.3.3) have an average intensity of 100 counts.

The standard deviations (σ) of the velocity components are computed over the total number of test samples of 4600. The magnitudes vary depending on the velocity component, pitch case, and wake location on the farm. Higher magnitudes in standard deviation are present in the near wake along the shear layer, as concluded in previous works of [25, 133]. These reach as high as $\sigma_x \approx 0.8\,\mathrm{m\,s^{-1}}$, $\sigma_y \approx 0.4\,\mathrm{m\,s^{-1}}$, and $\sigma_z \approx 0.3\,\mathrm{m\,s^{-1}}$ for the baseline pitch case $\beta = 0^\circ$. Within the wake, these values drop to $\sigma_x \approx 0.17\,\mathrm{m\,s^{-1}}$, $\sigma_y \approx 0.15\,\mathrm{m\,s^{-1}}$, and $\sigma_z \approx 0.1\,\mathrm{m\,s^{-1}}$, respectively. For the pitched cases, the σ remains a similar magnitude,

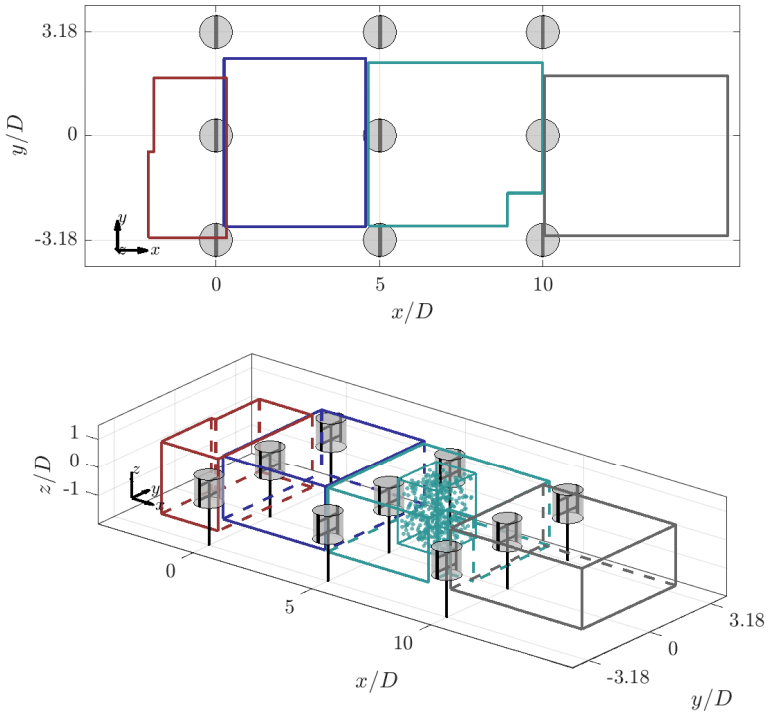


Figure 4.5: Top view (top) and isometric view (bottom) schematic of the wind farm arrangement. The wind turbines are shown at phase-locked positions $\theta = 0^{\circ}$, with the surrounding gray-shaded cylinders denoting the idealized AC surfaces. The grid lines reflect the constant grid spacing between the turbines normalized by diameter D. The wind direction flows in the positive x direction. The outlines of the overall measurement volume obtained in the inflow, between the first and second row, between the second and third row, and outflow (gray) are shown in dark red, blue, cyan, and gray, respectively. In the isometric view, a single measurement volume, as described in Section 4.3.3, is illustrated in the region between the second and third row. A representation of the instantaneous HFSB is provided in this volume as well.

with increases in the lateral and axial velocity components of up to $\sigma_y = \sigma_z \approx 0.6\,\mathrm{m\,s^{-1}}$ in the near wake within the shear layer. Within the induction region of the farm, the standard deviation of the unperturbed freestream is $\sigma_x = \sigma_y = \sigma_z = 0.05\,\mathrm{m\,s^{-1}}$, and increases in magnitude near the induction region of the first rotor row to $\sigma_x = \sigma_y = \sigma_z = 0.3\,\mathrm{m\,s^{-1}}$. The corresponding velocity uncertainty ϵ is computed using Equation (4.1):

$$\epsilon = \frac{z_a \sigma_{x,y,z}}{\sqrt{N}}, \tag{4.1}$$

where N is the number of uncorrelated measurement samples within each bin, and z_a is the coverage factor. A value of $z_a = 2$ is selected to achieve a 95% confidence interval of the normal Gaussian distribution. Given that the 4600 recordings are considered, which are time-averaged, the number of samples per bin is on the order of 900,000. Given the selected bin size, this indicates a substantial number of samples per bin per time instance. Rather, $N = 4600$ is used as the number of uncorrelated samples per bin, which is a conservative

estimate. Hence, the velocities reach a maximum of $\epsilon_x = 0.02\,\mathrm{m\,s^{-1}}$, which is only 0.67% of the freestream velocity $U_\infty = 3\,\mathrm{m\,s^{-1}}$. The large number of samples per bin suggests that a higher-resolution mesh would be attainable. However, the robustness of the chosen size resolves all large-scale vortices of interest while keeping the required memory to a minimum.

Furthermore, the diffraction diameter of the particle images d_{diff} is calculated using Equation (4.2) [124]

$$d_{\mathrm{diff}} = 2.44 \times f_\# \times (M+1) \times \lambda, \tag{4.2}$$

where $f_\# = 22$ is the numerical aperture, $\lambda \approx 500 \times 10^{-9}$m is the wavelength of light. The resulting diffraction diameter is $d_{\mathrm{diff}} = 27.65\mu$m. Given the camera pixel size of 20μm, the ratio is 1.4, which would result in minimal peak locking errors [124].

4.4 Results

4.4.1 Rotor thrust performance

Prior to the flowfield measurements, the thrust of an isolated rotor as a function of the tip-speed ratio is measured. These results are compared to the measurements of [73], who used the same geometry with the exception of profiled struts, as described in Section 4.3.2. In this work, the tip-speed ratio is varied using rotor rotational frequency ω while keeping the inflow wind speed constant at $U_\infty = 3$m/s. In the work of [73], the rotor loads were measured at an inflow speed of $U_\infty = 5$m/s. The streamwise and lateral thrusts, $C_{T,x}$ and $C_{T,y}$, are defined as follows:

$$C_T = \frac{T}{0.5\rho U_\infty^2 A}, \tag{4.3}$$

where T is the measured thrust component, ρ is the air density, and A is the frontal area of the rotor. The measured streamwise and lateral thrust coefficients are shown in Figure 4.6 for the three pitch cases via solid lines and compared to published results in dashed lines.

As with the results of [73], the streamwise thrust coefficient increases and decreases when applying a positive and negative pitch, respectively. This difference is amplified as the tip-speed ratio increases. The decrease in thrust for the negative pitch case can be attributed to the reduction in load in the intrinsically more efficient upwind passage (as described in Section 4.2). The increased load in the downwind passage does not account for that lost upwind and is further hindered by dynamic stall effects, as confirmed via blade-level measurements of [131] at mid-span. As reported by [131], the blade loads increase significantly in the UW quadrant for the positive pitch case before reducing due to stall in the UL quadrant. The streamwise thrust measurements in this campaign compare well to those published by [73] for the baseline and negative pitch cases but exhibit systematically higher values for the positive pitch case on the order of 13% at a tip-speed ratio of 3. This discrepancy can likely be attributed to the difference in strut profile and pitch adapter design, as well as the difference in free stream wind speed and diameter based on Reynolds number.

Pitch case β [°]	$C_{T,x}$	$C_{T,y}$
-10	0.72	0.39
0	0.79	0.03
10	0.92	0.10

Table 4.2: Measured thrust coefficients at tip speed ratio $\lambda = 3.5$

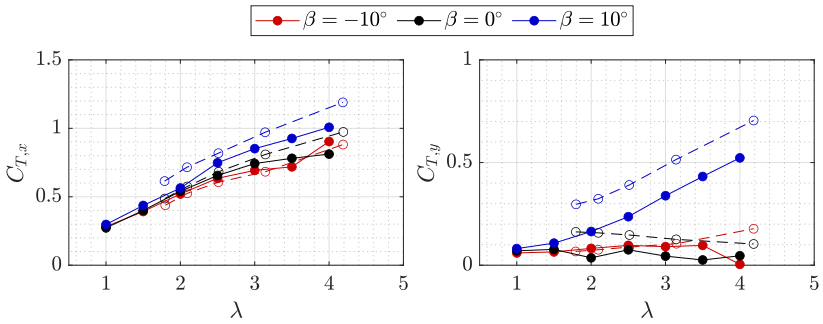


Figure 4.6: Streamwise (left) and lateral (right) thrust coefficients as a function of tip-speed ratio for the three thrust coefficients. The solid and dashed line corresponds to recorded results from this experiment and those reported by [25], respectively. All measurements of this experiment are recorded at a constant wind speed of 3m/s.

The lateral thrust coefficients are positive across all pitch cases, confirming the intrinsic asymmetric loading of the VAWT in favor of the windward side. For the positive pitch mode, the lateral force increases drastically compared to the baseline case by $\Delta C_{T,y} = 0.29$ (a factor of 14.3), while the negative pitch case increases by $\Delta C_{T,y} = 0.05$ (a factor of 3.8) at a tip-speed ratio of 3.5. The lateral force in the baseline case decreases as the tip-speed ratio increases, as the loading between the windward and leeward halves becomes more uniform. As in the streamwise thrust case, the positive pitch shows the largest discrepancy to results published by [73], which is again ascribed to the differences in the VAWT models and the Reynolds numbers. For the results presented, a constant tip-speed ratio of $\lambda = 3.5$ was maintained, with thrust coefficients tabulated in Table 4.2.

4.4.2 Streamwise vorticity system

As discussed in Section 4.2, the wake topology is governed by the modified trailing vorticity system of the rotor when in "vortex generator" mode. The iso-surfaces of the normalized streamwise vorticity $\omega_x D/U_\infty$ are shown for the three modes of operation in Figure 4.7, calculated using a three-point central finite difference scheme. The values are flooded by $\omega_x D/U_\infty = \pm 1$ for the vortex generator modes, and $\omega_x D/U_\infty = \pm 0.4$ for the baseline case. Furthermore, the normalized vorticity at discrete cross-stream locations x/D = 2.5, 7.5, and 12.5 is presented in Figure 4.8. The vectors show the in-plane velocities, and the solid black line indicates the projected frontal area of the central rotor column. The dominant

vortical structures stemming from the respective AC quadrants are labeled, following the same naming convention described in Section 4.2. The label S corresponds to structures stemming from the interfaces between the struts and the blade. Given the symmetry about the $z/D = 0$ plane, only the structures on the upper half of the wake are labeled.

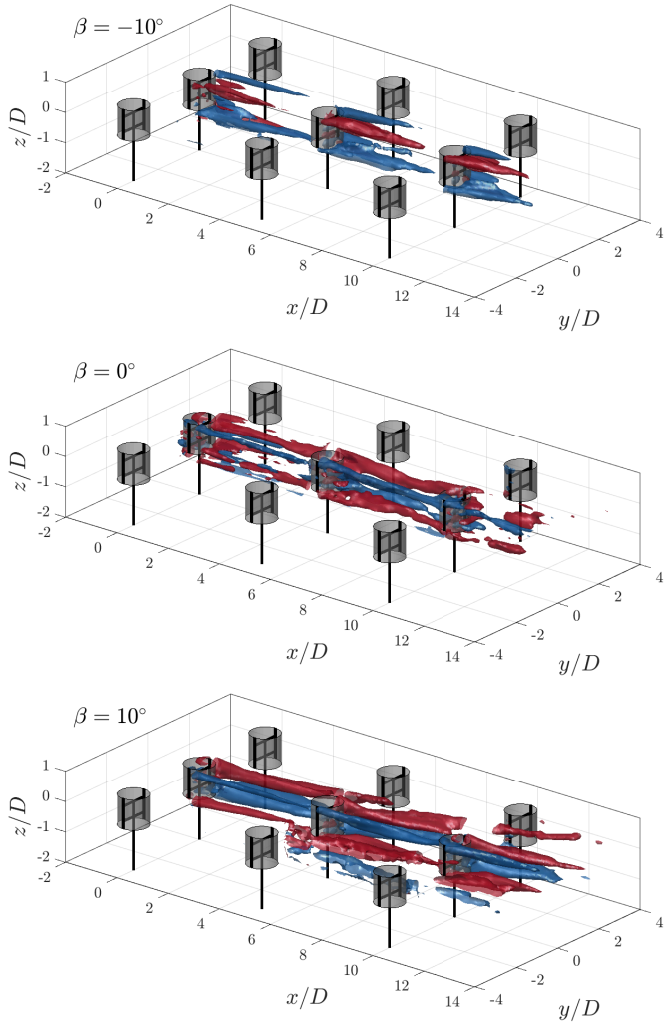


Figure 4.7: Iso-surfaces of the streamwise vorticity contours at $\omega_x D/U_\infty = \pm 1$ for pitch cases $\beta = \pm 10°$, and $\omega_x D/U_\infty = \pm 0.4$ for $\beta = 0°$. The rotors are shown at a $\theta = 0°$ phase, with the gray-shaded cylinders representing the idealized actuator cylinder load.

For the baseline case, there are no dominant vortical structures stemming from the AC quadrants behind the first rotor $x/D = 2.5$, with a presence of both upwind and downwind generated vortices on the windward and leeward sides. The UW vortex persists longer in the wake, reaching the second rotor, whereas the DW extends up to approximately $x/D =$

3, confirming the intrinsically higher load of the upwind half. Similarly, on the leeward half of the rotor, the UL vortex persists until the second rotor in the column. The intrinsically higher load and the windward half of the cycle are further highlighted by the difference in sizes of these vortical structures as they convect through the wake. In addition to the quadrant-based vortical structures, streamwise vorticity due to the struts is present. The same structures were observed by [25] and persist both on the windward and leeward sides. The streamwise vorticity structure behind the second rotor is analogous to that of a bluff body cylinder [142], with dominant counter-clockwise and clockwise rotating structures on the windward and leeward sides, respectively. These structures induce a significant axial contraction of the wake, evidenced by the induced downwash and upwash on the upper and lower halves, respectively. As the inflow velocity of the second rotor has been reduced significantly (as evidenced in the next section Section 4.4.3), the effective tip-speed ratio of the rotor will increase significantly (as the rotational frequency is kept constant), as well as the thrust coefficient. The structures persist in the wake until reaching the third rotor in the column. Behind the third rotor at $x/D = 12.5$, the same structures persist but at much lower strengths, as evidenced in the iso-surfaces.

For the positive pitch case $\beta = 10^{\circ}$, the dominant vortical structures are those generated on the upwind half of the cycle, namely the UW and UL as seen at $x/D = 2.5$, as discussed in Section 4.2. The UW structure is larger than the UL due to the higher load on the windward side. Due to the significant lateral force induced on the wake when pitching the blades, the structures convect towards the windward side. Those generated on the UW quadrant convect more due to their higher strength. Unlike the baseline case, the inflow for the second rotor recovers to a much higher degree due to the injection of high momentum flow from above the rotor, and hence, it exhibits a similar vortical structure to that of the first rotor. The UW-generated vortex for the rotor on the neighboring column has convected within the measurement volume at around $y/D = -2.0$ at $x/D = 7.5$. Compared to the structures of the first rotor, the UL vortices convected further inside the projected frontal area. Finally, behind the third rotor at $x/D = 12.5$, three UW-generated vortices are present in the measurement volume, namely those generated by the second and third rotors in the column, as well as the second rotor in the neighboring column on the leeward side. As seen in the iso-surfaces, the flooded structures generated by the third rotor do not extend as far as the second, suggesting a weaker structure and an accelerated diffusion. This is likely a result of the decrease in rotor load, linked to the inflow of the ejected wake from the leeward side columns, as discussed in Section 4.4.3.

Finally, for the negative pitch case, the dominant vortical structures in the wake are generated in the DW and DL quadrants. Behind the first rotor at $x/D = 2.5$, the DW structure remains concentrated around the upper blade tip, whilst that on the DL convects within the projected area of the rotor. The CVP on the leeward side induces a lateral injection of high-momentum flow into the wake. As in the baseline pitch case, vortices generated by the struts are apparent, albeit only on the leeward side. Behind the second rotor at $x/D = 7.5$, the same dominant structures persist, with seemingly higher strengths. The DW-generated vortex has convected above and towards the center axis of the rotor, while the DL has spread across the entire diameter of the rotor. The CVP between the upper and lower blades on the leeward side induces a significant injection of momentum into the wake while ejecting the wake out from the windward side. Behind the rotor at

$x/D = 12.5$, the same behavior persists. As in the case of the positive pitch blades, the vortical structures do not extend as far in the wake as in the aforementioned volumes, presumably due to the lower thrust of the third rotor and increased turbulence further in the wind farm wake.

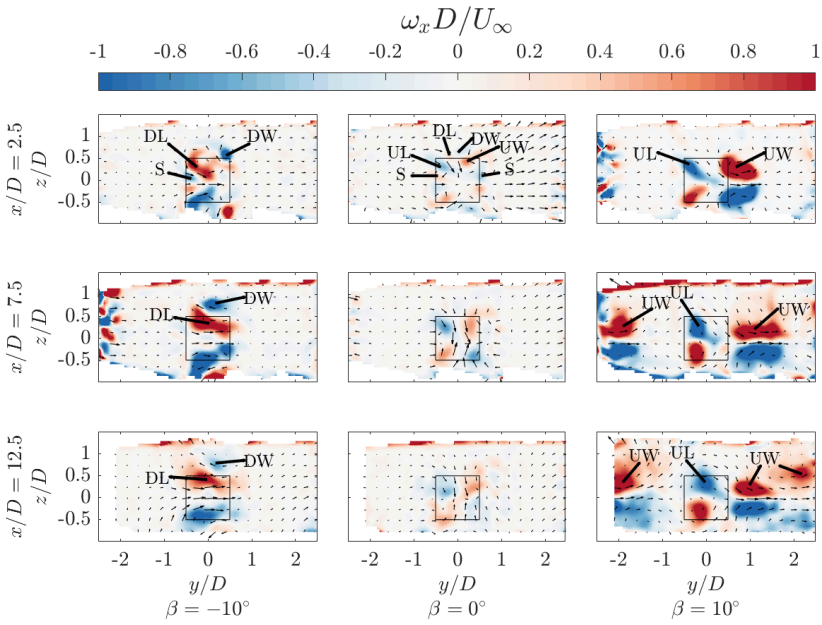


Figure 4.8: Normalized streamwise vorticity at $\omega_x D/U_\infty$ for the three pitch cases at streamwise locations x/D = 2.5, 7.5, and 12.5. The black outlined square indicates the projected frontal area of the rotors, and the vectors show the in-plane velocity components. The streamwise vortical structures generated by each AC load quadrant are labeled, as described in Section 4.2. The label S corresponds to structures generated at the interface between the struts and the blade.

4.4.3 Wake topology

As discussed in Section 4.2, the streamwise vorticity system is an important driver of the wake topology. The normalized streamwise flow component U_x/U_∞ is shown as iso-surfaces in Figure 4.9 for the baseline and vortex generator mode cases. The normalized streamwise flow is flooded at values U_x/U_∞ = 0.9 and 0.5, shown in orange and blue, respectively. The swept volumes of the rotors are shaded gray to represent the idealized actuator cylinder surface. Furthermore, the wake at discrete cross-stream distances x/D = 2.5, 7.5, and 12.5 is shown in Figure 4.10 for the same cases. Finally, the normalized streamwise velocity component at the symmetry planes y/D = 0, and z/D = 0 are shown in Figure 4.11 and Figure 4.12, respectively. In-plane velocity vectors are shown for all cases. The contours at the symmetry plane $y/D = 0$ include the wake boundary at $U_x/U_\infty = 0.6$. The contours at the symmetry plane $z/D = 0$ show the wake center via a white line as calculated using the

center of mass approach [143], as shown in Equation (4.4).

$$y_c(x) = \frac{\iint y\Delta U(x,y,z)\mathrm{dydz}}{\iint \Delta U(x,y,z)\mathrm{dydz}} \tag{4.4}$$

where $\Delta U(x,y,z) = U_\infty - U_x(x,y,z)$. The integration is performed at discrete cross-stream planes x/D. As the wake is symmetric about $z/D = 0$, the integration domain is constrained to $z/D \geq 0$ such that the available data is consistent across all pitch cases. For the baseline and negative pitch cases, the lateral domain is constrained to $-1.6 \leq y/D \leq 1.6$. In contrast, the positive pitch case is constrained to $-0.75 \leq y/D \leq 2.3$ to limit the impact of the wakes of the neighboring column on the computation. Beyond the third rotor's wake $x/D > 10$, the wakes between the central column and neighboring column rotors combine and become difficult to separate.

The baseline case $\beta = 0^\circ$ exhibits the most significant flow deficit, evident by the largest blue flooded region in the isosurfaces and blue area in the cross-stream plane $x/D = 2.5$. The cross-stream plane confirms the asymmetric load profile of the rotor, with an asymmetric wake directed towards the windward side. Similar topologies have been experimentally measured by [25, 37]. This asymmetry grows as the wake progresses downstream, as seen by the deformation of the blue-shaded wake core at $U_x = 0.5$, as well as the wake center line in Figure 4.12. The wake at the symmetry plane $y/D = 0$ exhibits a maximum flow deficit at approximately $x/D = 2.5$, at which point a gradual wake contraction occurs in the axial direction, evidenced by the in-plane vectors. The second and third rotors in the column are immersed in the wakes of the upstream rotors, evidenced by the extension of the orange-flooded regions within the measurement volumes. The flow at the symmetry planes has a gradually shorter wake length for the second and third rotors in the column, presumably due to decreased rotor thrust with a lower inflow velocity, as seen in Figure 4.12. The asymmetry in the wake grows throughout the farm, as seen at $x/D = 7.5$ and 12.5, with larger regions of flow deficit concentrated on the windward sides of the rotor. As there is no major lateral force component, shown in Section 4.4.1, the wakes of the surrounding columns do not become visible in the measurement domain until toward the end of the farm volume. As discussed in reference to the streamwise vorticity, the axial contraction of the wake at the symmetry plane $y/D = 0$ increases significantly behind the second and third rotors in the column. In contrast, the width of the wake in the lateral direction grows as the wakes superimpose.

For the positive pitch case $\beta = 10^\circ$, a significant lateral deflection of the wake towards the windward side is evident from the iso-surfaces and cross-stream plane $x/D = 2.5$. This is consistent with the significant increase in the measured lateral force of an isolated rotor, as discussed in Section 4.4.1. In addition to the lateral wake deflection, there is a significant axial contraction of the wake due to the influx of high momentum from above and below the rotor. The work of [25] demonstrates a similar wake topology. The wake contraction is evident by the cross-stream planes, and the significant decrease in wake length is seen at the symmetry plane $y/D = 0$. This significant wake re-energization is also evident in the reduction in blue-shaded regions of the iso-surfaces compared to the baseline operating case. Given the recovered incoming flow for the second rotor, the wake deflection process is still effective, as seen from the symmetry plane $z/D = 0$. Also evident is the appearance of the deflected wake in the measurement domain from the neighboring column on the

leeward side, starting at approximately $x/D = 2$. These wakes continue to travel laterally within the measurement volume and impinge on the third rotor in the column, as seen by the iso-surfaces and the cross-stream plane at $x/D = 12.5$. The wake center line gradually approaches $y_c/D = 0$ behind the third rotor as the wake from the neighboring column on the windward side enters the projected frontal area of the central rotors.

Finally, for the negative pitch case $\beta = -10^\circ$, the wake is re-energized from the sides whilst ejecting low momentum flow out from above and below the rotor, evident by the elongated wake shape on the axial direction in Figure 4.9 and cross-stream plane $x/D = 2.5$. The injection of momentum laterally is asymmetric in favor of the leeward side and grows as the wake progresses in the farm, as seen at cross-stream planes $x/D = 7.5$ and $x/D = 12.5$. This follows the discussion of the modification and convection of the dominant downwind vortices in Section 4.4.2. This mode of operation is clear when observing the flow at the symmetry plane $y/D = 0$, with gradual growth in flow deficit above and below the rotor plane, whilst flow is re-energized at the wake rotor center plane. The wake at the symmetry plane $z/D = 0$ confirms the measured increase in the lateral load of the rotor, as seen by the deflection of the wake towards the windward side. However, when considering the entire cross-section of the wake, the wake center line is concentrated around $y_c/D = 0$. This is due to the portion of the wake that has been ejected axially above the rotor, which connects gradually towards the leeward side, as seen in the cross-stream planes.

4.4.4 Wake recovery

The contours shown in Section 4.4.3 give a qualitative indication of the wake recovery mechanism of the vortex generator modes. To indicate the quantitative recovery of streamwise velocity in the wake, the normalized streamwise velocity deficits $1-(U_x/U_\infty)$ at symmetry plane $y/D = 0$ at cross-stream planes x/D = 2.5, 7.5, and 12.5 are shown in Figure 4.13, each 2.5D from the central column rotors. In addition, the lateral average of the velocity within the projected regions of $-0.5 \leq y/D \leq 0.5$ (projected frontal area) and $-1.6 \leq y/D \leq 1.6$ (central column grid size) are presented, denoted as $y/D \pm 0.5$ and $y/D \pm 1.6$, respectively. Additionally, the normalized axial velocity component U_z/U_∞ for each case is presented.

The streamwise velocity distributions about the symmetry plane y/D = 0 confirm the vortex generator mode of operations discussed in Section 4.2. For the baseline case, there is a large deficit behind the first rotor in the column, reaching $1-(U_x/U_\infty)$ = 1.1, suggesting a small region of backflow in the wake, visible in Figure 4.11. The deficits are lower behind the second and third rotors as the rotors produce less thrust, yielding shorter wake lengths, as discussed in Section 4.4.3. The maximum deficits behind the second and third rotors are $1-(U_x/U_\infty)$ = 0.63 and $1-(U_x/U_\infty)$ = 0.6, respectively. The profiles for all three cross-stream locations are relatively symmetric about the z/D = 0 plane with minor differences due to the rotor tower, consistent with the discussion in Section 4.2. The axial velocity behind the first rotor at $x/D = 2.5$ is low in magnitude and reaches a local minimum of $U_z/U_\infty = -0.04$ near the rotor tips, suggesting a wake expansion. Behind the second and third rotors, the profile approaches that of the positive pitch case, suggesting a significant wake contraction, as discussed in Section 4.4.3, with minima of $U_z/U_\infty = -0.16$ in the upper half.

For the vortex generator mode with negative pitch $\beta = -10^\circ$, the flow behind the first rotor is substantially recovered compared to the baseline case within the range $-0.5 \leq$

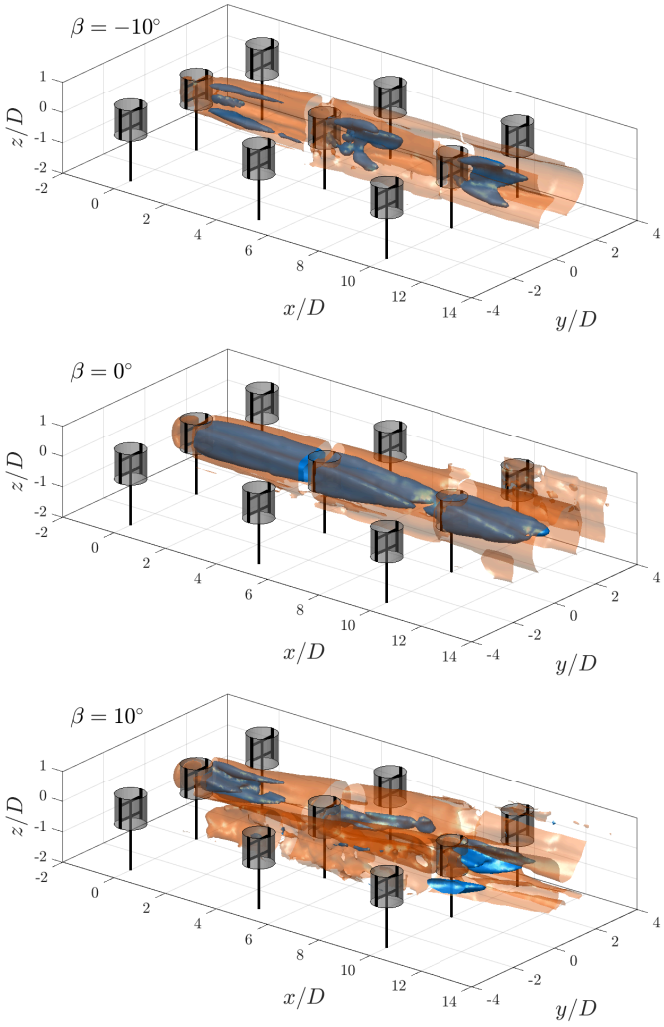


Figure 4.9: Iso-surfaces of the normalized streamwise velocity U_x/U_∞ = 0.5 and 0.9 in blue and orange, respectively, for the three pitch cases. The rotors are shown at a phase-locked position θ = 0°, with the gray-shaded cylinders representing the idealized actuator cylinder load.

$z/D \leq 0.3$, reaching a maximum deficit of $1-(U_x/U_\infty) = 0.26$. As the wake is ejected out axially above and below the rotor, as suggested by the U_z/U_∞ profile, the flow deficits above and below the projected frontal area of the rotor are greater than the baseline case, reaching $1-(U_x/U_\infty) = 0.5$. The wake region extends up to a height of $z/D = 0.9$ compared to the baseline case of $z/D = 0.6$, with a maximum upwash of $U_z/U_\infty = 0.1$ above the rotor plane. Behind the second rotor, the maximum deficit decreases to $1-(U_x/U_\infty) = 0.12$. The wake region continues to expand above and below the rotor, encompassing a larger range above $z/D = 1.3$, while reaching a lower maximum deficit of $1-(U_x/U_\infty) = 0.34$. Behind the

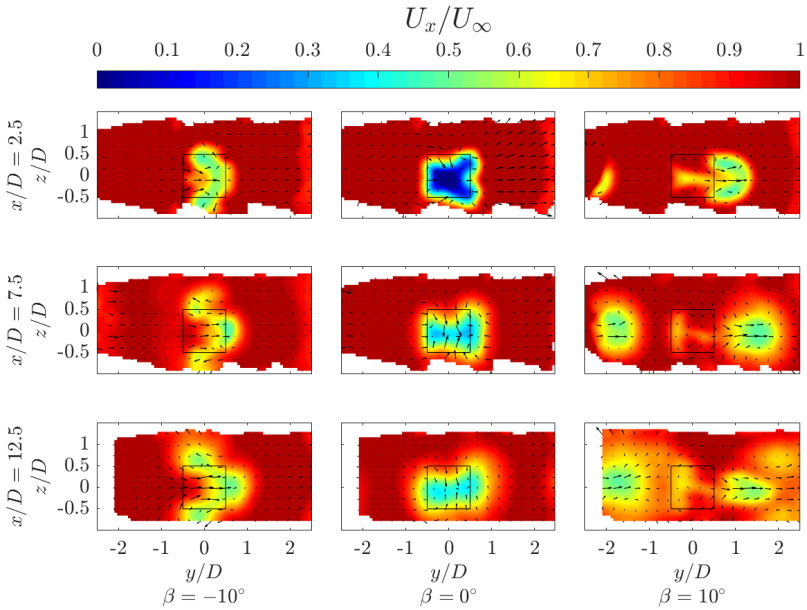


Figure 4.10: Normalized streamwise velocity U_x/U_∞ for the three pitch cases at stream-wise locations x/D = 2.5, 7.5, and 12.5. The black outlined square denotes the projected frontal area of the rotor, and the vectors show the in-plane velocity components.

third rotor, the wake region expands even further above the area of the rotor and reaches a maximum deficit within the bounds of the rotor of $1-(U_x/U_\infty) = 0.23$. The maximum upwash decreases between the cross-stream planes $x/D = 7.5$ and 12.5, from $U_z/U_\infty = 0.16$ to 0.1, respectively. This is due to the decrease in vortex strength, as seen in Figure 4.8.

Finally, for the vortex generator mode with positive pitch $\beta = 10°$, the wake is axially contracted whilst ejected out laterally. Hence, a significant reduction in the streamwise flow deficit behind the first rotor is evident, with a maximum deficit of $1-(U_x/U_\infty) = 0.32$. The wake region has also contracted, reaching a height of $z/D = 0.3$, suggesting freestream flow within the projected frontal of the rotor, highlighted in Figure 4.11. The downwash on the upper half of the rotor reaches a local minimum of $U_z/U_\infty = -0.2$. Behind the second rotor, the maximum wake deficit decreases to $1-(U_x/U_\infty) = 0.17$ whilst maintaining a similar wake width. The local minima of the downwash remain similar, with $U_z/U_\infty = -0.18$. The location of this minima shifts due to the larger deflection of the wake behind the second rotor, as seen in Figure 4.12. The symmetry above and below the rotor begins to deviate behind the third rotor as the wakes of the rotors on the neighboring column enter the measurement volume, as shown in Figure 4.10. Similarly, the maximum magnitudes of the downwash and upwash on the upper and lower halves of the wake, presumably due to the different lateral locations of the UL vortices, as shown in Figure 4.8.

When taking the lateral average within the projected frontal area of the rotor $-0.5 \leq y/D \leq 0.5$, the trend is similar to the non-averaged profile. The baseline case exhibits the highest flow deficit across all three measurement planes, with similar maximum deficits

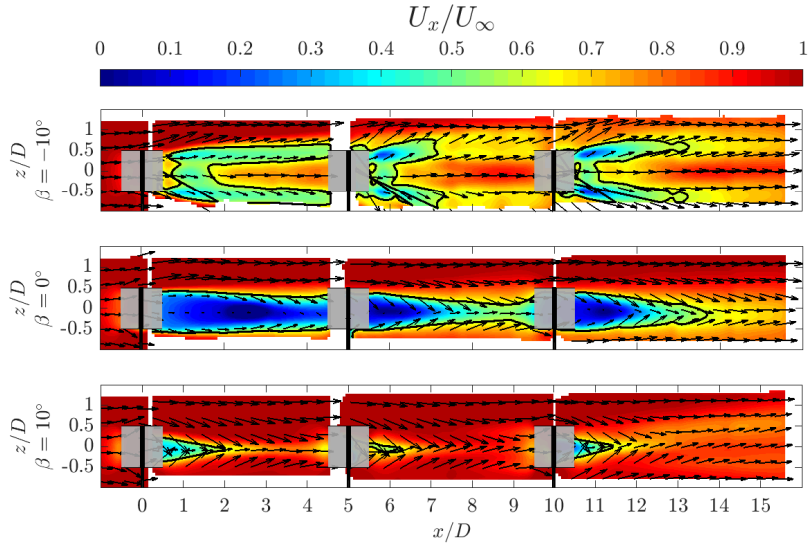


Figure 4.11: Normalized streamwise velocity U_x/U_∞ for the three pitch cases at the constant lateral plane y/D = 0. The vectors show the in-plane velocity components. The thick black line denotes the wake boundary at $U_x/U_\infty = 0.6$. The grey shaded squares represent the idealized actuator load surface, and the black volumes show the rotor at a phase of θ = 0°.

behind the second and third rotors. For the negative pitching case $\beta = -10°$, the mean streamwise velocity recovery within the projected frontal area of the rotor is higher than the baseline case across the three measurement planes. As described in the aforementioned case, the wake is ejected out axially above and below the rotor, leading to higher average deficits within the extended lateral domain beyond $z/D \geq 0.5$ compared with the baseline case. The profile does not exhibit notable peaks in streamwise flow deficit above and below the rotor, as with the profile from the symmetry plane $y/D = 0$. Finally, for the positive pitch case $\beta = 10°$, the trend is similar to that on the symmetry plane. The axial flow profiles also maintain a similar trend to the non-averaged case. However, a clear difference appears for the positive pitch case, where the maximum magnitude decreases more rapidly between the cross-stream planes, from $U_z/U_\infty = 0.13$ to 0.02 at $x/D = 2.5$ and 12.5, respectively. This can be attributed to the gradual convection of the UL vortices within the projected volume of the rotors.

When extending the domain for the lateral average to $-1.6 \leq y/D \leq 1.6$, the relationships between the three modes of operation begin to deviate from the aforementioned cases. In general, the deficits increase downstream as the wakes superimpose and the deflected wakes from the neighboring columns enter the extended domain. Behind the first rotor, the baseline case $\beta = 0°$ exhibits the highest deficit with $< 1 - (U_x/U_\infty) >= 0.3$. However, due to the extended domain in the lateral direction, the negative pitch case $\beta = -10°$ exhibits the highest wake recovery with $< 1 - (U_x/U_\infty) >= 0.1$ compared to the positive pitch case $\beta = 10°$ with $< 1 - (U_x/U_\infty) >= 0.19$. This is because the ejected wake of the positive pitch

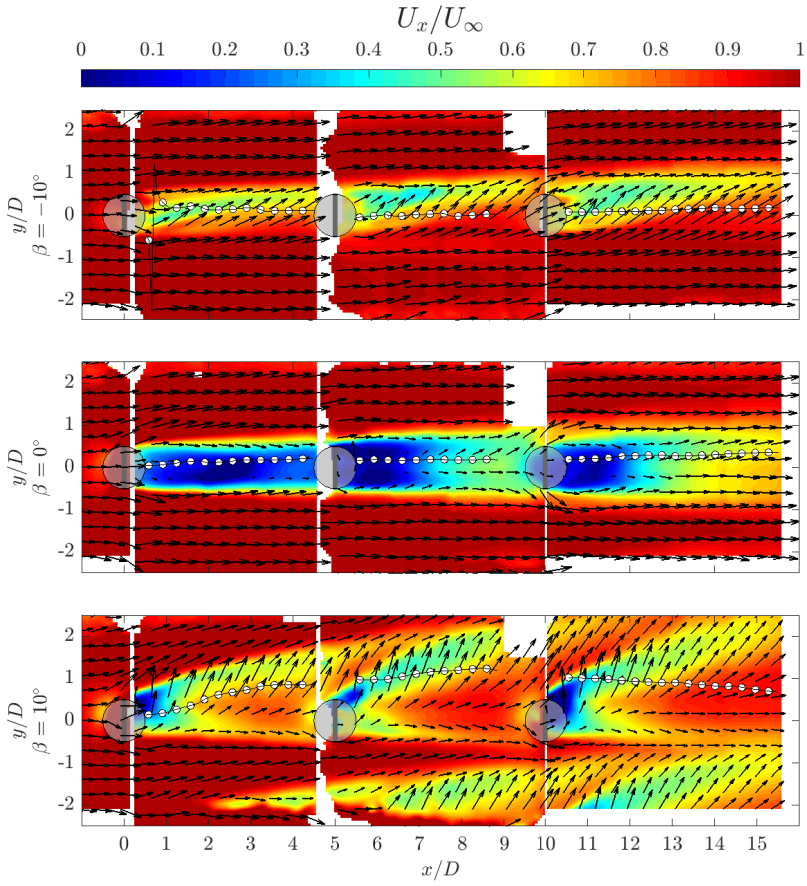


Figure 4.12: Normalized streamwise velocity U_x/U_∞ for the three pitch cases at the constant axial plane $z/D = 0$. The vectors show the in-plane velocity components. The white markers show the wake center as computed using Equation (4.4). The grey shaded squares represent the idealized actuator load surface, and the black volumes show the rotor at a phase of $\theta = 0°$.

mode of operation falls within the extended lateral range, whereas the axially ejected wake of the negative pitch mode falls outside the integration window. Behind the second rotor, the relationship between the three modes of operation remains the same, with higher maximum streamwise deficits. The maximum deficits between the positive pitch case and baseline become more similar as the wakes from the surrounding columns deflect within the interrogation volume. Finally, behind the third rotor, the maximum flow deficits for the baseline and positive pitch case are very close in magnitude, with $< 1-(U_x/U_\infty) >= 0.33$ and $< 1-(U_x/U_\infty) >= 0.31$, respectively. This is attributed to the deflected wakes from the neighboring column for the positive pitch case, seen in Figure 4.12.

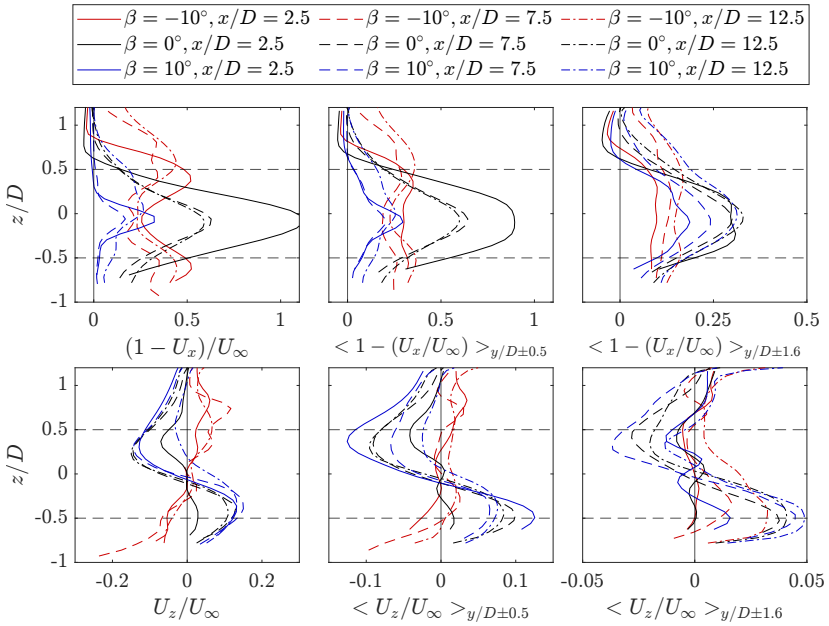


Figure 4.13: Normalized streamwise deficit $1-(U_x/U_\infty)$ and axial U_z/U_∞ velocity profiles at discrete cross-stream measurement planes x/D = 2.5, 7.5, and 12.5 for the vortex generator and baseline modes of operations. (Left column) the normalized velocity profiles about the y/D = 0 symmetry plane. (Middle column) lateral-averaged streamwise velocity profiles within the projected frontal area of the rotor $-0.5 \leq y/D \leq 0.5$. (Right column) lateral-averaged velocity profiles within the lateral domain $-1.6 \leq y/D \leq 1.6$. The horizontal dashed lines indicate the upper and lower bounds of the rotor's projected frontal area.

4.4.5 Available power

The flowfield contours shown in Section 4.4.3 visually confirm the injection of high momentum flow into the wake for both vortex generator modes, given the availability of freestream inflow for the second and third rotors in the central column. To further highlight the efficacy of these modes of operation on the replenishment of kinetic energy in the wake, the potentially available power in the wake is quantified at a selected cross-stream location using the coefficient of available power f_{AP}. A similar analysis has been performed by [25, 67, 85] to highlight the replenishment of high momentum flow inside a selected domain, and is computed as:

$$f_{AP}(x, y_0, z_0) = \iint_S U_x^3(x, y, z)/U_\infty^3 \mathrm{dzdy}, \tag{4.5}$$

where U_x^3/U_∞^3 is the coefficient of available power at a select cross-stream plane x. The surface integral is computed within a defined domain (S), which is centered at y_0, z_0 in the lateral and axial directions, respectively. The available power coefficients throughout the central column of the wind farm are shown in Figure 4.14 for the three modes of operation. The average available power is computed within the projected frontal area of the central column rotors $y_0/D = z_0/D$ = 0. The vertical dashed lines indicate the boundaries of the

rotor-swept areas for the central column. Note that, as the powers of the rotors in the farm were not measured, the presented curves are not scaled to account for the extracted power from the flow of the rotors within the central column.

For the baseline case within the projected frontal area of the rotor, the available power does not surpass 20% between the first and second rows. The AP reaches a minimum of $< U_x^3/U_\infty^3 >$ = 0.06 at x/D = 1.4 before steadily recovering due to the inherent diffusion of the wake. Between the second and third row, the AP recovers much faster, consistent with the shorter wake length observed in Figure 4.11 and Figure 4.12, as well as the lower recorded thrust coefficient of the second rotor. The AP reaches a maximum of 0.25 at x/D = 9 before decreasing upstream of the third rotor in the column due to its induction. Finally, downstream of the third rotor, the AP increases at a similar rate to the previous case, reaching a recorded maximum of 0.42 at x/D = 15.5.

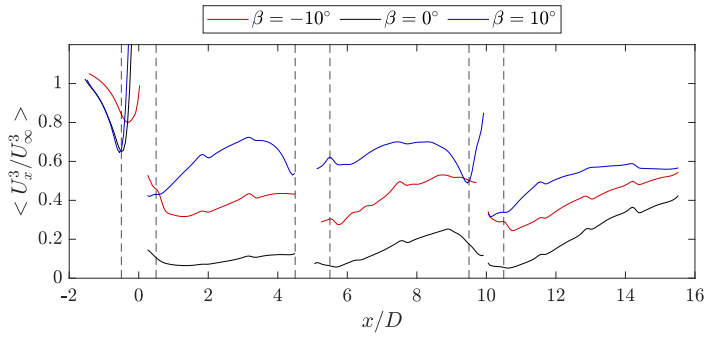


Figure 4.14: Mean available power $< U_x^3/U_\infty^3 >$ as calculated using Equation (9.6) for the three pitch cases over streamwise distance x/D within the projected frontal area of the central rotor column $-0.5 < z/D, y/D < 0.5$. The vertical black dashed lines correspond to the boundaries of the swept volumes of the central column rotors.

For both vortex generator control strategies, the available power in the wake is higher than in the baseline case within the projected frontal area of the rotor. The case where momentum is injected from above the rotor $\beta = 10^\circ$ exhibits higher AP across all measurement domains compared to the alternative case of $\beta = -10^\circ$. Directly behind the first rotor, the negative pitch case reaches a minimum AP of 0.32 at x/D = 1.3 before gradually increasing. The positive pitch case reaches a maximum AP of 0.72 at x/D = 3.2 before a steep drop due to the amplified induction of the second rotor. This drop due to induction is not as visible in the negative pitch case as the load shifted from the upwind quadrant. Between the second and third rotors, the AP is higher directly downstream of the rotor for the positive pitch case compared to the aforementioned volume. However, a comparable maximum AP is reached of 0.7 at a similar distance from the rotor of x/D = 8.4 before dropping due to the induction of the third rotor. Contrarily, the negative pitch case reaches a higher maximum compared to the previous volume of AP = 0.53 at x/D = 8.7. Finally, behind the third rotor, the positive pitch case shows an overall lower AP compared to the previous volumes. Inspection of the flow fields in Section 4.4.3 sheds light on the reason why the deflected wakes from the side columns have entered the domain directly downstream of the third rotor of the central column. Conversely, the negative pitch case shows a similar rate of increase in AP compared to the aforementioned volume as the wakes from side

columns deflect far less compared to the positive pitch case, reaching a comparable AP of 0.54 at the final measurement location of x/D = 15.5.

To shed light on the potential optimal placement of further downstream turbines with the freedom to have lateral offsets, the AP coefficient is computed within the projected frontal area of the rotor centered at different lateral offsets to $-1.5 \leq y_0 \leq 1.5$ overall all streamwise measurement planes. These are presented as a contour plot in Figure 4.15 for the three modes of operation, where the solid black line indicates where $f_{\text{AP}} = 0.7$, i.e., a 70% recovery of the maximum AP from the streamwise flow. Furthermore, the sliding window AP are extracted at three discrete streamwise locations x/D = 2.5, 7.5, and 12.5 for three modes of operation and shown in Figure 8.10.

For the baseline case, the wake is concentrated within the projected frontal area of the rotor, with beyond 70% AP on the windward and leeward sides of the rotor. The AP distribution is slightly asymmetric, with more of a deficit on the windward side of the rotor. This is consistent with the asymmetric loading of the rotor described in Section 4.2. Behind the second and third rows, the depleted energy regions grow on either side of the rotor as the wake superimposes on each other, as seen in Figure 8.10 by the gradually flattening curves and diminishing maximum AP deficits, increasing from 0.08 at x/D = 2.5 to 0.2 at x/D = 12.5. For the negative pitch case where momentum is entrained through the sides of the rotor, the region where AP falls below 70% is narrower as the wake is ejected out of the volume axially. Consistent with the increase in the lateral load shown in Section 4.4.1, the wake deflects towards the windward side, yielding lower AP potential for rotor positions in that direction. The AP is higher than that of the baseline case across all lateral positions, as shown in Figure 8.10. Finally, for the positive pitch case, the regions of AP below 70% are deflected towards the windward side of the rotor, yielding a large region in the leeward side where a potential rotor can experience close to 100% of the AP. Within the range of $-0.6 \leq y_0/D \leq 0.4$, the AP of the positive pitch case is higher than the other two modes of operation, beyond which yields lower AP on the windward side. Behind the second rotor, the wake of the rotor in the first row persists on the windward side. On the leeward side, the region of high potential AP is smaller due to the wake of the rotors in the neighboring column. Finally, behind the third rotor, the region where the AP surpasses 70% is again reduced between the wakes of the third rotor and neighboring columns. This mode of wake recovery yields higher AP at x/D = 12.5 in a narrow lateral spacing window of $-0.1 \leq y_0/D \leq 0.9$.

4.4.6 Surface momentum flux

The discussion in Section 9.4.3 highlighted the potential for increased energy density of a VAWT farm using a wake recovery strategy. To help quantify the process of wake recovery, a volume analysis of the energy equation is adopted. Similar techniques have been used by [67, 144], while works of [25, 85] used the momentum equation terms to highlight the recovery processes of individual VAWTs and HAWTs. The mean kinetic energy (MKE) equation can be derived from the momentum equation and is formulated as [67]:

$$\frac{\partial\left(\frac{1}{2}U_x^3\right)}{\partial x} = -\frac{\partial\left(\frac{1}{2}U_yU_x^2\right)}{\partial y} - \frac{\partial\left(\frac{1}{2}U_zU_x^2\right)}{\partial z} - U_x\frac{\partial\left(\overline{U_x'U_x'}\right)}{\partial x} - U_x\frac{\partial\left(\overline{U_x'U_y'}\right)}{\partial y} - U_x\frac{\partial\left(\overline{U_x'U_z'}\right)}{\partial z} \tag{4.6}$$

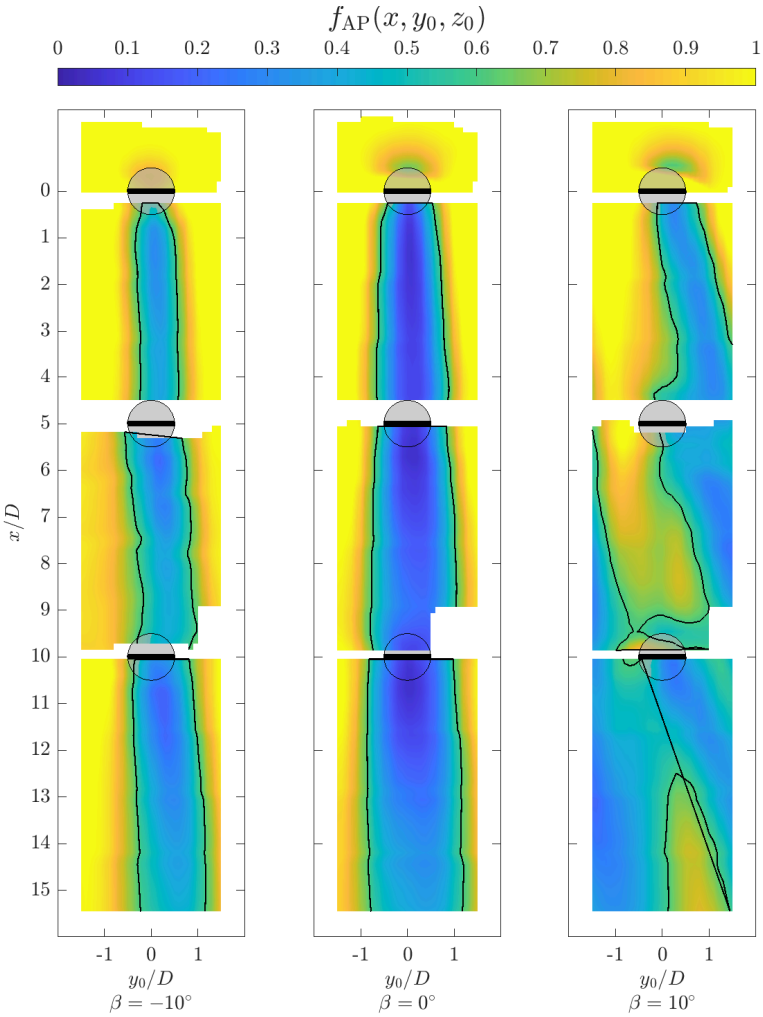


Figure 4.15: Available power as calculated using Equation (9.6) for the three pitch cases over all streamwise distances x/D and lateral offsets y_0/D ranging from -1.5 to 1.5. The gray areas indicate the top-view areas of the rotor and the idealized actuator surface. The black contour lines show where f_{AP} = 0.7, i.e., 70% of the maximum available power provided by the streamwise flow.

The expressions denoted with primes are the fluctuations of the temporally averaged velocity components in each direction with subscripts x, y, z. As in the work of [25, 85], the equation is rearranged to equate the advective and Reynolds stresses contributions towards the streamwise energy recovery term. The viscous forces are neglected due to the sufficiently high diameter-based Reynolds number. The pressure term is omitted as it was not measured. Furthermore, terms regarding the Coriolis, thermal buoyancy, and turbine forcing, as considered in the work of [144], are exempted from focusing on the driving advective process of the streamwise vorticity system.

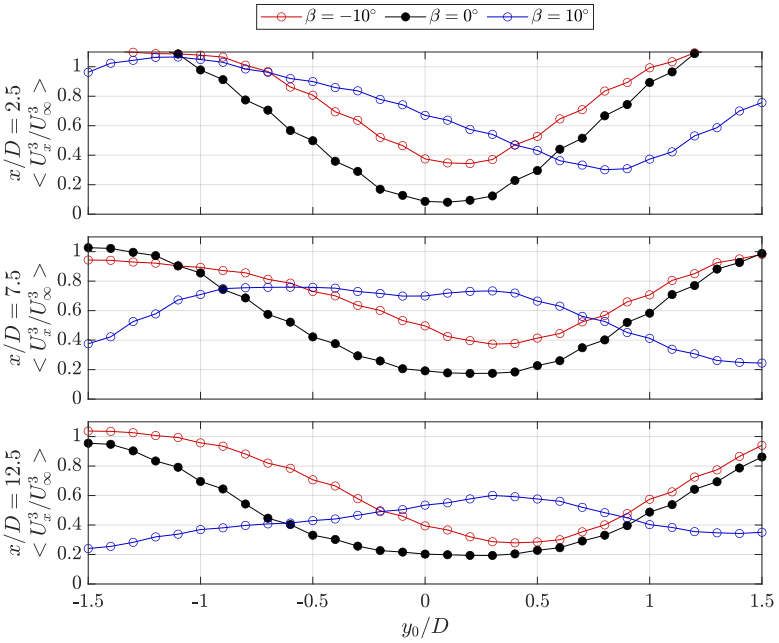


Figure 4.16: Available power as calculated using Equation (9.6) for the three pitch cases at discrete streamwise distance x/D of 2.5, 7.5, and 12. The AP is computed within the projected frontal area of the rotor $-0.5 < z/D, y/D < 0.5$ with a lateral center y_0 with the discrete measurement plane.

To investigate the relative contributions of the aforementioned terms towards wake re-energizing within the wind farm, a control volume analysis is adopted, as in the works of [67, 144]. The proposed control volume is illustrated in Figure 8.18. The volume encompasses the entire measurement domain in the streamwise direction, ranging between $-2 \leq x/D \leq 16$. The upper and lower surfaces of the control volume are taken as the heights of the upper and lower blade tips $-0.5 \leq z/D \leq 0.5$. Finally, the lateral size is taken as the diameter of the wind turbines, with $-0.5 \leq y/D \leq 0.5$. Given the limited measurement domain in the axial direction, this ensures an equal surface area is considered for the flux on the axial and lateral surfaces. As the mean kinetic energy along the streamwise direction is the most critical towards turbine performance, the focus is placed on the flux of energy lateral and axial surfaces, while the inflow and outflow surfaces (S_1 and S_2, respectively) are omitted from the subsequent analysis.

Following the procedure outlined by [144], the volume integral of the terms in Equation (4.6) can be simplified by applying the divergence theorem to rewrite the terms to a surface integral form. This is simplified further by considering that velocities normal to the surfaces do not contribute to the flux. Hence, the fluxes through the normals of the control surfaces $S_{3,4,5,6}$ can be expressed as:

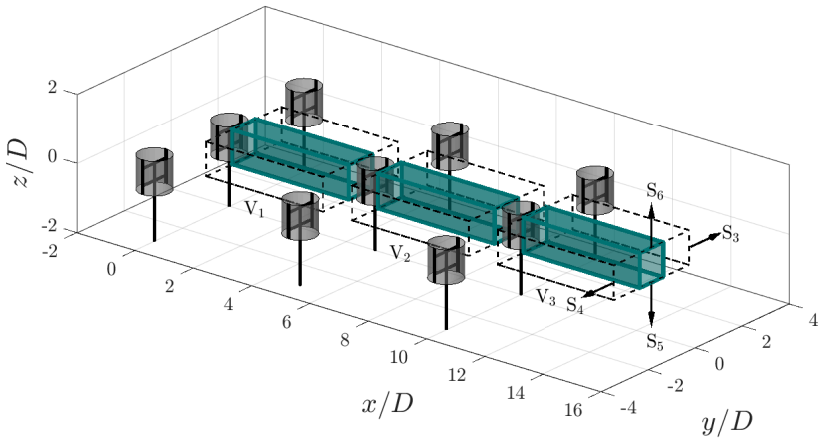


Figure 4.17: Schematic of the wind farm control volumes, denoted as V_1, V_2, and V_3, corresponding to the flow behind the first, second, and third rotor of the central column, respectively. The shaded regions are the volumes within the projected areas of the rotors of the central column ($-0.5 \leq y/D \leq 0.5$), while the dashed black lines indicate the edges of the central cells of the farm grid ($-1.6 \leq y/D \leq 1.6$). The fluxes are evaluated through the lateral and axial surfaces S_3, S_4, S_5, and S_6, respectively. The gray shaded cylinder indicates the idealized AC surface of the rotors, which are shown at a phase-locked position of $\theta = 0^\circ$.

$$\text{Surface 3} : \iint_{S_3} U_x \left(0.5 U_y U_x + \overline{U_x' U_y'}\right) dS_3 \tag{4.7}$$

$$\text{Surface 4} : -\iint_{S_4} U_x \left(0.5 U_y U_x + \overline{U_x' U_y'}\right) dS_4 \tag{4.8}$$

$$\text{Surface 5} : -\iint_{S_5} U_x \left(0.5 U_z U_x + \overline{U_x' U_z'}\right) dS_5 \tag{4.9}$$

$$\text{Surface 6} : \iint_{S_6} U_x \left(0.5 U_z U_x + \overline{U_x' U_z'}\right) dS_6 \tag{4.10}$$

In this case, surfaces S_4 and S_5 are given negative signs such that flux entering and leaving the volume is denoted as positive and negative, respectively.

The advective and Reynolds stress contributions towards the fluxes through each surface, as denoted in Equation (4.7), are presented in Figure 4.18 and Figure 4.19, respectively. The line integrated fluxes across the denoted axial and lateral surfaces are computed as a function of the streamwise position x/D for the three modes of operation within the farm grid lateral boundaries of $-0.5 \leq y/D \leq 0.5$. The values are normalized by the $D/U_\infty^3 L$, where L is the integration length in the lateral direction, in this case, $L = D$.

For the baseline pitch case, a minimal flux across the lateral boundaries of the volume is visible, consistent with the flowfield visualized in Section 4.4.3. The surfaces show a degree of symmetry consistent with the wake expansion shown in Section 4.4.3. For the negative pitch case, the trend in flux on S_3 steadily decreases within a volume when

traveling downstream, consistent with the lateral deflection of the wake core on the windward side of the rotor. Correspondingly, the flux on the leeward side of the rotor (S_4) is higher in magnitude as high momentum freestream flow is injected into the wake. This reaches increasing maximum magnitudes of 0.05, 0.06, and 0.08 in Volumes 1, 2, and 3, respectively. This increase in flux is apparent when considering Figure 4.8, where an increasing asymmetric lateral inflow is shown as the CVP convects towards the upper and lower boundaries of the rotor. The positive pitch case exhibits the highest magnitude in lateral advection on S_3, reaching maximums of 0.07, 0.1, and 0.08 in Volumes 1, 2, and 3, respectively. This high lateral flux component is attributed to the ejection of the wake on the windward side of the rotor. Meanwhile, on the S_4, there is an injection of momentum, which grows in magnitude between the first and second volumes. Leading up to the third rotor in the column, the momentum injection decreases significantly due to the wake of the neighboring column on the leeward side.

Given the uniform inflow case of this study, the flow remains symmetric about the plane $z/D = 0$, as noted in the previous analysis in Section 4.4.3 and Section 4.4.2. Hence, the fluxes about S_5 and S_6 are also the same. Minor differences between the magnitudes of the two surfaces can be attributed to the tower's presence and other measurement noise. Hence, the discussion will focus on S_6 as the representative case. The positive pitch case shows the highest magnitudes in the first volume. The injection of momentum steadily decreases as the dominant CVP convects towards the windward direction. Compared to the baseline case, the flux steeply decreases leading up to the second rotor due to the upwind loaded induction. The baseline pitch case transitions from a positive flux as the wake expands to a negative value due to the asymmetric wake profile shown in Section 4.4.3, where flow is injected on the leeward side. This negative flux grows minimally in maximum magnitude between the volumes, from 0.02 to 0.03 in Volumes 1 and 3. Conversely, the negative pitch case shows a close to zero flux across the surface across all volumes. Although the wake is ejected out axially above the rotor, as shown in Section 4.4.3, the strong asymmetry in the wake and dominance of lateral influx of momentum yield minimal vertical velocity magnitudes on the upper and lower surfaces of the rotor.

Overall, the fluxes of the Reynolds stress terms, illustrated in Figure 4.19, are an order of magnitude lower than that of the advective, demonstrating the dominance of the advective terms over the Reynolds stresses in the recovery of kinetic energy in the farm. For all pitch cases, the highest magnitudes are concentrated near the wakes of the rotor. For the positive pitch, the largest magnitude flux is on S_3 due to the ejection of the wake. Unlike the case with the advective terms, the baseline case exhibits higher magnitudes in flux on the upper and lower surfaces of the control volume (S_5, S_6) compared to the pitched modes of operation. This highlights the relative importance of turbulent mixing towards the wake recovery for the baseline operation of the rotor.

The discussion above gives an indication of the surface fluxes as a function of the downstream location. The surface-integrated fluxes for each volume are shown in Figure 4.20. Here, the sum of the advective and Reynolds stress contributions towards the flux is considered, as dictated in Equation (4.7). In addition, the total flux of each surface over all three volumes is shown in the bottom tile of Figure 4.20.

As discussed in relation to Figure 4.18, the integrated fluxes of S_5 and S_6 remain similar due to symmetry for the three pitch cases. The negative pitch case shows a discrepancy in

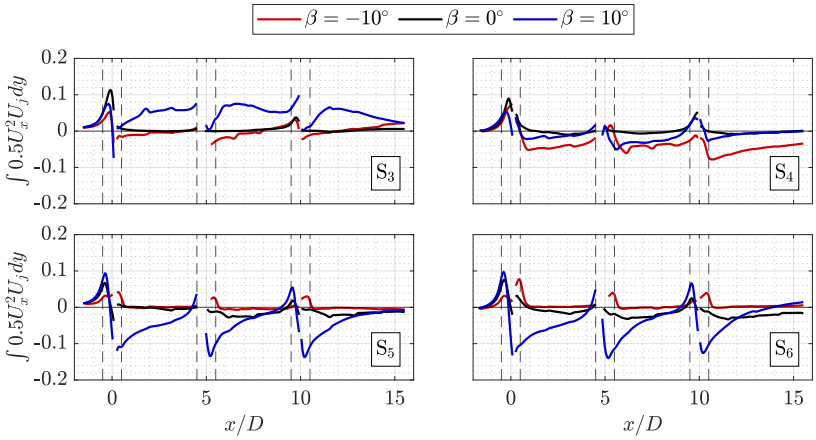


Figure 4.18: Line integrated advective flux terms as a function of downstream position x/D through the surfaces $j = S_{3,4,5,6}$, as noted in Figure 8.18 for the three modes of operation. The flux terms are integrated within the lateral boundaries $-0.5 \leq y/D \leq 0.5$. All fluxes are normalized by the ratio of the turbine diameter to the product of the free stream wind speed and lateral integration length, $1/U_\infty^3 L$, where $L = D$ in this case. The vertical dashed line denotes the edges of the central rotor volumes. The propagated relative error following the spatially evolving uncertainties discussed in Section 4.3.5 is on the order of 1%.

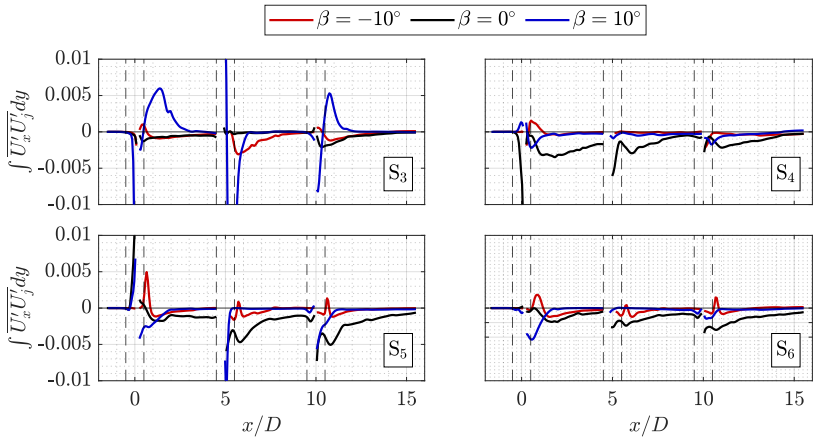


Figure 4.19: Line integrated Reynolds stress flux terms as a function of downstream position x/D through the surfaces $j = S_{3,4,5,6}$, as noted in Figure 8.18 for the three modes of operation. The flux terms are integrated within the lateral boundaries $-0.5 \leq y/D \leq 0.5$. All fluxes are normalized by the ratio of the turbine diameter to the product of the free stream wind speed and lateral integration length, $1/U_\infty^3 L$, where $L = D$ in this case. The vertical dashed line denotes the edges of the central rotor volumes.

Volumes 2 and 3 with opposite signs of minimal magnitude. For the positive pitch case, the flux through S_3 decreases between Volume 1 and 3 due to the presence of the wake of the

neighboring column. The vertical flux through S_6 also decreases in magnitude from 0.05 to 0.03 between Volumes 1 and 3. For the negative pitch case, the flux magnitude injection from S_4 increases from 0.04 to 0.06 between Volumes 1 and 3. In general, the largest fluxes for the baseline case are evident on the axial control surfaces, growing from 0.01 to 0.03 between Volumes 1 and 3, reaching a similar magnitude to the positive pitch case.

Considering the sums between all volumes for each control surface, it is evident that the positive pitch case exhibits the highest magnitude in flux, both with the ejection of the wake on S_3 and injection of high momentum flow from S_6. The negative pitch case demonstrates the highest momentum injection through the leeward surface S_3. The baseline case demonstrates minimal flux across the lateral surfaces, with higher magnitudes in the vertical injection of momentum from S_6, attributed to the domain CVP discussed in Section 4.4.2.

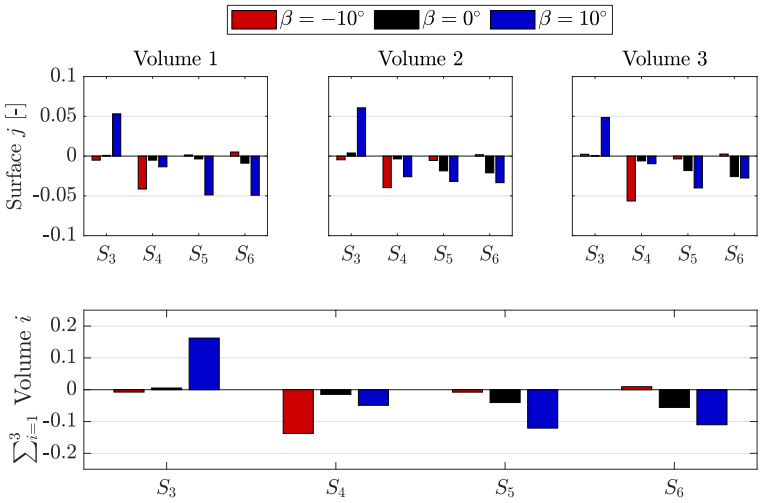


Figure 4.20: Surface integrals of the control surfaces ($j = 3, 4, 5$) as described in Equation (4.7), where Volume 1, 2, and 3 (i) correspond to the volumes behind the first, second, and third rotors, respectively. The sum of surface fluxes over all three volumes is shown in the bottom plot. All values are normalized by the $1/U_\infty^3 S_i$. The surface areas between all four surfaces are constant, with $S_i = 4D^2$. The propagated relative error following the spatially evolving uncertainties discussed in Section 4.3.5 is on the order of 1%.

To give a visual representation of the fluxes in the wind farm volume, the sum of the axial and lateral advective contributions towards the flux at discrete cross-stream planes x/D = 2.5, 7.5, 12.5 for the three modes of operation is shown in Figure 4.21. The vectors show the in-plane velocity components, and the projected frontal area of the central rotor column and wind farm grid size are shown via solid and dashed lines, respectively. In this case, the magnitudes of the in-plane velocity components are taken to compute the advective flux.

Consistent with Figure 4.20, the positive pitch case demonstrates higher magnitudes in advective flux at all cross-stream locations. However, the largest magnitudes are present at

the symmetry plane of the rotor $z/D = 0$, where the wake is ejected out laterally, driven by the dominant lateral flow component as indicated by the vectors. This trend remains consistent on the windward side of the rotor. Meanwhile, on the leeward side, the wake of the neighboring column connects within the measurement domain and projected frontal area of the rotor at $x/D = 12.5$, as evidenced in Figure 4.10. However, as this wake has low magnitudes in streamwise flow, the advective transport of momentum is lower.

For the negative pitch case, larger magnitudes in advective momentum entrainment are present on the leeward side of the rotor, which grows in magnitude between the volume behind the first and second rotors in the column. This is consistent with the vortex topology discussed in Section 4.4.2.

Finally, for the baseline case, the advective flux is low behind the first rotor due to the lack of a dominant vortex pair in the wake, as shown in Section 4.4.2. Behind the second and third rotors, advective flux is concentrated above and below the projected rotor surface, and the dominant cylinder-like vortex pair entrains momentum. However, the magnitude is not as high as the positive pitch case as the streamwise flow components are lower in magnitude due to the wake incident on the first rotor in the column, as shown in Figure 4.10.

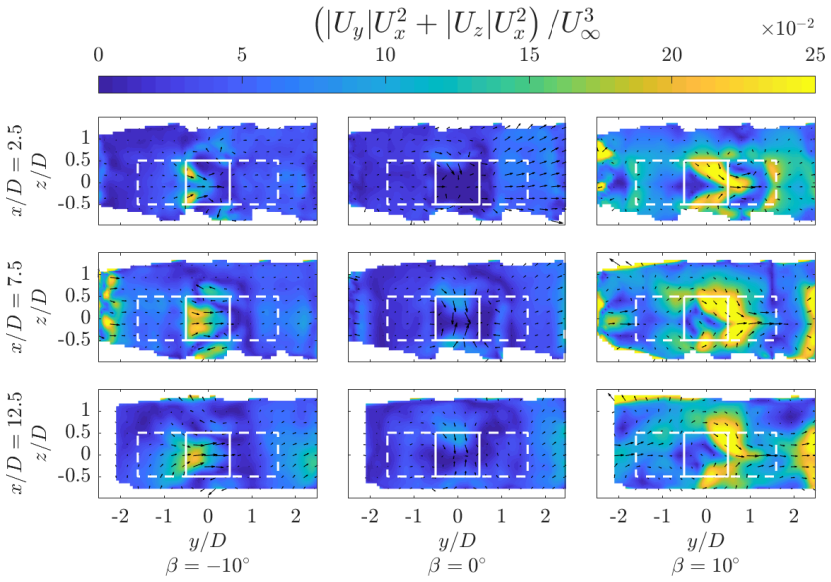


Figure 4.21: The sum of the lateral and axial advective contributions towards the flux at discrete cross-stream planes x/D = 2.5, 7.5, and 12.5 for the three pitch cases. The magnitudes of the velocity components $|U_y|$ and $|U_z|$ are considered to isolate the regions of momentum transfer. All values are normalized by the free-stream velocity component U_∞^3. In-plane velocity vectors are also shown. The box delineated by the solid white line denotes the projected frontal area of the central rotor column, and the white dashed line the grid size of the farm $-1.6 \leq y/D \leq 1.6$.

To shed light on the total advective momentum flux within the farm grid area, the

average sum of lateral and axial advective flux as a function of height z/D and cross-stream location x/D within the lateral domain $-1.6 \pm y/D \pm 1.6$ is shown in Figure 4.22. Consistent with the results above, the positive pitch case demonstrates the highest magnitudes in advective flux, growing in size when progressing further downstream in the farm. High magnitudes of flux are concentrated around the top and bottom of the rotors as high momentum flow is injected into the volume. Although the magnitudes at mid-span are lower, they are still notable as the wake is ejected out laterally. The negative pitch case demonstrates minimal mean advective flux behind the first rotor but grows in magnitude to approximately 1.2 behind the second and third rotors. The shape confirms that most of the advection of flux occurs at the mid-span of the rotor. As expected, the baseline pitch case exhibits minimal magnitudes of flux, with no significant wake deflection. Marginally larger fluxes are apparent at the upper and lower surfaces of the rotor due to the dominant cylinder-like CVP commented on in Section 4.4.2.

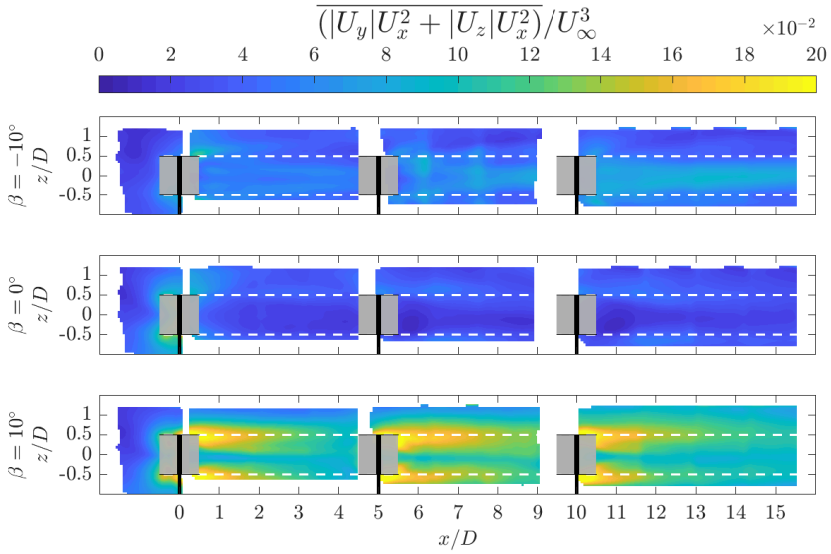


Figure 4.22: Average sum of the lateral and axial advective contributions towards the flux as a function of height z/D and cross-stream location x/D. The fluxes are averaged over the lateral domain $-1.6 \leq y/D \leq 1.6$ and normalized by the free stream flow U_∞^3. The gray-shaded region shows the rotors of the central column.

4.5 Conclusions

The theory behind the "vortex generator" VAWT wake control strategy using fixed-blade pitch was described, highlighting the expected modes of re-energization in the wake for cases where the blades are pitched in versus pitched out. The modes of operation of the wake control strategy were confirmed by the streamwise vortex topology within the farm. An energization of the upwind and downwind vortices is achieved by pitching the blade

inward and outward, respectively. For the former case, a significant influx of momentum from above and below the rotor was observed in the wake topology in parallel with a significant lateral deflection of the wake, consistent with thrust measurements of an isolated rotor. For the latter case, where the blades are pitched out, the downwind energized vortices induce an upwash of the wake while injecting high momentum flow from the sides of the rotor.

The efficacy of these modes towards wake re-energization was highlighted by considering a proxy of the available power in the wake. Once again, as the power of the rotors was not measured, the balance between the penalty associated with the steering turbine and that gained in the farm as a whole was not evaluated. The exaggerated pitch angles were selected to stay consistent with prior work performed by [135] and to magnify the benefits associated with modifying the rotor loading with wake recovery in mind. However, such large pitch angles are likely not to be applied for full-scale rotors, especially positive pitches, given the unsteady load fluctuations stemming from the large degree of flow separation in the upwind passage [33]. Nonetheless, these results demonstrate a proof-of-concept of the vortex generator mode for VAWT wake re-energization of a farm scale. When considering the case of a potential rotor directly in line with the central column, an available power recovery for the positive pitch case reaches a maximum of 72.4% at $x/D = 3.2$, which is a factor of 6.4 higher than the baseline case. Meanwhile, the recovery within the farm for the negative pitch case reaches a maximum of 53% at $x/D = 8.8$ (approx. 3D downstream of the second rotor), with a factor of 2.1 higher than the baseline case. This analysis was extended to allow for lateral offsets of hypothetical downstream rotors in the farm, highlighting the high potential for staggered arrangements. Although the positive pitch case showed the highest recovery rate for the inline rotor case, given the lateral deflection of the wake, the regions of high AP diminish on the windward side of the central column. These lucrative regions are further diminished on the farm when the wakes from the neighboring columns begin to fall within the projected area of the rotor column. Finally, the re-energization mechanism of the farm was highlighted by adapting a volume analysis of the mean kinetic energy equation. The fluxes through the lateral and axial surfaces of the central rotor column confirm the working principle of the vortex generator mode and shed light on its efficacy on a farm scale.

III

The X-Rotor vertical-axis wind turbine

4

5

Experimental characterization of the X-Rotor wake within the volume of rotation

This chapter presents phase-locked measurements within the volume of rotation of the X-Rotor with the absence of secondary rotors.

The results focus on the temporal and spatial evolution of the vortical structures shed by the blades as well as their subsequent impacts on the local induction. The measurements indicate a notable impact of the tip and shed vortices of the coned blades on the upwash and downwash within the rotor, which alternates as the vortical structures convect through the volume.

This chapter is based on **Bensason D.**, Sciacchitano A., Simao Ferreira C. Near wake of the X-Rotor vertical-axis wind turbine. *Journal of Physics: Conf. Series.* 2023. [134].
The data supporting this study is openly available in the 4TU.ResearchData repository at `https://doi.org/10.4121/e9952537-44aa-4715-beec-800444a35aa2`.

5.1 Introduction

As discussed in Chapter 2, the X-Rotor [28] is a radical rethink of the traditional VAWT geometry, which includes coned blades in the shape of an "X" with wingtip mounted HAWTs responsible for generating electrical power. Studies concerning the X-Rotor have been focused on the structural performance and cost expenditure modeling [28, 103], yielding results that suggest a potential cost of energy reduction of 20%. However, the impact of this coned blade geometry on the surrounding flowfield has yet to be investigated. This three-dimensional aspect will inflict a notable vertical component in the local induction field of the turbine. Consequently, the near and far wake dynamics will be affected, suggesting serious implications for farm-level aerodynamics, installation, and control strategies. This work is a first step towards experimentally quantifying the unique aerodynamics of the X-Rotor. The flowfield at several planes and phases within the turbine volume is measured using stereoscopic particle-image velocimetry. Measurements focus on the induction, near-wake, and tip effects of a scaled X-Rotor. These experimental results will serve as a baseline for the comparison to the case with secondary rotors, presented in Chapter 6, and as a database for the development and validation of numerical models.

The experimental setup, including the scaled X-Rotor model, flow measurement system, and case overview, is provided in Section 5.2. The results are presented in Section 5.3. A subset of the measurement results are presented to comment on the spatial and temporal evolution of the wake. Finally, the concluding remarks are provided in Section 5.4.

5.2 Methods

5.2.1 Wind tunnel and turbine model

Experiments were performed in the Open Jet Facility (OJF) at TU Delft Aerospace Engineering Laboratories, illustrated in Figure 5.1 and detailed in Chapter 4. A controlled streamwise velocity of U_∞ = 4m/s is used throughout the experiment.

A 1:100 scale X-Rotor model is mounted in the center of the test section, as illustrated in Figure 5.1, and a schematic in Figure 5.2. The model consists of four straight NACA0021 airfoils with a constant chord of c = 0.075m attached to a stiff crossbeam of length 0.5m with the same profile and chord. The blades are made of extruded aluminum with a cross-section defined by [145], while the crossbeam is made of milled steel. The top and bottom blades have a tip diameter of D = 1.5m and coning angles of 60° and 40°, respectively, resulting in an upper and lower blade length of 1m and 0.65m, respectively. The rotor is supported via a tower with a diameter of 0.6m. All components are anodized black to minimize the laser reflections. The resulting rotor solidity $\sigma = \sum cL_N/A$ is 0.15, where L_N is the blade height, and A = 1.29m^2 is the projected frontal area of the rotor. As the spans of the upper and lower blades vary, the solidity ratio is summed for each individually. The wind tunnel blockage ratio is 0.16, considering the projected frontal area of the rotor. The model is mounted on a frame and driven at a constant rational speed of 21.3 rad/s, resulting in a tip-speed ratio $\lambda = \omega R/U_\infty$ of 4.0. The chord-based Reynolds number of Re_c = 8.1×10^4 at the tip. Instrumentation for measuring the shaft torque, rotational frequency, and turbine thrust vectoring is included in the frame. A detailed overview of the instrumentation and frame dimensions is provided by LeBlanc et al. [145, 146].

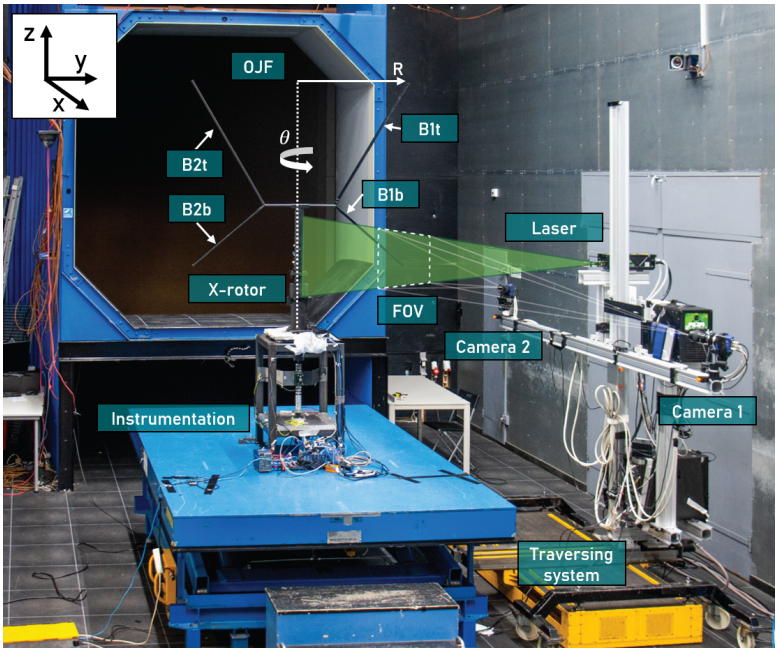


Figure 5.1: Experimental setup in the OJF wind tunnel at TU Delft. The main components of the setup and measurement systems are labeled. The direction of rotation and radius are marked for the X-Rotor model at phase θ= 0°. A visualization of the illuminated measurement plane is provided with dashed lines enclosing the field of view (FOV).

5.2.2 Flow measurement systems

A stereoscopic particle image velocimetry (PIV) system is used to measure several velocity fields at discrete cross-stream locations within the measurement volume of the X-Rotor. Water-glycol-based seeding is generated via a SAFEX smoke generator with an average particle diameter of 1 µm. The particles are illuminated with a Quantel Evergreen double-pulsed Nd:YAG laser with a sheet thickness of approximately 4 mm. Dual pulses with a wavelength of 523nm and 200mJ of energy are generated. Finally, images are captured at a frequency of 15 Hz using two LaVision Imager sCMOS cameras (16 bit, 2560x2160 pixles, 6.5 um pixel pitch) shooting from opposing sides of the laser sheet. With a focal length of 105 mm and numerical aperture 8, the resulting field of view (FOV) is approximately 43 cm × 30 cm, yielding a digital image resolution of 6 px/mm. A time separation of 280μs between images is used. Phase-locked acquisitions are achieved using an optical sensor between the rotor shaft and turbine base to receive a one-pulse-per-revolution signal when synchronizing the PIV setup. Desired phases are obtained by applying a time delay between the pulse signal and acquisition when considering the constant rotational frequency of the rotor. The resulting images are processed with a cross-correlation-based image interrogation algorithm with window deformation, with sizes of 128 px × 128 px and 64 px × 64 px and an overlap factor of 75 %. A total of 120 vector field images were captured for each measurement plane and averaged. As in Chapter 4, the camera and laser

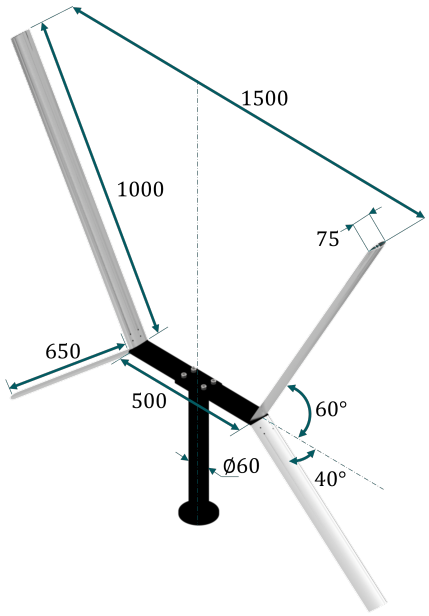


Figure 5.2: Wind tunnel scale X-Rotor schematic (dimensions in mm).

systems are rigidly connected and mounted on a traversing system, enabling a translation range in the x-axis and y-axis of 1.5 m and 0.5 m, respectively. Translation in the z-axis is achieved manually by shifting the rigid connection between the systems.

5.2.3 Flow measurement uncertainty

As in Chapter 4, the standard uncertainty ϵ of the velocity components is calculated using Equation (4.1), where $z_a = 2$ is the coverage factor, σ_U is the standard deviation of the velocity and $N = 120$ is the number of samples. The standard deviation of the velocity σ_U is made up of all three velocity components and varies within the measurement plane. In general, regions of high vorticity (tip vortices and shed vorticity) feature a velocity standard deviation of $\sigma_U = 0.24\,\mathrm{m/s}$ (the highest of which is out of the plane, the other two are $0.19\,\mathrm{m/s}$ and $0.15\,\mathrm{m/s}$). In regions where no vortical structures are present but still in the wake, the velocity standard deviation tends to be lower, around $\sigma_U = 0.05\,\mathrm{m/s}$ (similar for all the velocity components). Using the highest value for the calculation, the standard uncertainty of the mean velocity is $\epsilon = 0.04\,\mathrm{m/s}$, which is 1% of the free-stream velocity.

The diffraction-limited minimum image diameter d_{diff} is of practical significance for optical measurements such as PIV. Following Equation (4.2), the smallest particle image that can be obtained using our given imaging configuration [124].

The magnification factor is M=0.01, considering that the pixel pitch of the sCMOS cameras is 6.5 µm, and the sensor size is 2560 × 2160 pixels. The lens used has a focal length f of 105mm. Hence, the object imaging distance (d_o) is 101mm. The f-number $f_\#$ for this experiment was set to 8, and the laser light has a wavelength of $\lambda = 523\,\mathrm{nm}$ (catalog).

Hence, d_{diff} is 10.1 µm. The particle image diameter is $10.1/6.5 = 1.55$ pixels, which leads to limited peak locking errors [124].

5.2.4 Case description

The aforementioned measurement system captures phase-locked measurements of the flowfield at varying locations of the X-Rotor induction field, visualized in Figure 5.3. As defined in Figure 5.1, the coordinate system is such that x, y, and z are the streamwise, radial, and axial directions, respectively. The case of $x = 0$ corresponds to the center of the turbine tower in the streamwise direction and a phase of $\theta = 0^\circ$ when both blades lie on the $x = 0$ plane. The normalized cross-stream locations x/R = {-0.87, -0.53, -0.13, 0.13, 0.53, 0.87} were measured at phases θ = {0°, 45°, 90°, 135°}, where $R = 0.75$m is the turbine tip radius. At a given cross-stream location, several planes are measured in the y-axis and z-axis directions via the traversing system and stitched together. Due to time and storage constraints, not all phase and wake locations were measured in the same detail, with varying numbers of planes measured for each wake and phase pair. Further, due to the orientation of the cameras concerning the measurement planes, frequent masking operations are applied to the measurements to avoid shadows. Due to the placement of the PIV system, measurements focus predominantly on the windward passage of the blade, reaching up to approx. y/R = -0.53.

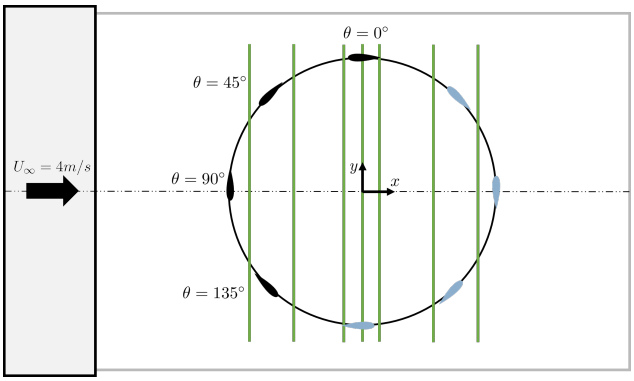


Figure 5.3: Scaled schematic of the top view of the setup. Blade 1 (black) phases are shown along with the respective positions of Blade 2 (blue). The measurement planes (green) are marked. The size of the airfoil cross-sections is not to scale.

5.3 Results

5.3.1 Phase-locked flow fields at $\theta = 90^\circ$

The phase-locked wake at $\theta = 90^\circ$ at streamwise location x/R=-0.13 is summarized in Figure 5.4. The normalized streamwise (U_x), axial (U_z), and lateral (U_y) velocities are shown along with the normalized streamwise vorticity (ω_x).

As these measurements are taken within the volume of rotation of the rotor, the wake has not yet expanded, and it is contained within the bounds of the shed vorticity of the blades. Characteristic of VAWTs, there is a clear presence of both shed-vorticity and tip-

vorticity [41, 53] stemming from both blades at the top and bottom of the rotor, labeled as B1 (at $\theta = 90^\circ$) and B2 ($\theta = 270^\circ$). The positions of these vortical structures are clearly visible, with those created by B1 coinciding on the edge of the volume and those of B2 inboard at y/R=0.5 due to their convection downstream. Note that the structures appear more outboard of the swept area on the top blades due to the deflection of the cantilevered nature of the blades and centrifugal forces. The shed vorticity of B2t and B2b appears in a curved shape, which is an artifact of the difference in convective time between spanwise locations of the coned blade and streamwise plane.

There are several variations in the streamwise flow deficit across the frontal area of the rotor. As noted above, local deficits due to the tip and shed vorticity of the blades are present. Additionally, there is a clear asymmetry in the wake with higher magnitudes of flow deficit present on the windward side of the cycle ($y/R > 0$) compared to the leeward side ($y/R < 0$). This is highlighted by the presence of streamwise flow on the order of $U_x/U_\infty = 0.9$ in both the upper and lower halves of the rotor.

The lateral velocity contour follows the average expansion of the wake with minor variations imposed by the shed and tip vorticity of the blades. The impact of the coned blades is once again visible along the shed vorticity path of B2, imposing variations in the expansion rates of the wake. There is a presence of a downwash on the upper half of the rotor ($z/R > 0$) and an upwash on the lower half ($z/R < 0$). Significant local variations in the average expansion are imposed by the curved vortical structures from B1 and B2 in both the windward and leeward halves of the cycle. The impact of the axial induction imposed by the vorticity and blade loading is visible in the deformation of the wake near the tip regions.

5.3.2 Flow field variation with phase

The discussion provided in Section 5.3.1 gives an overview of the phase-locked flowfield at the fixed cross-stream location. However, several phases need to be compared to make observations of temporal variations in the wake. The phase-locked flowfield at $\theta = 0^\circ$, 45°, and $\theta = 135^\circ$ are presented in Figure 5.5 (the case of $\theta = 90^\circ$ is shown in Figure 5.4). The results include the normalized streamwise flow, axial velocity, and streamwise vorticity.

At a phase $\theta = 0^\circ$, Blade 1 has yet to pass the upwind plane, and hence, only the presence of strong vortical structures generated by Blade 2 is visible. However, weak vortical structures shed by the top tip of Blade 1, which have convected and diffused downstream from the previous cycle, are also visible near the center of the rotor at $y/R = 0$. The vortical structures of Blade 2 are near the edge of the frontal area where Blade 1 is passing, suggesting the presence of blade-vortex interactions. Consequently, local variations induced by these structures in the axial flow are visible. Regions of upwash and downwash in both the upper and lower halves of the rotor suggest local regions of axial expansion and contraction.

With two co-rotating, closely-spaced vortices (B1 and B2) in the upper and lower halves at $\theta = 45^\circ$, the induced level of upwash and downwash in the lower and upper halves has increased in magnitude. Furthermore, vortical structures on the left side of the rotor ($y/R < 0$) stemming from the leeward quartile of the cycle are very visible.

The case of $\theta = 135^\circ$ at this cross-stream location is unique as we are slicing (or are just downstream) of the top tip-vortex shed by Blade 2 (B2t). The entrance and exit of the

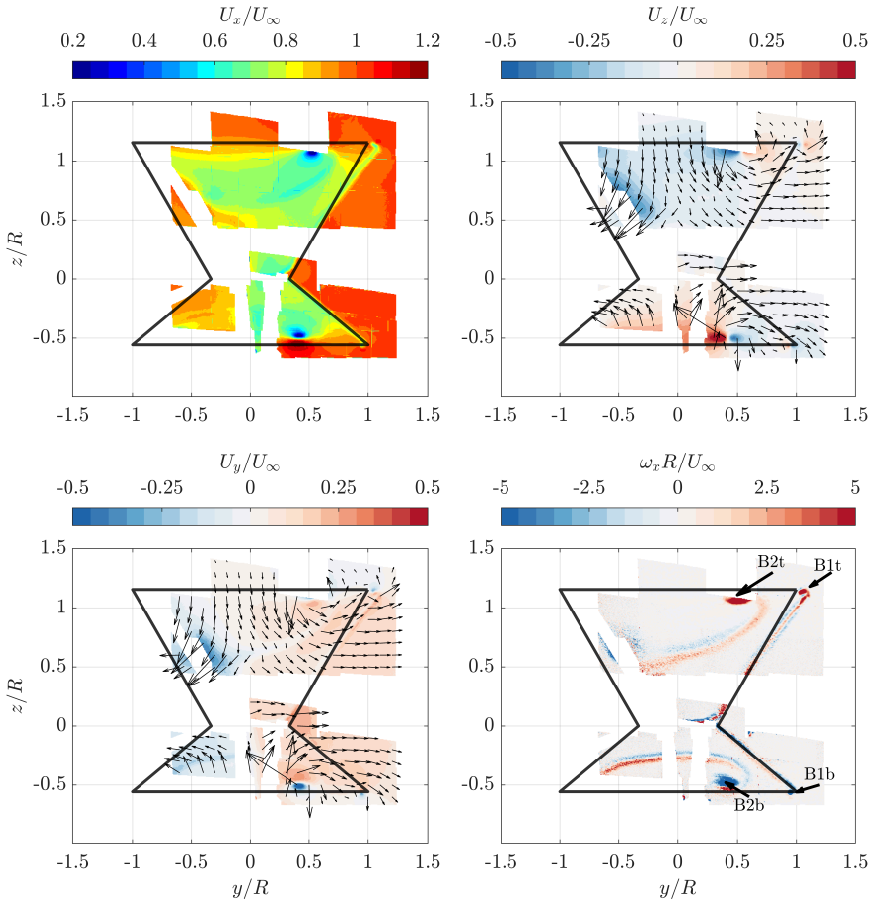


Figure 5.4: The wake at a streamwise location of x/R=-0.13 and phase-locked position of θ = 90°. Solid black lines indicate the projected frontal area of the rotor. Vortical structures produced by their respective blades are labeled, as described by Figure 5.1.

vortex from the measurement plane are evident from the streamwise velocity component, given the large, closely spaced areas of flow deficits. As we are downstream of the vortex, there is a large region of induced downwash in the upper half, with entrance and exit areas bound by the respective regions of upwash. Although the shed vorticity of the bottom blade (B2b) is visible, the tip vortex of the same magnitude in the upper half is not. This can be attributed to the larger deflection of the upper blades (and hence the difference in convective distance between the plane and the upper and lower blades) as well as the induction of the tower.

When evaluating the streamwise wake in consecutive temporal order across Figure 5.5 and Figure 5.4, a consistent asymmetry in the wake can be observed, where a heavier flow deficit is present on the right side of the rotor ($y/R > 0$). Consistent with results

and observations by [41], this wake asymmetry is driven by cyclic loading of the blades experienced in the windward and leeward quarterlies of the flow as well as the subsequent co-rotating and counter-rotating vortex pairs.

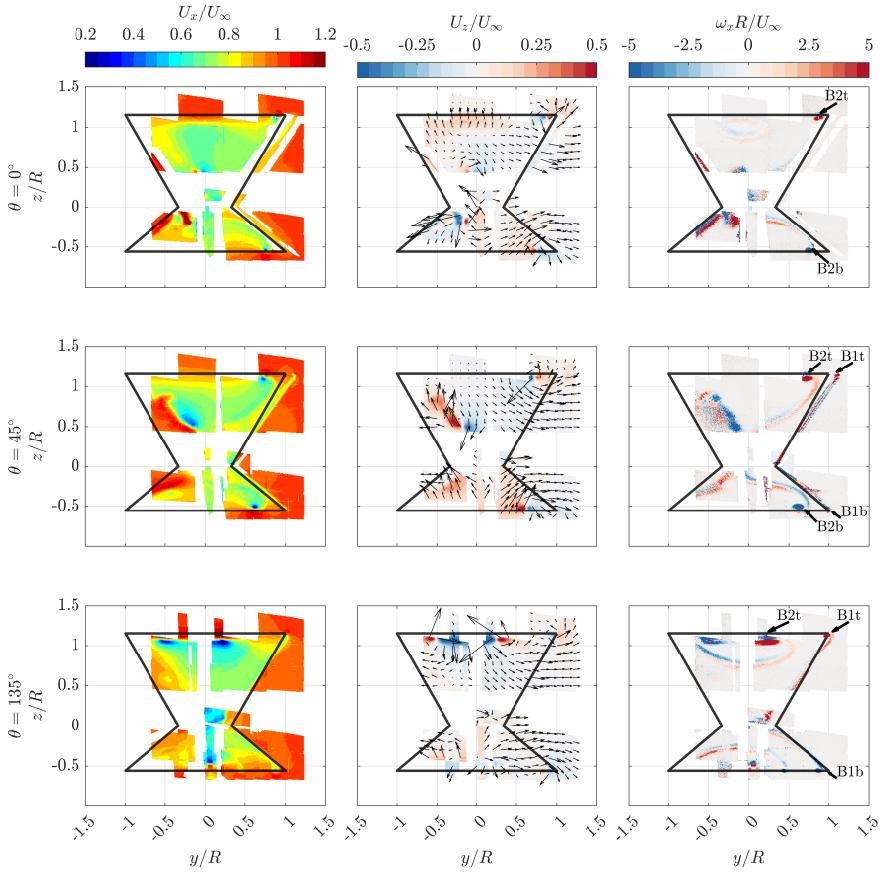


Figure 5.5: Normalized streamwise velocity U_x/U_∞, axial velocity U_z/U_∞, and streamwise vorticity $\omega_x c/U_\infty$ at a x/R=-0.13 and phase-locked position of $\theta = 0°$ (top row), $\theta = 45°$ (middle row) and $\theta = 135°$ (bottom row). The solid black lines indicate the projected frontal area of the rotor.

5.3.3 Spatial evolution of the wake

The results in Section 5.3.1 and Section 5.3.2 focused on the phased-locked measurements at x/R= -0.13 and illustrated a strong presence of axial induction component imposed by the tip and shed vorticity of the coned blades across several phases. These effects on the wake are further explored on an extended set of upstream and downstream locations shown in Figure 5.6.

Starting from the most upstream position, the wake at x/R = -0.87 shows a large local velocity deficit in the areas surrounding the tip-vortex of Blade 1. As this plane is not yet at

the tip, there is still an apparent flow deficit due to the shed vorticity of the blade. Consistent with the results discussed in Section 5.3.1, there is a large variation in streamwise velocity when moving along the span at a given y/R location due to the varying distances between the blade and plane location. More of the velocity deficits caused by B1t and B1b become present when moving further downstream to the location x/R=-0.53. A strong gradient in the streamwise flow velocity is evident both along the span of the blade as well as in the axial direction, ranging from U_x/U_∞ = 0.6 to 0.9 at z/R= 0.6 and 1.1, respectively.

The wake imposed by the tower is present at x/R=0.53 before recovering slightly in x/R=0.87. Similar to the $x/R = -0.87$ case, there are axial variations in the streamwise flow imposed by the local vorticity structures and varying convective times to spanwise locations on the blade. When viewing the streamwise locations in consecutive order, starting from the most upwind, the impact of the axial tip-vorticity and subsequent axial induction on the contraction of the wake becomes more evident. This contraction is seen on both halves of the turbine but seems to be more severe on the lower half, as discussed in Section 5.3.2. The axial contraction is complemented by the lateral expansion as suggested by the quivers in the downwind planes.

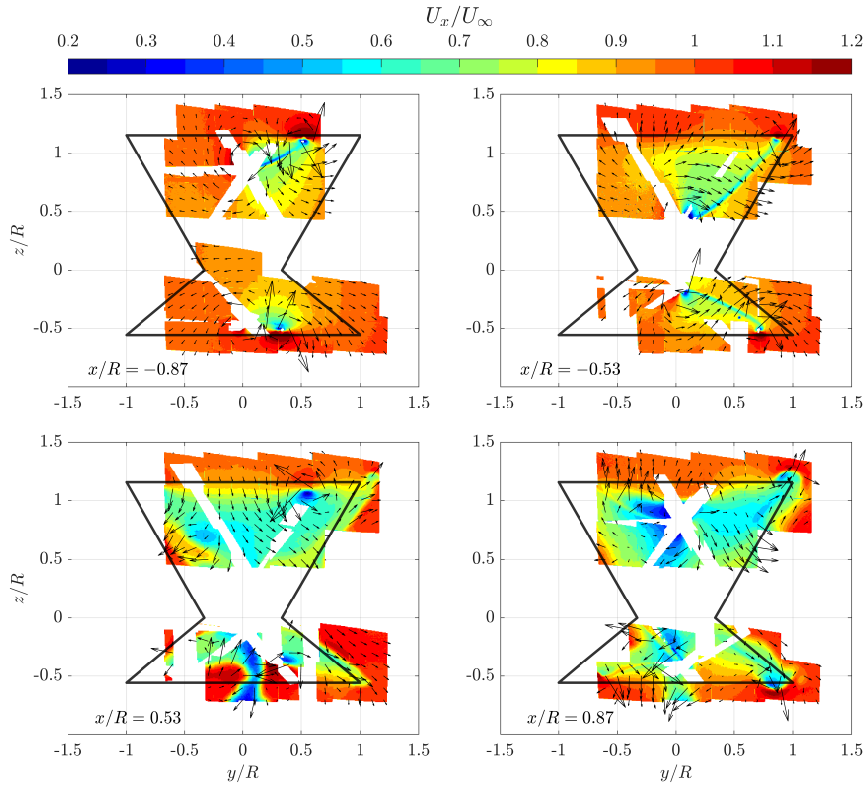


Figure 5.6: Normalized streamwise velocity U_x/U_∞ at a phase-locked position of $\theta = 90^\circ$ and streamwise locations $x/R = [-0.87, -0.53, 0.53, 0.83]$. The solid black lines indicate the projected frontal area of the rotor.

5.4 Conclusions

In this work, the near wake of the X-Rotor vertical-axis wind turbine was investigated experimentally. Particle image velocimetry was used to capture the flow field at several phase-locked positions and streamwise locations within the rotor's volume of rotation.

Characteristic phenomena of vertical-axis wind turbines were observed for this novel geometry, including the presence of both tip and shed-vorticity as well as blade-vortex interaction. Due to the coned nature of the blades, the shed vorticity appears in an elliptical shape when measured at a plane perpendicular to the flow. These structures induce local variations in the average expansion of the wake across different phases. When comparing several cross-stream locations at a fixed phase in the wake, a gradual axial contraction and lateral expansion can be observed. This process is driven by the tip and shed vortices in the near wake before convecting downstream and diffusing.

6

The impact of blade-tip mounted rotors on the X-Rotor vertical-axis wind turbine

The aim of this chapter is to experimentally demonstrate the aerodynamic gearbox concept using secondary rotors, introduced in Chapter 2. Furthermore, Particle image velocimetry measurements are taken at cross-stream planes within the volume of rotation of a scaled turbine model at several phase-locked positions to examine the spatial and temporal variation of the secondary rotor wake. The results are compared with the measurements without secondary rotors discussed in Chapter 5, focusing on the impact of the blade-tip mounted devices on the trailing tip-vorticity and mixing process.

This chapter is partly based on **Bensason D.**, Sciacchitano A., Simao Ferreira C. Experimental study of the impact of blade-tip mounted rotors on the X-Rotor vertical-axis wind turbine. *Journal of Physics: Conf. Series.* 2024. [147].
The data supporting this study is openly available in the 4TU.ResearchData repository at `https://doi.org/10.4121/0e7bdd8c-6aa5-49ff-9d79-0b39f998aece`.

6.1 Introduction

Blade-tip-mounted rotors are included on the bottom tips of the primary rotor. The geometry relies on an aerodynamic gearbox concept, where the primary rotor extracts mechanical power from the wind while the secondary rotors are responsible for driving electrical generators. This introduces a theoretical balance between the torque and thrust of the primary and secondary rotors, respectively, described in Chapter 2. This study aims to provide an experimental demonstration of the aerodynamic gearbox concept by measuring the primary rotor torque with and without secondary rotors in an open-jet wind tunnel. Phase-locked particle image velocimetry measurements are taken at several planes within the primary rotor's rotation volume to shed light on the spatial and temporal evolution of the wake stemming from the secondary rotors. The measurements are compared with cases without secondary rotors present to understand the local impact of the blade-tip mounted devices on the wake and trailing tip vortices, as well as the mixing process in the near wake using the measurements discussed in Chapter 5.

The remainder of the chapter is organized as follows: The experimental setup, measurement system, case overview, secondary rotor design, and performance are described in Section 6.2. A summary of the primary rotor torque and wake measurements are discussed in Section 6.3. Finally, conclusions are provided in Section 6.4.

6.2 Methods

6.2.1 Secondary rotor design and operating conditions

The experiments are performed in the Open-Jet Facility (OJF) of TU Delft's Aerodynamics Laboratories, as illustrated in Figure 6.1. A 1:100 scaled primary rotor model is used, with details of the geometry and the tunnel provided in Chapter 5.

The secondary rotors are sized by geometrically scaling the full-scale X-Rotor design [148]. The full-scale design includes a secondary rotor diameter of 9.4m. Given the aforementioned scaling ratio, the lab-scale diameter is $d_2 = 94$mm, as shown in Figure 6.2.

The secondary rotors are mounted to the bottom blade tips of the primary rotor, as visualized in Figure 6.1. The rotor is made of smoothed 3D-printed PLA and driven by a brushless motor. The motor is mounted to a 3D-printed sleeve of the same material and controlled using an electronic speed controller with governor control mode. The system is powered by a battery and programmed using an Arduino. The batteries and Arduino are mounted in the primary rotor crossbeam and tower, with cables running through the blades to the mounted motor units.

The relationship between the primary rotor torque and secondary thrust is expressed in Equation (2.1) assuming a 100% conversion efficiency between the extracted power of the primary rotor and the generated power of the secondary rotors. The expression can be simplified by considering the cycle averaged incident velocity of the secondary rotor is equal to the blade-tip speed of the primary rotor $\overline{U_I} = \omega_1 R_1 = \lambda_1 U_\infty$, and hence:

$$\frac{C_{P1}}{C_{T2}} = N\lambda_1^3 \frac{A_2}{A_1} \tag{6.1}$$

where C_{P1} and C_{T2} are the power and thrust coefficients of the primary and secondary rotors, respectively. The number of secondary rotors and the tip-speed ratio of the primary

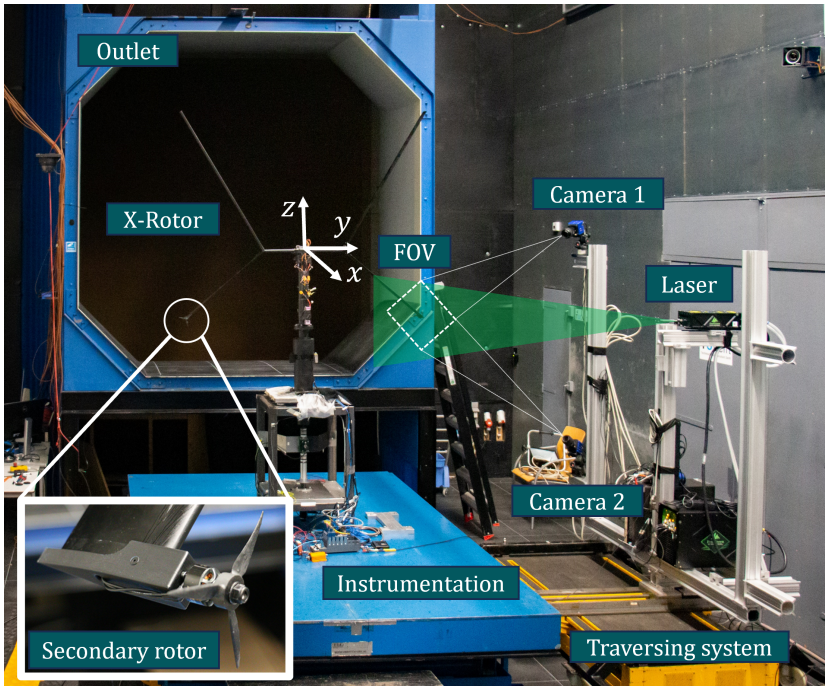


Figure 6.1: Experimental setup in the OJF with the main components labeled and a magnified view of the mounted secondary rotors.

rotors are expressed as N and λ_1, and the ratio between the frontal area of the secondary and primary rotor is expressed as $\frac{A_2}{A_1}$. As described in Chapter 2, several operating conditions are expected for the X-Rotor, requiring a detailed controller design to maintain the optimum performance. This study aims to demonstrate the balance at the control strategy of Mode 4, i.e., where the primary rotor torque and secondary rotor rotational frequency are kept constant. The balance expressed in Equation (6.1) requires a priory knowledge of the relationship between primary rotor performance C_{P1} and tip-speed ratio λ_1. Here, the tip-speed ratio of the primary rotor is taken as $\lambda_1 = 4$. Given a lack of experimental performance data for the X-Rotor model, a $C_{P1} = 0.4$ at this tip-speed ratio is assumed given prior numerical simulation by [146] for a straight-bladed VAWT of comparable frontal area. The bottom blade tips both house a secondary rotor; thus, $N = 2$. The frontal area of the primary and secondary rotors are $A_1 = 1.29\text{m}^2$ and $A_2 = 0.007\text{m}^2$, respectively. Hence, the desired secondary rotor thrust is calculated as $C_{T2} = 0.58$.

The chord and twist distributions of the secondary rotor are calculated using a backward BEM approach for a constant NACA4412 profile, which uses the geometric constraints, desired thrust coefficient, and tip-speed ratio [108]. This profile was selected given the availability of experimental polars at low Reynolds numbers [149]. The chord and twist distribution of the final design used in this campaign is shown in Figure 6.3. The thrust as a function of the tip-speed ratio was tested in TU Delft's W-tunnel, which is an open-jet wind tunnel with an outlet of 60cm×60cm. The streamwise loads were measured using the

same load balance system described in Chapter 4. The results are shown in Figure 6.3. The data points are fitted using a second-order polynomial curve. Given the aforementioned desired secondary rotor thrust coefficient and fitted curve, the required tip-speed ratio is $\lambda_2 = 4.6$, corresponding to an angular frequency of $\omega_2 = 1566$ rad/s, assuming the blade-tip velocity of the primary rotor of 16m/s.

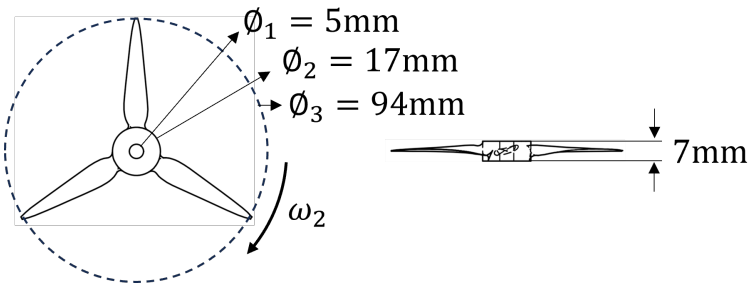


Figure 6.2: (Left) Front view and (Right) Side view of a schematic of the secondary rotor.

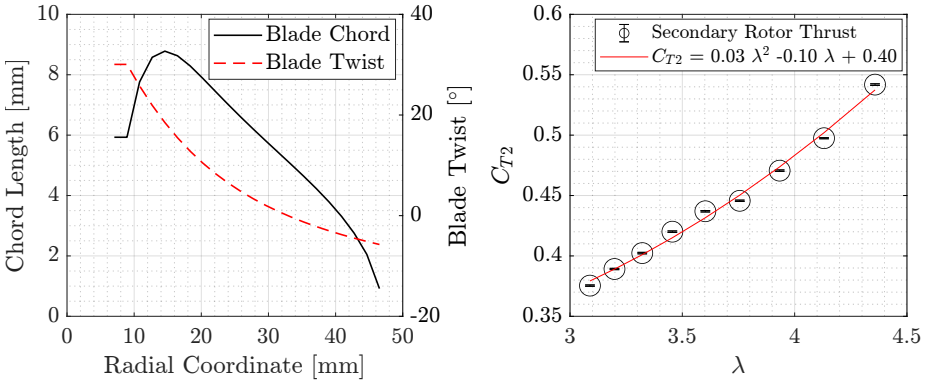


Figure 6.3: (Left) Secondary rotor chord and twist distribution. (Right) Experimental thrust curve of the secondary rotor as a function of tip-speed ratio. Error bars represent the 95% confidence interval of the estimation of the average value, and the red line shows a second-order fit to the data points.

6.2.2 Flow measurement system

A similar stereoscopic particle image velocimetry (PIV) setup is used to capture the flowfield at several cross-stream and phase-locked positions of the rotor as in Chapter 5. An overview of the setup is provided in Figure 6.1. The image resolution of the cameras is 2560px × 2160px and was used with a 105mm lens and numerical aperture of 8. The measurement plane's resulting field of view (FOV) is approximately 50cm × 30cm with an image resolution of 7.16px/mm. A total of 120 images are captured at an acquisition frequency of 15Hz at each FOV. The cameras and laser are rigidly mounted on a traversing system such that the FOV can be accurately moved and stitched in post-processing in streamwise and lateral directions.

6.2.3 Measurement cases

The aforementioned measurement system captures the flowfield at several phase-locked positions of the primary rotor and cross-stream locations, as shown in Figure 9.5. An overview of the measurement planes and primary rotor phase-locked position combinations is shown in Figure 6.4. Primary rotor phase-locked positions are measured between $\theta = -15^\circ$ and $\theta = 90^\circ$ at increments of 15°. The upwind windward (UW) and downwind windward (DW) quadrants correspond to primary rotor phase ranges $0^\circ < \theta < 90^\circ$ and $270^\circ < \theta < 360^\circ$, respectively. The measurement planes are concentrated within the volume of the rotor at the transition between the upwind and downwind half, namely at $x/R_1 = [-0.40, -0.13, 0, 0.13, 0.40]$, and extend mainly within the windward half of the cycle.

For the sake of clarity when discussing the origin of certain flow structures in the wake, the theoretical trailing tip-vorticity of the bottom blade is shown as a function of the primary rotor phase-locked positions in Figure 6.4. For this visualization, no wake expansion or induction is assumed. Hence, the trailing structures simply convect downstream at a rate of the freestream velocity U_∞ upon their conception. The solid and dashed lines correspond to the trajectories stemming from the blade at the noted primary rotor phases and those stemming from the second blade (at a phase difference of $\theta = 180^\circ$). These are denoted as B1 and B2, respectively. The solid horizontal green lines correspond to the measurement planes. In addition to color-coding the theoretical tip-vortex trajectories based on the phase-locked position, a visualization of the structures based on the generation phase is also provided, i.e. from which phase in the cycle the tip-vortex was shed. Given the simplified assumption of omitting the induction, the generation phase can be expressed geometrically as:

$$\theta_{\text{Generation}} = \arccos\left(\frac{y_{\text{core}}}{R_1}\right), \tag{6.2}$$

where y_{core} is the lateral vortex core position.

In addition to a discussion of the spatial and temporal evolution of the secondary rotor wake, a comparison to the baseline results (data without secondary rotors from Chapter 5) is drawn. These comparisons focus mainly on overlapping primary rotor phase and measurement plane combinations between the two experiments, namely at x/R_1 = -0.13,0.13 and primary rotor phase-locked positions θ = 45° and 90°. Although the primary rotor phase $\theta = 135^\circ$ was not measured with secondary rotors, this measurement combination at the aforementioned planes is also considered when discussing the vortex circulations from B1 and B2.

To maintain consistent with the baseline measurements, the wake is measured at a constant rotational frequency of the primary rotor of ω_1 = 21.3rad/s, corresponding to a tip-speed ratio $\lambda_1 = \omega_1 R/U_\infty$ of 4, with a chord-based Reynolds number of $\text{Re}_c = \rho U_\infty \lambda_1 c/\mu$ = 8.1×10^4.

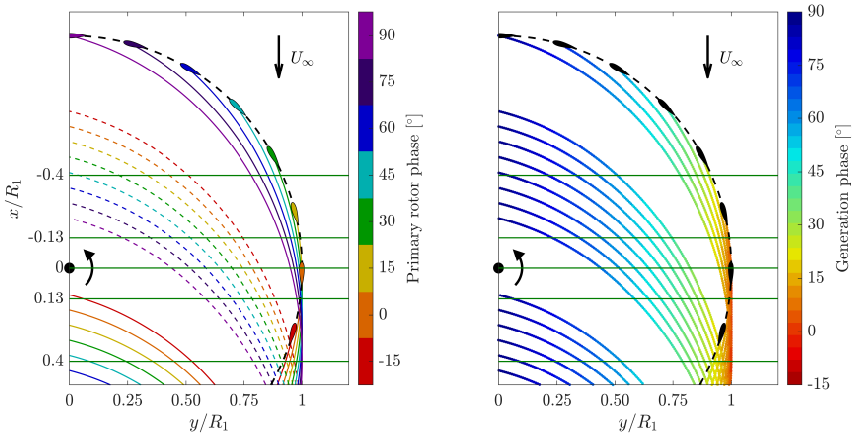


Figure 6.4: (Left) The theoretical blade-tip vortex trajectory color-coded by the primary rotor phase. The solid and dashed lines correspond to the trajectories shed by the two blades of the primary rotor. The solid black dashed line indicates the blade-tip trajectory of the primary rotor, and the green lines are the measurement planes. (Right) The theoretical blade-tip vortex trajectory is color-coded by the phase at which the vortex is generated.

6.3 Results

6.3.1 The wake of the secondary rotor

The normalized streamwise velocity and vorticity in the wake of the secondary rotor are shown in Figure 6.5 and Figure 6.6, respectively. The black dashed line indicates the trajectory of the bottom blade tip of the primary rotor, whilst the solid colored line corresponds to the theoretical trajectory of the trailing vortical structures, consistent with the color coding illustrated in Figure 6.4. The following observations can be drawn from the results:

- **Direction of vortex rotation:** As discussed in reference to the baseline results in Chapters 5 and 7, the direction of rotation of the trailing vorticity for VAWT is a function of the loading direction of the blade in the inertial frame of reference and the sign of this bound circulation, which flips in direction at θ =0° and 180° as the pressure and suction sides of the blades reverse. Consideration of the trailing vortices confirms this as all of the vortices stemming from B2, which have been generated in the UW quadrant at phases $\theta_{\text{Generation}} > 30^\circ$ are blue (clockwise). Meanwhile, those generated in the DW quadrant, such as the structure shown at $x/R_1 = 0.4$ at $\theta = -15^\circ$, are predominantly red (counterclockwise). The structures generated in the UW quadrants, which have convected to the measurement planes concentrated at the center of the rotor $-0.13 < x/R_1 < 0.13$, show concentrations of both positive and negative vorticity. This is due to the non-perpendicular intersection of the intrinsically curved vortex structure stemming from the blade tips and the secondary rotor. The vorticity stemming from the secondary rotor is predominantly azimuthal (as with a HAWT or actuator disk); however, when intersected at an angle, the

vorticity is effectively projected into the measurement plane, splitting the originally azimuthal vorticity into positive and negative streamwise vorticity regions.

- **Blade-vortex and vortex-vortex interactions:** As described in Chapter 2, blade-vortex interactions and vortex-vortex interactions are intrinsic phenomena of VAWTs. A visual inspection of Figure 6.4 suggests blade-vortex interactions to occur in the DW quadrant of the cycle at phases close to $\theta = -15^\circ$. In Figure 6.6, this is evident at $\theta = -15^\circ$ and $\theta = 0^\circ$ at $x/R_1 = 0.40$ as the secondary rotor passes directly through the trailing vortex structure of B2. Considering areas where the theoretical trailing vortex trajectories of B1 and B2 overlap would indicate regions where vortex interactions occur. At the measurement plane $x/R_1 = 0.13$, the structures of B1 and B2 are in close proximity up until $\theta = 30^\circ$, resulting in a straining out process of the B2 structure [150]. This process evolves temporally at the most downwind measurement plane $x/R_1 = 0.40$, resulting in a counter-rotating vortex pair that gradually diffuses and convects outward. Interestingly, this counter-rotating vortex pair is visually analogous to the vortex pairs generated by a yawed wind turbine, as described in Chapter 2. A visual inspection of the temporal evolution of the wake at the most downwind measurement plane begins to approach a similar topography to the signature kidney-shaped wake of a yawed turbine [143]. It is worth mentioning that although a yawed wake of the secondary rotor is expected, as discussed in Chapter 2, the maximum expected geometric angle of attack for the blade would not surpass 14.5° (given $\lambda_1 = 4.0$). Furthermore, when considering the induction, the effective angle of attack would be reduced even further in magnitude in the downwind half [151]. Hence, the counter-rotating vortex pair observed here is likely due to the vortex interactions between B1 and B2 rather than those generated by the yawed secondary rotor.

- **The emergence of the primary rotor tip-vortex:** As discussed with the first point, the structures generated by B2 within the measurement domain have a dominant and coherent clockwise rotation, whilst those generated by B1 have both red and blue regions due to the angled measurement plane with respect to the vortex filament. This poses the question: Why does the trailing vortex structure transition from a dual clockwise/counterclockwise pair to a single dominant rotation direction? This can be understood by considering the loading and subsequent trailing vorticity of the primary rotor blade and secondary rotor separately. The load of the primary rotor blade is steadily increasing throughout the UW quadrant due to the increasing angle of attack (shown in Chapter 2), resulting in an increasingly stronger trailing tip-vortex. Meanwhile, the secondary rotor load (thrust) would gradually decrease as it yaws out of the flow and the incident velocity decreases [108]. Hence, as the primary rotor generation phase gradually increases, the trailing tip-vortex of the primary rotor blade will dominate over the secondary rotor azimuthal vortex ring. Although the entirety of this process is not captured in the measurement planes, evidence of this is visible upon inspecting the temporal evolution of the most upstream measurement plane $x/R_1 = -0.4$, starting from $\theta = 30^\circ$. As structures generated further in the UW cycle convect through the plane, two distinctly different regions become present, namely, the more coherent blade-tip-vortex from the primary rotor (blue, towards

the center of the rotor) and the turbulent region of mixed vorticity stemming from the heavily yawed secondary rotor.

- **Vortex trajectory:** The structures from B1 coincide with the predicted trajectories to a high degree, whilst those stemming from B2 present more significant lateral deviations at certain plane and phase combinations. In the upwind measurement planes, the structures appear laterally offset towards the center of the rotor compared to the predicted trajectories, whilst more outside the rotor volume on the downwind planes. This is likely due to many factors that are not considered in the simplified formulation of the vortex trajectory, such as the temporally and spatially varying vertical and lateral flow within the coned blade geometry. A quantification of the trajectories is discussed in Section 6.3.4.

6.3.2 The aerodynamic gearbox principle

To experimentally verify the aerodynamic gearbox concept, the change in primary rotor torque ΔQ_1 with and without the secondary rotors (SR) present is measured, presented as a function of azimuth over 200 cycles in Figure 6.7. The horizontal dashed lines indicate the cycle-averaged values for the two cases. Note, as the delta with respect to the baseline case (without SR) is considered, the average coincides with $\Delta Q_1 = 0$. The primary rotor torque decreases with the presence of the secondary rotors as they add a counter torque to the system. The magnitude of the counter torque added by the secondary rotors ΔQ_1 is 0.98Nm. To determine whether the difference in primary rotor torque is proportional to the design thrust coefficient, the cycle averaged thrust can be approximated using a simplified moment arm approach using Equation (6.3):

$$C_{T2} = \frac{\Delta Q_1}{0.5 \rho N R_1 \overline{U_I}^2 A_2} \tag{6.3}$$

where ρ is the air density, and $\overline{U_I}$ is the flow speed at the blade tip of the primary rotor. This approach assumes a decoupled performance between the primary and secondary rotors, i.e., that the primary rotor torque remains unchanged with and without secondary rotors. This is likely untrue, as the interaction of the tip region of the primary rotor blade with the secondary rotor wake will cause a net reduction of the torque of the primary rotor, leading to an overestimation in the calculated secondary rotor thrust. In this case, the cycle averaged flow speed at the blade tip of $\overline{U_I} = \lambda_1 \times U_\infty = 16$m/s is used. Hence, the thrust coefficient of the secondary rotor can be approximated to be $C_{T2} = 0.60 \pm 0.12$. This agrees well with the design value described in Section 6.2.1. We can, therefore, confirm that the machine is operating as intended and that the aerodynamic gearbox concept is feasible. This design secondary rotor thrust results in a change in the primary rotor power coefficient of $\Delta C_{P1} = 0.41$, consistent with the design case described in Section 6.2.1.

6.3.3 Wake comparison: secondary rotor & baseline

The secondary rotor wake was discussed in Section 6.3.1, and the torque of the primary rotor was used in Section 6.3.2 to experimentally verify the aerodynamic gearbox concept. Differences in the normalized streamwise flow and vorticity between the cases with and

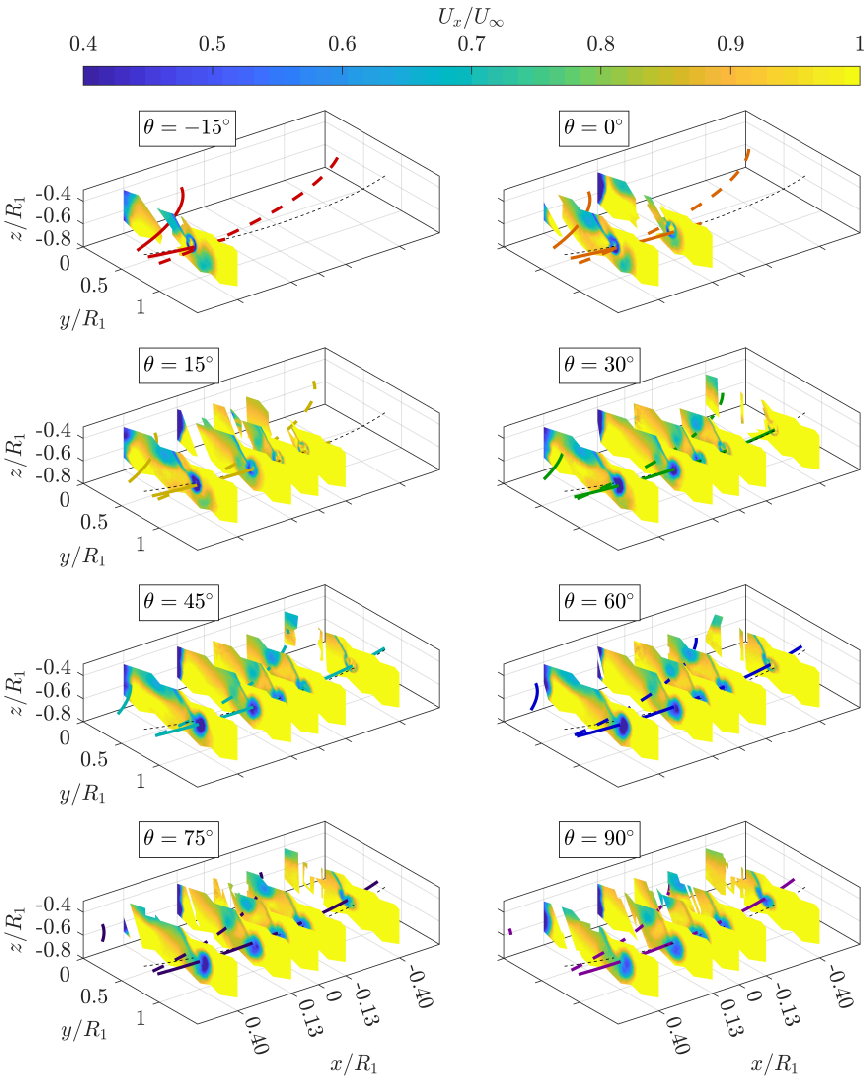


Figure 6.5: Normalized streamwise velocity distributions as a function of phase-locked rotor position θ and measurement plane x/D. The black dashed line indicates the trajectory of the bottom blade tip of the primary rotor. The phase-dependent solid and dashed curves correspond to the trajectories of B1 and B2 as denoted in Figure 6.4. Note that the scale of the x-axis is doubled to increase the spacing between the measurement planes.

without secondary rotors (SR) are shown in Figure 6.8 and Figure 6.9. The frontal area of the primary rotor is outlined at a phase of $\theta = 0°$, and the vectors show the in-plane velocity components. For the contours with secondary rotors, the projected frontal area is shown at the primary rotor phase $\theta = 0°$.

As with the secondary rotor, the measurement planes intersect two trailing tip-vortices

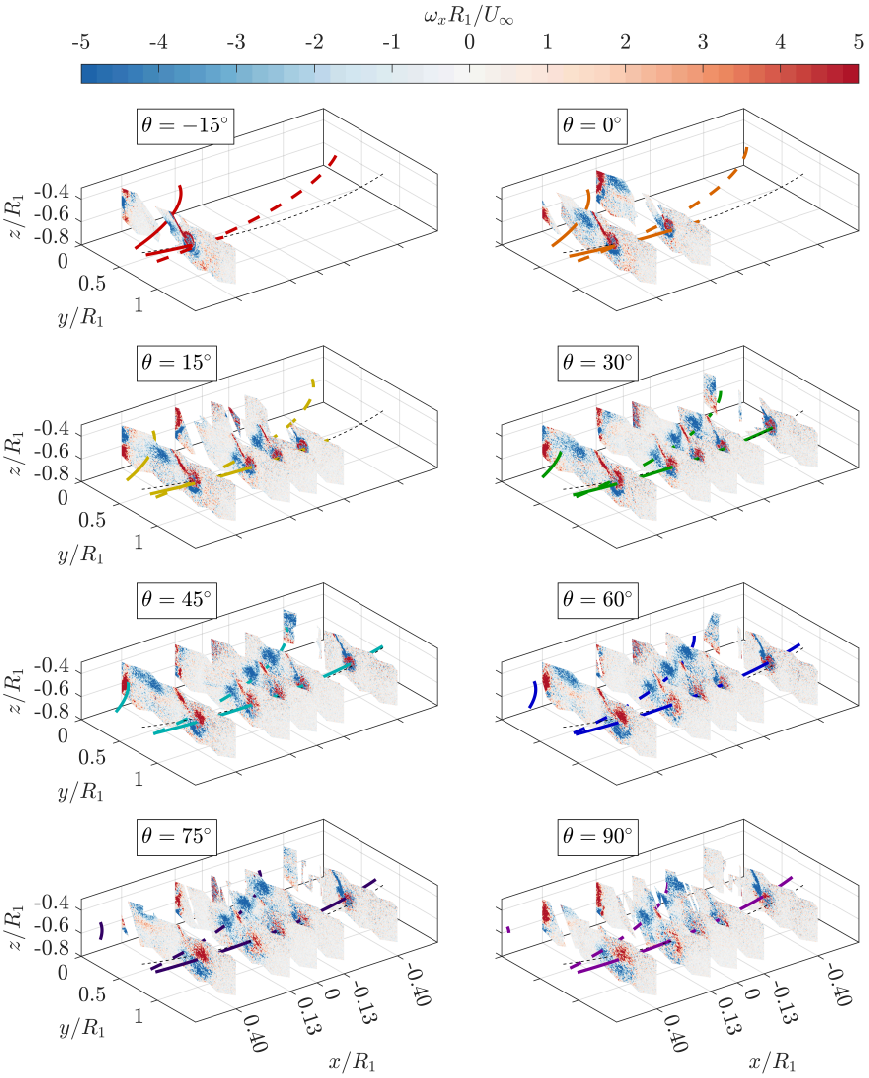


Figure 6.6: Normalized streamwise vorticity distributions as a function of phase-locked rotor position θ and measurement plane x/D. The black dashed line indicates the trajectory of the bottom blade tip of the primary rotor. The phase-dependent solid and dashed curves correspond to the trajectories of B1 and B2 as denoted in Figure 6.4. Note that the scale of the x-axis is doubled to increase the spacing between the measurement planes.

for the baseline case, stemming from B1 (towards the edge of the wake) and B2 (inboard). Visually, these fall within similar vicinities between the two cases. Unlike the case with secondary rotors, the baseline case exhibits coherent vortical structures with directions dictated by their generation in the UW quadrant. The size of the vortical structure of both B1 and B2 appears larger for the case with secondary rotors, likely due to the accelerated

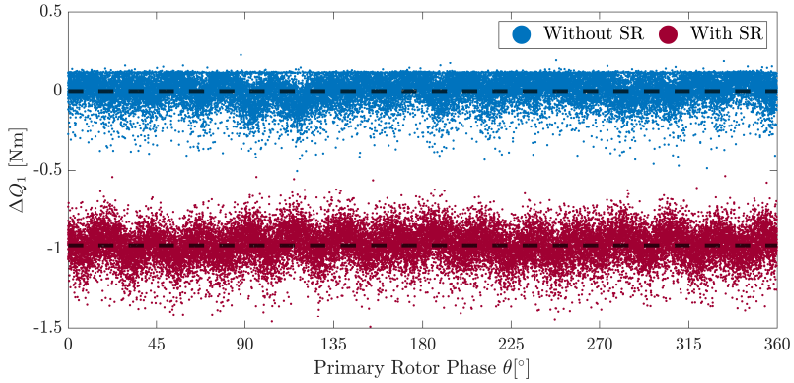


Figure 6.7: Change in primary rotor torque with respect to the case without secondary rotors (SR) as a function of primary rotor azimuth over 200 cycles. The black dashed lines show the mean change in torque for the respective cases. Note the mean of the case without secondary rotors is zero.

diffusion of the vortex as it interacts with the wake of the secondary rotors. A further notable difference between the two cases is the in-plane velocities, signifying the local cross-flows. Whereas the baseline case demonstrates a significant outwash beyond $y/R_1 > 1$ for all phase and plane combinations, the corresponding region for the case with SR shows systematically smaller magnitudes. A similar trend is also visible for the wake contraction below the projected frontal area of the rotor at the combination $x/R_1 = 0.13$, $\theta = 45^\circ$, where larger magnitudes in upwash are evident for the baseline case compared to the SR case. These variations are likely due to the lack of coherent vortical structures for the SR case imparted by the wake-induced diffusion, resulting in a reduction in the induced cross-flow in the wake.

6.3.4 Tip-vortex trajectory

As commented in Section 6.3.1, there is a visual agreement between the theoretical and measured trailing vortex trajectories. However, to evaluate the impact of the secondary rotors on the circulation and to compare the vortex dynamics with the baseline case, these trajectories are quantified. The vortex cores are evaluated at each measurement plane and phase combination using one of two techniques. For the cases where coherent vortex structures are apparent, such as those stemming from B1 and B2 in the baseline case, and B2 for the cases with secondary rotors, the approach defined by [152] is used. Here, the vortex center identification is based on the dimensionless scalar function Γ_1, whose variable quantifies the local streamline topology of the flow by measuring the alignment between velocity vectors and radial position vectors within a surrounding region. Physically, Γ_1, indicates the degree of rotational coherence in the flow, and $\max(\Gamma_1)$ would indicate the vortex core.

This technique proves difficult to implement for the structures emitted by B1 with secondary rotors, given the high degree of mixing and lack of a coherent structure. Hence, a center of mass approach was adopted using the vorticity magnitude, expressed as:

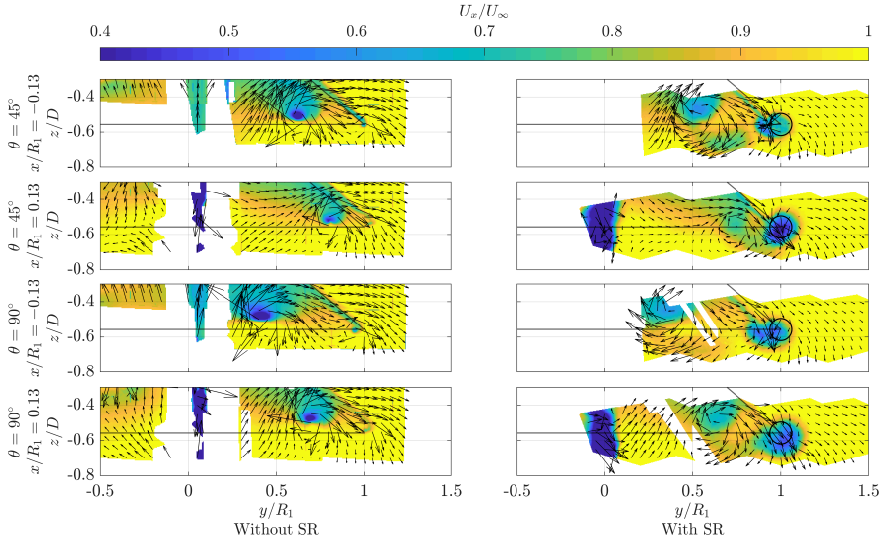


Figure 6.8: Normalized streamwise velocity U_x at discrete cross-stream and primary rotor phase combinations with and without secondary rotors (SR). Vectors represent the in-plane velocity components. The bottom section of the primary rotor frontal area is shown at a phase of θ=0° with a thin black line.

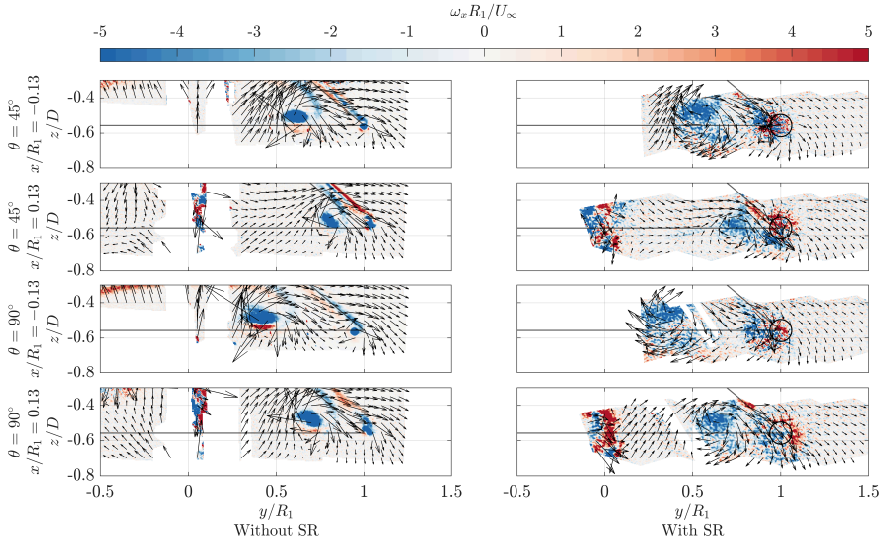


Figure 6.9: Normalized streamwise vorticity ω_x at discrete cross-stream and primary rotor phase combinations with and without secondary rotors (SR), where D = 1.5m is the tip diameter. Vectors represent the in-plane velocity components. The bottom section of the primary rotor is shown at a phase of θ=0° with a thin black line.

$$y_{\text{core}}(x) = \frac{\int \int_S y|\omega_x|(y,z)\text{dydz}}{\int \int_S |\omega_x|(y,z)\text{dydz}}, \qquad z_{\text{core}}(x) = \frac{\int \int_S z|\omega_x|(y,z)\text{dydz}}{\int \int_S |\omega_x|(y,z)\text{dydz}}, \tag{6.4}$$

where $|\omega_x|(x, y, z)$ is the vorticity magnitude at a given point in the measurement plane, and S is the surface over which the integration is performed. Given the limited measurement domain and presence of up to two vortices (B1 and B2) for most plane and phase combinations, a trimmed integration window S is used when evaluating the vortex core for the B1 case. As the visual inspection of Figure 6.6 suggested a good agreement between the measured and predicted trajectories, the theoretical vortex core location was used as the center of the trimmed region. A trimmed window size with a width and height of $0.3R_1$ and $0.25R_1$ was found to be the best balance between maximizing the available measurement height and width while capturing as much of the diffused vorticity. It is worth mentioning that this method does not isolate the cores of the B1 and B2 trailing vortices in regions of heavy interaction, particularly at the measurement plane $x/R_1 = 0.40$. The evolution of the vortex filaments is shown in Figure 6.10. The top-view (xy-plane) provides insight into the lateral evolution of the structure, while the back-view (yz-plane) demonstrates the axial convection of the vortical structures. Solid markers correspond to vortex cores measured for the baseline case.

The evolution of the B1 vortex matches to a high degree with the theoretical trajectory, with minor lateral offsets growing at the latter measurement phases. Furthermore, in the axial direction, the cores are concentrated at the height of the bottom blade tip. As these structures are still currently being generated in the windward passage of B1, there has been less time for the lateral and axial induction to impact the trajectory of the vortex filament. Similar observations have been made by [127] using time-revolved 3D measurements around the blade tip of a VAWT. The omission of the secondary rotor shows minor differences in the vortex trajectory for B1.

The trajectory of the B2 filament demonstrates larger discrepancies with the theoretical curve. As these structures have convected through the upwind measurement volume, they have deformed in both the axial and lateral directions. The trailing tip-vortex deformation of a VAWT was experimentally measured by [41], who concluded a vertical inboard movement towards the center of the rotor volume, accompanied by an outboard movement at the extremities of the rotor on the windward and leeward side. This distribution in tip-vortex convection over the rotor width was commented on by [153] using numerical simulations, who attributed the asymmetry to the blade motion and blade wake interaction. It is important to note that although the general convection tip-vortex inboard within the projected area of the rotor is a consequence of the inboard-induced velocity of the vortex generated in the upwind cycle [25], the deformation during its convection downstream would likely differ between the X-Rotor and H-type geometry given the added three-dimensionality of the coned blades on the vertical and lateral induction, as commented on in Chapter 5.

6.3.5 Vortex circulation

A comparison of the wakes provides a qualitative understanding of the impact of the secondary rotors on the trailed and shed vortical structures, highlighting the clear impacts on the shapes and magnitudes with the presence of secondary rotors. To quantify these impacts of the secondary rotors on the blade loads and trailing vortices more concretely, we investigate the circulations of these structures. In theory, the circulation of the vortex trailed by the blade tip should be conserved, assuming the load of the blade is the same

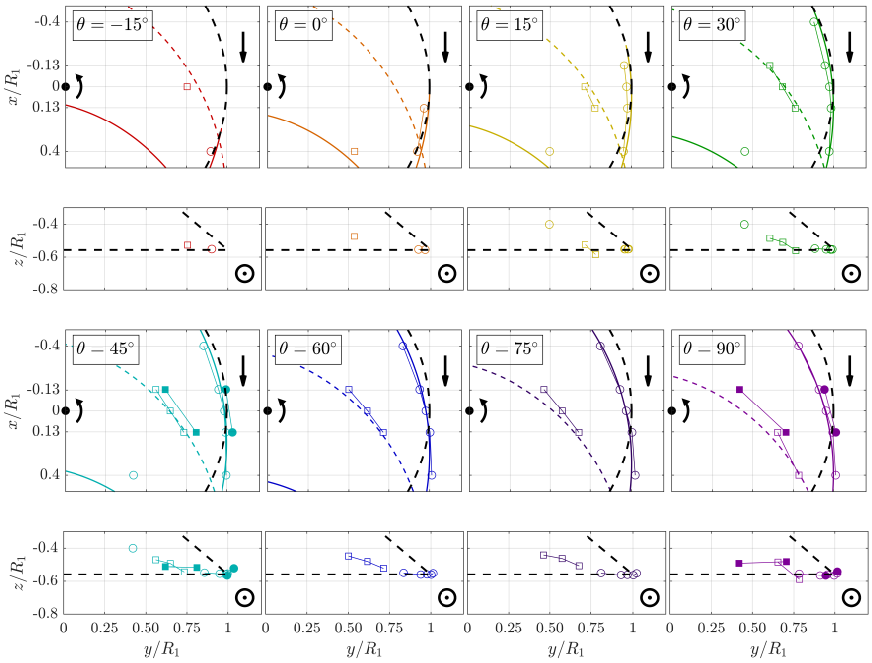


Figure 6.10: Theoretical versus measured trailing tip-vortex, with filled and empty data points corresponding to baseline and secondary rotor cases, respectively, and circular and square markers corresponding to B1 and B2, respectively. In the top view plots (xy-plane), the solid and dashed lines indicate the theoretical trajectories for B1 and B2, as described in Figure 6.4, while the black dashed line indicates the bottom blade-tip trajectory. On the back view plots (yz-plane), the black dashed line indicates the projected frontal area of the rotor. The black arrow and circular target marker indicate the flow direction.

with and without the secondary rotors. However, we can expect the phase-dependent integrated load of the blade to be slightly lower with the secondary rotors, as its induction will reduce the perceived velocity around the blade tip and subsequent load.

The circulation Γ for both the baseline and secondary rotor case is calculated using the surface integral of the vorticity field, described as:

$$\Gamma = \int_S \omega_x \, dS \approx \sum_i \omega_{x,i} \Delta S, \tag{6.5}$$

where S is the surface over which the vorticity is integrated. Given the discrete grid points of measurements i, the circulation is approximated as the sum of the product of vorticity and ΔS, defined as the size of the individual grid cells.

The integration domain is defined as a circular contour centered at the vortex core location defined in Figure 6.10 with a diameter of 200mm, translating to $2.1d_2$ (twice the diameter of the second rotor). This size was chosen to maximize the surface area in the axial direction to capture as much as possible of the mixed vorticity with the secondary rotors, most notably at measurement planes $-0.13 \leq x/R_1 \leq 0.13$, as well as the larger

diffused vortices stemming from B2 in both cases. The computed circulations are shown in Figure 6.11 as a function of both the primary rotor measurement phase and generation phase. Although the circulations are calculated around the tracked vortex cores, the reported generation phases are based on the theoretical positions of the vortices, illustrated in Figure 6.4. As the lateral trajectories between the tracked and theoretical match well for B1 in both cases, this will have a minor impact on the generation phase formulation. Note that an additional measurement plane and phase combination for the baseline case, namely $x/R_1 = 0.13$ at $\theta_{\text{Blade}} = 135^\circ$, is included.

When plotting the circulations as a function of the primary rotor measurement phase, the general trend is an increase in circulation magnitude at a given plane as the blade progresses. For the most downstream measurement plane $x/R_1 = 0.4$, the circulation is positive as the structure is generated in the DW quadrant, as discussed in Section 6.3.1. When plotting as a function of the generation phase, the circulations collapse towards a close to linear increase in magnitude. This is a consequence of the blade load progression of a VAWT blade. As discussed in Chapter 2, the blade load (of which the normal load is dominant) steadily increases in the UW quadrant of the cycle as the effective angle of attack increases. Assuming a linear relationship between the angle of attack and blade load, the bound circulation will increase proportionally [153]. As the blade is finite in length, one can consider it as a lifting line at any given rotor phase, with horseshoe vortices of equal and opposite strength as the bound circulation on each tip, resulting in the linear increase in tip-vortex strength with the generation phase. This trend was confirmed by [154], who compared experimentally derived tip-vortex circulations for a straight-bladed VAWT with simulated results, demonstrating the linear increase in circulation in the early phases of the blade in the UW quadrant. When comparing with the baseline results, we see a similar linear trend in circulation, with magnitudes falling incident on the linear curve. This suggests that the secondary rotor has a minor effect on the blade loading of the primary rotor, and hence the trailing vorticity strength. Furthermore, although the blade-tip vortex appears to be more diffused with the presence of the secondary rotor, for both B1 and B2, the circulation governed by the primary rotor tip-vortex is conserved to a high degree.

6.3.6 Mixing and energy flux

As discussed in Section 6.3.3, the presence of the secondary rotor seemingly reduces the induced flow of the tip-vortices of the primary rotor, especially for the structures associated with B1 at the generation close to 0°. Meanwhile, non-cohesive vortex structures suggest a large amount of turbulent mixing stemming from the SR. Contours of turbulent kinetic energy $k = \frac{1}{2}\left((\overline{U_x'})^2 + (\overline{U_y'})^2 + (\overline{U_z'})^2\right)$ are shown in Figure 6.12 for the overlapping primary rotor and cross-stream plane measurements. As the wake measurements are phase-locked, the terms denoted with primes represent the fluctuating components of the single phase in the periodic cycle of the wake.

The wake behind the secondary rotor of B1 shows the largest concentration of TKE in the wake. As described in Section 6.3.1, the load on the SR is greatest when close to perpendicular to the flow, yielding more significant flow deficits and turbulent mixing. As the structures stemming from B2 have been generated at phases further in the UW cycle, where the SR is reduced, the concentration of k in the wake is diffused.

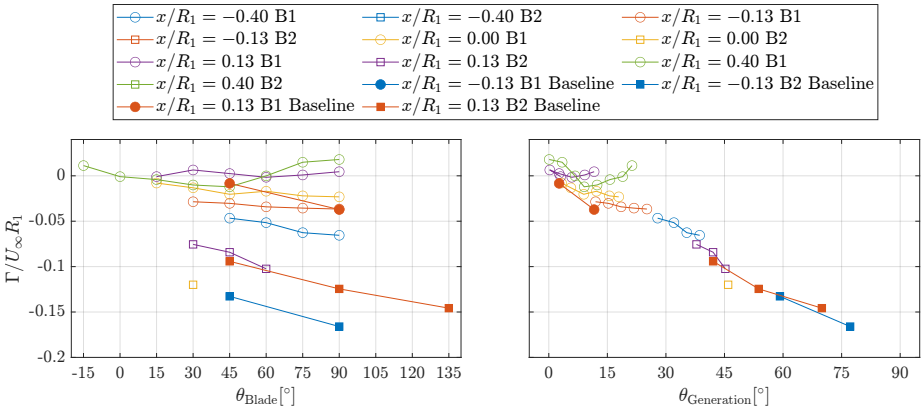


Figure 6.11: Normalized circulation for the secondary rotor (hollow markers) and baseline case (filled markers) as a function of (left) the primary rotor measurement phase and (right) the generation phase, as defined by Equation (6.2). The circular and square markers correspond to B1 and B2 measurements, respectively.

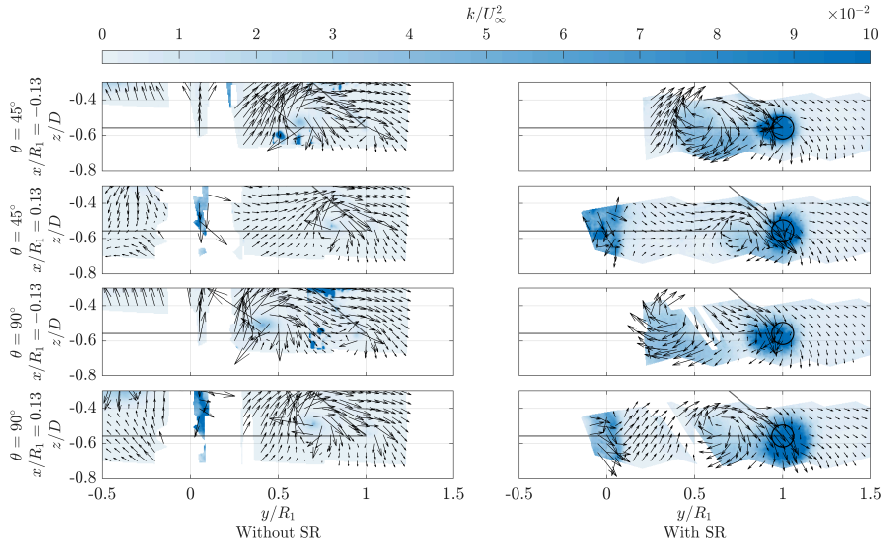


Figure 6.12: Contours of turbulent kinetic energy, where k is at the discrete cross-stream and primary rotor phase combinations with and without the secondary rotor (SR). Vectors represent the in-plane velocity components. The bottom section of the primary rotor is shown at a phase of θ=0° with a thin black line.

As in Chapter 4, the advective and Reynolds stress contributions towards the flux of streamwise kinetic energy shed light on the mixing process in the wake. The distributions of these fluxes are plotted across the bottom surface of the projected primary rotor area $z/R_1 = -0.56$ in Figure 6.13. The distributions are shown at the overlapping measurement planes $x/R_1 = [-0.13, 0.13]$ and for all measurement phases for the secondary rotor (solid lines) and at $\theta = [45^\circ, 90^\circ]$ for the baseline case (dashed lined).

For the baseline case, the peaks and troughs of the advective contributions correspond to the induced axial flow of the shed vortical structures in the wake, as visualized by the in-plane vectors in Figure 6.9. The higher peaks of the advective fluxes towards the center of the rotor ($y/R_1 = 0$), as well as the overall higher magnitudes of the upwind measurement plane $x/R_1 = -0.13$ are consistent with the circulations of the structures quantified in Section 6.3.5. Whilst the case with secondary rotors also exhibits local peaks and troughs, the magnitudes in the advective flux are decreased significantly. As discussed in Section 6.3.3, this is due to a combination of the reduction in induced flow from the coherent vortical structures of the baseline case as well as the significant wake deficit imparted by the secondary rotors.

Given the measurement location within the volume of rotation of the rotor, the advective contributions of the coherent vortical structures are an order of magnitude higher than the flux of the Reynolds stress for the baseline case. Similarly, the secondary rotors show negligible magnitudes towards the center of the rotor, even where the vortical structures of B2 convect through the plane. However, in the regions of the wake of B1, a significant jump in flux is apparent, surpassing the advective contribution.

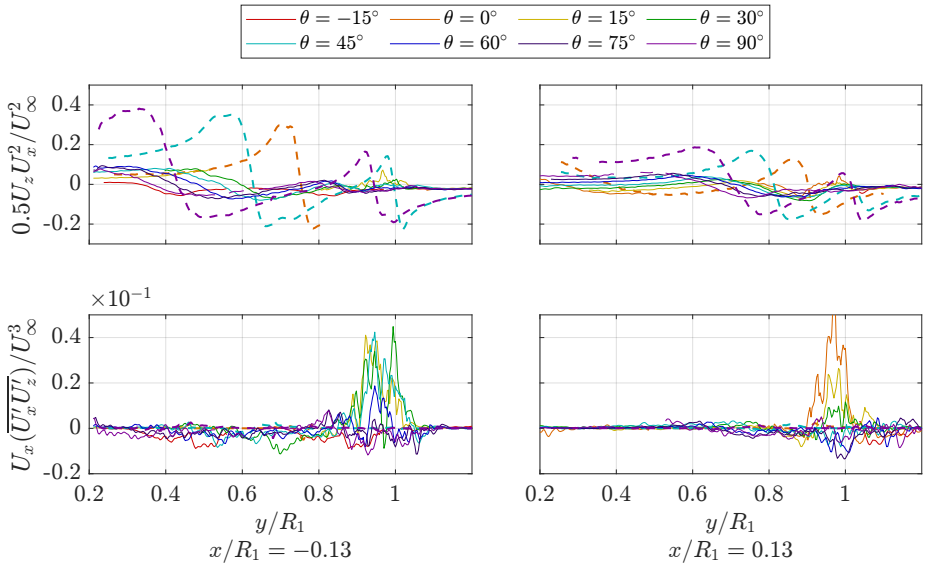


Figure 6.13: Primary rotor phase-dependent distributions of advective and Reynolds stress contributions towards the flux of streamwise kinetic energy across the bottom of the projected frontal area of the rotor $z/D = -0.56$. The solid and dashed lines correspond to the cases with and without secondary rotors, respectively.

6.4 Conclusions

A scaled X-Rotor vertical-axis wind turbine with secondary rotors was tested in an open-jet wind tunnel. The results are compared to cases without secondary rotors to experimentally demonstrate the aerodynamic gearbox working principle of the design, as well as the impact of secondary rotors on the trailing vorticity and mixing process in the near wake.

The main findings can be summarized as follows:

- The thrust of the secondary rotors can be accurately predicted using a simplified cycle average approach of the primary rotor torque. This experimentally demonstrates the balance between the primary rotor torque and secondary rotor thrust, coined the aerodynamic gearbox.
- At phases where the load of the secondary rotor is highest (close to $\theta = 0^{\circ}$), the wake induces a high degree of turbulent mixing. However, as the secondary rotor progresses through the upwind windward quadrant, its load decreases as it yaws out of the flow. Meanwhile, the primary rotor blade load increases, yielding a dominant and coherent tip-vortex structure shed in the wake.
- The secondary rotors create a local wake with an accelerated diffusion of the tip vortex, leading to a decrease in induced in-plane velocity gradients both on the edge and within the volume of rotation of the rotor. While the baseline case demonstrated higher advective contributions toward the flux of kinetic energy due to the coherent vortical structures, by close to a factor of 10, the secondary rotors significantly increased the turbulent contribution within their wake by up to a factor of 30 near the blade tips.
- When considering the strengths of the trailing tip-vortices as a function of the phase in which they are generated in the upwind windward quadrant, a linear increase is drawn. Whilst the presence of the secondary rotors increases the diffusion of the trailing-tip vortex structure, the circulation is conserved to a high degree when compared to the baseline measurement cases.

7

The near wake deformation of the X-Rotor with pitched blades

Up to now, the baseline wake aerodynamic features of the X-Rotor have been experimentally measured and discussed, focusing on the primary (Chapter 5) and secondary rotor (Chapter 6). However, the X-Rotor's potential for farm-scale applications has yet to be elucidated. This can be investigated by means of near-wake measurements (outside the volume of rotation of the rotor). Furthermore, the efficacy of established wake re-energization techniques, such as the "vortex generator" described in Chapter 2, when applied to the novel X-Rotor geometry, has yet to be experimentally or numerically investigated.

The present chapter provides an experimental demonstration and proof-of-concept for the wake recovery mechanism of the novel X-Rotor VAWT. The phase-locked flowfield is measured at several streamwise locations along the X-Rotor's near-wake using stereoscopic particle image velocimetry (PIV) with fixed-pitch offsets applied to the blades. The streamwise vortex system of the upper half of the X-Rotor is first hypothesized and then experimentally verified.

This chapter is based on **Bensason, D.**, Sciacchitano, A., Giri Ajay, A., and Simao Ferreira, C. A Study of the Near Wake Deformation of the X-Rotor Vertical-Axis Wind Turbine With Pitched Blades. *Wind Energy*, 2024 [133]. The data supporting this study is openly available in the 4TU.ResearchData repository at `https://doi.org/10.4121/e43ddd4d-6d93-4f50-b1ce-01bc0df1bda4`.

7.1 Introduction

The previous chapters have explored the wake aerodynamics of the novel X-Rotor with and without secondary rotors. As discussed in Chapter 2, various techniques have been proposed to steer the wake of a VAWT and, intern increase the potential energy density of an offshore wind farm. The results by [25] showed massive potential for H-type VAWTs for farm installation using the passive blade pitch technique dubbed the "vortex generator" strategy. Building on the previous experimental investigations around the X-Rotor in Chapters 5 and 6, the efficacy of fixed pitch settings on the wake control is of particular interest given the X-Rotor's design for offshore applications.

The present work investigates the impact of the "vortex generator" strategy on the near wake of the primary rotor using phase-locked stereoscopic PIV, focusing on the trailing vortex system and subsequent recovery mechanism. Numerical studies [106] have investigated the impact of fixed-blade pitch on the blade loads and performance of a full-scale X-Rotor VAWT, demonstrating a penalty in power performance of the primary rotor of up to 20% depending on the tip-speed ratio. However, these studies lacked an analysis of the impacts of this strategy on the wake.

The remainder of this manuscript is structured as follows. A theoretical analysis of the X-Rotor vortex system is provided in Section 7.2. A description of the experimental setup and case overview is provided in Section 7.3. The results and key findings are presented and discussed in Section 7.4 and followed by a summary and conclusions in Section 7.5.

7.2 Wake re-energization mechanism

The dominant role of streamwise vortices on the wake topology and deflection of a vertical-axis wind turbine was experimentally demonstrated by [25]. This phenomenon can be shown by simplifying the loading of a VAWT using the actuator cylinder approach, as shown numerically by [44]. A top-view of the loading on this idealized cylinder is shown in Figure 7.1 which follows the same theory as in Chapter 4. The sectors of the VAWT cycle are upwind windward (UW), upwind leeward (UL), downwind leeward (DL), and downwind windward (DW). The vectors indicate the normal loading direction and magnitude of the blade throughout the cycle. Unlike in Chapter 4, the load is assumed to be uniformly distributed in the upwind and downwind halves and dominated by the normal load contribution of the blade [44], with the upwind half loaded more heavily for the zero pitch case. A detailed overview of the streamwise vorticity generation as a function of the actuator cylinder loading is provided by [25]. A representation of the streamwise vortices is shown in Figure 7.2. The upper half of the X-Rotor VAWT is demonstrated at a phase-locked position of $\theta = 0^\circ$ with a grey shaded cone to represent the actuator surface. The upper tips are shaded red and blue to mark areas where positive ($+\omega_x$, counter-clockwise) and negative ($-\omega_x$, clockwise) streamwise vorticity is generated by the blade, respectively. As described in Chapter 4, generation and shedding of streamwise tip-vortices are an intrinsic feature of VAWT aerodynamics, where the strength and direction of rotation are functions of the phase of generation.

Note that the spanwise vorticity generated by the blade is not presented in this schematic, as it is not a dominant feature in the wake recovery mechanism [155]. Idealized streamwise vortices generated from each AC quadrant are shown with their respective

idealized propagation paths shaded. The intersection of these vortices with an arbitrary cross-stream plane (shaded trapezoid section) in the near wake is visualized on the right side of Figure 7.2 with the quadrants from the AC labeled. The vortices generated in the upwind half of the cycle induce an inboard flow on the upper section of the rotor as opposed to the downwind vortices, which induce an outboard flow. The vortices marked with A and B represent the dominant streamwise vortex in the leeward and windward halves of the rotor, respectively. Consistent with the zero pitch AC shown in Figure 7.1, these are the vortices generated in the UL and UW quadrants, respectively.

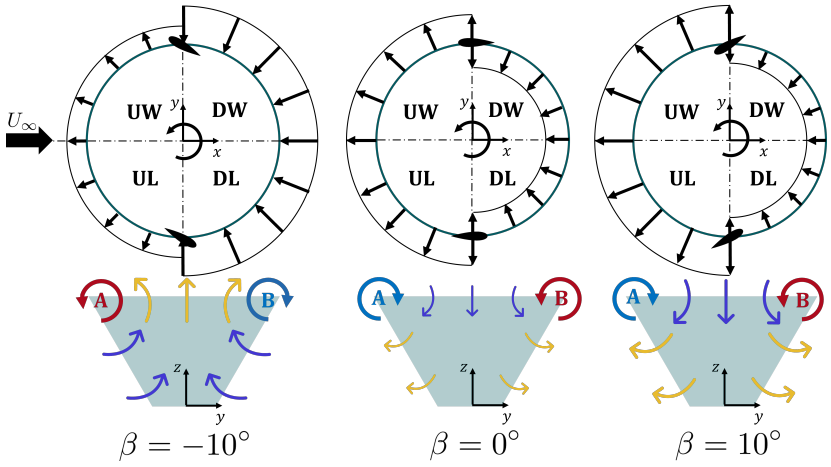


Figure 7.1: The first row shows a schematic of the simplified force fields over the rotation cylinder of the X-Rotor adopted by [25]. The schematics include blades (exaggerated in size) at azimuths $\theta = 0^\circ$ and 180° for fixed pitch settings $\beta = -10^\circ, 0^\circ$, and 10°, respectively. The curved arrows indicate the anti-clockwise direction of rotation. The second row illustrates the frontal area of the rotor (shaded) along with the dominant streamwise vortices labeled A and B as defined in Figure 7.2 with the rotation directions when in the inertial frame of reference.

Along with the idealized load distribution of the baseline zero pitch case, the cases for fixed pitch settings of $\beta = -10^\circ$ and $\beta = 10^\circ$ are shown in Figure 7.1. As theorized and verified in Chapter 4, the negative pitch case shifts the rotor load to the downwind half of the rotor, whilst the positive pitch to the upwind half, strengthening the trailing vortices of the respective quadrants.

To understand the impact of these streamwise vortices on the wake topology of the rotor, we assume that the aforementioned structures marked A and B are the dominant sources of induced flow. Hence, although the edges of the rotor wake include counter-rotating vortex pairs (CVPs), it is assumed that the weaker vortices stemming from the less loaded quadrants will merge with the dominant structure. This assumption has been experimentally and numerically validated [25, 44]. These vortices are visualized in Figure 7.1 on the bottom row when intersecting a cross-stream plane in the near wake of the rotor. Blue and yellow vectors are added to visualize the movement of perturbed flow (wake) and freestream flow, respectively. For the baseline case of $\beta = 0^\circ$, the dominant vortices are those from the UW and UL. These vortices induced a downwash, where freestream flow is injected from above the actuator while the wake is ejected from the side. The mode

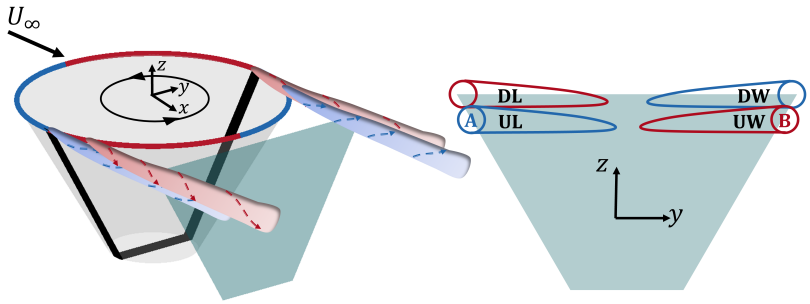


Figure 7.2: An isometric schematic of the upper half of the X-Rotor at blade pitch $\beta = 0^\circ$. Dominant tip-vortex filaments are color-coded based on the quadrant in which they are generated (blue and red), matching the colored blade tip trajectory. The intersection of these vortical structures on a streamwise plane (shaded) is shown on the right. The vortices are labeled based on the quadrant in which they are generated, where U and D correspond to upwind and downwind, respectively, and W and L correspond to windward and leeward, respectively. The dominant streamwise vortices are labeled A and B for the leeward and windward sides, respectively.

of operation is similar for the positive pitch case of $\beta = 10^\circ$ with higher magnitudes in downwash. Finally, the negative pitch case $\beta = -10^\circ$ has dominant vortices stemming from the DL and DW quadrants of the cycle. As a result, free-stream flow is injected from the sides of the rotor while the wake is ejected from the top of the actuator.

For the simplified cases shown in Figure 7.1, the loads generated in the upwind and downwind halves are perfectly balanced between the leeward and windward sides; as a result, lateral forces generated in the upwind and downwind are null. Hence, there would be no net lateral deflection of the wake, which would deflect symmetrically about the vertical axis. This theory holds for an infinite number of blades [156]. However, in practice, the loads generated in the leeward and windward halves of the rotor are not symmetric in magnitude, and hence, a lateral deflection is also expected [25, 56]. This level of asymmetry increases as the number of blades on the rotor decreases.

7.3 Methods

7.3.1 Wind tunnel and X-Rotor model

Experiments are performed in the Open Jet Facility (OJF) at TU Delft Aerospace Engineering Laboratories. Details of the tunnel are provided in Chapter 4. A controlled streamwise velocity of $U_\infty = 4\text{ms}^{-1}$ is used throughout the experiment. The same 1:100 scale X-Rotor model as in Chapter 5 is used in this experiment and is mounted in the center of the test section, as illustrated in Figure 9.5.

7.3.2 Flow measurement system

A similar stereoscopic particle image velocimetry (PIV) system is used to measure several velocity fields at discrete cross-stream locations in the wake of the X-Rotor as in Chapter 5. Seeding is generated via a SAFEX smoke generator and illuminated with a Quantel Evergreen double-pulsed Nd:YAG laser with a sheet thickness of approximately 4mm. Details on

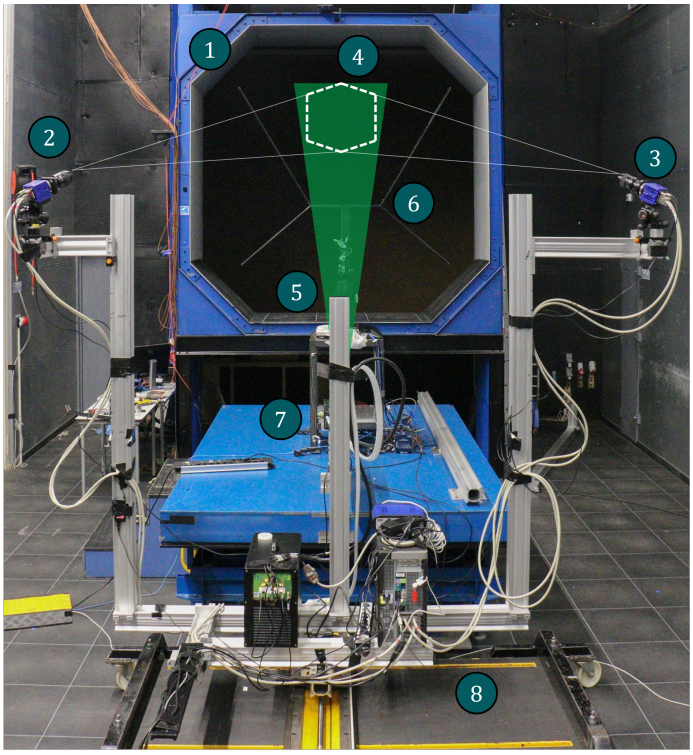


Figure 7.3: Experimental setup in the OJF. A visualization of the measurement plane is provided (green cone) along with labeled key components of the measurement system.

the seeding and illumination are provided in Chapter 5. Images are captured at a frequency of 15Hz using two LaVision sCMOS cameras. With a focal length of 105mm, numerical aperture 8, and stereoscopic angle of 74.8° between cameras, the resulting field of view (FOV) is approximately 43 cm × 30 cm. A time of 320μs between images is used. Based on the numerical aperture of the lenses and the image magnification M = 0.01, the diffraction diameter of the particle images can be calculated using Equation (4.2) as 10.3μm. This is 1.5 times the pixel size (6.6μm), resulting in limited peak locking errors [124].

The resulting images are processed with a cross-correlation-based image interrogation algorithm with window deformation, with window sizes of 256px × 256px and 96px × 96px and an overlap factor of 75%. A total of 120 vector field images were captured for each measurement plane and phase averaged. The camera and laser systems are rigidly connected and mounted on a traversing system, enabling a translation range in the streamwise and lateral direction of 1.5m and 0.5m, respectively.

7.3.3 Case overview

The aforementioned measurement system captures phase-locked measurements of the flowfield across cross-stream locations in the X-Rotor's wake, as visualized in Figure 7.4. The origin of the coordinate system is taken as the center of the crossbeam, with the y and z defined as the lateral and axial directions, respectively. The cross-stream planes measured range from distances of 0.39m to 2.4m from the crossbeam center, corresponding to normalized distances of x/D = 0.26 and 1.6, respectively. The measurements from the three cross-stream planes x/D = 0.26, 0.90, and 1.6 are predominantly used in the results Section 7.4. However, an extended set of cross-stream planes was measured, with a complete overview provided in Appendix B.2. At a given cross-stream location, several planes are measured in the y-axis and z-axis directions via the traversing system described in Section 7.3.2 and stitched together when post-processing the results. Three fixed pitch settings were tested, namely, $\beta = 10^\circ$ (pitched in), $\beta = -10^\circ$ (pitched out), and $\beta = 0^\circ$ (baseline). These fixed pitch settings were realized by fabricating three crossbeams with respectively angled blade connection points. The wake is measured at a constant rotor rotational frequency of ω = 21.3rad/s, corresponding to a tip-speed ratio $\lambda = \omega R/U_\infty$ of 4 and diameter-based Reynolds number of $\mathrm{Re_D} = 4.4{\times}10^5$. Due to time constraints, the measurement focuses on the wake behind the upper blades of the X-Rotor, spanning from z/D = 0.15 to 0.8 for the pitched cases $\beta = 0^\circ$ and 10°, and z/D = 0.35 to 0.8 for the pitch case $\beta = -10^\circ$.

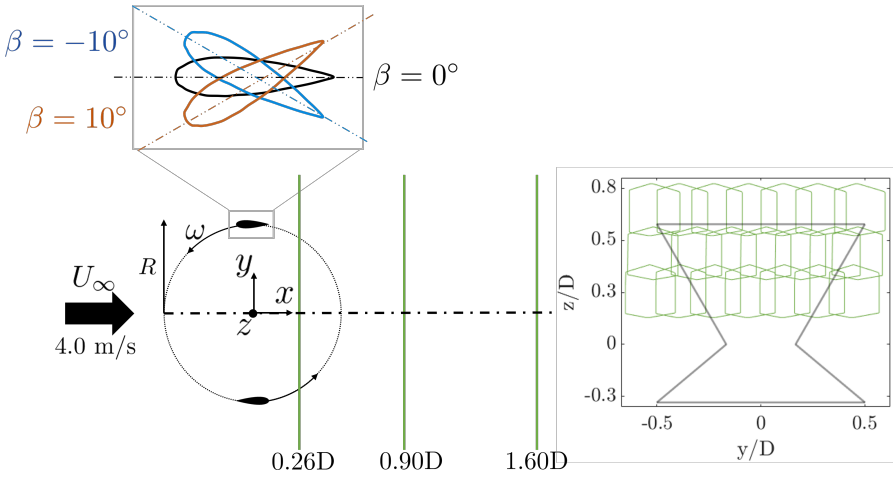


Figure 7.4: Schematic of the top view of the setup (left). Enlarged blades are shown at azimuths $\theta = 0^\circ$ and 180° with primary measurement planes (green) for the subsequent analysis marked. A magnified view of the blade orientation at fixed pitch settings $\beta = -10^\circ$ (blue) and $\beta = 10^\circ$ (brown) is provided. Frontal view of the measurement planes (right) for the example of x/D = 0.9 and pitch $\beta = 10^\circ$.

7.3.4 Numerical demonstration of rotor load distribution

As described in Section 7.2, the working principle of the "vortex generator" relies on the distribution of the rotor loading, which is a function of the blade loads. However, this study does not yield blade-level loading nor an integrated load for each blade. Hence,

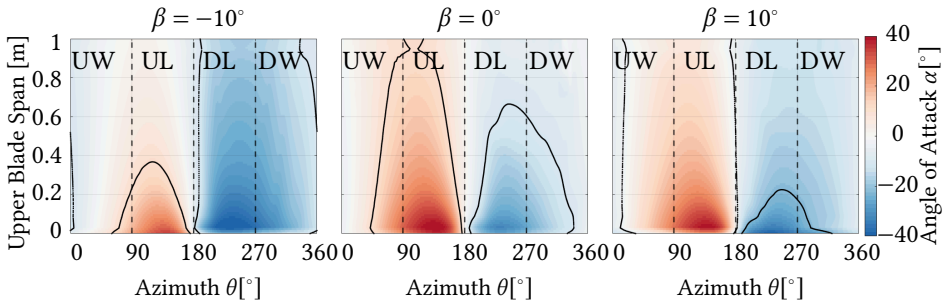


Figure 7.5: Effective angle of attack α of the top blades as a function of azimuth locations θ and normalized blade span position for each fixed pitch case. The black contour line indicates the static stall angle of the NACA0021 airfoil of α_{ss}= 9.1°. Vertical dashed lines separate the different quadrants of the rotor as described in Figure 7.1.

to support the arguments made in this work, simulations of the scaled X-Rotor model were run using the vortex lattice approach of the Code for Axial and Cross-flow Turbine Simulation (CACTUS) [157]. The upper blades of the X-Rotor are discretized into 18-blade sections and run for 13 revolutions to attain convergence with a second-order predictor time advancement scheme. The simulated load data of the final revolution is used in the subsequent discussion. The crossbeam and tower were not modeled in this numerical setup. A freestream flow of U_∞ = 4ms^{-1} is used for the simulation, with an XFOIL [158] statically simulated polar for a NACA0021 blade at Reynolds number 15×10^4, shown in Appendix B.1.

The numerical results of the effective angles of attack of the top blades at each spanwise location and rotor azimuth are shown in Figure 7.5 for each of the fixed pitch cases. The quadrants, as defined in Figure 7.1, are labeled along with a black contour line indicating the static stall angle of the NACA0021 blade. In this case, the static stall angle is simulated to be α_{ss} = 9.1°.

For the baseline pitch case of β = 0°, the region is where the stall angle gradually narrows in the upwind half of the cycle towards the tip of the upper blade. Below this, the blade experiences a large stall in the UL quadrant, initiated toward the end of the UW quarter. In the downwind half of the cycles, the flow remains attached for a larger section of the span while experiencing stall on the lower 60% of the span up to an azimuth of approximately θ = 330°. Consistent with the description in Section 7.2, a negative pitch offset ($\beta = -10°$) to the blade reduces the angles of attack experienced in the upwind half of the rotor significantly and, consequently, reduces the loads of the blades. However, the magnitudes of the angle of attack are increased drastically in the downwind half. As a result, the blade is stalled for a majority of this half of the cycle, with sections falling within the stall limit for the upper sections of the span. Similarly, the positive pitch case ($\beta = 10°$) systematically lowers the angles of attack experienced by the blade in the downwind half of the cycle, with a very small region of spans falling within the stall limit. However, the angles surpass the stall limit in the upwind half of the rotor across all spanwise locations, starting at an azimuth of approximately θ = 16°.

Although large regions of separated flow across all pitch cases for span-wise locations near the root section are evident, the most significant contribution of aerodynamic load

stems from the regions closer to the tip. Hence, to further understand the impact of blade pitch as a function of rotor azimuth for the blade as a whole, the blade integrated normal load is shown in Figure 7.6 for each fixed pitch case. The blade integrated loads C_N are shown similarly to Figure 7.1. Furthermore, the percentage difference with respect to the pitch case of $\beta = 0^\circ$ for the integrated load over the area of each quadrant is shown for the positive and negative pitch cases. The numbers are color-coded, with green and red signifying an increase and decrease, respectively.

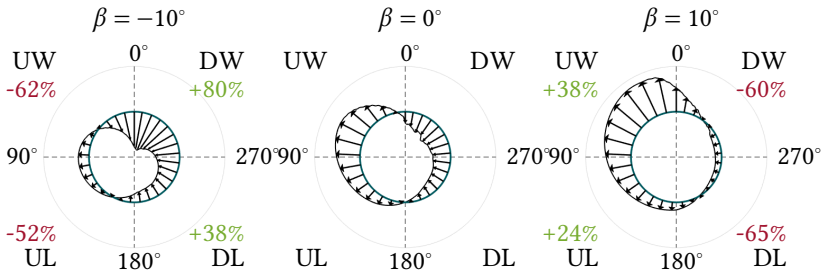


Figure 7.6: Numerical results of the blade integrated normal load C_N as a function of blade azimuth for each fixed pitch case. The solid circular line indicates the case where the normal load is zero. Flow comes from left to right. The percentage differences for each quadrant with respect to the zero pitch case $\beta = 0^\circ$ for the fixed pitch offsets are shown, with red and green signifying a decrease and increase, respectively.

7

Consistent with the angle of attack magnitudes in Figure 7.5 and the discussion in Section 7.2, the loading of the X-Rotor is higher in the upwind half for the baseline pitch case of $\beta = 0^\circ$. As mentioned in Section 7.2, the symmetric loading between the windward and leeward halves of the rotor is a simplification of the system. In reality, the loading in the windward half of the rotor is higher due to the asymmetric angle of attack variation and induction of the rotor, highlighted in Figure 7.5. For the positive pitch case $\beta = 10^\circ$, the normal load of the blade increases in the upwind half of the cycle, most significantly in the UW quadrant. Consequently, the load decreases in the downwind half of the cycle, consistent with Figure 7.5. Finally, the negative pitch case increases the normal loading of the blade in the downwind half of the rotor whilst reducing that in the upwind half. Not only does the action of pitching alter the magnitudes of blade load in the respective quadrants, but also the percentage of time spent in each quadrant with positive and negative normal loads. In the inertial frame of reference, depending on whether the blade is in the windward or leeward half of the cycle, the normal load direction governs the direction of vorticity generated at the tip, described in Section 7.2. For the negative fixed pitch case, the blade experiences a negative load coefficient (inward) for a larger percentage of the cycle in both the leeward and windward halves of the cycle compared to the zero pitch case. This confirms the dominance of the streamwise CVP generated in the download half of the cycle, as highlighted in Figure 7.1. Similarly, the positive pitch case increases the percentage of time the blade experiences a positive (outward) normal load in both the windward and leeward halves of the cycle, ascertaining the dominance of the upwind-generated vortices. Similar behavior was experimentally observed by [56] for a straight-bladed VAWT model.

7.3.5 Uncertainty in flowfield analysis

Given the relatively high complexity of the flow measurement system, we aim to quantify certain sources of uncertainty in the flow measurements. Following the procedure in Chapter 4, Equation (4.1) is used to calculate the standard uncertainty ϵ, with $z_a = 2$ as the coverage factor, and $N = 120$.

The spatial averages of the standard deviations are computed for the most upwind measurement plane $x/D = 0.26$, with the highest magnitude in the streamwise direction of $\sigma_x = 0.07\text{ms}^{-1}$ for the $\beta = 10^\circ$ case. This results in a standard uncertainty of $\epsilon_x = 0.013\text{ms}^{-1}$. Following the same procedure, the maximum standard uncertainties in the lateral and axial directions are of similar magnitude. Note that higher standard deviations are concentrated in regions of separated flow in the near wake of the X-Rotor due to the coned nature of the blades, as further described in Section 7.3.4 and Section 7.4.3.

In addition to the standard uncertainty of the phase-locked flow components, the standard uncertainty of the phase-locked streamwise vorticity component U_{ω_x} is calculated as:

$$U_{\omega_x} = \frac{\epsilon}{d}\sqrt{1-\rho(2d)} \tag{7.1}$$

where ϵ is the standard uncertainty in the axial (ϵ_z) or lateral (ϵ_y) direction [159]. The grid spacing of the integration window is denoted as d, and the cross-correlation coefficient of the spatially correlated velocities is denoted as $\rho(2d)$. Given a camera scaling factor of 7.27px/mm and correlation window size of 96px × 96px with a 75% overlap, the dimensional grid spacing is calculated as d = 3.3mm. The cross-correlation coefficient adopted for this work is $\rho(2d) \approx 0.45$ [159], yielding a standard uncertainty in the streamwise vorticity in the regions of separated flow as $U_{\omega_x} = 3\text{s}^{-1}$.

A further source of uncertainty when dealing with phase-locked measurements is phase unsteadiness in the system. This can be attributed to either vibration in the measurement system or errors in the time delay for the triggering of the cameras and laser system. When the wake has low magnitudes in velocity and gradients, the unsteadiness in the system will have a minimal impact on the average value. However, in cases where there are large flow gradients, such as regions near the tip-vortex of the rotor, the impacts of this unsteadiness can be larger on the computed average.

The percentage error in the velocity magnitude $|U|$ with respect to the mean value $|U_{120}|$ is shown in Figure 7.7. Rather than showing the convergence over the entire range, the analysis is performed for two subsets of $N = 60$ cycles. The convergence of randomized acquisitions are denoted as $|U_{1-60}|$ and $|U_{61-120}|$ for the two subsets respectively. The convergence is tested for two representative cases where we expected lower and higher gradients. For the low gradient representative case the the convergence at the center of the wake with pitch $\beta = 0^\circ$ at $x/D = 0.26$ is shown, as illustrated by the sub-figure in Figure 7.7. The curves for both subsets of acquisitions fall consistently below a 1% difference with respect to the average over the full range of acquisitions $|U_{120}|$. For the high gradient representative case the the convergence near the windward vortex for a pitch case $\beta = 10^\circ$ at $x/D = 0.4$ is shown. The difference with respect to the mean of the full range is higher compared to the $\beta = 0^\circ$ case for both subsets of acquisitions. Both fall within a 1% difference beyond a sample size of $N = 20$. The percentage difference PD between the converged subsets of values for the two pitch cases is computed as follows:

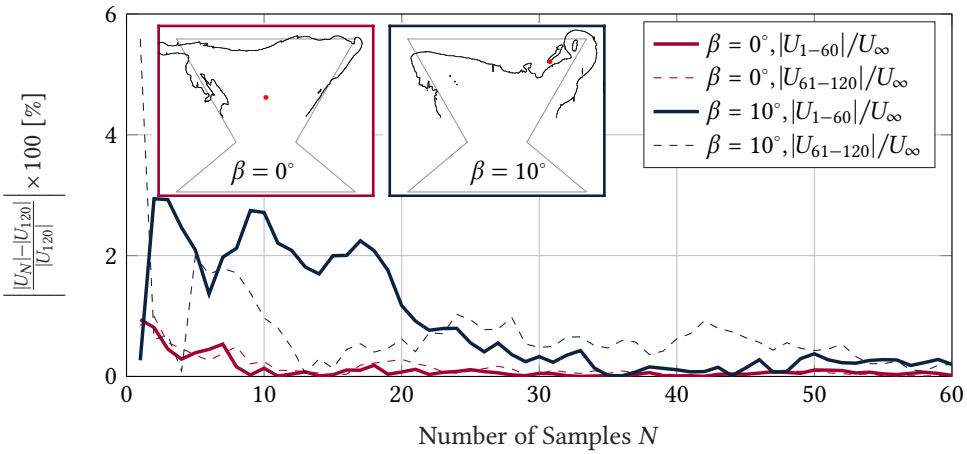


Figure 7.7: Statistical convergence of the difference in phase-locked velocity magnitude $|U|$ with respect to the average over $N = 120$ acquisitions $|U_{120}|$ for subsets 60 data acquisitions. The convergence of a case near the center of the wake for pitch case $\beta = 0^\circ$ at $x/D = 0.26$ is shown in red, and that for $\beta = 10^\circ$ at $x/D = 0.4$ is shown in blue. The respective color-coded wake shapes for the two cases are shown with red dots indicating the point at which the convergence is presented.

$$PD = \frac{\left||U_{1-60}| - |U_{61-120}|\right|}{\frac{|U_{1-60}|+|U_{61-120}|}{2}} \times 100 \tag{7.2}$$

Using the final converged values for the subsets, the percentage difference for the pitch cases $\beta = 0^\circ$ and 10° are computed as 0.03% and 0.40%, respectively. This analysis has been performed for several other locations in the wake across all pitch cases to confirm a converged data set.

Finally, uncertainty associated with the traversing and subsequent stitching of measurement planes is addressed. As described in Section 7.3.3, a traversing system is used to acquire several measurement planes at a given streamwise location before being stitched together when post-processing the results. Uncertainties in this process may arise in the stitching from random and human errors in the traversing system operation, as well as the accuracy of the system itself. The root-mean-square error (RMSE) for the velocity magnitudes is computed for the overlapping regions of planes as follows:

$$\text{RMSE} = \sqrt{\frac{\sum_{i=1}^{N}(|U_{1,i}| - |U_{2,i}|)^2}{N}} \tag{7.3}$$

where $|U_1|$ and $|U_2|$ are velocity magnitude values at a given index i in an overlapping regions between two planes and N is the number of overlapping indices. The RMSE for overlapping acquisitions in the same regions as discussed with Figure 7.7 are computed as 0.23ms^{-1} and 0.13ms^{-1} for the pitch cases $\beta = 0^\circ$ and 10°, respectively. Once again, the

same analysis was conducted for overlapping acquisitions at different locations in the wake of all pitch cases to ensure the accuracy of the stitching process.

7.4 Results

7.4.1 Velocity fields

The phase-locked streamwise, lateral, and axial velocity contours are shown in Figures 7.8 to 7.10 for each of the fixed pitch cases at cross-stream locations x/D = 0.26, 0.90, and 1.60. All velocities are normalized by the free stream velocity U_∞ with a black contour of the wake at U_x/U_∞ = 0.9. The frontal area of the rotor at an azimuth of $\theta = 0^\circ$ is shown via a grey line with quivers showing the in-plane velocities in black. An extended set of measurements at more cross-stream planes is shown in Appendix B.2.

The measurements do not extend towards the upper blades' roots, so the pitch case's wake $\beta = -10^\circ$ does not display streamwise flow deficits below $0.6U_\infty$. The wake shape shows an elongation in the axial direction that extends when moving along in the streamwise direction, with a more pronounced extension on the windward half of the rotor. This axial stretching of the wake is confirmed by the strong presence of axial flow U_z in the upper section of the wake, shown in Figure 7.10. In addition to the axial expansion, a radial contraction is also evident on the leeward side of the rotor, shown in Figure 7.9. This is consistent with the strong positive radial flow of $0.3U_\infty$ in the leeward half of the rotor throughout the wake. This is complemented further by the negative radial flow components on the windward side of the rotor.

The measurements for the pitch case $\beta = 0^\circ$ extend further towards the roots of the upper blades and feature higher streamwise flow deficits of up to $0.3U_\infty$ than the aforementioned case. Minimal expansion has occurred in the near-wake region; hence, the wake profile follows the coned shape of the rotor. Similar to results reported by [41], a difference in the flow deficits between the windward and leeward halves of the rotor is visible due to the asymmetric loading of the rotor, which is further highlighted by heavier radial wake extension on the windward side of the rotor. This asymmetry has also been observed by [25] and can be further justified by the vorticity distributions in the wake, discussed in Section 7.4.2. Unlike the negative pitch case, there is minimal axial flow with magnitudes around $0.1U_\infty$ in areas distant from tip-vortices. A change in magnitude and location of local upwash and downwash in the near wake across the cross-stream locations is evident. This is due to the coherent shed and tip vortical structures within the rotation volume in the rotor having periodic induced velocities. The radial flow suggests a general wake expansion with positive and negative magnitudes of U_y on the windward and leeward sides of the rotor, respectively.

Finally, the positive pitch case $\beta = 10^\circ$ shows a significant radial deflection of the wake towards the windward side of the rotor, similar to the results reported by [25] for straight-bladed VAWTs. The positive pitch case features a more significant flow deficit than the aforementioned cases directly behind the rotor. This can be attributed to the higher lift generated by the advancing blades on the windward side of the rotor. This further translates to an increased lateral force induced on the flow, as confirmed by Figure 7.9, leading to a wake expansion radially outward on the windward side. Starkly different from the negative pitch case, the wake shape suggested an axial contraction that extends in

the streamwise direction. This is concentrated mainly on the windward half of the rotor and is visible via the large vertical downwash on the order of $0.3U_\infty$ shown in Figure 7.10. This is accompanied by a strong presence of positive radial flow on the windward side and negative on the leeward side.

7.4.2 Verification of the vorticity system

The measured streamwise vorticity at cross-stream locations $x/D = 0.26$, 0.90, and 1.60 is shown in Figure 7.11 for the fixed pitch cases $\beta = -10^\circ$, 0°, and 10°. In-plane velocity vectors are illustrated to help locate the vortical structures labeled based on the convention proposed in Section 7.2. The black contour line indicates where $U_x/U_\infty = 0.9$, and the grey enclosed curve indicates the frontal area of the rotor. An extended set of measurements at more cross-stream planes is shown in Appendix B.2.

For all pitch cases, the vortical structures are clearly present at the $x/D = 0.26$. As this plane is still within the volume of rotation, the presence of shed vorticity of the blade is visible, specifically for the $\beta = -10^\circ$ and 10° cases. For the pitch cases $\beta = 10^\circ$, the vortex generated in the UW quadrant (B) creates a dominant downwash of the wake, contracting the wake perimeter to within the frontal area of the rotor. Due to the high strength of this vortex, that of the previous blade is also visible, which has been convected downstream. The UL vortex (A) is also present but visibly weaker and hence induces a similar axial contraction of the wake on the leeward side of the rotor, but to a lesser degree. The negative pitch case $\beta = -10^\circ$ exhibits a similar CVP with opposite direction to the aforementioned case as predicted in Section 7.2. The vortices generated in the DW (B) and DL (A) quadrants are dominant and induce an axial expansion of the wake. Once again, the windward vortex is seemingly stronger in magnitude. The upwind vortex, albeit weaker, has convected inward towards $y/D = 0$ and includes a regional upwash of the wake. Finally, the case with no pitch $\beta = 0^\circ$ exhibits three vortical structures towards the windward side of the rotor with alternating rotation direction. As this plane is still within the volume of rotation and these are phase-locked measurements, the tip-vortices of the passing and previously passed blade are visible. In this case, the DW-generated vortex (B) stems from the blade, which has just passed and is now at phase-locked position $\theta = 0^\circ$. The surrounding vortex pairs (B) were generated in the UW quadrant by the two blades in the previous cycles that have convected downstream.

The impact of the vortex system on the wake increases in the next cross-stream plane $x/D = 0.90$. For the case of $\beta = 10^\circ$ the size of the UW vortex (B) has grown and convected slightly downward towards $z/D = 0$. The surrounding shed vorticity of the blade has dissipated as we exit the volume of rotation of the rotor. The induced downwash of the vortex has increased due to the larger size of the structure, causing a larger degree of wake deformation and a region of high-speed flow within the frontal area of the rotor. The UL vortex (A) is not labeled at this cross-stream location, as it has seemingly diffused. However, its impact on the wake is still present at this location, with a slight axial contraction on the leeward side of the rotor. For the pitch case $\beta = -10^\circ$, the DW vortex (B) has diffused and convected upward above the AC surface. In contrast, the DL vortex (A) has increased in strength while continuing to induce a strong axial contraction of the wake. The zero pitch case $\beta = 0^\circ$ once again exhibits two tip-vortices generated in the UW quadrant (B) of the cycle, which have convected downstream, as well as the vortex generated in the DW

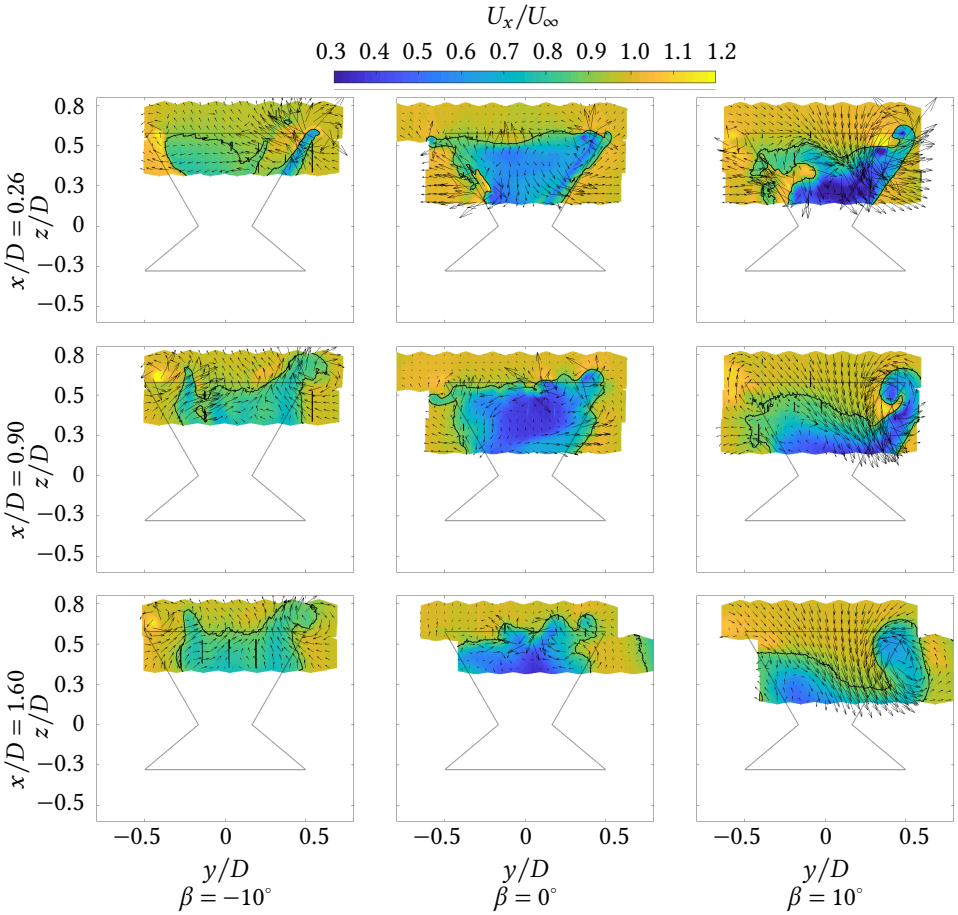


Figure 7.8: Normalized streamwise flow (U_x/U_∞) at cross-stream locations x/D = 0.26, 0.90, and 1.60 for fixed pitch cases $\beta = -10^\circ$, 0°, and 10°. The grey solid line shows the frontal area of the rotor at an azimuth of 0° with a black contour line showing where $U_x/U_\infty = 0.9$. Quivers show the in-plane velocity vectors.

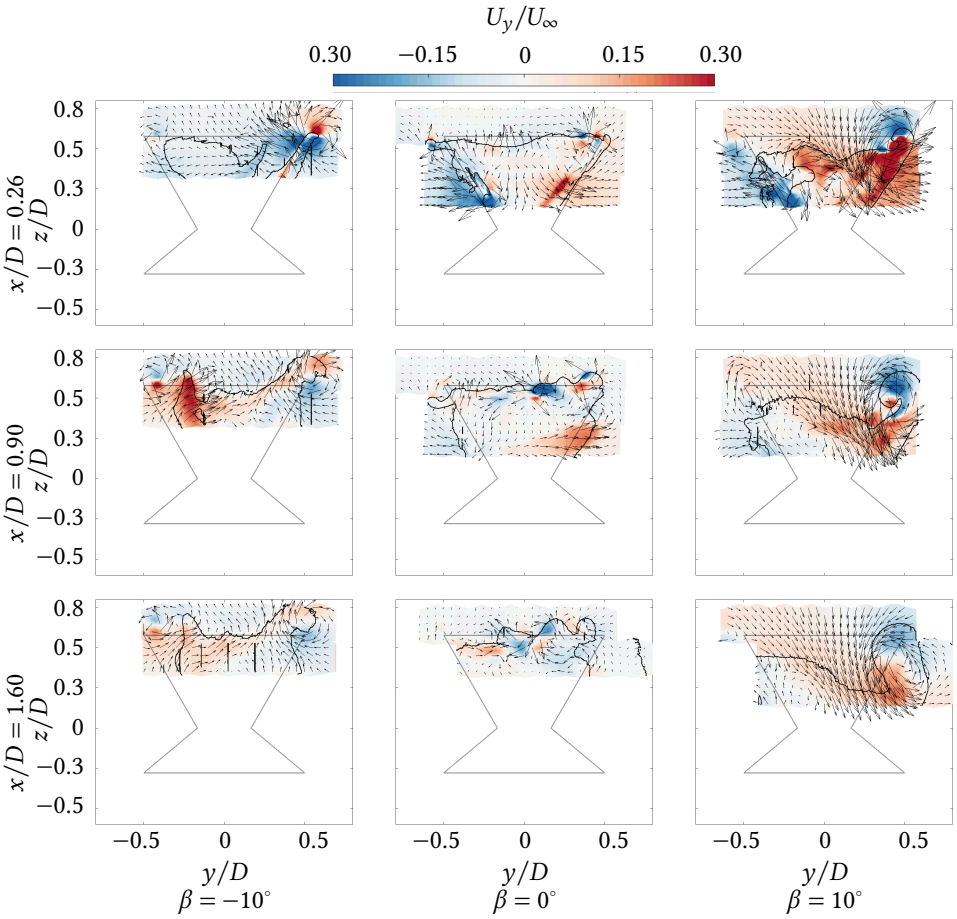


Figure 7.9: Normalized lateral flow (U_y/U_∞) at cross-stream locations x/D = 0.26, 0.90, and 1.60 for fixed pitch cases $\beta = -10^\circ$, 0°, and 10°. The grey solid line shows the frontal area of the rotor at an azimuth of 0° with a black contour line showing where $U_x/U_\infty = 0.9$. Quivers show the in-plane velocity vectors.

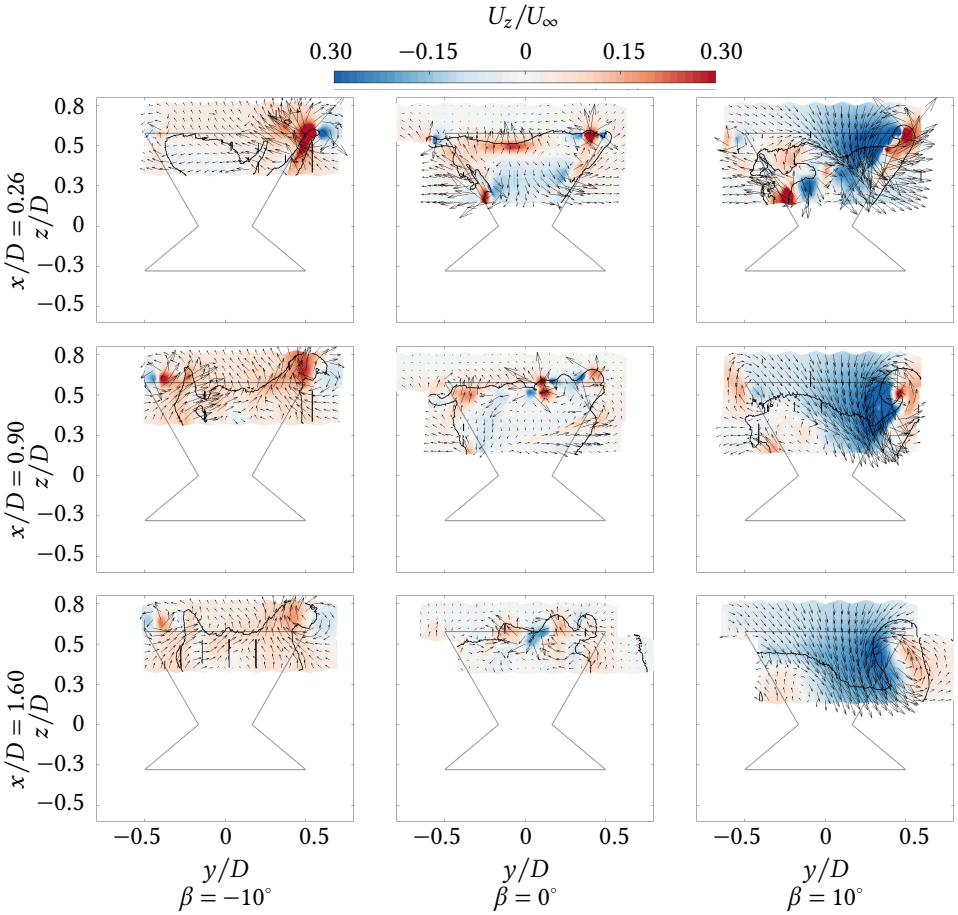


Figure 7.10: Normalized axial flow (U_z/U_∞) at cross-stream locations x/D = 0.26, 0.90, and 1.60 for fixed pitch cases $\beta = -10^\circ$, 0°, and 10°. The grey solid line shows the frontal area of the rotor at an azimuth of 0° with a black contour line showing where $U_x/U_\infty = 0.9$. Quivers show the in-plane velocity vectors.

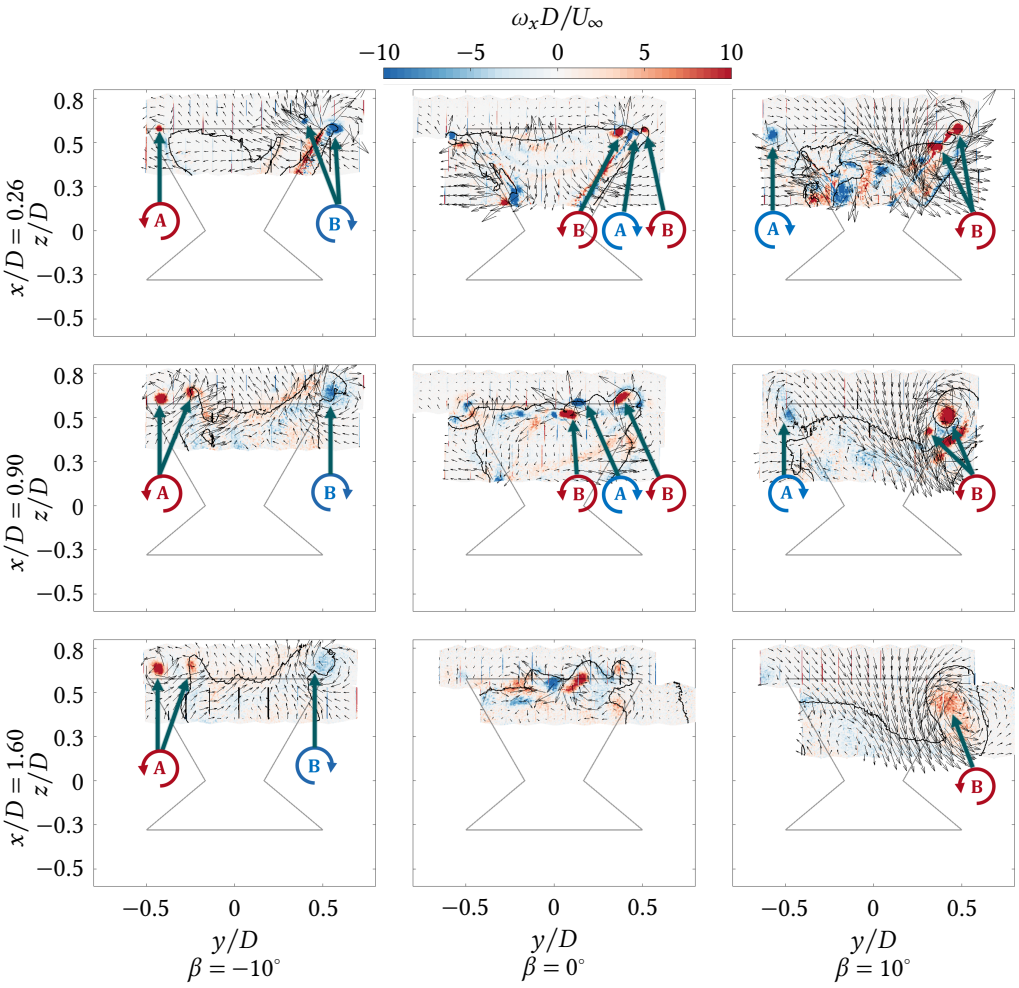


Figure 7.11: Streamwise vorticity contours at cross-stream locations x/D = 0.26,0.90, and 1.60 for fixed pitch cases $\beta = -10^\circ$, 0°, and 10°. Vortices are labeled for clarity, corresponding to markings presented in Figure 7.1. The black contour line indicates where U_x/U_∞ = 0.90. The grey line represents the frontal area of the rotor.

quadrant (A) of the blade, which has just passed.

Finally, the most downstream plane x/D = 1.60 suggests that the vortical structures across all pitch cases are still present but have diffused and mixed substantially. For the positive pitch case $\beta = 10^\circ$, the UW vortex (B) has diffused to a degree where no clear core is identifiable. However, the structure continues to induce a local downwash on the windward side of the rotor, with freestream flow being injected from the upper surface of the AC. Little difference in the wake structure on the leeward side of the rotor is notable compared to the previous cross-stream location presented. The negative pitch case $\beta = -10^\circ$

still displays two coherent vortex structures, which have both convected above the actuator surface. The zero pitch case $\beta = 0^\circ$ shows no coherent vortex structures due to the mixing process of the closely spaced CVP in the near wake. This mixing and turbulent diffusion is intrinsic to VAWTs [41]. The outward motion (above the AC surface) of the vortex structures generated on the windward side of the rotor has been observed experimentally [41] and numerically [154] and can be attributed to the interaction of the tip-vortices of the blade in quadrant UW and the second blade generated in the DW quadrant.

To further highlight the relative impact of blade pitching on the strengths of the tip-vortices, Figure 7.12 shows the maximum streamwise vorticity strengths $max(\omega_x)$ of the vortices in the windward (W) and leeward (L) halves of the rotor as a function of the cross-stream location. The maximum vorticity is normalized by the highest vortex recorded, which is that of the positive pitch case on the windward side $max(\omega_{x,+10})$ at $x/D = 0.26$.

Across all cases, the maximum vorticity magnitude tends to decrease when moving further downstream in the wake. This is consistent with the observations made of Figure 7.11 and can be attributed to the mixing and diffusion process of the tip-vortex structures. A deviation from this trend is evident at $x/D = 0.5$ for the vortex of the negative pitch case on the leeward side, where there is an increase in strength from the previous plane. As explained in Section 7.2, negative blade pitch causes greater loads to be applied to the downwind half of the rotor. Hence, the generation of a strong tip-vortex occurred in the DL quadrant of the cycle and has a delayed appearance in the flowfield compared to the heavily loaded upwind case of the positive pitch. The peak vorticity at the most upstream plane $x/D = 0.26$ corresponds to the vortex generated in the UL quadrant of the cycle, and that at $x/D = 0.5$ in the DL quadrant, as labeled in Figure 7.11.

The maximum vorticity strengths on the leeward side of the rotor for the positive pitch case remain low in magnitude across all streamwise planes. As described in Section 7.2, positively pitching the blade increases the blade loading in the upwind half of the rotor with an increase in relative angle of attack across the span. As shown in Figure 7.5, the angles of attack eventually exceed the stall angle toward the end of the UW quadrant of the cycle. Hence, the blade is stalled for a large portion of the cycle's UL quadrant, leading to a weaker tip-vortex structure. A similar phenomenon occurs for the negative pitch case in the DW quadrant of the cycle. With the higher angle of attack magnitudes in the downwind half of the rotor, the blade stalls in the DL quadrant of the cycle, leading to a separated flow majority in DW quadrant of the cycle and, hence, a weaker tip-vortex structure.

7.4.3 Phase-locked flow fluctuations

The normalized standard deviation (SD) magnitude $|\sigma| = \sqrt{\sigma_u^2 + \sigma_w^2 + \sigma_v^2}/U_\infty$ where σ denotes the standard-deviation of the phase-locked velocity component, is plotted in Figure 7.13. Previous work [76] relied on a combination of phase-locked and time-averaged data to isolate mean, periodic, and random velocity terms. As no time-averaged results are available, the standard deviation term encompasses the quality of the phase-lock as well as local turbulent flows in the wake. The lack of time-averaged data hinders the isolation of these two components as done in previous works [25, 160]. However, as turbulent flow would lead to higher standard deviations, this approach succeeds in giving a relative indication of regions with unsteady flow separation and turbulence.

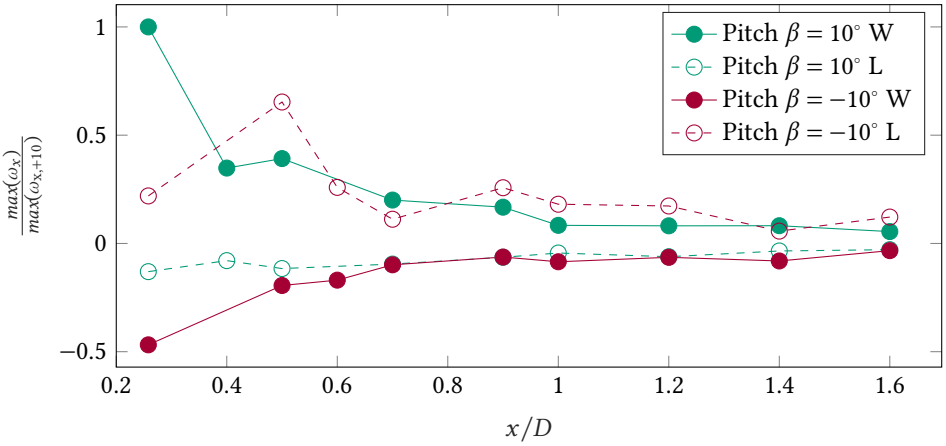


Figure 7.12: Maximum streamwise vorticity $max(\omega_x)$ strength as a function of cross-stream location for the positive and negative pitch cases. Solid lines indicate vortices on the windward side (W) and dashed on the leeward (L). Values are normalized by the maximum vorticity of the inward vortex in the positive pitch case at $x/D = 0.26$ ($max\ (\omega_{x,+10})$).

The first row shows $|\sigma|$ for the cross-stream plane $x/D = 0.26$. For the zero pitch case, SD magnitudes are highest at the edge of the wake. Large magnitudes are evident in the regions where coherent shed vorticity is present from the blade that has just passed, with slightly weaker values than those generated by the previous blade. A clear transition from attached to separated flow is visible on the windward side of the rotor at around $z/R = 0.37$. This corresponds to a local tip-speed ratio of $\lambda = 3.0$. A similar separation region is evident on the leeward side of the rotor. For the positive pitch case $\beta = 10^\circ$, moderate intensities are evident at the edges of the wake. The tip vortices have high magnitudes of SD, indicating some meandering of the vortex structures and hence smearing in the phase-lock. Furthermore, a large region of high SD is evident on the windward side of the rotor. This region corresponds to the intersection of the measurement plane of the generated shed vorticity from the blade passing through the UL quadrant of the cycle. As expected, the blade is heavily stalled in this region due to high magnitudes in relative angle of attack, specifically in regions moving towards the blade's root where the local tip-speed ratio decreases. For the negative pitch case, high magnitudes in SD are evident on the windward side of the rotor following the blade's trajectory. This is generated by the blade that just exited the DW quadrant of the cycle, where the angle of attack magnitudes are increased through the pitching action, presumably leading to stall. The shed vorticity of the previous blade generated in the UW quadrant appears at a lower magnitude and more inboard towards $y/D = 0$, as seen in Figure 7.11. The shed vorticity on the leeward side of the rotor is generated in the UL quadrant, where the angles of attack are systematically reduced through the pitching action, leading to more attached flow along the span of the blade.

The second row is at a cross-stream plane of $x/D = 0.9$. The zero pitch case shows peaks in SD at the tip vortices. Once again, moderate streaks of SD are apparent at the edge of the wake as well as along the shed vorticity of the blades. As this is now further

in the wake, these structures have begun to diffuse and deform compared to the previous plane. The positive pitch case shows a high standard deviation on the tip vortex as before, which has grown in size. As in the zero pitch case, high SD is not only concentrated along the perimeter of the wake but also quite dominant within. This can be attributed to shed vorticity structures that have convected downstream, generated by the blade in the UW quadrant. As in the previous plane, the blade is expected to be stalling here due to the systematic increase in the angle of attack across the span. The negative pitch case shows moderate intestines in SD along the deformed edge of the wake. The windward side of the rotor shows a presence of high SD within the wake, which can be attributed to the stalled blade of the DW quadrant that has convected downstream.

Finally, the third row shows the SD at the cross-stream plane x/D = 1.6. The zero pitch case has moderate SD concentrated along the perimeter of the wake with high magnitudes concentrated around the mixing and diffusing tip-vortex structures. At the edge of the measurement domain, a path of high SD is evident where the edge of the open jet is reached. For the positive pitch case, the distribution looks the same as in the previous plane, with a decrease in magnitude due to diffusion. The negative pitch case shows similar behavior to the previous plane as well as the positive pitch case. Given the convective speed of U_∞ (without considering rotor induction) and the rotational frequency of 21.3 rad/s, the wake structure has convected approx. x = 0.8D in one cycle, explaining the similarity between the flow fields at x/D = 0.9 and 1.6.

7.4.4 Kinetic energy flux

To highlight the impacts of fixed blade pitch on the wake re-energization, the axial advective component of the mean-kinetic energy (MKE) flux above the rotor is shown in Figure 7.14. The importance of vertical fluxes towards the replenishment of energy in farm arrays has been highlighted by [77]. A control volume approach is taken, as proposed by [67] and used in Chapter 4, where the vertical fluxes above the rotor at z/D = 0.7 within the diameter of the rotor (-0.5 < y/D < 0.5) are computed. For typical HAWT farms, the dominant term is typically the turbulent-induced vertical flux. However, due to the modified trailing vortex system, the advective component is more dominant in the wake re-energization procedure of the X-Rotor with pitched blades. Hence, only the advective flux of MKE $-0.5U_zU_x^2$ is presented, normalized by the freestream flow. The profile is extracted over all cross-stream locations of the rotor. The mean profile is presented via a solid line, with the shaded region representing the standard deviation across all cross-stream planes.

The axial MKE flux above the rotor does not change drastically as a function of cross-stream location across all pitch cases in these near-wake measurements. The pitch $\beta = 0^\circ$ case shows a relatively flat curve around a zero magnitude flux, indicating minimal energy transfer above the rotor. Despite this, the mean curve does fall above zero on the leeward side due to the downwash of the vortex in the UL quadrant. Due to the asymmetry in the wake discussed in Section 7.4.1, the flux magnitude becomes negative on the windward side of the rotor. In this region, there is a higher magnitude of variety between the different cross-stream planes, as evidenced by the larger shaded area. As discussed in Section 7.4.1, the aforementioned asymmetry grows between the windward and leeward sides of the rotor when moving downstream.

The negative pitch case $\beta = -10^\circ$ exhibits a predominantly negative axial flux magnitude

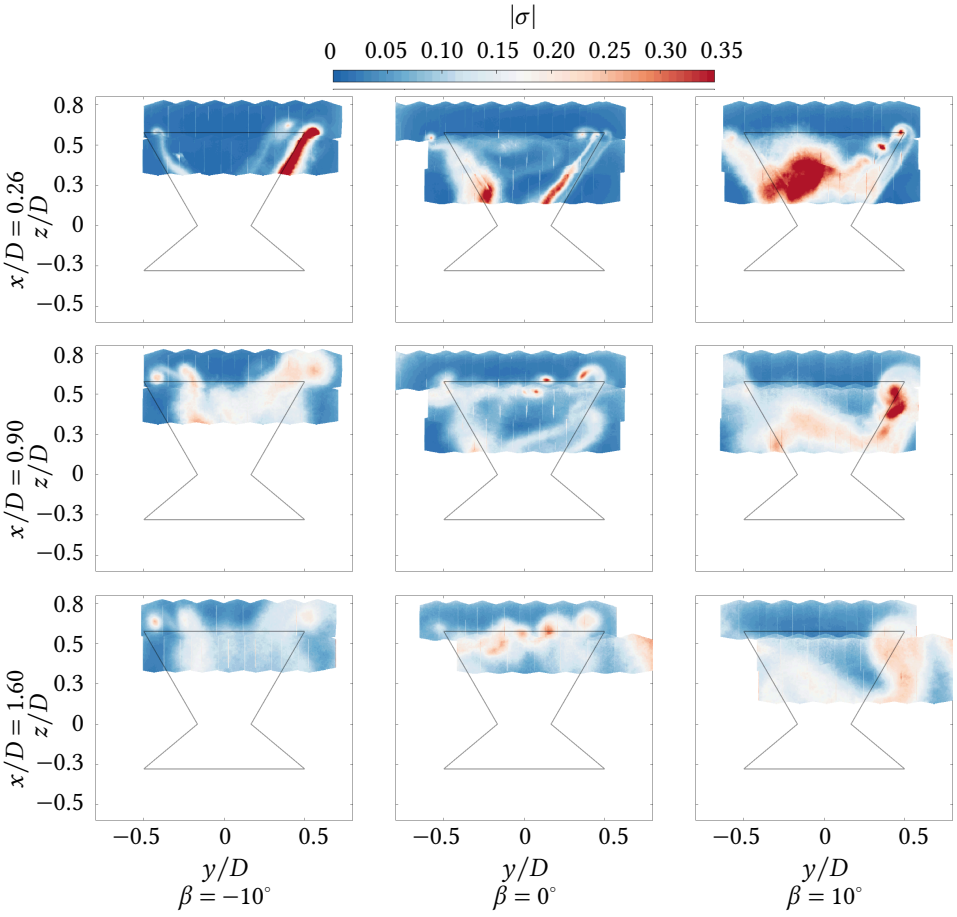


Figure 7.13: Normalized standard deviation magnitude, $|\sigma|$, contours at cross-stream locations x/D = 0.26,0.90, and 1.60 for fixed pitch cases $\beta = -10^{\circ}$, 0°, and 10°. The grey line represents the frontal area of the rotor.

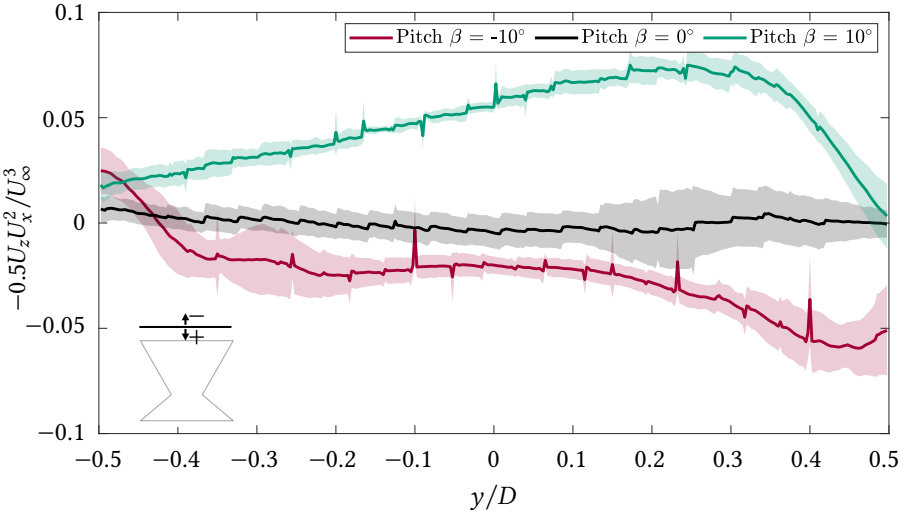


Figure 7.14: Normalized axial advective MKE flux $-0.5U_zU_x^2/U_\infty^3$ through a line at $z/D = 0.7$ within the diameter of the rotor (-0.5 < y/D < 0.5) at cross-stream locations 0.26 < x/D < 1.6 for the three pitch cases. The mean profile across all cross-stream locations is shown via a solid line and a shaded area signifying the standard deviation. The icon at the bottom left of the figure illustrates the line through which the flux is considered, with the respective positive and negative directions marked.

across the entire diameter of the rotor. This is consistent with the impact of the vortex system on the wake topology, described in Section 7.4.2. The magnitude increases at the edge of the windward side due to the strong DW vortex, which has convected above the rotor. Similarly, the magnitude is positive for a small portion on the leeward side of the rotor due to the DL vortex, which has convected inward towards $y/D = 0$. More significant variations as a function of cross-stream location are apparent at the regions near the dominant vortices due to the time taken for the structures to form, as discussed in Section 7.4.2.

Finally, the pitch case $\beta = 10^\circ$ shows a consistent positive magnitude in flux, signifying a downwash. The downwash magnitude is significantly higher on the windward side of the rotor due to the UW vortex's higher strength than the UL, as highlighted in Figure 7.12. As a result, the flux magnitudes on the windward side are high before decreasing when moving toward the leeward side of the rotor. Unlike the aforementioned pitch cases, minor variation as a function of cross-stream location is apparent. As the positive pitch case is an upwind phenomenon discussed in Section 7.4.2, the vortex system is already established when measuring downstream. The positive pitch case has a higher magnitude in axial MKE flux on average across the rotor diameter, with $< -0.5U_zU_x^2/U_\infty^3 > = 0.05$ compared to -0.03 and 0 for the negative and zero pitch settings, respectively.

7.5 Conclusions

The role of the X-Rotor's loading on the wake topology is defined using the actuator cylinder (AC) theory and further validated using the CACTUS numerical model. The numerically obtained angle of attack distribution across the X-Rotor's upper blades and subsequent azimuthally resolved loading confirm the impacts of fixed blade pitch on the load distribution of the X-Rotor. This working principle is further validated and demonstrated through an experimental study of the near wake of a scaled X-Rotor using stereoscopic PIV measurements. The results confirm the theoretical load distribution modifications realized by fixed-blade pitch and align with previous works that theoretically defined and demonstrated the impact of fixed-blade pitch on an H-Type VAWT.

The velocity components and the streamwise vorticity in the wake reveal two distinct modes of operation. For the positive pitch case (pitched in), the strength of the upwind vortex is dominant, leading to flow entrainment axially from the free stream, complemented by an ejection of the wake in the lateral direction. Conversely, for the negative pitch case (pitched out), the strength of the downwind vortex is dominant, leading to an opposing direction of rotation and, subsequently, a wake ejection axially upward and flow entrainment laterally from the sides. The standard deviation of the phase-locked flow fields sheds light on regions where the blade is presumably stalling along the coned span due to the local differences in tip-speed ratio. Further, the change in effective angle of attack through fixed-blade pitch also triggers stall onset in certain quadrants of the rotor's motion as the stall angle is surpassed. A comparison of the flowfield with the theoretical blade integrated load distribution confirms this behavior. Finally, an analysis of the kinetic energy above the rotor volume confirms the wake re-energizing mechanism of the X-Rotor, highlighting the constructive induction of the large-scale tip vortices on streamwise energy recovery.

The presented results highlight the streamwise vorticity system's critical role in the momentum transfer in the wake of the X-Rotor VAWT. Further, this mechanically simple wake control mechanism of fixed blade pitch would yield huge potential for farm-scale installation of X-Rotor VAWTs due to the aforementioned benefits in wake recovery.

8

The full wake topology of the X-Rotor with the fixed-pitch wake recovery strategy

This chapter builds Chapter 7 by providing an experimental study of the wake topology of the entire scaled-down X-Rotor using this control technique up to a wake location of $x/D = 6$. Stereoscopic particle-image velocimetry measures the time-averaged wake topology with and without the "vortex generator" strategy.

This chapter is based on **Bensason D.**, Sciacchitano A., Simao Ferreira C. On the wake re-energization of the X-Rotor vertical-axis wind turbine via the vortex-generator strategy, *Wind Energy Science*, 2025 [161].
The data supporting this study is openly available in the 4TU.ResearchData repository at `https://doi.org/10.4121/fa5aa65d-7619-4424-b921-e82f7d12a5fb`.

8.1 Introduction

This work aims to quantify the wake recovery potential and process of the X-Rotor with and without the "vortex generator" mode. Hence, this study builds on the promising results of Chapter 7 by scaling the primary rotor model down to 1:250 such that the entire wake further downstream can be measured. The vorticity system stemming from the unique rotor geometry is hypothesized in Section 8.2. Cross-plane wake measurements are collected in an open jet wind tunnel using a stereoscopic particle image velocimetry setup up to six diameters away from the rotor, described in Section 8.3. The wake topology at different modes of operation is presented in Section 8.4.1, followed by an assessment of the available power in the wake in Section 8.4.2. The aforementioned vorticity system is verified in Section 8.4.3 and linked to the modified wake shapes. The dominant role of the vortex system is further elucidated in Section 8.4.4 by predicting the wake recovery modes using a simplified point-vortex model. Finally, the mean kinetic energy replenishment process is detailed in Section 8.4.5. The main conclusions and outlook on future work are discussed in Section 8.5.

.

8.2 Background on vortex-generator wake control

As described in both Chapter 4 and Chapter 7, the load distribution of VAWT can be modeled using the actuator cylinder approach [43, 44, 106]. The working principle described in Chapter 7 is extended to encapsulate the full rotor and is shown in Figure 8.1. The rotor cycle is divided into four quadrants: upwind windward (UW), upwind leeward (UL), downwind leeward (DL), and downwind windward (DW). Arrows represent the magnitude and direction of normal blade loads, assuming uniform load distribution within upwind and downwind halves, with higher loads upwind under zero pitch [44]. Due to the X-Rotor's coned blades, local tip-speed ratios and loading profiles vary along the span, introducing unsteady effects. Quadrants are color-coded (red and blue) to indicate counter-clockwise and clockwise trailing vortex rotation, respectively, linked to blade loading and bound circulation, which reverses at $\theta = 0^\circ$ and 180°.

Below the idealized actuator load schematics, the projected frontal area of the rotor is shown via a shaded region at a generic downstream position. The intersections on the wake plane of the dominant vortex pairs for each pitch case are represented via circular arrows, color-coded by their directions at the upper blade tips. Black and grey arrows correspond to the direction of high and low momentum flow, stemming from the free stream and wake, respectively. Each case is described as follows:

Baseline case $\beta = 0^\circ$: For the baseline pitch case, the blade will operate in its own wake in the downwind half of the cycle, leading to an intrinsic higher load in the upwind half [56]. However, in the near wake, both vortex structures stemming from the upwind and downwind half of the rotor will be visible (red and blue), as concluded in Chapter 7. The directions of rotation of the tip-vortices of the bottom blade will be mirrored to that of the upper tips with a circulation. As the bottom blades are shorter and coned at a different angle, they will experience a different cyclic flow variation and, subsequently, loading profile. Following Helmholtz's theorem, the instantaneous circulation of the vortex shed at the root will be a function of those shed at the top and bottom tips. For the baseline case,

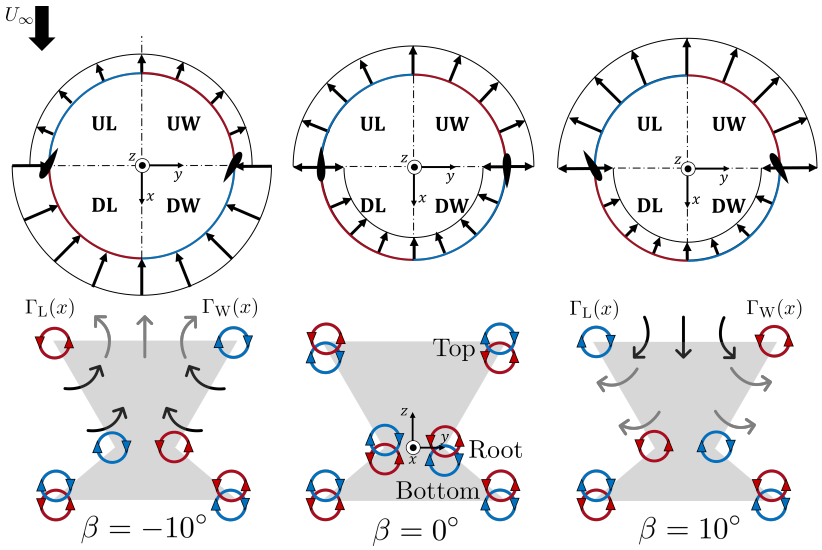


Figure 8.1: Schematic representation of the simplified force fields of the actuator cylinder for the three pitch cases (β) adapted from [133]. The blades are exaggerated in size and are located at $\theta = 0^\circ$ and 180°. Each quadrant of the cylinder is labeled with $0^\circ < \theta < 90^\circ$, $90^\circ < \theta < 180^\circ$, $180^\circ < \theta < 270^\circ$, and $270^\circ < \theta < 360^\circ$ corresponding to upwind windward (UW), upwind leeward (UL), downwind leeward (DL), and downwind windward (DW), respectively. The rotor cylinder edge is color-coded red and blue based on the direction of the trailing vortex, counterclockwise and clockwise, respectively, for the upper blade tips. The corresponding frontal area of the rotor (grey-shaded) at a generic plane in the wake is shown for each pitch case. The dominant trailing vortices (round arrows) stemming from the Top, Bottom, and Root sections of the blades are illustrated along with the induced cross-plane movement in the flow, with low momentum wake and high-speed flow disguised by grey and black arrows, respectively. The streamwise dependent circulations of the windward and leeward vortices from the top blades are denoted as $\Gamma_W(x)$ and $\Gamma_L(x)$, respectively, for the pitched cases.

the loads generated by the upper and lower blades are similar in magnitude between the windward and leeward quadrants, with the largest differences in the peak loads close to $\theta = 90^\circ$ [106], and would hence result in a weak root vortex in the streamwise direction. Further, assuming a symmetric load between the windward and leeward sides of the rotor, the strengths and directions of the structures will be mirrored.

Pitched-in $\beta = 10^\circ$: In this case, the load is shifted towards the upwind half of the rotor, as seen by the increase in length of the vectors on the AC. Subsequently, the trailing vortices generated in the upwind quadrants of the upper blades would be strengthened, and they are shown as the dominant counter-rotating vortex pair (CVP) on the tip of the projected frontal area. These induce a downwash in the wake, where high-momentum free-stream flow is injected from above the rotor, while the low-momentum wake is ejected laterally from the sides. The idealized symmetric behavior of this wake morphing is linked to the assumption that the loads on the upwind half of the cycle are symmetric (constant). However, as observed in Chapter 7, the vortex on the windward side of the rotor is more dominant as the blade loading on the UW quadrant is higher than in the UL, as confirmed via blade load measurements of [56]. This phenomenon is intrinsic to VAWTs as the effective angles of attack experienced by the blade in the UW quadrant are higher than

in the UL. The resulting asymmetry in the wake was also observed by [25] for an H-type VAWT, resulting in the wake being ejected out more dominantly on the windward side. Assuming the circulation of the bottom blade remains constant (as it is not pitched), the direction of the root vortex will be opposite to that of the upper blade tip.

Pitched-out $\beta = -10^{\circ}$: In this mode, the load is shifted towards the downwind half of the rotor. As a result, the directions of the dominant CVP are flipped as the downstream trailing vortices are energized on the upper blades. These are in opposing directions as the positive pitch case and, in turn, induce an upwash in the wake, with low momentum flow being ejected out from above the rotor while high-speed free stream flow is injected from the sides. Similar to the positive pitch case, the symmetry is linked to the assumption that the load is evenly distributed along the downwind half of the rotor. However, as observed by Chapter 4, the loads in the DW quadrant are higher in magnitude compared to the DL, leading to a stronger vortex on the windward side and asymmetry in the topology. As before, assuming an unchanged circulation of the bottom blade, the root vortices will be in the opposite direction to those generated in the upper blade tips.

The results in Chapter 7 suggest a significant dependence of the pitched recovery modes on the dominant CVP of the top blades. Hence, a simple model using Lamb-Oseen vortices is used to predict the axial flow component at the top of the rotor as a function of downstream location. At a discrete downstream measurement plane (x), the vortex cores ($y_{\mathrm{W,L}}(x), z_{\mathrm{W,L}}(x)$), point-vortex circulations ($\Gamma_{\mathrm{W,L}}$), and viscous length scale ($\eta_{\mathrm{W,L}}$) are considered for both the windward and leeward vortices, denoted with subscripts W and L, respectively. The induced axial velocities by the windward and leeward vortices are denoted as $U_{z,\mathrm{W}}(y,z)$ and $U_{z,\mathrm{W}}(y,z)$, respectively, and are expressed as [162]:

$$U_{z,\mathrm{W}}(y,z) = \frac{\Gamma_{\mathrm{W}}(x)(y - y_{\mathrm{W}}(x))}{2\pi r_{\mathrm{W}}^2(x)} \left(1 - \exp\left(\frac{-r_{\mathrm{W}}^2(x)}{4\eta^2(x)}\right)\right), \tag{8.1}$$

$$U_{z,\mathrm{L}}(y,z) = \frac{\Gamma_{\mathrm{L}}(x)(y - y_{\mathrm{L}}(x))}{2\pi r_{\mathrm{L}}^2(x)} \left(1 - \exp\left(\frac{-r_{\mathrm{L}}^2(x)}{4\eta^2(x)}\right)\right) \tag{8.2}$$

Here, the radial distance from the vortex core to the measurement point is $r_{\mathrm{W}}(x) = \sqrt{(y - y_{\mathrm{W}}(x))^2 - (z - z_{\mathrm{W}}(x))^2}$ and $r_{\mathrm{L}}(x) = \sqrt{(y - y_{\mathrm{L}}(x))^2 - (z - z_{\mathrm{L}}(x))^2}$ for the two vortices. The net-induced axial flow component is the sum of the two and is denoted as $U_z(y,z)$.

$$U_z(y,z) = U_{z,\mathrm{W}}(y,z) + U_{z,\mathrm{L}}(y,z) \tag{8.3}$$

8.3 Methods

8.3.1 Wind tunnel and turbine model

The experiments were carried out in the Open-Jet Facility (OJF) of the TU Delft Aerospace Engineering faculty with details provided in Chapter 4. The X-Rotor model is an in-house designed geometrically scaled 1:250 version introduced by [28], which is mounted on the adjustable table as shown in Figure 8.2. The rotor solidity $\sigma = \sum cL_N/A$ is 0.15, where $\sum cL_N$ is the sum of the products of the blade height and chord for each of the four blades, and $A = 0.2057\mathrm{m}^2$ is the projected frontal area of the rotor. This solidity is close to that of the full-scale model which is $\sigma = 0.17$ [106], with the difference due to the use of a straight

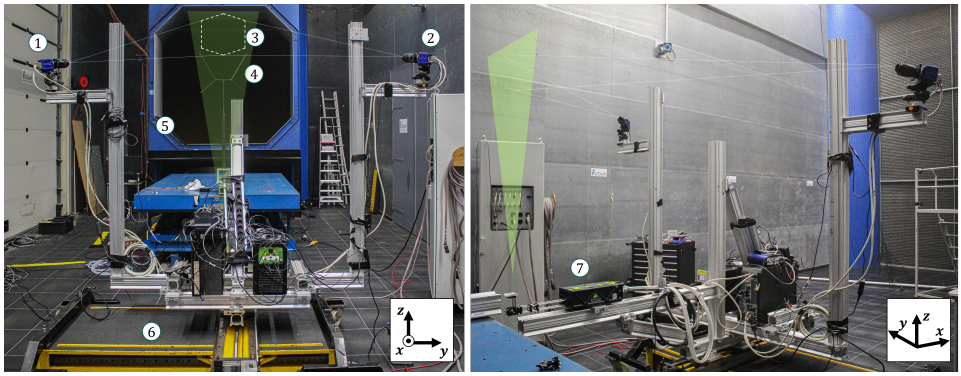


Figure 8.2: Experimental setup in the OJF from two different views. A visualization of the measurement plane (green triangle) is provided, along with a representation of the camera viewing direction. The main components are labeled and defined as follows: ① Camera 1, ② Camera 2, ③ field-of-view, ④ X-Rotor model, ⑤ OJF outlet, ⑥ Traversing system, ⑦ Laser.

blade rather than tapered. A detailed schematic of the rotor system is provided in Figure 8.3. The X-Rotor geometry is mounted on a 1.2m long shaft with a diameter of 15mm. This shaft passes through an aluminum tower of constant external and internal diameters of 50mm and 20mm, respectively. The tower houses a roller bearing with an internal diameter of 15mm at the top and bottom of the rotor tower to increase the stability of the shaft whilst minimizing any deflections. Finally, this tower is mounted to a rotor stand, which connects to an in-house designed three-component balance. Details on the balance are provided in Chapter 4. Before the flowfield measurements, the scaled rotor model thrust performance was tested as a function of the tip-speed ratio in the OJF using this balance.

The X-Rotor model consists of four blades, which are mounted to a cross-beam at the root, as shown in Figure 8.3. The rotor has a tip diameter of $D = 0.6$m on both the bottom and top half. The blades on the upper and lower halves of the rotor are 0.375m and 0.238m with coning angles of 60° and 40°, respectively, yielding a total length of 0.4m and 0.26m when including the extruded profile of the adapters at the root. All blades are made in-house using a carbon-fiber hand layup technique. They are untwisted and untapered with a constant NACA0021 profile with a chord $c = 0.03$m and a hollow section of the same profile with a wall thickness of approximately 1mm. The cross-beam is 0.2m long and has the same profile and chord as the blades, with the direction of the leading edge flipping at the center point (connection with the extruded rod) such that it faces the direction of rotation for a counter-clockwise rotating system. Different fixed-pitch adjustments are realized by interchanging modular adapter pieces within the root section of the cross-beam, as shown in Figure 8.3. For this experiment, fixed-pitch adapters for $\beta = -10°$, 0°, and 10° are designed to allow qualitative comparison with previous works by [25, 133]. As the bottom blades are not pitched, they are not modular and are fixed in the design of the cross-beam at a constant pitch angle of $\beta = 0°$. The cross-beam and modular pitch adapters are 3D-printed out of Aluminium AlSi10Mg with a layer thickness of 50 μm and tolerance of 0.2mm. The surface roughness is on the order of 1-3 μm after tumbling. All components of the X-Rotor are painted black to minimize the laser reflections. The wind

Pitch case β [°]	$C_{T,x}$	$C_{T,y}$
-10	0.66	0.02
0	0.77	0.03
10	0.79	-0.26

Table 8.1: Measured streamwise (x) and lateral (y) thrust coefficients C_T. All standard deviations of the measured coefficients fall below ±0.01.

tunnel blockage ratio is 0.03, considering the project frontal area of the rotor.

The streamwise and lateral thrusts, $C_{T,x}$ and $C_{T,y}$, respectively, are given by:

$$C_{T,x} = \frac{T_x}{0.5\rho U_\infty^2 A}, \qquad C_{T,y} = \frac{T_y}{0.5\rho U_\infty^2 A}, \tag{8.4}$$

where T_x and T_y are the measured streamwise and lateral thrust [N], respectively, and ρ = 1.225 kg/m^3 is the air density. The averages and standard deviations measured over five trials (each with 10 seconds at 1600Hz) are shown in Table 8.1. The behavior in the cycle-averaged thrusts is similar to those reported by [25], with a decrease and increase in streamwise thrust for the pitch cases $\beta = -10^\circ$ and $\beta = 10^\circ$, respectively, of +2% and -14%. A decrease in streamwise thrust when applying a negative pitch is attributed to the decrease in effective angle of attack perceived by the blade in the upwind passage of the blade, as highlighted by the discussion of [25], and by load and flowfield blade-level measurements of [56, 131] for lab-scale H-Type Darrieus VAWTs. Conversely, the increase in streamwise thrust for the positively pitched case is due to the increase in the effective angle of attack in the upwind passage, as commented on by [56]. Similar to the trend in streamwise thrust, the lateral thrust for the negative pitch decreases by 8% in magnitude. However, for the positive pitch case, the force increases by over one order of magnitude. This increase is attributed to the significant increase in blade load in the UW quadrant and, subsequently, the lateral imposed force of the actuator on the flow, visualized by the increased normal forces shown in Figure 8.1.

For the baseline case of β = 0°, the lateral thrust is on the order of 30x lower than the streamwise thrust, whereas in the case reported by [25], the lateral thrust was in a similar order to that of the streamwise component, only being 5x smaller. This can be attributed to the larger tip-speed ratio in this experiment, yielding a higher degree of symmetry.

8.3.2 Flow measurement system

The velocity fields in the wake were obtained using a stereoscopic particle image velocimetry (PIV) approach. Details regarding the seeding and illumination are provided in Chapter 5. Images were recorded at 15Hz using two LaVision sCMOS cameras with a sensor and pixel size of 2560px × 2160px and 6.5μm, respectively. Images were recorded from the downwind side of the laser sheet, as shown in Figure 8.2. Both cameras mounted lenses of 105mm focal length, set at a numerical aperture of $f_\# = 8$. The stereoscopic angles of Camera 1 and Camera 2 were 42° and 46° relative to the normal to the measurement plane, respectively, and were positioned approximately 2.3m and 2.4m from the plane, resulting

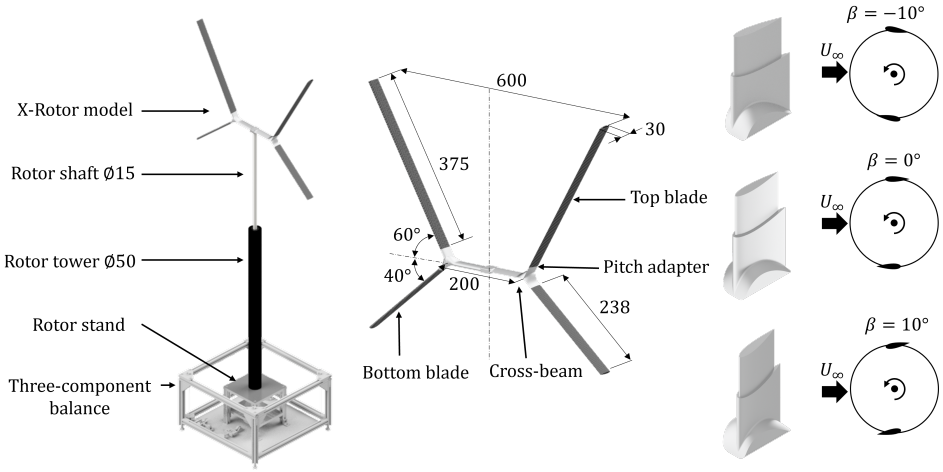


Figure 8.3: (Left) Rendered schematic of the X-Rotor model mounted to the three-component balance, with the main components labeled. (Middle) Dimensioned and labeled schematic of the scaled X-Rotor model. (Right) Rendering of the three pitch adapters with a top-view representation of the pitch direction convention, with positive and negative pitching in and out towards the tower, respectively. All dimensions are in mm.

in a field of view (FOV) of approximately 31 cm × 30 cm, and a digital image resolution of 7.5 px/mm. A time separation of 200μs between image pairs was used. Given the numerical aperture and the magnification factor of the images of $M = 0.04$, the diffraction diameter of the particle images can be calculated using Equation (4.2) as $d_{\text{diff}} = 10.8\mu m$. This results in a ratio of particle image diameter to pixel diameter of 1.6, resulting in limited peak locking errors [124].

The images were acquired and processed using LaVision's DaVis 8 software. First, background removal was applied to the image pairs by subtracting a minimum time filter with a length of five images. Next, the image pairs were processed using a cross-correlation-based image interrogation algorithm with window deformation, with a window size of 64px and an overlap factor of 75%, resulting in a vector spacing of 2.1mm (0.004D). Finally, the resulting velocity fields were averaged over time. A total of 300 vector field images were acquired for each measurement plane. Given the rotational frequency of the rotor and acquisition frequency, this results in approximately 160 rotor revolutions.

The camera and laser systems were rigidly connected and mounted on a traversing system, as shown in Figure 8.2. This enabled a translation range in the streamwise and lateral direction of 1m and 1.5m, respectively. Hence, several FOVs were acquired and stitched together in post-processing without re-calibrating the acquisition system, as highlighted in Section 8.3.3.

8.3.3 Measurement cases

The wind tunnel was operated at a constant wind speed of U_∞ = 2.7 m/s. The rotational frequency of the rotor was maintained at ω = 49.95rad/s, resulting in a tip-speed ratio of $\lambda = \omega R/U_\infty$ = 5.55 and a diameter-based Reynolds number of 1.1×10^5. The time-averaged

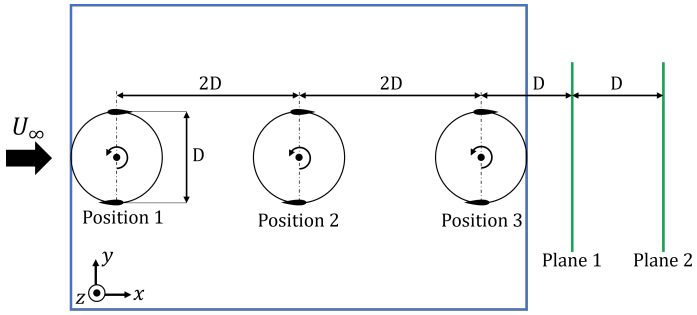


Figure 8.4: Top-view schematic of the experimental setup, with the coordinate system at the bottom left. The three positions of the X-Rotor on top of the OJF adjustable table are shown along with the normalized spacings. The two measurement planes, Plane 1 and Plane 2, are shown via green solid lines with their respective spacing. The rotor trajectories are shown via solid black lines, with the rotation direction marked. The blade profile sizes are exaggerated for clarity.

wake of the X-Rotor was measured using the aforementioned measurement system. The wake was measured at two streamwise positions, Plane 1 and Plane 2, as marked in Figure 8.4, which are separated by 1D from each other. The X-Rotor model was shifted between three positions (Positions 1, 2, and 3), each separated by 2D in the streamwise direction. This way, the wake is measured in the region of $1 \leq x/D \leq 6$ at increments of 1D, where the origin $x = y = z = 0$ is defined as the center of the tower and crossbeam structure, and the y and z directions are defined as lateral and axial, respectively.

As stated in Section 8.3.2, several fields-of-view were measured at a given streamwise plane by traversing the PIV system laterally (in the y-direction) using a traversing system, having an accuracy of $\pm$ 0.01mm. A total of four lateral planes were measured at a given height and streamwise wake position. Furthermore, different measurement heights (z-direction) are realized by adjusting the height of the table to which the rotor is mounted. A total of three heights were acquired for each streamwise wake position. An overview of the measurement planes at a streamwise location of x/D= 3 is shown in Figure 8.5 for the three pitch cases. The overlap between planes is approximately 74mm and 70mm in the lateral and axial directions, respectively. The measurement domain is more symmetric for the baseline pitch case $\beta = 0^\circ$, whilst those for the positive $\beta = 10^\circ$ and negative $\beta = -10^\circ$ cases are weighted more on the upper half of the rotor. This is to capture more of the momentum transfer above the rotor caused by the adjusted pitch on the upper blades, as highlighted in Chapter 7. The velocities in the overleaping regions of the individual measurement planes are treated using a weighted average.

8.3.4 Measurement uncertainty

Following the procedure in Chapter 4, Equation (4.1) is used to compute the expanded uncertainty ϵ of the velocity, where the coverage factor $z_a = 2$ and $N = 300$.

Across all pitch cases, the maximum uncertainty occurs at the most upwind measurement plane of $x/D = 1$ along the shear layer of the wake, consistent with the observations of [25]. The maximum standard deviation occurs for the lateral velocity component of the positive pitch case with $\sigma_y = 0.59$ m/s, resulting in an expanded uncertainty of $\epsilon_y = 0.07$

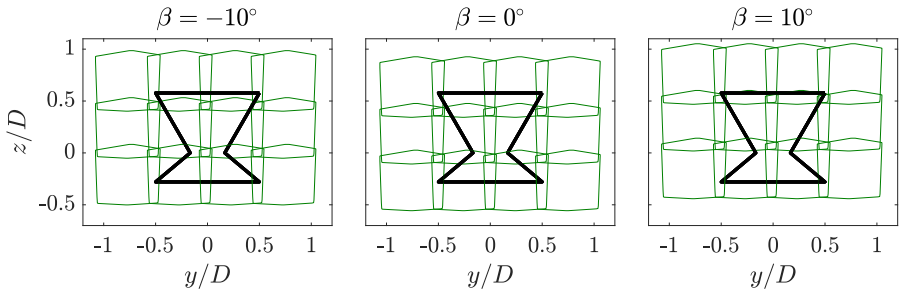


Figure 8.5: Measurement planes at a constant streamwise location x/D = 3 for the three pitch cases.

m/s.

The uncertainty of the streamwise vorticity component U_{ω_x} is computed using Equation (7.1), where ϵ is the standard uncertainty in either the lateral (ϵ_y) or axial direction (ϵ_z), the grid spacing of the interrogation window is denoted as d, and the $\rho(2d)$ is the cross-correlation coefficient of the spatially correlated velocities. Given the final interrogation window size of 64px and a scaling factor of 7.45 px/mm, d = 4.3mm. The cross-correlation coefficient is approximated to be $\rho(2d) \approx 0.45$ [159]. Using the maximum expanded uncertainty of ϵ_y = 0.07 m/s, the uncertainty of the streamwise vorticity is computed as U_{ω_x} = 11.9 s^{-1}. This value drops by a factor close to 10 outside the shear layer of the wake.

8.4 Results

8.4.1 Wake topology

The time-averaged normalized streamwise wake contours are shown in Figure 8.6 for the three modes. For the baseline case, the wake maintains the X-shape up to x/D = 1 as it is still expanding, consistent with the results shown in [134]. Further downwind, the wake features a lateral contraction near the upper and lower blade tips and expansion near the center of the crossbeam. Meanwhile, the wake is expanding axially above and below the rotor.

The negative pitch mode shows a distinctly different topology from the baseline case. The wake shape suggests a vertical stretch and lateral contraction of the wake compared to the baseline case. This deformation is consistent with that predicted in Section 8.2, with low momentum flow ejected axially whilst high energy free-stream flow is injected from the sides. An asymmetry in the deformation is evident, with the wake ejection favoring the windward side of the rotor. This is attributed to the intrinsically higher blade loading experienced by the blade during its windward passage, leading to asymmetric strengths and topologies in the streamwise vortices, discussed further in Section 8.4.3.

For the positive pitch mode, the wake exhibits a substantial deformation, with a large portion of the projected frontal area of the rotor subject to free stream flow. The wake contracts axially while being ejected laterally on the windward side of the rotor, similar to the results of [133]. Furthermore, this is consistent with the significant lateral thrust component shown in Table 8.1. This substantial downwash of the wake is consistent with

the movement predicted in Section 8.2. Once again, there is a notable asymmetry, with a larger downwash on the windward side of the rotor. As in the negative pitch case, this is due to the higher blade load on the windward passage. This asymmetry is linked to the streamwise vortex strength, discussed further in Section 8.4.3.

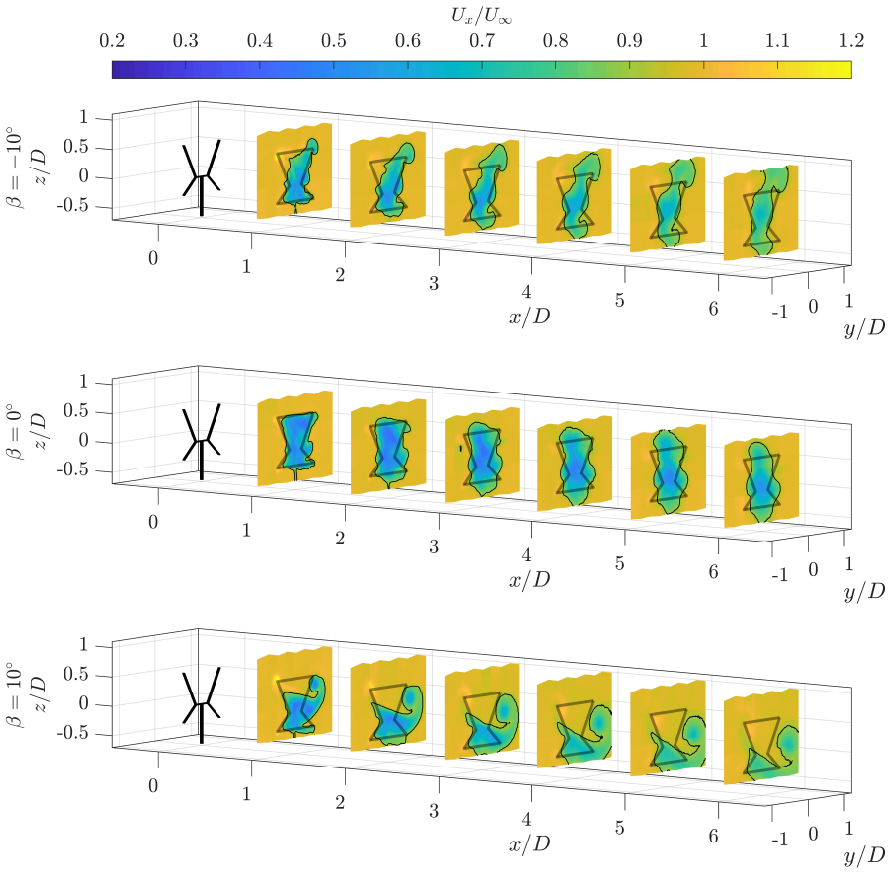


Figure 8.6: Normalized streamwise flow component (U_x/U_∞) at discrete cross-stream planes. The black solid line shows the frontal area of the rotor at an azimuth of 0° with a black contour line showing where U_x/U_∞ = 0.9. The scale in the streamwise direction is doubled to have the planes more spaced apart for observation.

To further quantify the wake deformation of the X-Rotor, the wake center, area, and perimeter are presented in Figure 8.7 and Figure 8.8, respectively. The wake center is computed using the "center of mass" approach in the lateral (y) and axial directions (z). This approach is widely accepted as an experimental method for tracking the wake center for VAWTs [21, 25], HAWTs [163], as well as low-order models [143]. At each streamwise measurement location, the wake center is defined as:

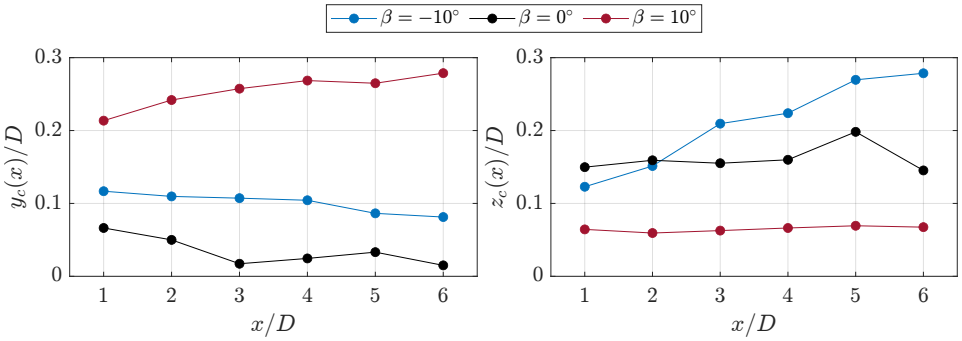


Figure 8.7: (Left) Normalized wake center development for the three pitch cases computed using Equation (8.5) in the lateral direction $y_c(x)/D$ and (right) axial direction $z_c(x)/D$.

$$y_c(x) = \frac{\int\int y\Delta U(x,y,z)\mathrm{dydz}}{\int\int \Delta U(x,y,z)\mathrm{dydz}}, \qquad z_c(x) = \frac{\int\int z\Delta U(x,y,z)\mathrm{dydz}}{\int\int \Delta U(x,y,z)\mathrm{dydz}}, \tag{8.5}$$

where $\Delta U(x,y,z) = U_\infty - U_x(x,y,z)$. The integrals are computed over the entire available measurement area at each streamwise location. The wake center development in the lateral and axial directions is plotted for each pitch case in Figure 8.7.

For the baseline case, a seemingly symmetric axial expansion of the wake is observed, while the lateral flow deficit is concentrated more on the windward side of the rotor. However, as the wake develops, the wake center moves towards the center. The axial movement of the wake center is minimal due to the aforementioned symmetry. The center of the wake sits around the geometric center of the rotor of $z/D = 0.15$.

For the positive pitch case, the wake center is laterally displaced towards the windward side of the rotor by a factor of approximately four compared to the baseline case at the most upwind measurement plane $x/D = 1$. This is consistent with the discussion above and the significant increase in the lateral thrust coefficient reported in Table 8.1. This lateral displacement increases as the wake evolves due to the strong advection imposed by the windward vortex, which moves laterally outward. In this case, the wake center's axial position remains constant at a lower position compared to the other two pitch cases. This can be attributed to the large-scale windward vortex, which remains above the crossbeam height.

Finally, in the negative pitch case, the wake center follows a similar trend to the baseline case in the lateral direction, with a systematically higher wake center towards the windward side of the rotor. Visually, this is consistent with the discussion above, where the wake is contracted and pushed more toward the windward side of the rotor. The axial location of the wake center steeply increases downstream as the wake is ejected out axially above the rotor in a non-symmetric fashion between the upper and lower halves of the rotor, unlike the baseline pitch case.

The wake area and perimeter for the different modes are shown in Figure 8.8. The wake boundary is defined as $U_x/U_\infty = 0.9$, as visualized by the black contour lines in Figure 8.6. The perimeter is computed by taking the sum of the Euclidean distances between the

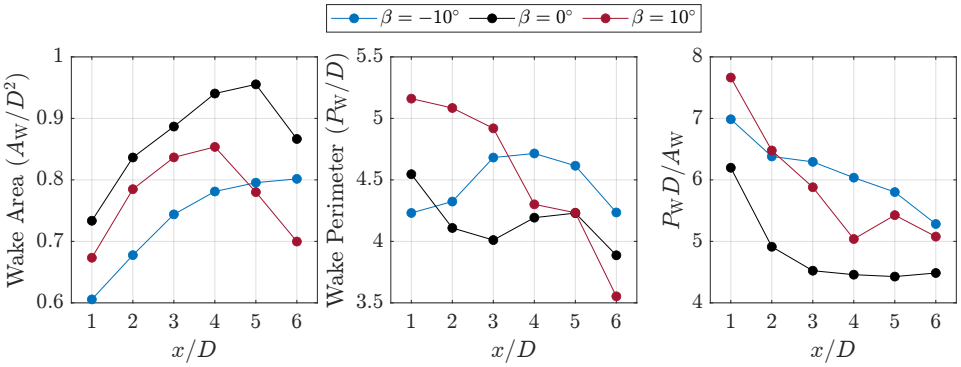


Figure 8.8: The normalized wake area A_W and perimeter P_W for the three modes of operation across all measurement planes. The ratio between the perimeter and area is shown in the final panel. The wake areas are defined as the boundary where $U_x/U_\infty = 0.9$, as visualized in Figure 8.6.

boundary coordinates. The work of [164] highlighted the importance of the ratio between the wake perimeter and area (P_W/A_W) towards the streamwise momentum recovery rate for an actuator surface of generic shape. This link has been numerically and experimentally observed for both HAWTs and VAWTs, where turbulent contributions towards the energy recovery in the wake are concentrated along the shear layer [37, 84].

The wake area for the three modes increases moving downstream. The baseline case exhibits systematically higher areas than the pitched modes of operation. The positive pitch case shows a local maximum at $x/D = 4$, which is an artifact of the wake movement outside the measurement domain, as shown in Figure 8.6. Similarly, the wakes for the negative and baseline cases begin to exit the measurement domain at $x/D = 5$. The negative pitch case exhibits the smallest areas across the measurement planes, presumably due to the lower streamwise thrust. In the near wake ($x/D \leq 3$), the positive pitch case has the longest perimeter, which decreases substantially at $x/D = 4$ as it leaves the measurement domain. The negative pitch case has a shorter perimeter only at $x/D = 1$ compared to the baseline case. As will be discussed in Section 8.4.3, the onset of the deformation induced by the streamwise vorticity system of the negative mode is delayed compared to the others as it relies on the loading of the downwind half of the rotor. The ratio between the perimeter and the wake area is a critical metric as discussed by [164], who established the linear dependence between P_W/A_W and the rate of streamwise momentum recovery. Both the negative and positive pitched modes of operation yield systematically higher magnitudes in this ratio, highlighting their favorable aptitude towards streamwise momentum recovery.

8.4.2 Available power

The turbine's frontal areas at the streamwise locations in the wake shown in Figure 8.6 visually suggest a significant increase in the high-momentum flow available for downstream turbines, which are in line with the upstream rotor. The available power in the wake is quantified at each cross-stream location using the coefficient of available power f_{AP}, expressed in Equation (9.6). A similar analysis has been performed by [85] and [25].

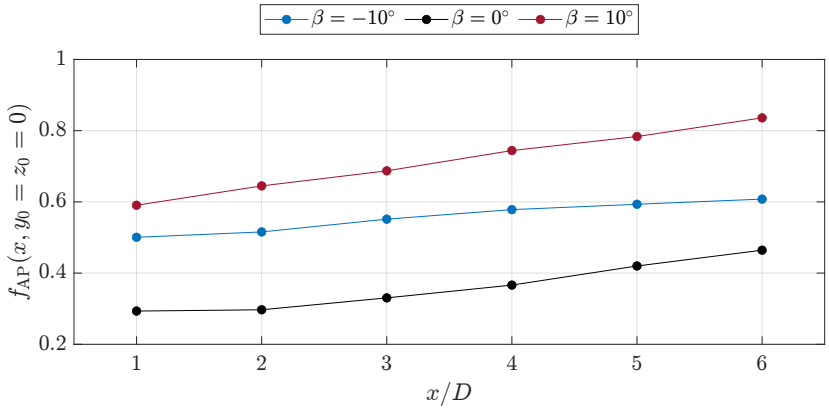


Figure 8.9: Available power for each of the pitch cases calculated using Equation (9.6) over the projected frontal area of the rotor on the measurement planes centered at the normalized lateral coordinate $y_0/D = 0$ (directly downstream without any lateral offset).

$$f_{AP}(x, y_0, z_0) = \iint_S U_x^3(x_0, y, z)/U_\infty^3 \mathrm{dzdy} \tag{8.6}$$

The ratio U_x^3/U_∞^3 is the available streamwise wind power at a given measurement plane x. The surface integrated value is taken within the protected frontal area of the rotor (S) centered at y_0, z_0. The available power coefficient across all measurement planes is shown in Figure 8.9 for each pitch case. The coefficient is computed over a frontal area centered at $y_0/D = z_0/D = 0$ (directly in line with the upstream rotor) for each case.

For the baseline case, the available power steadily increases as the wake develops due to the inherent recovery and diffusion. The available power increases by 58% between $x/D = 1$ and $x/D = 6$. Both of the wake control strategies increase the available power across all streamwise measurement locations. For the negative pitch case $\beta = -10^\circ$, the available power increases by 70% and 31% at $x/D = 1$ and $x/D = 6$, respectively, compared to the baseline case $\beta = 0^\circ$. The net increase between the two extreme measurement planes for the negative pitch case is 22%. Consistent with the previously discussed results, the positive pitch case $\beta = 10^\circ$ exhibits the higher recovery of available power in the wake between the two pitch cases. In this case, the coefficient increases by 103% and 83% at $x/D = 1$ and $x/D = 6$, respectively, compared to the baseline case $\beta = 0^\circ$. The net gain in available power of the positive pitch case is also higher than its negative counterpart, with an increase of 40% between the two extreme measurement planes.

To further understand potential optimal placements of downwind turbines that could have lateral offset to that upwind, the available power coefficient is computed with a sliding integration window and shown in the form of a contour plot in Figure 8.10 for each pitch case. Dashed and solid lines indicate the positions where $f_{AP} = 0.5$ and 0.75, respectively.

For the baseline case, the available power deficit is concentrated directly downstream of the rotor with a slight asymmetry, evident by the availability of $f_{AP} > 0.75$ across all downstream positions around y_0 = -0.4 on the leeward side. This asymmetry is consistent with the discussion in Section 8.4.1 and can be attributed to the asymmetric loading profile

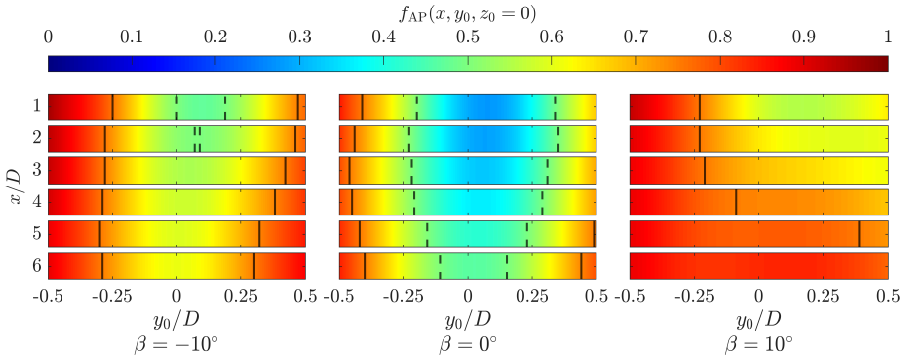


Figure 8.10: Available power distribution for each of the pitch cases integrated within the projected frontal area of the rotor (Equation (9.6)) centered at the normalized lateral coordinate y_0/D. Note that within a band for a given wake position x/D the values are constant, with no interpolation between measurement planes in the wake. The dashed and solid lines correspond to lateral positions where $f_{AP} = 0.5$ and 0.75, respectively.

of the rotor. This would suggest a favorable placement of a hypothetical downstream turbine on the leeward side of the rotor, consistent with the results of [25].

The negative pitch case exhibits a similar shape to the baseline case, with systematically higher coefficients in available power. In this mode, the wake is ejected out above the rotor, as discussed in Figure 8.7. As the control volume is not shifted in height ($z_0 = 0$), the available power deficit remains concentrated more directly downstream of the rotor. In this case, coefficients $f_{AP} > 0.75$ are available on both the leeward and windward sides of the rotor. Similar to the pitch case $\beta = 0°$, there is an asymmetry in the wake with a more significant deficit on the windward side. The recovery $f_{AP} > 0.5$ is realized across all lateral positions beyond x/D= 2, once again highlighting the wake recovery re-energizing potential of the negative pitch case.

Finally, the positive pitch case has shown the most significant potential for downstream turbines. In this mode, the wake is ejected out laterally towards the windward side of the rotor, as discussed in Figure 8.7. This is also evident by the available power perceived by potential downstream turbines, where the deficit is skewed towards centers positioned on the windward side, consistent with the results of [25]. Coefficients $f_{AP} > 0.75$ are available across all measurement planes on the leeward side of the rotor, starting at $y_0 = -0.24$ at x/D = 1. By x/D = 5, all possible locations feature $f_{AP} > 0.75$ across all leeward positions up to $y_0 = 0.38$ on the windward side. Unlike the negative pitch case, $f_{AP} > 0.5$ is realized across all measurement planes and lateral center locations.

8.4.3 Vortex system validation

The normalized streamwise vorticity system is presented in Figure 8.12 for all measurement planes. The most upstream measurement plane of x/D = 1 is isolated in Figure 8.11 for a comparison to the proposed vorticity system presented in Section 8.2. Selected vorticity structures are labeled with the corresponding quadrant in which they were generated based on Figure 8.1, with subscripts T, R, and B corresponding to those stemming from the top blade tip, root, and bottom tip, respectively.

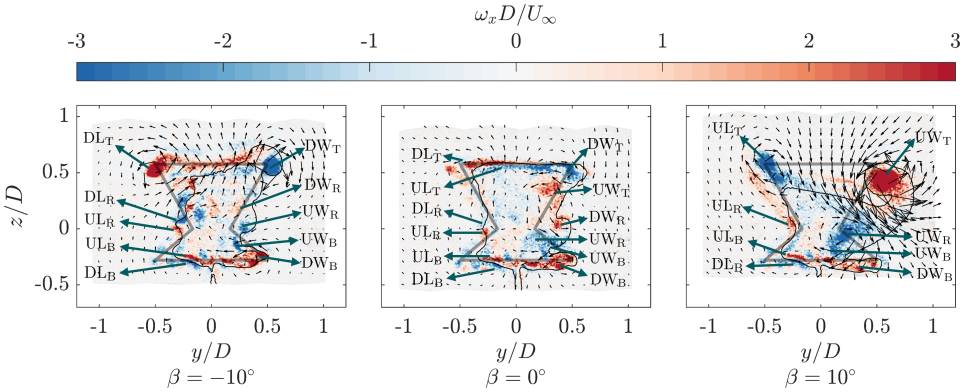


Figure 8.11: Normalized streamwise vorticity $\omega_x D/U_\infty$ at x/D = 1 for the three pitch cases. The black solid line shows the frontal area of the rotor at an azimuth of 0° with a black contour line showing where U_x/U_∞ = 0.9. The vectors show the in-plane velocity. The identifiable vortex structures are marked corresponding to Figure 8.1, with subscripts T,R, and B corresponding to structures generated by the top, root, and bottom blade.

Consistent with the results of [21, 25, 41], the streamwise vortex structures are generated predominantly at the blade tips according to Helmholtz's theorem. Given that the results are time-averaged, no coherent vortical structures shed by the blades are visible in the near wake at the baseline pitch case of $\beta = 0°$. Alternating patches of positive and negative vorticity stem from different quadrants due to the periodic changes in inflow conditions perceived by the blade [134]. These vortical structures diffuse rapidly in the wake, becoming almost indistinguishable beyond x/D = 3, as seen in Figure 8.12. The structures stemming from the upper blade tips are as hypothesized in Figure 8.1. The structures arising from the downwind quadrants (DW_T, DL_T) appear above those generated in the upwind quadrants (UW_T, UL_T) due to their direction of rotation, where the vortices about the periphery of the rotor induce an inboard and outboard velocity in the upwind and downwind halves, respectively. The structures stemming from the roots are weaker on the leeward half of the rotor compared to the windward half, consistent with the intrinsic asymmetric loading of a VAWT. The structures from the bottom blade tips mirror those in location and direction to the top blades, as hypothesized in Figure 8.1.

For the negative pitch case, a dominant CVP is visible due to the increased blade load and subsequent circulation on the downwind passage. These results are consistent with the theorized trailing vorticity system by [25] for a straight-bladed VAWT. However, as the X-Rotor is not symmetric and the bottom blades are not pitching, a complimentary CVP is absent on the bottom tips. The structure with positive vorticity on the leeward side of the rotor convects inward towards the center of the rotor whilst both migrate upward. The shift in load towards the downwind half energizes the streamwise vortices DL_T and DW_T. This CVP induces an upwash in the wake, evident by the in-plane vectors, while entraining free stream flow from the sides of the rotor. The in-plane vectors suggest a similar strength between the two structures, indicating a close to idealized balance between the DW and DL quadrants, as shown in Figure 8.1 and the minimal measured lateral thrust coefficient in Table 8.1. In the root region, both the UL and DL vortices have the same orientation as for the baseline pitch case. The DL_R shows a higher magnitude in vorticity compared to the

baseline case, consistent with the shift in load downstream as hypothesized in Section 8.2. On the windward side, the upwind vortex UW_R shows a similar magnitude to that of the baseline case, while that from the downwind half DW_R shows a notable decrease. This is a discordance with the expected behavior shown in Figure 8.1, suggesting a higher load produced on the lower blade compared to the upper blade when pitched. As the bottom blades are not pitched, the trailing vorticity system stemming from the bottom tips remains similar to the baseline pitch case.

The positive pitch case also shows a dominant CVP stemming from the upper blade tips in a mirrored direction to the negative case. This is consistent with the results of [101] and is due to the shift of rotor load towards the upwind half of the cycle. The vortex generated on the windward side of the rotor is larger and stronger than that on the leeward side. This is consistent with the load distribution among the UW and UL quadrants of the cycle, discussed in Section 8.2. The windward vortex moves down considerably towards the lower half of the rotor and outward laterally. Meanwhile, the leeward vortex remains close to the tip of the projected frontal areas, with slight movement in the same direction as the windward vortex. The vortex stemming from the UW quadrant (UW_T) has convected downward and laterally out, while that generated in the UL quadrant (UL_T) remains close to the blade-tip of the projected area. As described in Section 8.2, this CVP induces a significant downwash in the wake while convecting high-momentum streamwise flow from above the rotor and ejecting the wake out from the side. The in-plane vectors suggest that the UW_T is stronger than the UL_T, departing from the simplification made in Section 8.2 regarding the uniform load distribution in the upwind half of the rotor. This is further highlighted by the non-symmetric wake deformation, which favors the windward side. This is consistent with the load measurements presented in Table 8.1, where a significant lateral thrust is measured for the positive pitch case. Similar to the tip-vortices, the root vortices are also energized on the upwind passage on the windward (UW_R) and leeward side (UL_R). As hypothesized, these are in the opposing direction to that of the upper blade tip. Following the same reasoning as the tip vortex, the root vortex on the windward side is more dominant than that on the leeward side due to the asymmetric loading between the upwind quadrants. Finally, the trailing vorticity stemming from the bottom blade tips remains similar to the baseline pitch case $\beta = 0^\circ$ as these blades are not pitched. On the windward side, the vorticity stemming from the UW quadrant (UW_B) has merged with the root vortex UW_R as they are co-rotating.

8.4.4 The role of the dominant CVP

The hypothesized vortex system was verified in Section 8.4.3 and linked to the wake deformation presented in Section 8.4.1. This section demonstrates the strong dependence between the dominant CVP observed for the pitched modes of operation and their modes of recovery using the simplified point vortex model described in Section 8.2.

First, the vortex cores are evaluated for the two pitched cases at all downstream locations, shown in Figure 8.13. The cores are identified using the maxima Γ_1, as introduced by [152]. Previous studies have used this method [85] for vortex tracking of wind-tunnel scale wind turbine models. The arrows indicate the direction of motion of the vortex cores between the measurement planes. Consistent with the observations in Figure 8.12, the windward vortex of the positive pitch case moves the most in the downward and outward

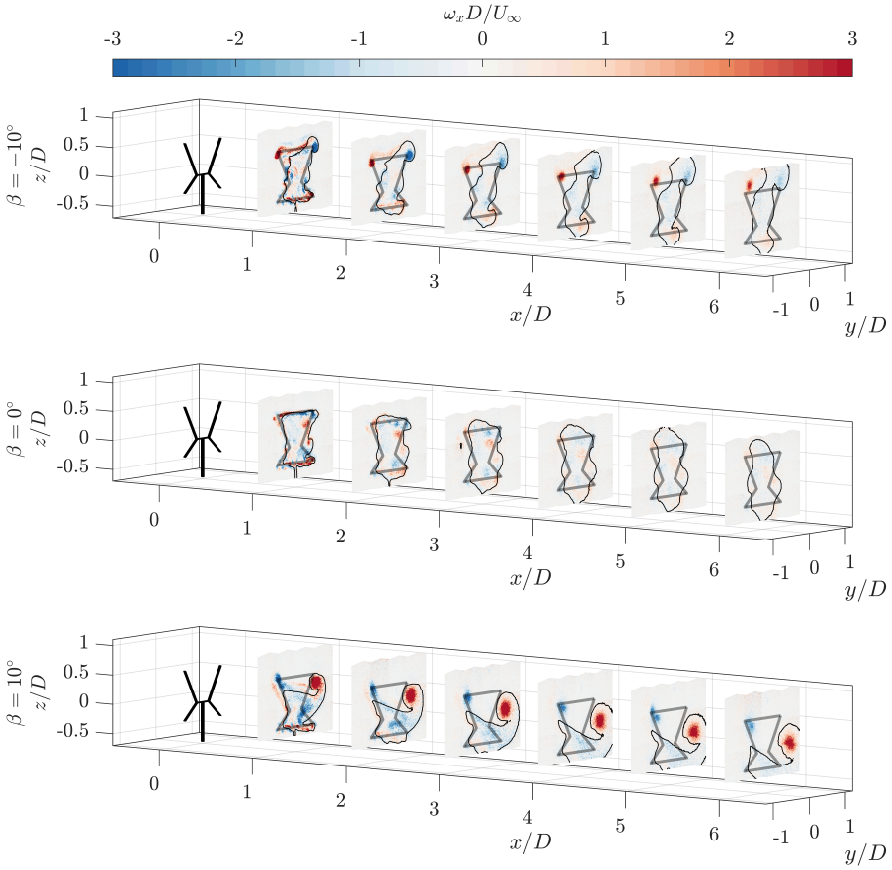


Figure 8.12: Normalized streamwise vorticity component ω_x at discrete cross-stream planes. The black solid line shows the frontal area of the rotor at an azimuth of 0° with a black contour line showing where U_x/U_∞ = 0.9. The scale in the streamwise direction is doubled to have the planes more spaced apart for observation.

8

direction. The lateral deflection of this vortex is consistent with the high lateral load of the rotor resulting from the heavily loaded UW quadrant. Similarly, the leeward vortex moves downward and toward the center of the rotor. For the negative pitch case, the directions of rotation of the vortices are mirrored with respect to the positive case, as seen in Figure 8.12. With the flipped direction of the CVP, the windward and leeward trailing vortices convect above the rotor. The displacement, however, is not as large as in the positive pitch case due to the lack of a strong lateral force component of the rotor in this mode of operation.

Next, the circulations of the tip-vortices are shown in Figure 8.13-right, computed by taking the outline of the vortex core where $\Gamma_2 = 2/\pi$, as defined by [152] and using the surface integral approach denoted in Equation (6.5). Across all cases, the circulation decreases slightly when progressing further downstream due to turbulent diffusion, but is conserved for the most part due to the low inflow turbulence. Consistent with the induced

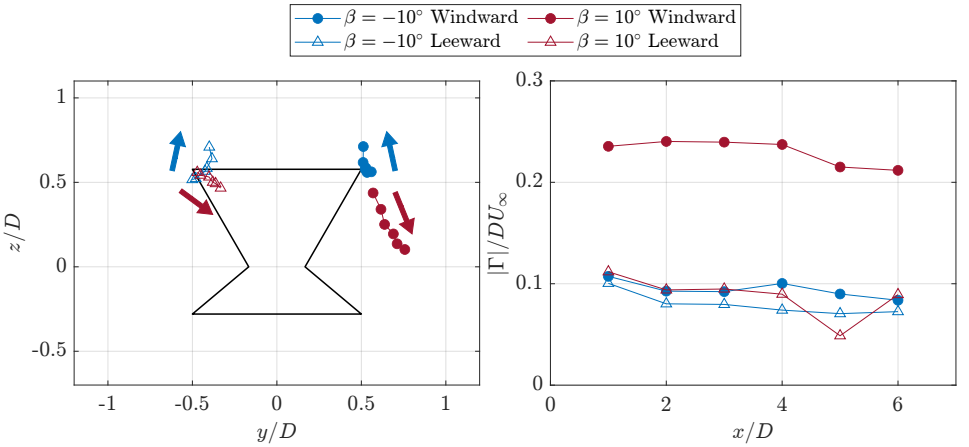


Figure 8.13: (Left) Trajectories of the dominant CVP cores for each pitch case. The arrows show the direction of movement of the vortical structures in the wake. (Right) Evolution of vortex circulation magnitude integrated over patches identified using the Γ_2 defined by [152]. Circle and triangle markers correspond to the structures generated on the windward and leeward sides, respectively.

in-plane velocities discussed in Section 8.4.3, the circulation of the windward vortex of the positive pitch case is the largest, around 2.5x greater than the rest, whilst that from the leeward side averages around $|\Gamma|/U_\infty D = 0.1$. The strengths of the vortices of the negative pitch case are similar in magnitude across all measurement planes around $|\Gamma|/U_\infty D = 0.1$. However, those stemming from the windward side of the rotor are systemically higher due to the asymmetric loading of the rotor.

The maximum streamwise vorticity magnitude of the vortex core $\max|\omega_x|D/U_\infty$ is shown in Figure 8.14 for the two pitch cases. Due to diffusion, the maximum magnitude decreases further downstream in the wake. For the positive pitch case, the trailing vortex from the windward side has a higher peak vorticity magnitude across all measurement planes, consistent with the topology shown in Section 8.4.3. Meanwhile, the opposite is true for the negative pitch case, where beyond the $x/D = 2$ wake position, the leeward side vortex demonstrates a larger maximum vorticity magnitude than the windward side. This is visually consistent with the topology shown in Section 8.4.3, where the leeward vortex remains more constant in size and strength, while that on the windward side diffuses. The magnitude of these two structures stabilizes to a constant value beyond $x/D = 2$ around $\max|\omega_x|D/U_\infty = 4$ and 1.7 for the leeward and windward vortex, respectively.

Finally, $\eta(x)$ is the viscous length scale of the vortex defined by [165] as the integral of the eddy viscosity. This length scale is used to quantify how a vortex spreads over time due to diffusion, as demonstrated by [85]. A similar approach is taken as the aforementioned work by considering the dominant CVP for the vortex generator cases as idealized Lamb-Oseen vortices, defined as [166]:

$$\omega_x(x,y,z) = \frac{\Gamma}{4\pi\eta^2(x)} \exp\left(-\frac{r^2}{4\eta^2(x)}\right), \tag{8.7}$$

where Γ is the circulation of the vortex, $r^2 = (y-y_c)^2 + (z-z_c)^2$ is the radial location

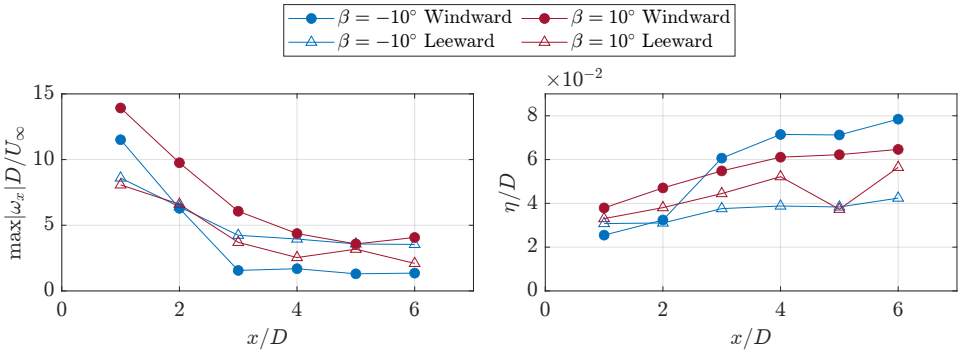


Figure 8.14: (Left) Evolution of the maximum normalized streamwise vorticity magnitude $\max|\omega_x|D/U_\infty$ at the vortex core. (Right) The normalized viscous length scale η/D as a function of downstream position. The definition is given along with Equation (8.7).

from the vortex core, with y_c, z_c defined as vortex cores, shown in Figure 8.13. In this work, the length scale is solved for by rearranging Equation (8.7) as:

$$\frac{\omega_x(x,y,z)}{\Gamma(x)} = k(x)\exp\left(-r^2 k(x)\pi\right), \tag{8.8}$$

where $k(x) = 1/(4\pi\eta^2(x))$, and $\Gamma(x)$ is the circulations of the vortex cores as presented in Figure 8.13. The curve-fitter tool in MATLAB is used with this pre-described relation to evaluate the constant k given the experimental distributions of streamwise vorticity about the dominant CVP cores using a non-linear least-squares approach. An overview of the curve-fitted distributions is shown in Appendix C.1. Given the $k(x)$ values from the curve-fitting procedure, the viscous length scale can be calculated as a function of downstream location for each of the dominant CVP as $\eta = \sqrt{1/(4\pi k)}$. The normalized length scale is shown in Figure 8.14 for each of the dominant vortices as a function of downstream location. The diffusion rates of the windward and leeward vortices of the positive and negative pitch cases are similar. The leeward vortex of the negative pitch case has the lowest length scale, consistent with its shape and strength shown in Figure 8.12. Meanwhile, the diffusion of the windward vortex for the negative pitch case demonstrates a large jump in magnitude between $x/D = 2$ and $x/D = 3$, consistent with the contours shown in Figure 8.12. The leeward vortex for the positive pitch case has an outlier at $x/D = 5$ due to the outlier in the input circulation, shown in Figure 8.13.

With the vortex core locations, circulations, and viscous length scale defined, the axial induced velocity of the dominant CVP can be calculated using Equation (8.3). The distribution of $U_z(y,z)$ as a function of downstream plane at the height of the blade tips $z/D = 0.58$ is presented in Figure 8.15. The solid and dashed lines correspond to the experimentally measured and analytically obtained results for the two pitch settings.

The distributions between the experimental and analytical curves for the negative pitch case have a good match across all downstream planes. Up to $x/D = 4$ the flow close to the leeward vortex is consistent between the two, reaching percentage differences of approx. 4% of the free stream flow. The flow close to the windward vortex remains in

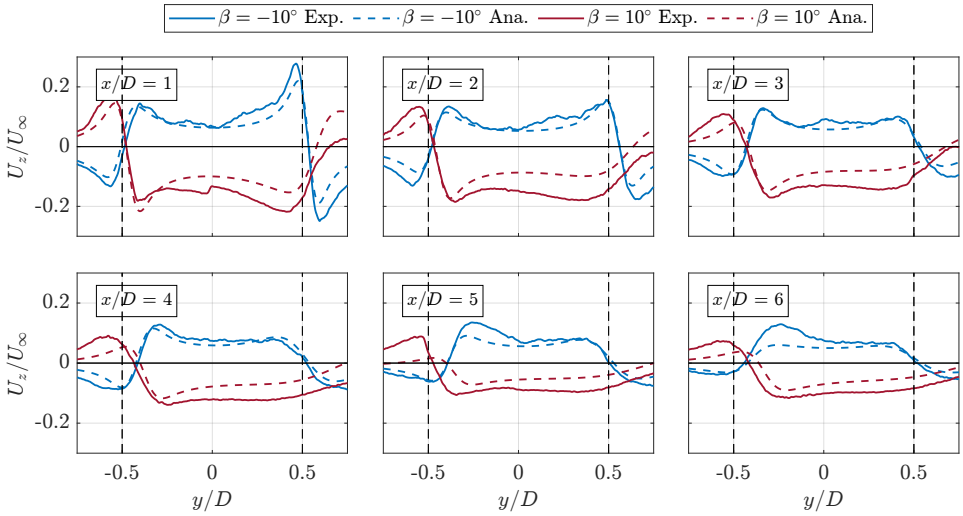


Figure 8.15: A comparison of the experimental (solid line) and analytical (dashed) axial velocity distribution U_z/U_∞ at $z/D = 0.58$.

good agreement throughout the wake, suggesting an accurate quantification of the vortex circulation and diffusion rate, with differences around 1%. The average differences within the bounds of the projected frontal area of the rotor, denoted by the dashed black lines, range from 1% to 3% of the free stream flow at $x/D = 3$ and $x/D = 6$, respectively.

The positive pitch distributions show higher discrepancies from the analytical model compared to the aforementioned case. There is a closer agreement on the leeward side of the rotor within the area of the rotor before gradually deviating towards the windward side. A large discrepancy is visible at $x/D = 5$, again due to the outlier in vortex circulation as discussed concerning Figure C.1. The average difference in velocity normalized by the free stream component ranges from 6% to 3% at $x/D = 2$ and $x/D = 6$, respectively. The disagreements between the curves when approaching the windward side of the rotor can partly be attributed to the quality of the curve-fitted values and the neglect of the root vortex when predicting the induced flow. As shown in Figure 8.11, the root vortex from the upwind windward passage for the positive pitch case is more dominant than the negative pitch operation mode. A further consideration is the importance of the three-dimensionality of the flow of a VAWT, which is further magnified when the blades are pitched. The windward vortex for the positive pitch case convects the most, as highlighted in Figure C.1. The resulting misalignment between the vortex core and measurement plane is a common feature in experimental studies of helicopter aerodynamics [167, 168]. A correction angle is applied based on the swirl and out-of-plane flow derivative component, which is not measured in this study. Nonetheless, the predicted axial flow components at the top of the rotor match well with the experimental results, highlighting the importance and dominance of the main CVP towards the wake deformation and deflection and, in turn, the momentum recovery.

8.4.5 Mean kinetic energy replenishment

Thus far, the ability of the modified vortex system to entrain high-energy flow in the wake has been discussed through qualitative observation in Section 8.4.1 and the increase in available power in Section 8.4.2. However, the main contributions towards this streamwise recovery have yet to be quantified. Previous studies have used the mean kinetic energy (MKE) equation to isolate the advective and turbulent contributions towards the wake recovery [37, 67, 144]. The MKE equation is written as [144]:

$$\underbrace{\overline{U_j}\frac{\partial K}{\partial x_j}}_{\mathrm{A}} = \underbrace{-\frac{\partial(\overline{u_i'u_j'}\overline{U_i})}{\partial x_j}}_{\phi}\underbrace{-\frac{\overline{U_i}}{\rho}\frac{\partial \overline{P}}{\partial x_j}}_{\mathrm{P}}+\underbrace{\overline{u_i'u_j'}\frac{\partial \overline{U_i}}{\partial x_j}}_{\epsilon} \tag{8.9}$$

where $K = \frac{1}{2}(\overline{U_x^2}+\overline{U_y^2}+\overline{U_z^2})$ is the mean kinetic energy and $\overline{P}$ is the mean static pressure. The overbars and primes denote time-averaged and fluctuating quantities. The time-dependent term ($\partial\overline{U_i}/\partial t$) is omitted as the results are time-averaged. Furthermore, as in the works of [25, 85], the viscous term is omitted given the sufficiently high Reynolds number. The terms are grouped by A, ϕ, P, and ϵ, which correspond to terms regarding the advection of MKE, the turbulent flux of MKE, work due to the mean pressure field, and the dissipation of MKE via turbulence, respectively. The MKE equation is further simplified and expanded as follows:

$$\underbrace{\overline{U_x}\frac{\partial K}{\partial x}}_{A_x} = \underbrace{-\overline{U_y}\frac{\partial K}{\partial y}}_{A_y}\underbrace{-\overline{U_z}\frac{\partial K}{\partial z}}_{A_z}\underbrace{-\frac{\partial(\overline{u_i'u_j'}\overline{U_i})}{\partial x_j}}_{\phi}+\underbrace{\overline{u_i'u_j'}\frac{\partial \overline{U_i}}{\partial x_j}}_{\epsilon} \tag{8.10}$$

where the MKE advection terms A is split in each direction x, y, z. As the pressure was not measured in this study, it is omitted from the subsequent analysis. The terms are arranged such that the contributions towards the streamwise advection of MKE are isolated, as done in the studies of [25, 67]. The terms of Equation (8.10) are presented as contour plots at a cross-stream position of $x/D = 3$ for the three fixed-pitch cases in Figure 8.16. The in-plane spatial derivatives $\partial/\partial y$ and $\partial/\partial z$ are calculated using a second-order central difference scheme. Similarly, the term including the streamwise gradients ($\partial/\partial x$) is approximated using a second-order central difference scheme across all measurement planes. Given the rearrangement of the terms in Equation (8.10), red and blue in Figure 8.16 are sources and sinks in streamwise MKE contribution.

As the negative pitch case has a lateral contraction and axial expansion of the wake, the wake perimeter shows shades of red and blue for A_y and A_z, respectively. This implies an influx of energy from the sides of the rotor, which contributes to an increase in streamwise MKE A_x, whilst the wake is being ejected out axially, leading to a decrease in A_x above the rotor. Conversely, the axial advective term A_z for the positive pitch case shows a large red region at the top of the wake, where the free stream flow is injected into the wake. Meanwhile, blue-shaded regions are concentrated on the bottom of the wake as local MKE decreases outside the rotor surface. The lateral advective component A_y is predominantly negative in the wake area as flow is ejected out, with a red region visible close to $y/D = 1$ coinciding with the core. Nonetheless, the magnitude of K injected axially dominates

the net effect within, as seen by the A_x contour. The baseline pitch case exhibits similar behavior to the negative pitch case, with a lateral contraction near the upper and lower blade tips, leading to a red A_y distribution. Unlike the negative case, the root region shows a local expansion with a blue region. Meanwhile, the A_z shows a concentration of blue at the top and bottom of the rotor as the MKE of the free stream flow is slowed by the ejected wake. The net effect on the streamwise MKE term A_x is similar to that of the negative pitch case, with regions of increased streamwise advection along the lateral perimeter of the wake and decreases above the rotor.

The turbulent flux of MKE ϕ is concentrated along the wake perimeters. [25] observed similar trends for an H-type VAWT, which is due to the turbulent mixing within the shear layer. Although the magnitudes are lower than the advective MKE terms (A), this highlights the importance of increasing the wake perimeter for accelerated MKE recovery, as discussed in Section 8.4.1. Similarly, the dissipation of MKE due to turbulence ϵ is concentrated along the shear layer of the wake perimeter. These are an order of magnitude lower than the other terms due to the low inflow turbulence and hence play a minor role in the wake recovery process.

To condense the relative contributions of the aforementioned distributions to a single number for the three cases across all measurement planes, the spatial average within the projected rotor frontal area of each term from Equation (8.10) is shown in Figure 8.17. Additionally, a residual term is included, where Residual = $\mathrm{A} + \phi - \epsilon$, in accordance with Equation (8.9).

Consistent with the contours shown above, the dominant term for the negative pitch case is A_y as flow is injected from the sides of the rotor. Meanwhile, the dominant term for the positive pitch case is A_z as flow is injected from above the rotor plane. A gradual increase is evident in the streamwise advection of MKE for the baseline case. In the near wake, $x/D \leq 3$, the negative pith case has higher magnitudes than the baseline case, reaching a maximum of $D/U_\infty^3 < \overline{U_x \partial K/\partial x} >= 0.01$, before decreasing. This is likely due to the rapid diffusion of the windward vortex and plateau in maximum vorticity, as discussed in Section 8.4.4. Meanwhile, the positive pitch case shows a steadily high magnitude of $D/U_\infty^3 < \overline{U_x \partial K/\partial x} >= 0.02$.

Finally, the flux of MKE is evaluated using a control volume approach, with a schematic of the volume shown in Figure 8.18. The control volume lateral surfaces on the windward and leeward sides are denoted as S_3 and S_4, respectively. Finally, the bottom and top control surfaces in the axial direction of the control volume are denoted as S_5 and S_6, respectively. The top and bottom surfaces are taken at the heights of the upper and lower blade tips $z/D = 0.58$ and $z/D = -0.28$, respectively. The lateral surfaces are taken at the edges of the projected frontal area of the rotor, $y/D = \pm 0.5$. Note that the surface normals to the inflow and outflow of the volume (S_1, S_2) are not evaluated.

Upon taking the volume integral of Equation (8.10), the divergence theorem can be applied to rewrite the terms to a surface integral form [144]. This is simplified as velocity components tangent to the control volume surfaces do not contribute to the flux. Furthermore, as the streamwise component is the dominant contributor towards the MKE ($U_x \gg U_y$ and U_z), the subsequent analysis focuses on the streamwise budget, as done in [67]. Hence, the fluxes through the lateral and axial surfaces S as denoted in Figure 8.18 can be expressed as:

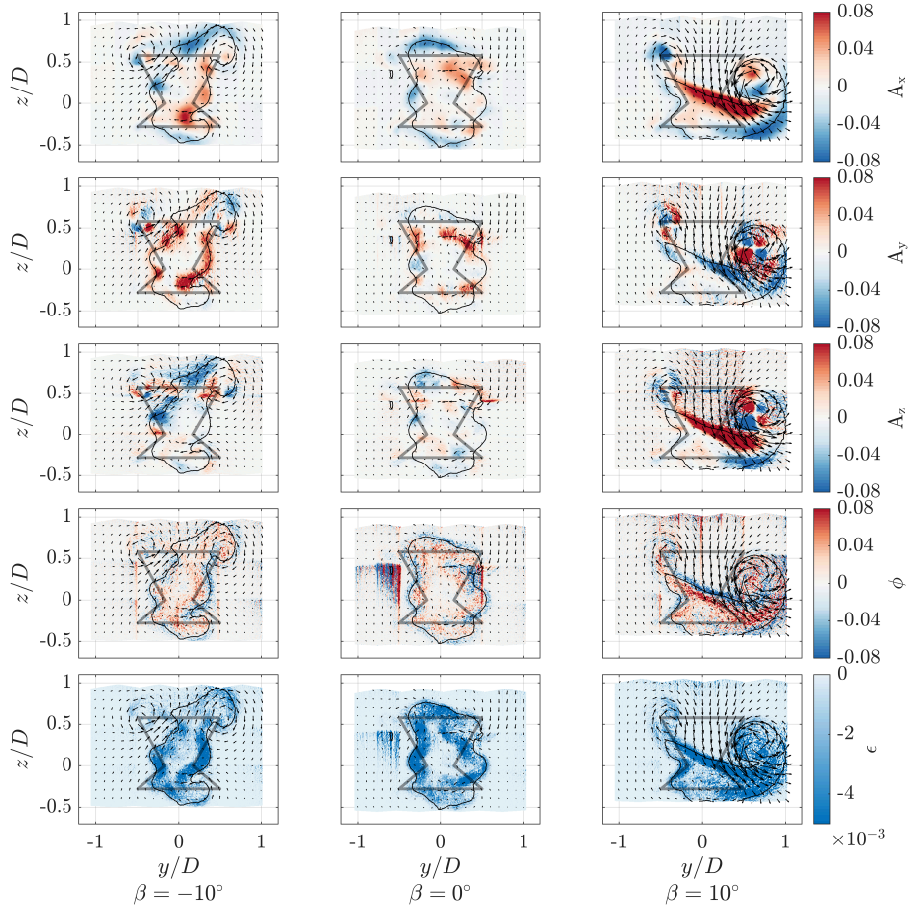


Figure 8.16: Spatial distributions of the terms in Equation (8.10) for the three modes of operation at $x/D = 3$. All terms are normalized by D/U_∞^3, and the vectors correspond to the in-plane velocity vectors. The projected frontal area of the rotor and wake perimeter at $U_x/U_\infty = 0.9$ is shown via a gray and black line, respectively.

$$\text{Surface 3} : \iint_{S_3} \overline{U_x}\left(0.5\overline{U_y U_x} + \overline{U_x' U_y'}\right) dS \tag{8.11}$$

$$\text{Surface 4} : -\iint_{S_4} \overline{U_x}\left(0.5\overline{U_y U_x} + \overline{U_x' U_y'}\right) dS \tag{8.12}$$

$$\text{Surface 5} : -\iint_{S_5} \overline{U_x}\left(0.5\overline{U_z U_x} + \overline{U_x' U_z'}\right) dS \tag{8.13}$$

$$\text{Surface 6} : \iint_{S_6} \overline{U_x}\left(0.5\overline{U_z U_x} + \overline{U_x' U_z'}\right) dS \tag{8.14}$$

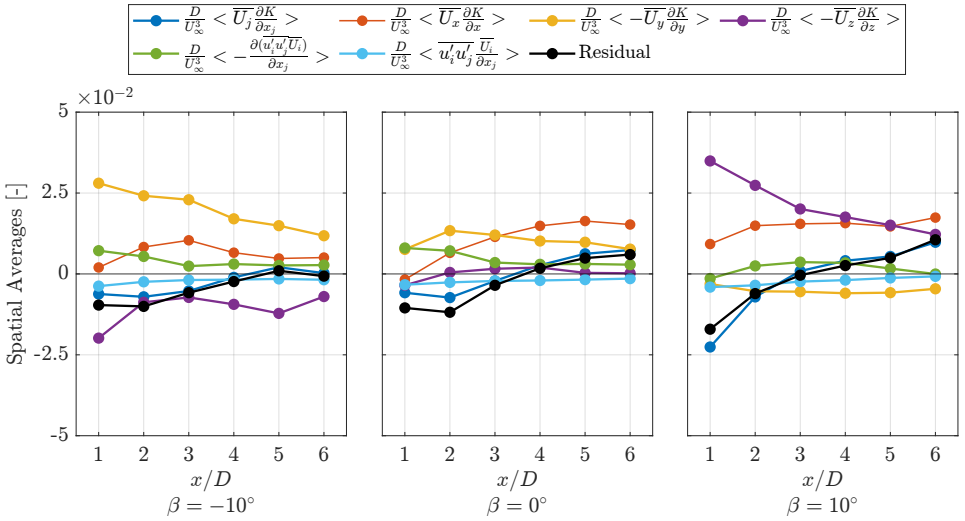


Figure 8.17: Section averaged term from Equation (8.10) for the three pitch cases across all measurement planes. Note that the sum of the advective flux terms A is shown along with the discretized terms in x, y, z. All terms are normalized by D/U_∞^3.

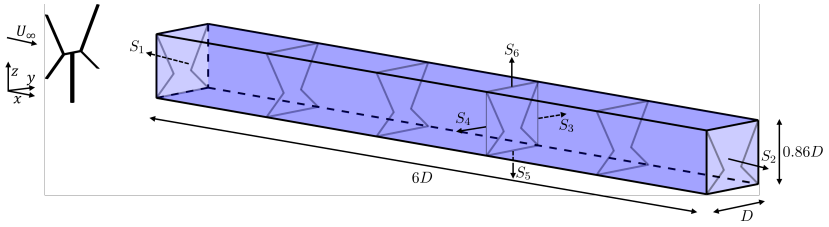


Figure 8.18: Schematic of the finite length control volume encapsulating the rotor frontal area (grey solid lines). The control volume surfaces (shaded blue) are denoted with S_i where i indicates the surface number (ranging from 1 to 6). The size of the control volume is denoted by the diameter normalized length, with the respective coordinate system provided and the mean flow direction indicated.

Positive and negative magnitudes correspond to flux outside and inside the control column, respectively. The distribution of the flux terms across each surface as defined is shown in Figure 8.19. The translucent lines are the distributions across each measurement plane, while the solid thick lines are the mean across each wake position. The vertical and horizontal black dashed lines denote the edges of the control surface, as defined by the maximum edges of the projected frontal area of the rotor. The sums are normalized by the free stream flow component.

The baseline case exhibits a negative flux along the upper surface S_6 due to the expansion of the wake. There is minimal flux across the bottom surface S_5 given the lack of a dominant CVP. A small negative flux is evident on both lateral surfaces of the control volume (S_3,S_4), signifying an injection of free stream flow within the volume. The magnitudes are higher on the windward side (S_3) of the rotor due to the asymmetric load profile and subsequent

trailing vorticity system, highlighted in Section 8.4.3. Furthermore, the mean curves demonstrate higher peak flux magnitudes on the upper half rotor on both the windward and leeward sides. This mode of operation is consistent with the wake topology in Figure 8.6, where a substantial area of the wake is axially contracted while expanding in the lateral direction, and some thinner regions of wake deficit are expanding above and below the frontal of the rotor, forming a "peanut" shape.

The negative pitch case demonstrates a dominant positive flux along the upper surface S_6, consistent with the large upwash induced by the CVP. Beyond the frontal area, the flux reverses when crossing the vortex cores. The maximum magnitude of the average flux is higher on the leeward blade tip (S_4), consistent with the accelerated diffusion of the windward vortex shown in Figure 8.14. The magnitudes are lower along the bottom surface S_5, following a similar distribution to the baseline case. The fluxes on the lateral surfaces follow a similar trend to the baseline case with higher magnitudes. On the windward surface S_3, the injection of flow is highest on the upper half of the rotor due to the dominant CVP. Near the root region, the magnitude is also higher than the baseline case due to the modification of the root vortex, as discussed in Section 8.4.3, before overlapping again with the baseline case beyond the lower blade tip. On the leeward surface S_4, the flux reaches a peak magnitude near the upper blade tip due to the strong trailing vortex, before steadily decreasing in magnitude towards the lower surface.

Finally, the positive pitch case exhibits a significant negative flux along the upper surface S_6 of the control volume due to the injection of free stream flow in the wake induced by the dominant CVP. On the bottom surface S_5, the average flux remains positive beyond the blade tip on the windward side due to the significant movement of the vortex as highlighted in Figure 8.13, exposing the wake to a consistent downwash. Conversely, the distribution of flux near the leeward tip on the bottom surface is similar to the aforementioned pitch cases due to the lack of a dominant CVP and asymmetric load profile. On the windward surface S_3, the flux is predominantly positive as the wake is ejected out of the control volume. The cross-stream specific curves show a gradually decreasing maximum magnitude, which occurs lower in the rotor as the wake progresses and the tip-vortex convects downward. On the leeward surface S_4, the flux remains positive as the wake expands laterally, with larger magnitudes concentrated along the upper half of the rotor due to the induction of the tip-vortex.

Given the lack of volumetric data and the large spacing between the measurement planes, the surface integrals for the axial and lateral surfaces cannot be computed. Instead, a line integrated value across the surfaces of the projected frontal areas of the rotor is presented in Figure 8.20. The line integrals are computed along the defined surfaces, with lengths of D for S_5 and S_6, and $0.86D$ for S_3 and S_4. These boundaries correspond to the dashed boundaries shown in Figure 8.19. The trends confirm the mechanism highlighted above, where the major sources of MKE flux are through the upper surface S_6. The positive and negative pitch cases exhibit an increased flux by factors of 20 and 10, respectively, compared to the baseline case at $x/D = 1$. Meanwhile, along the bottom surface (S_5), minimal deviations from the baseline case are present, as discussed above. Consistent with the distributions shown in Figure 8.19, the positive pitch case shows a gradual increase of MKE flux starting at $x/D = 4$ as the induced downwash of the downward convecting tip vortex becomes prevalent. Unlike the top and bottom surfaces, the lateral surfaces (S_3

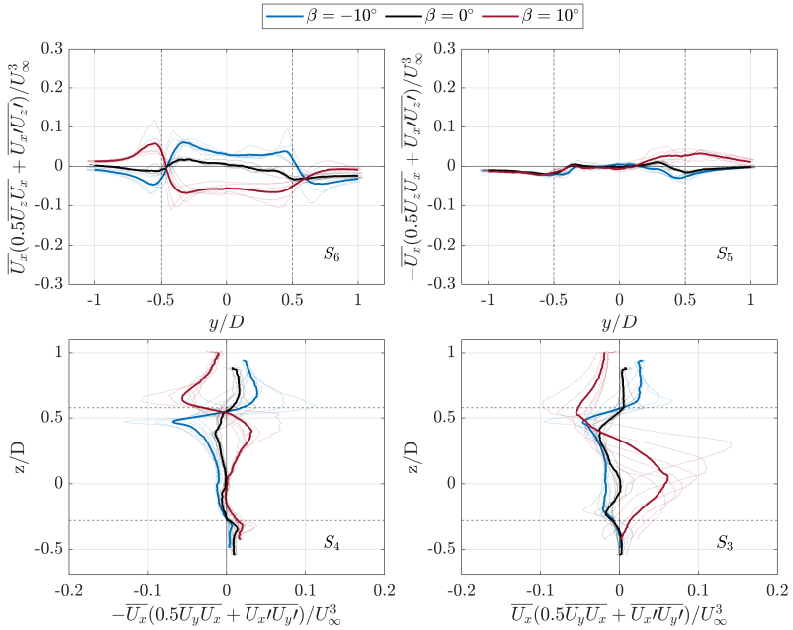


Figure 8.19: Axial and lateral components of the time-averaged streamwise MKE equation shown in Equation (8.9) for the three pitch cases, normalized by the freestream flow component. The translucent lines show the distributions along the control volume surfaces at each measurement location in the wake, and the solid thick line shows the mean across all positions. The vertical and horizontal black dashed lines show the edges of the control volume, as shown in Figure 8.18. The labels towards the bottom right of the figures correspond to the control surfaces.

and S_4) demonstrate similar magnitudes in flux for each pitch case. Both the negative and positive pitch cases show the largest differences in flux in the near wake before gradually converging. The positive pitch case demonstrates larger differences up to $x/D = 4$ due to the significant difference in circulation of the CVP.

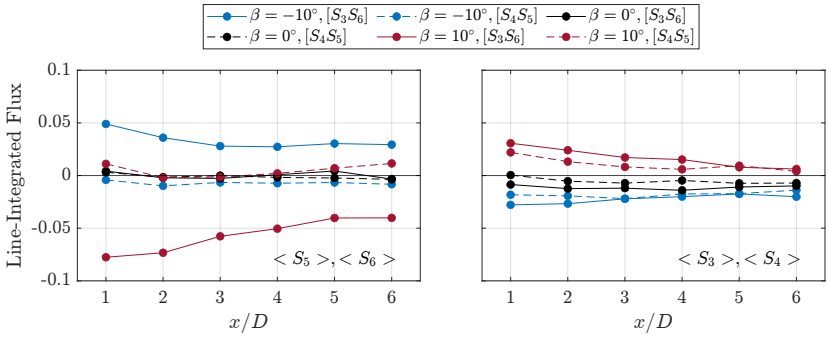


Figure 8.20: Line integrated MKE flux through the respective surfaces shown in Figure 8.18 for each pitch case, with (left) showing the axial surfaces and (right) the lateral. The solid and dashed lines correspond to the bottom axial surface and leeward side, $[S_5, S_4]$, and top axial and windward side $[S_6, S_3]$, respectively. The line integrals are normalized by the product of the free stream velocity and length of the integration domain, $U_\infty^3 L_{a,l}$, where the subscripts a and l refer to the axial and lateral surface lengths, respectively. In this case, $L_a = D$ and $L_l = 0.86D$.

8.5 Conclusions

This study presents cross-plane stereoscopic PIV measurements of the wake of the X-rotor VAWT using the "vortex generator" wake control strategy using passive blade pitch, elucidating the distinct wake deflections and deformations attributable to the streamwise vorticity field.

The available power coefficient for hypothetical in-line turbines shows a systematically higher available power across all measurement planes for the pitched modes compared to the baseline case. The positive pitch case yields the highest potential with an increase as high as 117% at $x/D = 2$, compared to an increase of 74% at the same measurement plane for the negative case. Furthermore, the available power coefficient for downstream rotors with lateral offsets highlights the asymmetry in the wake, with a potential for higher power on the leeward side of the rotor for all pitch cases. The authors reiterate that the power penalty associated with the pitched turbine was not measured. Hence, the balance between power lost by the rotor and gained in the wake is not evaluated. Nonetheless, these results demonstrate a proof-of-concept of the vortex generator mode for X-Rotor and the possible potential of its application on a farm scale.

The trailing vortices system is hypothesized using the AC theory and verified using the experimental results. The baseline pitch case shows minimal wake deformation due to the lack of dominant CVP pairs in the wake. A dominant CVP is formed on the upper blade tips which injects high-speed flow from above the rotor into the wake while ejecting low-speed wake out from the side when pitching the blades inward. Conversely, when pitched outward, the dominant CVP draws high-speed flow from the sides of the rotor while ejecting the wake axially upward. As only the upper blades are pitched, the CVP is formed only on the upper half of the rotor, while the trailing vorticity system stemming from the bottom blades remains similar between the three pitch cases. The strengths of the root vortices are also modified when pitching the upper blade tips, as they are a function of the circulation balance between the upper and lower blades. However, in the context of the wake topology modulation, these play a minimal role compared to the dominant

CVP upper blades. The experimentally derived circulations, trajectories, and diffusion rates of the dominant CVP stemming from the upper blades are used to model the axial flow component above the rotor using a simple point-vortex approach. The predicted distributions match very well with the experimental values, highlighting the dominance of the modified trailing vorticity on the wake recovery modes.

An analysis of the contributions of each term from the MKE equation further highlighted the differences between the different pitch cases. The contributions of the transport of MKE due to turbulence were minimal for the pitched cases compared to advective terms, highlighting the dominance of the advective process of the trailing vortices on the wake recovery mechanisms of the X-Rotor. A spatial average of the terms within the projected frontal area of the rotor across all measurement planes in the wake demonstrated the importance of the axial advective component for the positive pitch case, whilst the negative case relies mainly on the lateral contribution. The mechanisms are further highlighted by an analysis of the flux of MKE in and out of a control volume around the rotor.

It can be concluded that the vortex-generator technique using passive blade pitch applied to the X-Rotor VAWT is an effective technique to accelerate the wake recovery, which is essential for achieving high-energy-density wind farms. Future efforts should be applied to quantify the trade-offs between the available power in the wake and that forfeited by the upwind rotor.

IV

The multi-rotor system

9

Wake re-energization of a VAWT-based multi-rotor system

The "vortex-generator" concept has been shown to significantly increase the available power in the wake of a VAWT. However, as discussed in Chapter 2, this is a "coupled" technique, meaning it relies on the rotor operation itself.

Unlike these rotor geometries, the MRS offers the potential to apply a "de-coupled" wake control strategy using the supporting structure of the rotors.

This study investigates the performance and near-wake behavior of a Vertical Axis Wind Turbine (VAWT)-based Multi-Rotor System (MRS) under two configurations: its baseline state and when augmented with external lift-generating devices designed for wake control. Wind tunnel experiments were conducted on a scaled VAWT-MRS model, where the wake was characterized using Particle Tracking Velocimetry (PTV).

This chapter is partly based on Broertjes T., **Bensason D.**, Sciacchitano A., Simao Ferreira C. Lift-induced wake re-energization for a vawt-based multi-rotor system. *Journal of Physics: Conf. Series.* 2024. [169].
The data supporting this study is openly available in the 4TU.ResearchData repository at `https://doi.org/10.4121/24529850-7f34-42b6-9f29-fcc1577bb1ae`.

9.1 Introduction

The advantages of Multi-rotor systems (MRS) were discussed in Chapter 2 and include potential benefits for up-scaling [115] as well as wake recovery benefits related to closely spaced rotors [116]. A VAWT-based MRS design was conceptualized by [27] with the goal of resolving many of the disadvantages of individual VAWTs compared to HAWTs whilst exploiting their advantages in a closely spaced arrangement of an MRS, visualized in Figure 9.1. A top-level development of the preliminary design was conducted, which considers the aerodynamics of high-aspect-ratio VAWTs, frame design, drive train design, floater design, and an evaluation of the O&M costs comparison.

Three 1GW-rated wind farms were considered, made up of 16MW HAWTs (baseline case), 48MW HAWT-based MRS, and 48MW VAWT-based MRS, respectively. The annual averages of energy production, loss, and corresponding revenue generation and loss were compared using an OPEX model. Relative to the baseline case, the VAWT-based MRS increased generated energy and revenue by 4% with a 2% increase in capacity factor. Meanwhile, the HAWT-based MRS reported a 7% and 4% decrease in the aforementioned annual averages, respectively. The authors conclude that despite the smaller rotor size, the HAWT-based MRS faced resource utilization issues, requiring an impractical number of personnel for maintenance. Meanwhile, the VAWT-based MRS requires fewer rotors and, hence, fewer components requiring repair, resulting in a more manageable fleet for maintenance. The authors do not elaborate on the geographic location, meteorological conditions, or aerodynamic modeling of the wind farm (whether wake losses are considered or not). Hence, it is assumed that the energy and revenue lost are due to reduced capacity during maintenance. The cost savings are realized by the following design characteristics of a VAWT-based MRS:

1. **Rotor arrangement**: HAWT-based MRS systems are typically arranged as honeycombs (as seen in Chapter 1) as staggering circular areas maximize the packing ratio (approximately 90%), defined as the ratio between the volume of bodies to the overall volume of space [170]. However, as VAWTs of rectangular (or square) shape, the packing ratio can be 100%, reducing the ratio between the supporting structure and the projected rotor area. This is assuming no tip clearance between rotors for both geometries.

2. **Rotor performance:** Closely spaced VAWTs have been shown to enhance their power performance due to the cumulative blockage effect, as discussed in Chapter 2.

3. **O&M impacts**: The omission of yaw and pitch systems enhances the system's reliability and avoids costly and frequent maintenance operations. The modularity of the system is also aimed at allowing on-shore maintenance without the need to move the entire system.

Furthermore, the application of a VAWT in an MRS addresses several challenges faced by individual VAWT systems, namely:

1. **High aspect ratio VAWTs**: High aspect ratio VAWTs minimize 3D effects such as blade-tip losses [44]. For tall single-rotor arrangements, challenges arise for the

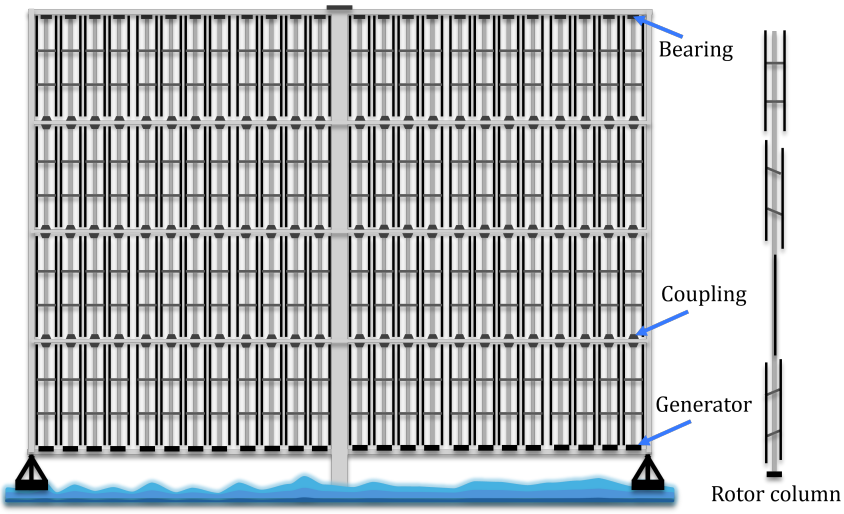


Figure 9.1: VAWT-based 48MW MRS concept adapted from [27]. A schematic of an isolated rotor column highlights the 45° phase offset between the rotors to achieve a smoother net torque profile.

support structure due to a long cantilever. However, the MRS integrates several VAWTs on a common shaft, which is fastened to the frame on both ends with bearings.

2. **Torque cycle**: The intrinsic unsteady loading of a VAWT leads to cyclic input torque fluctuations for the generator (discussed in Chapter 2). However, arranging several VAWTs on a common shaft with staggered phase offsets of 45° with respect to each other will result in a smoother net torque profile. Furthermore, the rotor columns can rotate in alternative directions, easing the net torque reaction required by a floater to balance.

The work of [120] compared the wake recovery process for an isolated HAWT and HAWT-based MRS, concluding an accelerated wake recovery in the near wake of the MRS due to the cumulative blockage effects, suggesting their potential for high energy-density applications. Established wake deflection strategies such as yaw were explored in the context of HAWT-based MRS (as discussed in Chapter 2), presenting various recovery modes depending on the yaw direction and combinations between individual rotors.

However, this is a coupled method, meaning that the operation (and consequently the performance) is modified to achieve the desired vorticity system. However, as discussed in Chapter 2, de-coupled wake steering and re-energization methods have been explored, which minimize the performance penalties on the rotors and, in some cases, even enhance them. The work of [88] numerically investigated the wake recovery potential of an isolated HAWT with finite wings arranged in various orientations surrounding the rotor, which can introduce cross-flow loading. Although this exploratory work highlighted the potential of de-coupled cross-flow generating devices for enhanced wake recovery, the question of how such devices can be realized in a real-world application was not addressed. However, as hinted in Chapter 2, a multi-rotor system (MRS) with a block design and supporting frame

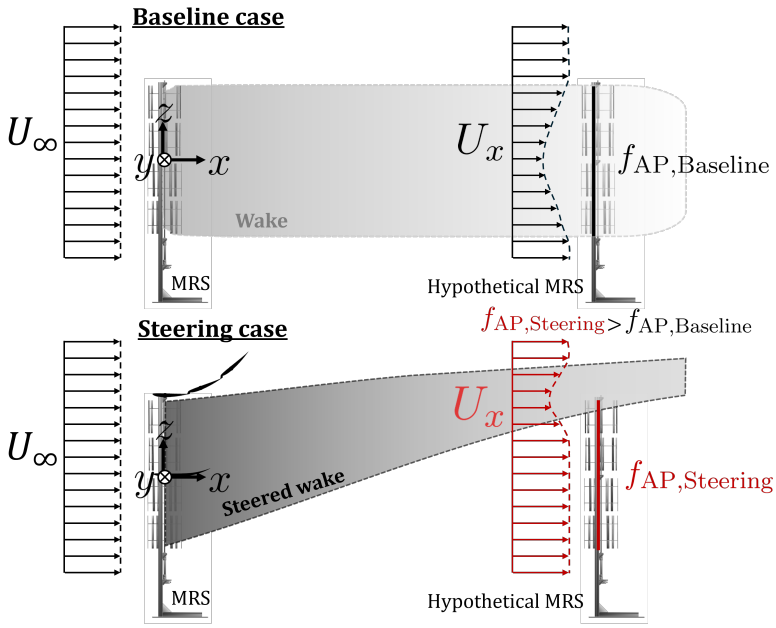


Figure 9.2: Working principle of a de-coupled wake steering technique applied to an MRS. The wake for the steering case is directed upward, resulting in higher incident streamwise velocity U_x on a hypothetical MRS downstream. Hence, the available power coefficient f_{AP} in the wake is higher than the baseline case.

presents a unique opportunity to implement a quasi-de-coupled wake recovery strategy, offering a solution to the open-ended question.

A schematic representation of the working principle of the de-coupled wake recovery using wings is shown in Figure 9.2. Compared to the baseline case where the wake is directly incident on a hypothetical downstream MRS, the case with a lift-induced wake recovery steers the wake vertically away, resulting in higher incident streamwise velocity U_x. Hence, the coefficient of available power f_{AP} for a hypothetical MRS in the wake would be increased in the steering case. This is the same working principle presented in [88], except, in this case, the lift-generating devices can be mounted to the frame of the MRS rather than be free-floating in space.

This chapter presents a proof of concept for an MRS with external lift-generating devices for enhanced wake re-energization and deflection. The working principle of lift-induced wake recovery through cross-flow loading for an MRS using finite length wings is introduced in Section 9.2. The setup and measurement technique used to obtain the first experimental dataset for the near wake of an MRS with wake steering is presented in Section 9.3. The results are discussed in Section 9.4, focusing on the streamwise vorticity system, wake topology, and subsequent wake recovery mechanisms. Finally, the conclusions are drawn in Section 9.5. The insights from this work will contribute significantly to the advancements of MRS and their applications towards high-energy density wind farm applications.

9.2 De-coupled lift-induced recovery

As touched on in Section 8.1, both wake deflection and re-energization depend on cross-flow loads and their magnitudes imposed on the wake. This is the reality for conventional wake steering methods for HAWTs, such as imposing a yaw or tilt misalignment, leading to dominant counter-rotating vortex pairs (CVP), which increase the advective recovery process in the wake (discussed in Chapter 2). The importance of the resulting vertical entrainment of momentum for accelerated recovery in wind farms has been established [77, 87].

Taking a wing of finite length, the induced cross-flow velocity in the wake can be formulated using classic lifting-line theory [162]. The vortex, circulation, and net vertical flow in the wake of a blade can be simplified as a horseshoe vortex, as shown in Figure 9.3. The horseshoe vortex consists of a bound vortex (blue) with two trailing vortices stemming from the blade tips (red), which induce a vertical cross-flow component U_z. The induced vertical velocity of the trailing vortices at a given measurement plane x is the same used in Chapter 8, and is expressed as:

$$U_{z,\text{trailing}}(y,z) = \frac{\Gamma(y-y_c)}{2\pi r^2}\left(1-\exp\left(\frac{-r^2}{4\eta^2}\right)\right), \tag{9.1}$$

where Γ is the vortex circulation, the vortex core position is y_c, z_c, the viscous length scale is denoted as η, and the radial distance from the vortex core to the measurement point in the plane is $r = \sqrt{(y-y_c)^2-(z-z_c)^2}$. Unlike the case in Chapter 8, the induced flow of the bound circulation for the finite span wing is also considered, and is expressed as:

$$U_{z,\text{bound}}(y,z) = \frac{\Gamma z}{4\pi C}\left(\frac{(y+\frac{b}{2})}{\sqrt{C+(y+\frac{b}{2})^2}} - \frac{(y-\frac{b}{2})}{\sqrt{C+(y-\frac{b}{2})^2}}\right), \tag{9.2}$$

where b is the span of the wing, and $C = x^2+z^2$. As two wings are used in this study, the net-induced flow at a given cross-stream measurement plane in the wake is expressed as:

$$U_z(y,z) = 2U_{z,\text{trailing,Top}}(y,z) + 2U_{z,\text{trailing,Mid}}(y,z) + |U_{z,\text{bound,Top}}(y,z)| + |U_{z,\text{bound,Mid}}(y,z)| \tag{9.3}$$

Evident from both Equation (9.1) and Equation (9.2), the induced flow is strongly dependent on the circulation of the wings. The circulation per unit span can be expressed as [162]:

$$\Gamma = C_L\frac{U_\infty c}{2} \tag{9.4}$$

where C_L is the sectional lift-coefficient, c is the chord length, and U_∞ is the inflow velocity. Hence, to increase the induced vertical velocity in the wake, either the sectional lift coefficient, chord length, or inflow velocity can be increased. This approach contrasts with traditional airplane wing design, where the focus is typically on reducing induced drag through features like winglets, which minimize the strength of tip vortices and improve efficiency, or by increasing the aspect ratio. In contrast, maximizing upwash and circulation

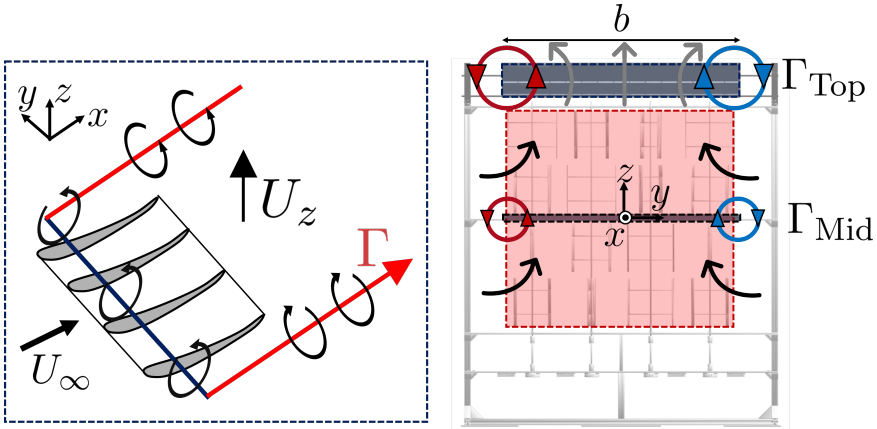


Figure 9.3: (Left) Representation of a finite wing as a horseshoe vortex made of the bound (blue) and free-trailing vortices (red) with circulation Γ. The induced vertical velocity is U_z. (Right) Schematic of the driving recovery mechanism behind the rotor at a generic wake position. The blue and red delineated areas indicate the wings and actuation surface, respectively. The cross-stream projections of the free-trailing tip-vortices of the top and middle blade are shown, with red and blue corresponding to CW and CWW rotation, respectively. The circulations of the vortices are denoted as Γ_{Top} and Γ_{Mid}, respectively. Black and gray arrows indicate the movement direction of high and low momentum flow, respectively.

via vortex strength is beneficial in applications such as wake recovery in wind farms, where the goal is to enhance vertical momentum entrainment.

In terms of design considerations, maximizing induced upwash and circulation involves several key strategies. First, a low aspect ratio is desirable, as it helps concentrate lift near the tips and strengthens the resulting vortices. Second, an untapered or minimally tapered wing planform ensures more uniform lift distribution, contributing to stronger tip vortices. Third, avoiding washout or tip twist helps maintain maximum lift at the tips, further intensifying the vortex strength. These considerations are fundamentally different from conventional wing design, where minimizing vortex strength is typically the priority.

As in Chapter 4, the projected cross-stream slices of the trailing vortices of the blades are shown in Figure 9.3 at a generic position in the wake, the actuator surface of the rotors is delineated in a red area while the projected frontal area of the top and middle wings are shown in blue. The sizes of the vortices stemming from the top and middle wings are relative to their circulation magnitudes Γ_{Top} and Γ_{Mid}, respectively. The dominant CVP stemming from the lifting wings induces a significant cross-flow in the wake, with an injection of high momentum flow from the sides of the rotor, whilst ejecting the low momentum wake out from about the actuator surface. This recovery mode is analogous to the negatively pitched cases from the "vortex generator" control strategy presented in Chapters 4 and 7.

9.3 Methodology

9.3.1 MRS model

The wind tunnel scaled MRS model is inspired by the design proposed by [27], which was also illustrated in Chapter 1. This block design consists of H-type VAWTs which are mounted on a central shaft. A rendering of the scaled test model fabricated for this experiment is shown in Figure 9.4. Four shafts of diameter 0.01m, each housing four VAWTs, are mounted on a frame, yielding a total of 16 rotors in 4x4 grid. The individual VAWT geometries follow the design of [25] and are the same used in the content described in Chapter 4. These two-bladed rotors have NACA 0012 profiles and a uniform diameter and span of d = 0.3m. The chord of the blades is 0.03m. Following the design suggestion of [27], the rotors along one shaft are staggered by 45° with respect to each other. Ideally, this would smooth the torque input for the generator of a full-scale design. The rotors are spaced 1.25d in the vertical and horizontal direction. A close spacing to exploit the benefits of closely spaced VAWTs, as discussed in Chapter 2, is balanced with sufficient tip clearance between the blades in the case of vibrations. The rotor columns are situated in the frame to minimize their impact on the flow, with a clearance of 0.75d between the edge rotors and the frame in the horizontal direction. The resulting actuation surface, defined as the tip-to-tip distance between the rotors on the edge, has a diameter and height of D = 1.43m and H = 1.35m. Here, $H \neq D$ as a larger spacing is used between the second and third rows of the rotor to allow for the space of the support frame and lifting wing.

Each rotor shaft is powered and controlled via a Maxon EC90 260W DC motor and ESCON 50/5 controller. The same method for powering the scaled rotors is used in the work of [25] and in this thesis (Chapters 4 and 8). Using this control method allows the testing of several combinations of rotation direction between the columns. In this work, a symmetric condition was tested to simplify the flow measurement system and required measurement volume, with the two columns on the right and left rotating counter-clockwise (CCW) and clockwise (CW), respectively.

9.3.2 High-lifting wings

As discussed in Section 9.2, cross-flow loads are introduced using wings mounted on the MRS frame. In this experiment, two wing geometries are used, mounted in the middle and above the actuator surface, as shown in Figure 9.4. A cross-section of the untwisted and untapered geometries is shown in Figure 9.6 along with their induced upwash, visualized using a smoke probe. Both wings are fabricated using 3D-printed PLA with an infill ratio of 55%. The surface is painted back to minimize reflections during acquisition and covered with a thin layer of epoxy resin to help with the rigidity, smooth the surface, and offer a water/liquid-resistant finish for the HFSB. Both wings have a span of 1.5m centered about the actuator surface, as shown in Figure 9.4. Given the limitations on the maximum printable heights of the 3D printer, several sections of 0.3m span were printed and glued together to achieve the total length. The following designs were selected based on preliminary load measurements tested in the M-Tunnel of TU Delft's Low-Speed Laboratory. A comprehensive overview of these preliminary experiments is documented in the master's thesis of Thomas Broertjes [171].

The dependence of the trailing vortex strength and upwash from the wings is directly

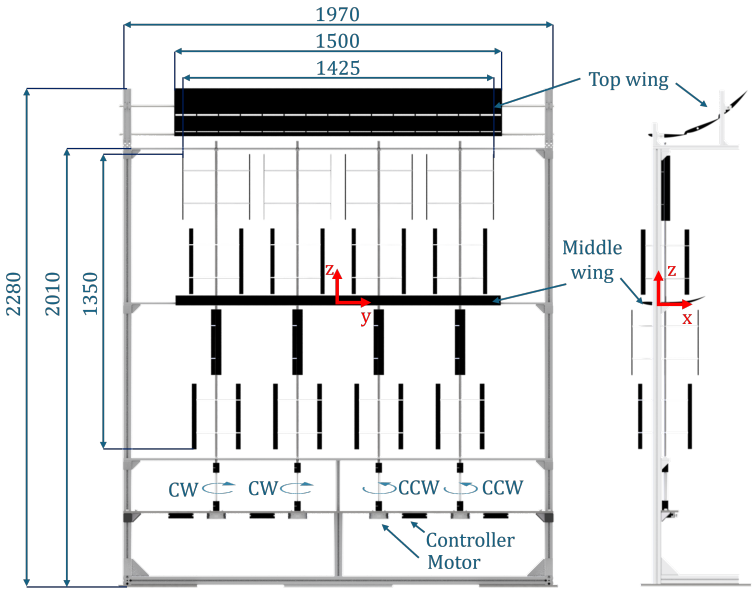


Figure 9.4: Rendering of the MRS system with the lifting wings mounted from the (left) back and (right) side view. The main components are labeled, and all dimensions are given in mm. The origin of the coordinate system is shown and taken as the center of the actuation plane, which coincides with the center of the middle wing.

related to the section-wise circulation along the wing span and, ultimately, the lift coefficient. Multi-element wings are a common geometry for increasing lift in adverse inflow conditions, evident by their extensive use for aircraft wings. An overview of the physics and resulting benefits of multi-element wings is provided by [172]. Given the larger available space above the MRS frame, a multi-element wing design would be ideal for generating a significant lift at low Reynolds numbers.

The top wing is a 3-element cascading design made of airfoils with an SD7032 profile and constant chord of 287.3mm. The individual elements are spaced (trailing edge to leading edge) by 6.5mm and 13.4mm in the horizontal and vertical directions, respectively, and connected via 3D-printed ribs. The cascading wing is mounted to the frame using an additional support structure as labeled in Figure 9.6, with 10mm steel rods fastened at the thickest points along the chord (59.9mm from the leading edge) of the first and third elements. The fastening points between the rod and the supporting structure can be translated vertically, allowing for a range of angles of attack to be tested, as indicated by the vertical arrows. The top wing is placed as close to the MRS frame while maintaining space between the rotor column rod, with 61mm between the supporting rod of the first element and MRS frame. The top wing has an overall chord length (leading edge of first element to the trailing edge of third element) of 504.5mm and an angle of attack of 28.8°. At an inflow speed of $U_\infty = 4.0$ the chord-based Reynolds number is $1.4\text{x}10^5$. The smoke probe provides a visualization of the large-scale tip-vortex at an inflow speed of $U_\infty = 4.0$m/s. The induced upwash is also evident in the general convection of the trailing vortex structure

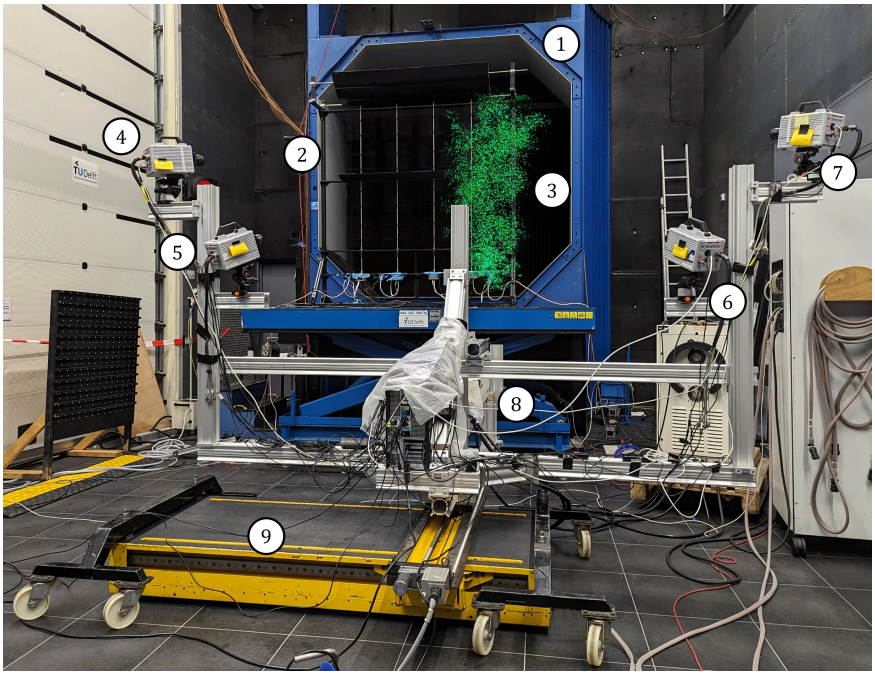


Figure 9.5: Experimental setup in the OJF. The main components are labeled and defined as follows: ① OJF outlet, ② MRS, ③ HFSB, ④ Camera 1, ⑤ Camera 2, ⑥ Camera 3, ⑦ Camera 4, ⑧ Laser, ⑨ Traversing system.

vertically upward.

The implementation of a high-lift wing in the middle of the MRS is a larger design challenge due to the limited space between the second and third rotor rows, as shown in Figure 9.4. A similar design approach to the top wing with cascading elements and a large chord would not fit, nor a single element with a large angle of attack. The final design, shown in Figure 9.6, was inspired by the S1210 airfoil given the high reported lift coefficient by [173] of 1.8 at low Reynolds numbers of $15x10^4$. The lift was simulated at a lower Reynolds number of $8x10^4$ using JavaFoil and modified to fit within the constrained space and have an increased camber near the trailing edge to achieve a lift coefficient of 1.6, resulting in a chord length of 304.3mm, and angle of attack 6.1°. Unlike the top wing, the middle wing does not have an external support structure and rather mounts directly on the horizontal support beam of the MRS, as shown in Figure 9.4. To achieve this, the profile is printed as a two-part constructing split at the mid-chord with a negative matching the rectangular support profile of the MRS frame. Furthermore, evenly spaced holes along the span are accounted for to allow the rotor columns to pass through without obstruction. At an inflow speed of $U_\infty = 4.0$ the chord-based Reynolds number is $0.8x10^5$. The smoke probe visualization demonstrates an upwash of the flow near the mid-span of the middle wing. However, given the smaller chord, angle of attack, and single-element airfoil, the expected lift force will be lower than the top wing.

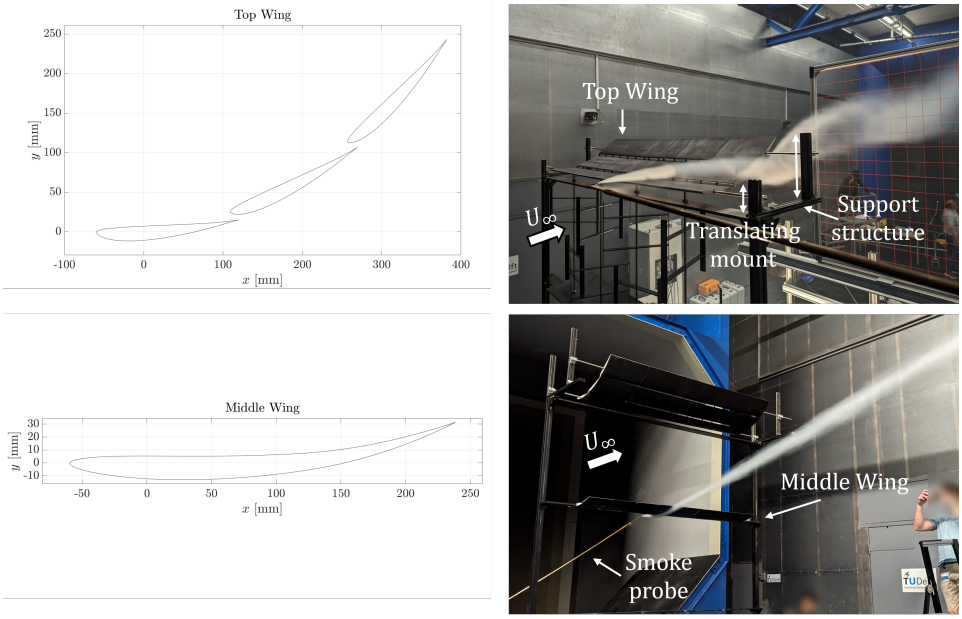


Figure 9.6: Technical drawings of the middle and top wing. The x-axis is consistent with the origin defined in Figure 9.4, whilst the y-axis origin is defined as $y = 0$ at the leading edge. Smoke probe visualizations of each wing are provided, with the upwash and tip-vortex structure of the top wing and induced upwash of the middle shown. The blades and main components are labeled along with the incoming flow direction.

9.3.3 Flow measurement technique

The velocity fields are obtained through three-dimensional Lagrangian Particle Tracking, as described in Chapter 3. A majority of the measurement system and data processing steps are identical to those in Chapter 4 with the exception of the illumination technique. In this case, a high-speed laser is used instead of LEDs to increase the measurement surface area at a discrete downstream plane. A similar measurement technique was used by [174] to perform large-scale wake measurements behind a full-scale cyclist in the OJF.

Seeding is generated using a rake placed in the settling chamber of the OJF made up of 200 nozzles, each releasing neutrally buoyant helium-filled soap bubbles (HFSB) at a rate of 30,000/sec and an average diameter of 0.4mm [137]. Given the rake dimensions and the contraction ratio of the outlet, the seeded streamtube is approximately 0.57m × 1.2m, as visualized in Figure 9.5. The resulting seeding concentration was, on average, 1 HFSB/cm^3 [127]. The rake has been shown to minimally impact the turbulence intensity of the incoming flow by 0.8% [138]. Given the limited size of the generated stream tube and desired lateral measurement volume, the seeding rake was translated along the width of the tunnel to adequately seed the desired measurement volume, described in Section 9.3.4.

The tracers are illuminated using a Quantronix Dawin-Duo Nd:YLF laser, with a wavelength and pulse energy of 527nm and 25mJ, respectively. A thick laser sheet of approximately 30mm was used to perform particle tracking in a plane. Given the free stream velocity of $U_\infty = 4$m/s, there will be seven particle tracks within the laser sheet with an

acquisition frequency of 1kHz.

The illuminated particles are recorded with four Photron FASTCAM SA1.1 high-speed cameras (CMOS, 12 bit, 20μm pixel pitch) with an image resolution of 1024px × 1024px. The cameras are fitted with lenses with 35mm focal length and set to a numerical aperture of f/11. An individual measurement plane is approximately 0.6m x 1.2m, resulting in a digital image resolution of 0.9px/mm with a magnification factor of M = 0.02. A total of 4000 frames are captured per measurement volume, with an acquisition time of 4s. Given the rotational frequency of the rotors of ω = 88rad/s, approximately 56 revolutions are captured. The illumination and imaging are synchronized using a LaVision PTU-X timing device.

As seen in Figure 9.5, the cameras and laser are rigidly mounted on a traversing system. This allows for the translation of the measurement volume in the streamwise and lateral directions, such that several can be stitched together without the need for recalibrating the acquisition system. The number of individual measurement volumes ranges between three and six, depending on the downstream location and configuration.

The acquired frames were processed using LaVisions DaVis 10 software. First, background removal is applied by subtracting a minimum time filter with a kernel of five images. Geometric calibration of the camera positions relative to the measurement domain was performed using a calibration plate, followed by a volume self-calibration using an unperturbed flowfield recording of particles [139]. The residual measurement errors fall below 0.1 pixels for all three cameras. Next, tracer trajectories were evaluated using the Shake-the-Box (STB) algorithm [126].

The individual STB volumes measured at a given cross-stream plane are stitched together with the corresponding lateral and streamwise offsets recorded using the traversing system, as described above. The total resulting measurement volume varies between the baseline and wing cases as well as the streamwise measurement plane. At $x/D = 2$, the total measurement volume for the baseline and wing case is 3.8m^2 and 4.5m^2, respectively. The wing cases generally consist of larger areas, as additional fields were recorded to capture the deflection of the wake. Finally, the binning step involves mapping particle tracks of the fully stitched volume on a Cartesian grid by spatially averaging over smaller cells [140]. In this study, all time stamps are binned together to yield a time-averaged wake measurement. The sub-volume size is 92×92×92 voxels used, where one voxel = 10mm. Given an overlap of 50%, the final grid spacing of the velocity vectors is 46mm.

9.3.4 Measurement cases

Prior to the flowfield measurements, the loading of the MRS is evaluated using a 6-component force balance to determine the operating condition for the wake measurements. The Dutch Aerospace Laboratory (NLR) manufactured and calibrated the balance. Under simultaneous loading, as in this experiment, loads up to 250N, 500N, and 500N can be measured in the streamwise, lateral, and vertical directions, respectively. The maximum uncertainties range between 0.06% and 0.23% [174]. Furthermore, the balance is used to perform in-situ lift and drag measurements of the selected wing designs. The flowfield is measured at a constant MRS operating rotational frequency of 88 rad/s (840 rpm). With a constant inflow velocity of U_∞ = 4 m/s, the resulting tip-speed ratio is $\lambda = 3.3$. An overview of the MRS loading for this design case is provided in Table 9.1. The thrust coefficients are

Case	$F_x[N]$	$C_{T,x}$
Baseline	13.2	0.70
With Wing *	13.4	0.71
With Wing	18.3	0.97

Table 9.1: Streamwise thrust measurements of the MRS in the baseline and with wing configuration. The case with * is with the drag of the wings removed.

	Isolated F_z [N]	Operating MRS F_z [N]
Top Wing	14.40	11.48
Middle Wing	2.39	2.02
Net	16.79	13.50

Table 9.2: Dimensional vertical force F_z of the top and middle wings is an isolated case, and with the MRS in operation

computed using Equation (9.5):

$$C_{T,x} = \frac{F_x}{0.5\rho U_\infty^2 A_{\text{act}}}, \tag{9.5}$$

where F_x is the mean average dimensional streamwise force measured by the balance, and $A_{\text{act}} = 1.92\text{m}^2$ is the frontal area of the rotor actuator surface.

The measured streamwise force increases by a factor of 1.4 with wings due to the added drag. When removing the wing-induced drag using the isolated wing measurements, the thrust of the actuator surface increases marginally by 0.2N. This can be attributed to the acceleration of flow induced by the suction side of the top wing on the rotor plane, similar to the effect of a ducted rotor. Similar observations were made by [88], as discussed in Chapter 2.

The vertical loading F_Z of top and middle wings in isolated settings (without the rotors) and with the rotors operating at the design tip-speed ratio is shown in Table 9.2.

For isolated cases, the top wing produces a lift that is a factor of six larger than the middle wing. This is to be expected as the upper blade has a much larger chord and is a multi-element design, whilst the middle blade has a constrained size due to its integration between the second and third rotor rows. The loads of the top and middle wings drop by similar factors of 1.3 and 1.2, respectively, when the MRS is operating. This can be attributed to the blockage effect that the MRS has on the inflow perceived by the wings, where a reduction in inflow speed will reduce the generated lift. This effect will presumably be coupled with the impact the blockage has on the inflow angle and, subsequently, the effective angle of attack, especially for the top wing, once again affecting the lift generation.

The near wake of the MRS was measured in two configurations, namely the baseline case, where no lifting wings are mounted, and the wing case, where both the top and middle wings are applied. An overview of the measurement planes for both configurations is provided in Table 9.3. Given the asymmetric operating condition of the rotors, measurements are concentrated around one-half of the MRS. Given the limited size of the acquisition field of

Configuration	x/D
Baseline	[1.0 1.5 2.0]
With Wing	[1.0 1.5 2.0 2.5]

Table 9.3: Measurement planes for the baseline and with wing configurations

view and seeding volume (described in Section 9.3.3), several lateral and axial planes are measured at a given cross-stream location and stitched together in post-processing.

9.4 Results

9.4.1 Wake topology

The wake topology will be strongly linked to the streamwise vorticity system generated by the lifting wings. The normalized streamwise vorticity ($\omega_x D/U_\infty$) and velocity (U_x/U_∞) profiles at all downstream positions are presented in Figure 9.7 and Figure 9.8 for the baseline and wing case, respectively. The red delineated rectangle indicates the projected frontal area of the actuator plane of the MRS, and the vectors show the in-plane velocity at each downstream position. To help highlight the impacts of the wings on the streamwise flow deficit and upwash in the wake, the profiles of the deficit $\Delta U = U_\infty - U_x$ and vertical flow U_z are shown in Figure 9.9 at the symmetry plane $y/D = 0$. Additionally, the laterally averaged values as a function of height in the domain $0 \leq y/D \leq 0.5$ of each component are denoted by $<>$.

For the baseline case in Figure 9.7, regions of alternating positive and negative vorticity are evident at $x/D = 1.0$ before gradually diffusing and eventually becoming indistinguishable at $x/D = 2.0$. These structures are the trailing tip-vortices of the individual rotors, with the rotation directions corresponding to the quadrants in which they are shed, as experimentally observed in Chapters 4 and 8 and in previous works of [25]. A strong degree of symmetry is evident in these structures about the $y/D = 0$ plane, confirming the asymmetric actuation achieved using the CW and CCW operating conditions, described in Section 9.3.1. There is a notably large region of positive (counter-clockwise) vorticity at $y/D \approx 0.75$ and $z/D \approx 0.60$. The exact cause of this structure is uncertain but is likely related to the presence of the supporting frame. The blockage induced by the actuator surface will induce an effective angle of attack for the horizontal flat plate of the structure, thus generating a lifting flat plate with a corresponding trailing tip vortex.

The topology of the streamwise flow component exhibits a coherent shape consistent with the rectangular actuator surface. At $x/D = 1.0$, the individual wakes of the rotors can be identified as well as pockets of high-speed flow. Similar results were observed by [120, 121] for HAWT-based MRS and are attributed to the blockage effect of closely spaced rotors, as discussed in reference to VAWTs in Section 2.2.1. This is highlighted by the fluctuating wake deficits at the symmetry plane in Figure 9.9. Both the individual wake structures and pockets of high-speed flow are strongly symmetric about the plane $y/D = 0$. The sizes of the high-speed pockets vary between the different columns, for example, that in the center between the counter-rotating rotors and those on the right between the co-rotating rotors. As discussed in Section 2.2.1 in relation to the work of [23], these operating conditions load the VAWT quadrants differently, leading to non-identical

blockage effects. When moving downstream, the pockets of high-speed flow begin to vanish as the individual rotor wakes combine towards a more uniform wake structure. The same process is noted by previous works of [120]. The flow deficits extend further vertically and laterally as the wake expands, evident from the in-plane velocity vectors. Regions of flow deficit outside the projected actuator surface at $y/D = 0.7$ are present due to the MRS frame, which gradually recovers when moving downstream. The asymmetry in the individual rotor wakes is apparent at $x/D = 1.0$ and downstream as the wake topography exhibits "kidney-shaped" wake structures. This asymmetry in the wake structure is intrinsic to VAWTs as discussed in Section 2.2.1 and experimentally shown in Chapter 4. At $x/D = 2.0$, the individual rotor wakes between the first and second rows, and the third and fourth have merged. However, the region between the third and fourth rows demonstrates a smaller wake deficit compared to the other two heights. This can likely be attributed to the impact of the horizontal beam at $z/D = 0$ in the support structure between the rows.

The case with wings, shown in Figure 9.8, exhibits a distinctly different behavior from the baseline case. Although the alternative vortex structures within the projected frontal area of the rotors are evident, the dominant structures are those stemming from the tips of the top and middle wings. At $x/D = 1.0$, the tip-vortex from the top wing and middle wing can be seen at $z/D = 0.7$ and $z/D = 0$, respectively. At $x/D = 2.0$, the equal and opposite structure from the middle wing is also visible on the left side of the MRS, given the extended measurement domain. The strength of the vortex from the top wing is seemingly stronger than that in the middle, evident by its size and induced upwash in the wake, evident by the in-plane vectors, and consistent with the results shown in load measurements in Section 9.3.4. Furthermore, the alternating trailing vortices stemming from the rotors also appear stronger in strength compared to the baseline case, especially when comparing at $x/D = 1.0$. This is likely due to the increase in MRS thrust due to the "ducted" effect the wings have, as discussed in Section 9.3.4. Given the dominance of the top wing vortex, the middle wing vortex is pulled upward due to their co-rotating nature, where at $x/D = 2.5$ the middle wing vortex is near the upper edge of the actuator surface $z/D = 0.5$.

The wake topology confirms the working principle of the lifting wings, with a lateral contraction and upwash of the wake outside the protected actuator area, as suggested by the in-plane vectors. The vertical velocity profiles in Figure 9.9 demonstrate systematically higher magnitudes across all heights of the MRS compared to the baseline case. In general, magnitude is highest towards the top of the MRS due to the strong induction of the top wing structures, whilst decreasing towards the base. At $x/D = 1.0$, a local maximum is also apparent at $y/D = 0.2$ due to the middle wing. Given this contraction, the individual wakes of the rotors are not as distinctive beyond $x/D = 1.0$ as in the baseline case, suggesting an earlier onset towards a single wake. The upwash becomes most evident at $x/D = 1.5$ and beyond as the flow begins to recover at the bottom of the actuator surface $z/D = -0.5$. Although the middle wing vortex induces an upwash in the wake, it also displaces some of the low momentum flow out laterally, leading to a local "hump" in the overall contraction near the middle of the MRS at $z/D = 0$. Overall, the wake area is increased compared to the baseline case due to the significant drag of the wings, in particular the top wing, evident by the significant flow deficit at $z/D = 0.7$ directly behind the MRS ($x/D = 1.0$). This is confirmed by the flow deficit shown in Figure 9.9 across all measurement planes above the actuation plane. Furthermore, the displaced wake of the middle wing is also apparent by

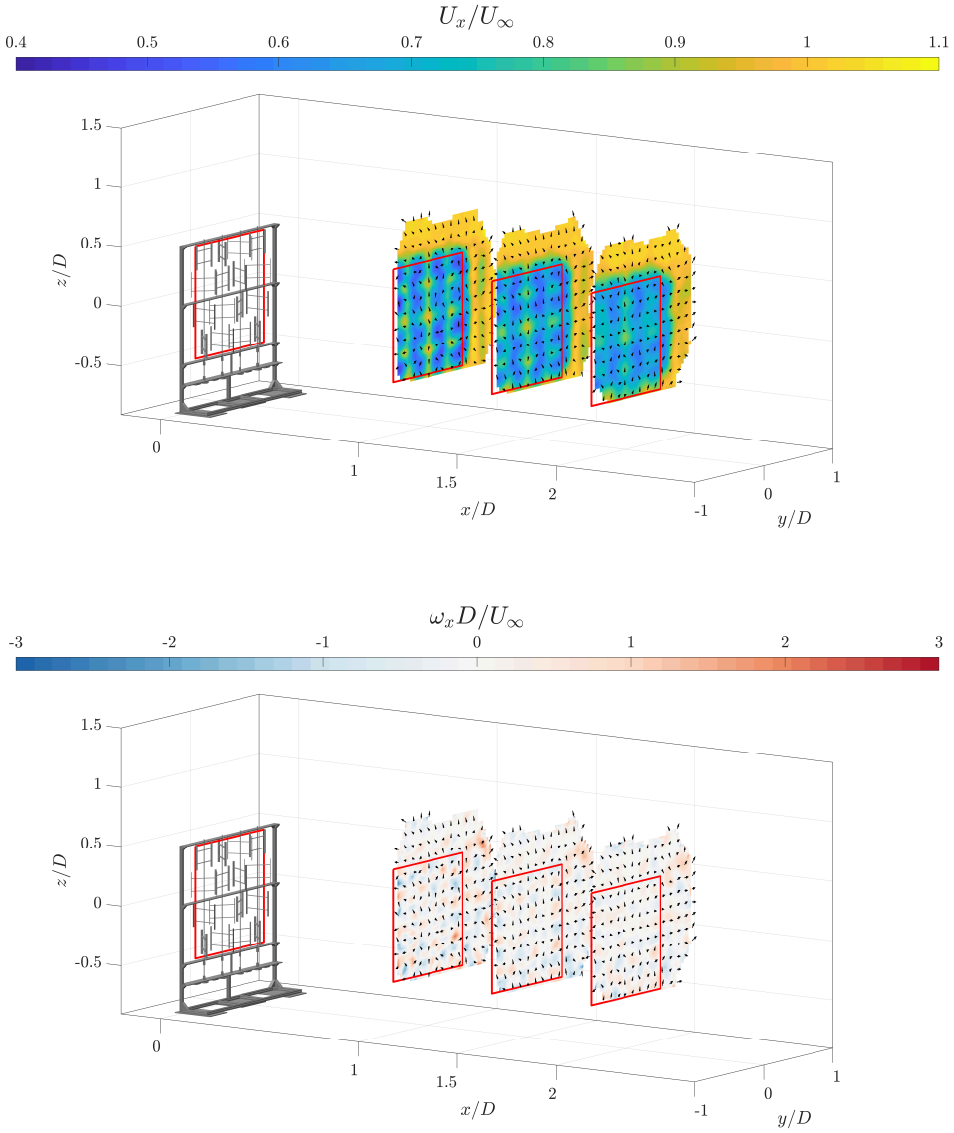


Figure 9.7: Flowfield at cross-stream locations $x/D = 1, 1.5, 2$ for the baseline case. (Top) Normalized streamwise velocity and (bottom) vorticity. The red delineated box is the projected frontal area of the actuation surface with diameter D. The vectors show the in-plane velocity vectors. Note that the scale in the x-axis is doubled to increase the spacing of the measurement planes.

the large local maximum in flow deficit at $z/D = 0.23$ at $x/D = 1.5$. Whereas this would be primarily driven by the top wing drag at $x/D = 1.0$, larger contributions from the displaced

wake of the MRS are expected downstream, highlighted by the notable decrease in section averaged ΔU at $x/D = 2.0$ compared to the baseline case. As discussed in reference to the vorticity system, the higher loading imposed by the wings on the MRS also leads to seemingly larger flow deficits behind each rotor, evident by the deeper blue at $x/D = 1.0$, and larger peaks in flow deficit about the symmetry plane in Figure 9.9.

9.4.2 Vortex circulation

The discussion in Section 9.4.1 confirmed the working principle of the lifting wings discussed in Section 9.2. Here, the vortex dynamics are quantified, namely the trajectories, strengths, and comparison with load-derived values from Section 8.3.3. The trajectory of the tip vortex cores stemming from the top and middle blades is shown in Figure 9.10. Given the counter-rotating nature of the vortices stemming from each wing, they propel upward as the wake progresses. Overall, the vortex core stemming from the middle wing travels further vertically compared to the top wing, with $\Delta z/D = 0.27$ versus 0.19, repetitively, between $x/D = 1$ and 2.5.

The maximum magnitudes in streamwise vorticity are shown in Figure 9.10. Consistent with the observations made in Section 9.4.1, the structure stemming from the top wing is consistently over twice as high across all measurement planes, confirming the magnitude differences measured using the load balance in Section 9.3.4. As with the vortex behavior related to the "vortex generator" strategy for VAWTs, the magnitude of the structures decreases as the wake progresses due to diffusion. The maximum magnitude of the vortex core from the middle wing reduces gradually by 60% between $x/D = 1$ and 2.5. Meanwhile, the top magnitude of the top wing structure reduces by 46% between $x/D = 1$ and 2.

The circulations of the top and middle tip vortices are computed by taking the surface integral of the vorticity, denoted in Equation (6.5), within a circular contour with radius r and centered about the vortex core. The integration radius is incrementally increased until the circulation is converged, which is taken as the point where the gradient with respect to the circulation falls below 1%. A schematic representation of the process and circulation convergence is shown in Figure 9.11 for the measurement plane $x/D = 2$. For the top and middle blades, the converged circulations (indicated via dashed lines) are $\Gamma_{\text{Top}}/cU_\infty$ = -0.71 and $\Gamma_{\text{Mid}}/cU_\infty$ = -0.27, respectively, corresponding to normalized radii of $r/D = 0.27$ and $r/D = 0.18$, respectively. Unlike the top blade vortex, the convergence of the middle blade vortex has an inflection point. This is because, as excessively large integration areas are considered, more of the impact of surrounding structures is considered (including the dominant top wing vortex). This is not the case for the top wing vortex, as the integration area exceeds the measurement domain before encompassing the middle blade structure.

The load-derived and flowfield-derived lift coefficients are compared in Table 9.4. The load-derived coefficient is obtained using the dimensional vertical forces presented in Table 9.2 during the operation of the MRS. Meanwhile, the flowfield-derived lift coefficient is calculated using Equation (9.4), based on the measured circulation of the tip vortices. As mentioned above, whilst the top-wing vortical structure converges only at $x/D = 2$ (given the available data), the converged circulation of the middle wing can be computed across all measurement planes. The convergence as a function of the cross-stream measurement plane is shown in Appendix D.1 for both wings. The cross-stream averaged converged circulation of the middle wing is $\Gamma_{\text{Mid}}/cU_\infty = -0.29$, with a standard deviation of 0.02.

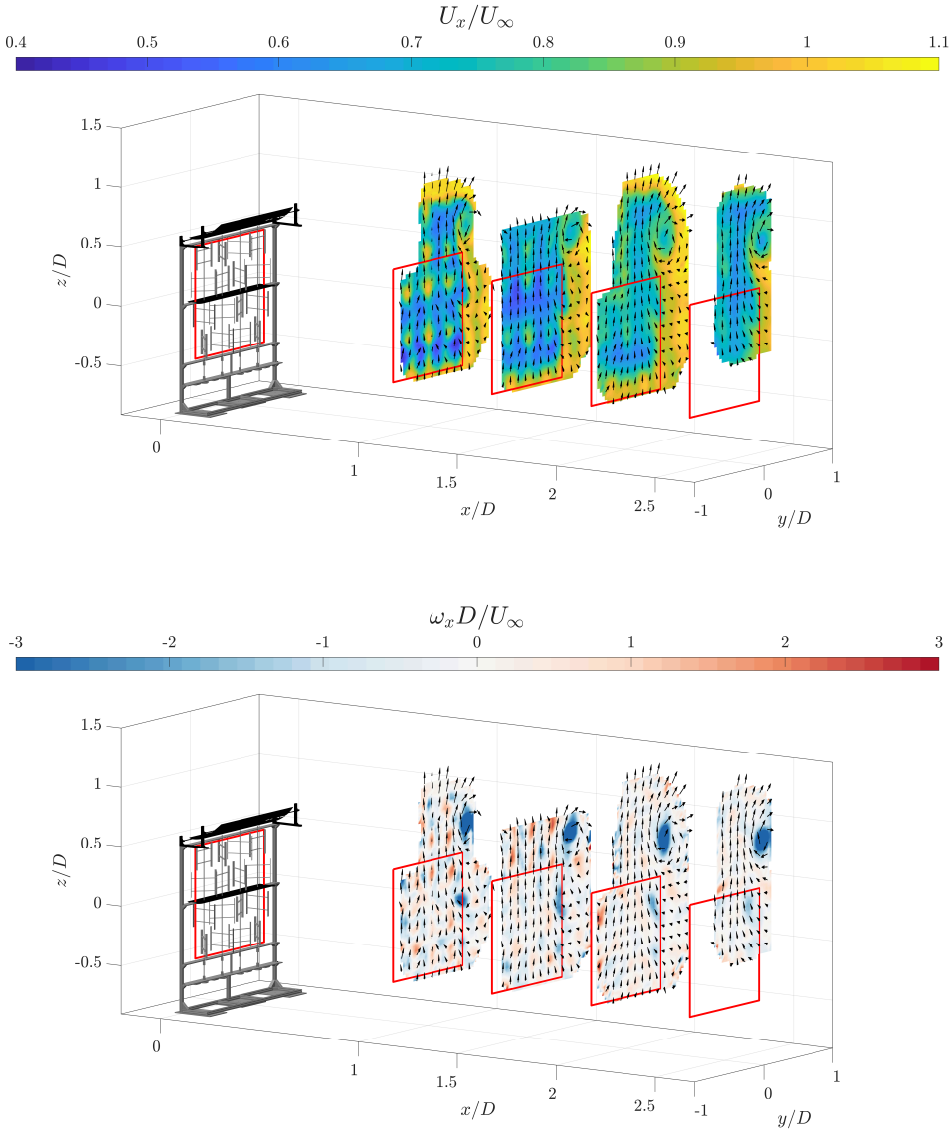


Figure 9.8: Flowfield at cross-stream locations $x/D = 1, 1.5, 2$ for the wing case. (Top) Normalized streamwise velocity and (bottom) vorticity. The red delineated box is the projected frontal area of the actuation surface with diameter D. Note that the scale in the x-axis is doubled to increase the spacing of the measurement planes.

The discrepancy between the load and flowfield-derived circulations is the highest for the middle wing. It can be attributed to several uncertainties about the load balance measurement and flowfield-derived value. The most obvious challenge lies with the flowfield

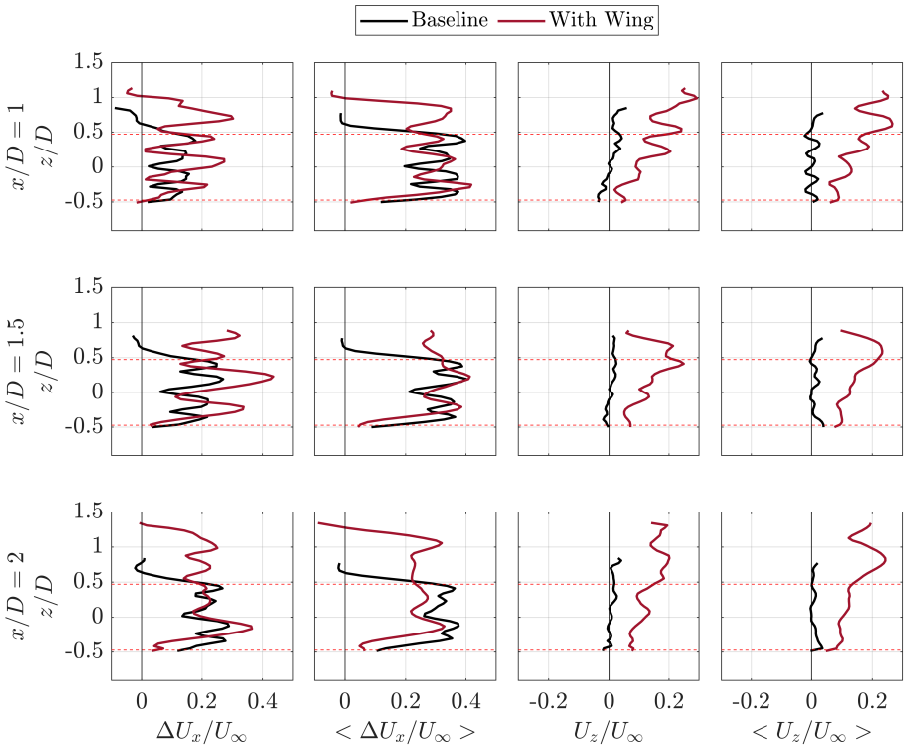


Figure 9.9: Normalized streamwise velocity deficit $\Delta U_x = U_\infty - U_x$ and axial velocity profiles (U_z/U_∞) at the symmetry plane $y/D = 0$ at cross-stream planes $x/D = 1.0, 1.5, 2.0$ for the baseline and wing cases. The red delineated box is the projected frontal area of the actuation surface with diameter D. The vectors show the in-plane velocity vectors. Note that the scale in the x-axis is doubled to increase the spacing of the measurement planes.

predicted value. Given the trajectory of the structure within the projected frontal area of the actuator and wake, a surface-integrated approach will include flow structures induced by the individual rotors themselves.

Given the derived circulations and vortex core locations, the upwash in the wake is predicted using the expression Equation (9.3). As in Chapter 8, the viscous length scale η is derived from the wake measurements, with the results shown in Appendix D.2 for both wing-tip vortices at $x/D = 2$. The comparison in the change in upwash $\Delta U_z = U_{z,\text{Wing}} - U_{z,\text{Baseline}}$ is shown at three discrete heights in the wake in Figure 9.12, namely the top ($z/D = 0.5$), middle ($z/D = 0$), and bottom ($z/D = -0.45$) of the actuator surface. An axial height just above the bottom was selected, given the lack of data at $z/D = -0.5$. Two curves for the derived upwash are shown, namely that using the flowfield-derived circulation (using the computed viscous length scales η) and the load-derived circulation (assuming a completely inviscid case where $\eta \to \infty$).

As the heights of interest do not fall incident on the vortex cores, the impact of the viscous length scale is negligible on the distribution of velocity, consistent with the expres-

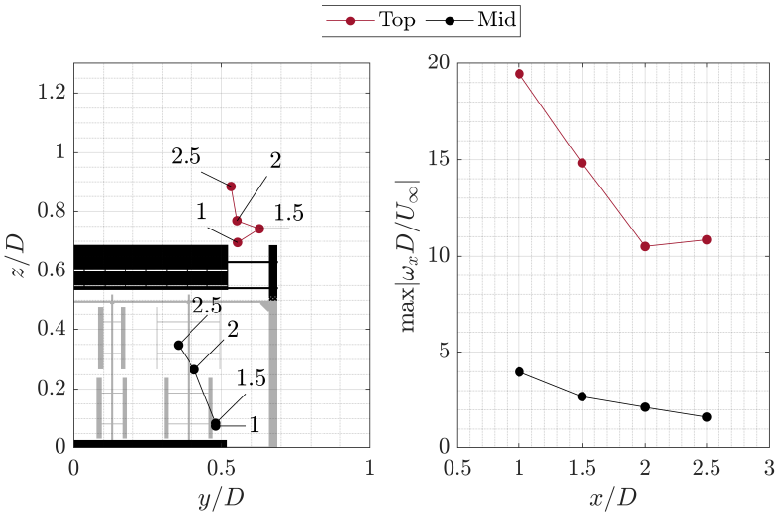


Figure 9.10: (Left) Tip-vortex trajectory of the top (red) and middle (black) blades. The data points are labeled with the corresponding cross-stream measurement plane x/D. (Right) The evolution of the maximum streamwise vorticity magnitude of the vortex cores for the top and middle blades.

	Load derived C_L	Circulation derived C_L	% Difference
Top Wing	1.55	1.42	8.75
Middle Wing	0.45	0.58	25.24

Table 9.4: Comparison between load and flowfield derived lift coefficients for the wing using data at $x/D = 2$. The standard deviation of the circulation-derived C_L is on the order of 0.02.

sion in Equation (9.1). Consistent in both the modeled and experimental distributions, the upwash of the wake increases when moving toward the top of the actuator surface due to the significant cross-flow generated by the top wing. Given the significant reduction in lift force of the middle wing compared to the top, as well as the distance between the structures and the bottom of the actuator surface, the change in upwash ΔU_z closely matches that predicted by the model at $z/D = 0.45$.

Contrarily, the discrepancies between the predicted and experimental curves grow when moving toward the top of the actuator, namely in the areas beyond the projected frontal area $y/D > 0.5$. At the top of the surface $z/D = 0.5$, this can likely be attributed to the blockage and flow structures associated with the supporting frame, as well as the supporting structure of the top wing. As discussed in reference to Figure 9.7, the corners of the supporting frame for the baseline case emitted vortical structures given the change in inflow angle induced by the actuator blockage. Given the change in the net blockage when adding the top wing (induced by larger actuator thrust, wing, and wing support structure), the simplified superposition of vertical velocities does not hold.

A similar discrepancy is evident at $z/D = 0$, though with a closer to systematic offset as compared to the top case. Here, the offset is established beyond $y/D > 0.4$, which coincides

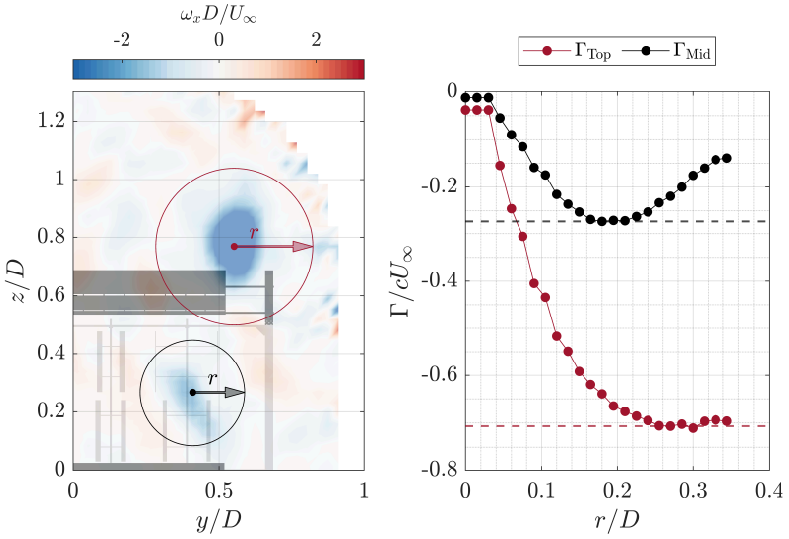


Figure 9.11: (Left) Normalized streamwise vorticity for the case with wings at $x/D = 2$. The vortex cores for the tip-vortices stemming from the top (red) and middle (black) wings are taken as the location of maximum streamwise vorticity magnitude. The normalized radii of the circles around the vortices are $r/D = 0.27$ and $r/D = 0.18$ for the top and middle vortices, respectively. (Right) Convergence of chord-normalized circulation with increasing radius of surface integration. The dashed lines indicate the value at which the gradient falls below 1%, corresponding to circulation values Γ_{Top}/cU_∞ = -0.71 and Γ_{Mid}/cU_∞ = -0.27.

with the lateral position of the vortex core. Hence, this is likely attributed to the notable stretching of the middle wing vortex induced by the dominant structure from the top wing. As the modeled distribution assumes a symmetric point vortex, vorticity and subsequent induced flow towards the right of the vortex are overestimated by the model, evident by the curve fitting shown in Appendix D.2. Despite these discrepancies, the upwash in the projected frontal area of the rotor is adequately predicted using the simplified model, highlighting the dominance of the streamwise vortical structures towards the induced recovery mechanism.

9.4.3 Available power

The contours shown in Section 9.4.1 visually confirm a wake deformation when adding lifting wings, with general convection of the wake outward from above the rotor, whilst high momentum flow is injected from the sides. To further highlight the efficacy of the lifting wings towards wake recovery, the available power for potential downstream MRS is quantified using the coefficient of available power f_{AP}. The same analysis has been performed in previous chapters (Chapters 4 and 8) to highlight the replenishment of high momentum flow inside a selected domain. The profiles of the mean streamwise flow component shown in Figure 9.9 within the projected area gave an idea of the mean flow as a function of height. Given the symmetry of this system, f_{AP} is computed using only half of the actuator surface using:

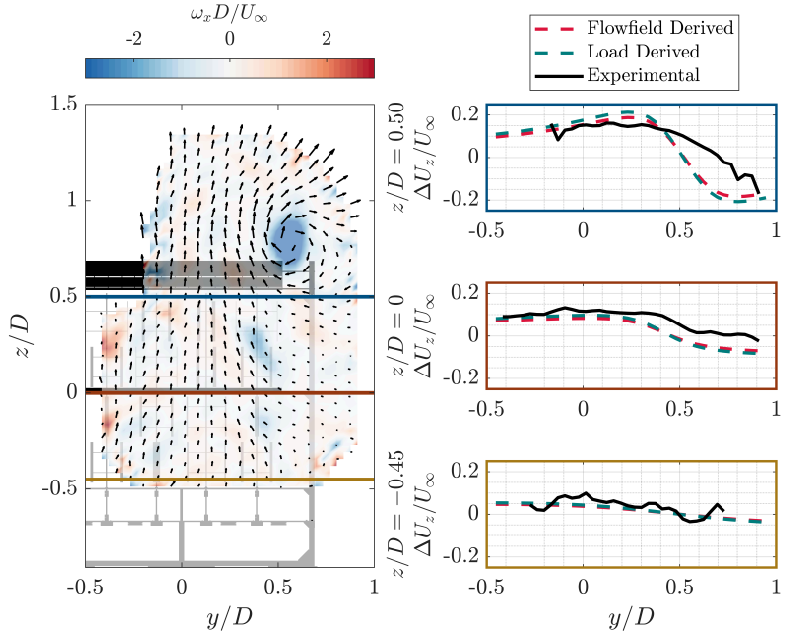


Figure 9.12: (Left) Normalized streamwise vorticity at $x/D = 2$ for the case with wings. The horizontal lines correspond to constant heights $z/D = -0.45$, 0, and 0.50. (Right) The distribution of the change in upwash between the wing and baseline case $\Delta U_z = U_{z,\text{Wing}} - U_{z,\text{Baseline}}$ at the constant heights marked at $x/D = 2$. The flowfield-derived and load-derived distributions correspond to those listed in Table 9.4, and the experimental distribution is extracted from the flowfield measurements directly.

$$f_{\text{AP}}(x, y_0, z_0) = \frac{2}{HD} \iint_S U_x^3(x, y, z)/U_\infty^3 \text{dzdy}, \tag{9.6}$$

where U_x^3/U_∞^3 is the available power at a select cross-stream plane x. The surface integral is computed within half of the projected frontal area ($S = HD/2$), which is centered at y_0, z_0 in the lateral and axial directions, respectively. A distribution of the available power at a cross-stream plane of $x/D = 2$ is shown in Figure 9.13 for the baseline and with the wing case. The projected frontal areas in which the surface integral is computed are shown via black and red delineated rectangles for the baseline and the wing case, respectively. The coefficient of available power as a function of cross-stream position is shown on the right panel. The value at $x/D = 2.5$ for the wing case is absent due to the incomplete data within the actuation area, as shown in Figure 9.8. Across all measurement planes, the available power behind the case with the lifting wing is higher than the baseline case. At $x/D = 1.0$ and 1.5, the wing cases increase the available power by a factor of 1.1, whilst at $x/D = 2.0$, the factor increase is 1.4. The baseline case exhibits a local maximum at $x/D = 1.5$, which is likely an artifact of the diminishing pockets of high-speed flow resulting from the closely spaced rotors balancing with the ongoing expansion in the near-wake.

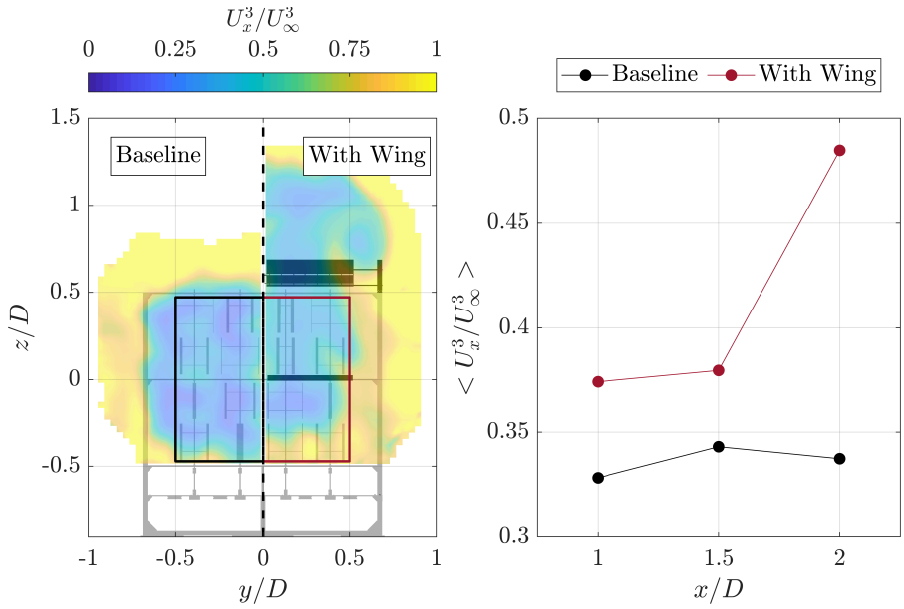


Figure 9.13: (Left) Spatial distribution of available power at $x/D = 2$ for the baseline and with wing cases. The black and red delineated boxes indicate the regions where the coefficient of available power is computed for the baseline and wing case. The vertical dashed line indicates the symmetry plane $y/D = 0$. (Right) The available power is a function of the downstream location.

9.4.4 Momentum recovery process

Thus far, the impact of the trailing vortex system from the wings on the wake topology of the MRS has been discussed in reference to the flowfields, and its efficacy confirmed via a discussion of the available power. As in Chapter 8 and in previous works by [25, 76, 84, 85], a common method to quantify the advective and turbulent contributions towards the wake recovery is the RANS equation in the streamwise direction. Given that this study measured the time-averaged wakes, a similar approach to the aforementioned studies can be performed using the RANS equation, denoted as follows:

$$U_x \frac{\partial U_x}{\partial x} = -U_y \frac{\partial U_x}{\partial y} - U_z \frac{\partial U_x}{\partial z} - \frac{1}{\rho}\frac{\partial p}{\partial x} - \frac{\partial \overline{U_x' U_x'}}{\partial x} - \frac{\partial \overline{U_x' U_y'}}{\partial y} - \frac{\partial \overline{U_x' U_z'}}{\partial z}, \tag{9.7}$$

where U_x, U_y, U_z are the time-averaged streamwise, lateral, and axial flow components, respectively. The values denoted with primes are the root-mean-square fluctuations concerning the temporally averaged values in each direction. The equation is rearranged such that the contribution of the advection and Reynolds stress terms towards the streamwise momentum advection term $U_x \frac{\partial U_x}{\partial x}$ can be evaluated. Similar to the case of [25, 85], the viscous terms are neglected due to the sufficiently high diameter-based Reynolds number of $2.3{\times}10^5$.

The available terms of Equation (9.7) are presented as contour plots at a cross-stream position of x/D = 2 for the baseline and with wing cases in Figure 9.14. As in Figure 9.13,

the two cases are shown on the same plot and distinguished at the symmetry line $y/D = 0$ via a black dashed line. The black and red delineated boxes denote the projected frontal area of the actuation surface of the MRS. The black markers indicate the wake shape at $U_x/U_\infty = 0.9$. The RANS term for each tile is provided at the bottom of the tile, with the first and second rows showing the advective and Reynolds stress terms, respectively. The in-plane spatial derivatives $\partial/\partial y$ and $\partial/\partial z$ are calculated using a second-order central difference scheme. The pressure is not measured in this experiment, so the term is omitted from this analysis. Furthermore, the terms containing the streamwise derivative ($\partial/\partial x$) are omitted, as the large spacing between the measurement planes does not allow for their calculations.

Given the arrangement of Equation (9.7), red and blue regions indicate a positive and negative contribution towards the streamwise momentum recovery, respectively. The vertical advection shows a concentration of blue and red at the top and bottom of the wake for the wing case, respectively. At the top, this corresponds with the interface of the displaced wake with the freestream flow. Below this, at $z/D = 1.0$, there is a red region, corresponding to the transition from the MRS wake to the wake core of the top wing, evident in Figure 9.8 and Figure 9.13. A similar region of lesser magnitude is seen at $z/D = 0.16$ due to the middle wing. At the bottom of the wake, the red region corresponds to the injection of high-momentum flow. In general, the baseline case exhibits much lower magnitudes in the redistribution of streamwise momentum. Notably, there are patches of positive contribution near the corners of the actuator surface, both on the top and bottom, presumably related to the induced flow of the supporting frame.

The lateral advective terms complement those in the vertical direction. For the case with wings, a strong negative region is present at the edge of the wake that has been ejected out, corresponding to an ejection of low momentum flow. Meanwhile, along the edge of the actuator surface $y/D = 0.5$, positive values persist due to the contraction of the wake, and hence an injection of high-momentum flow. Near the edge of the middle wing $z/D = 0.1$, a region of blue is present due to the fluxes induced by the trailing vortex. Similar behavior is seen at the vortex of the top wing at $z/D = 0.8$. The baseline case does not demonstrate any strong negative magnitudes in lateral flux. However, a region of positive advection exists about the wake perimeter corresponding to the wake expansion.

In general, the Reynolds stress terms are close to an order of magnitude lower than the advective terms for the case with a wing, highlighting the dominance of the advective process imposed by the trailing vortex system. For the baseline case, the advective and Reynolds stress terms are of similar order within the wake area.

9.4.5 Kinetic energy flux

The discussion in Section 9.4.4 sheds light on the process of redistributing momentum in the wake. However, to get an idea of the kinetic energy flux in the wake, the time-averaged mean kinetic energy (MKE) budget is examined. As before, only the streamwise component is considered, given that this is the main component extracted by the wind turbine. The approach is the same as taken in Chapter 8 and follows the method of [67]. Hence, upon taking the volume integral of Equation (4.6), the divergence theorem can be applied to rewrite the terms to a surface integral form [144]. The vertical and lateral kinetic energy fluxes due to the mean flow components can thus be written as $0.5U_zU_x^2$ and $0.5U_yU_x^2$,

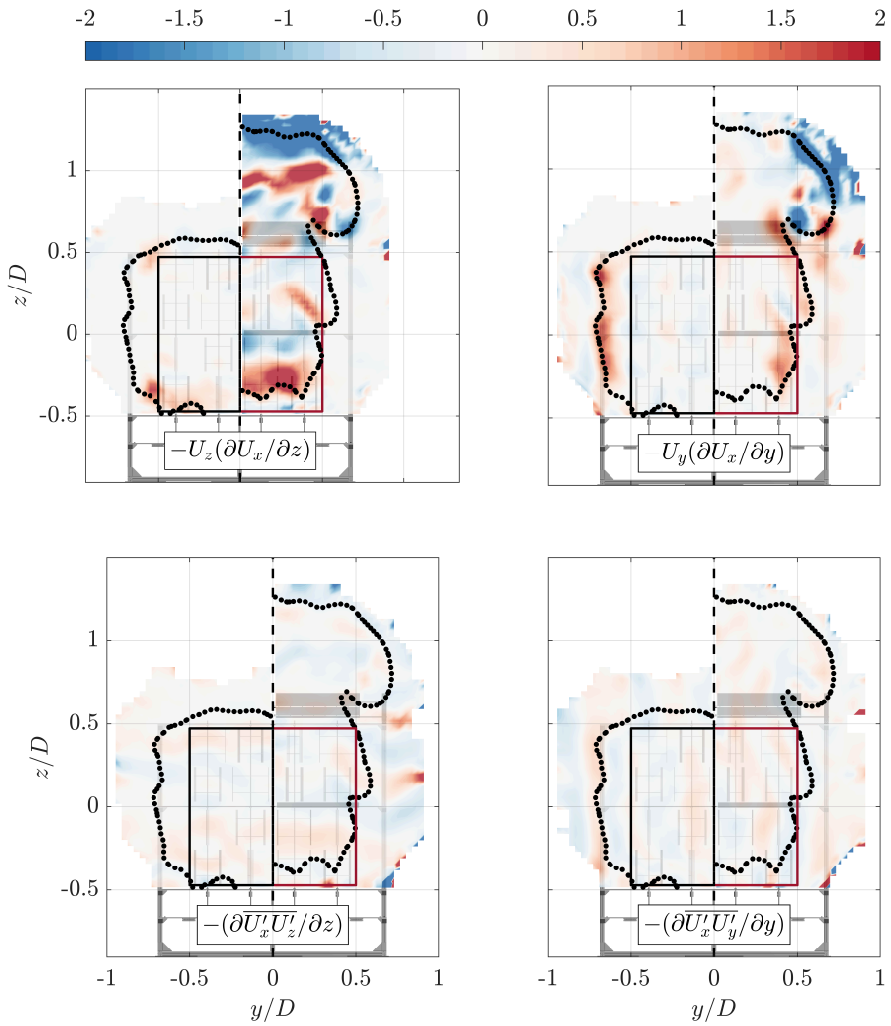


Figure 9.14: Spatial distributions of the advective and Reynolds stress terms from the RANS equations Equation (9.7) at $x/D = 2.0$, labeled at the bottom of the MRS. The left and right sides of the plots correspond to the baseline and with wing case, separated by a black dashed line at the symmetry plane $y/D = 0$. The black and red delineated boxes indicate half of the projected area of half of the actuation surface for the baseline and with the wing case. The black markers indicate the wake shape, where $U_x/U_\infty = 0.9$.

respectively. Similarly, those due to the turbulent components can be written as $U_x\overline{U_x'U_z'}$ and $U_x\overline{U_x'U_y'}$, respectively. The spatial distribution of the normalized flux terms at $x/D = 2.0$ for the baseline and with wing case is shown Figure 9.15. As before, the vertical black dashed line denotes the symmetry plane between the two cases, and the flux term is shown noted at the bottom of each tile, with the top and bottom row denoting the flux due to mean and turbulent flow, respectively.

The fluxes confirm the modes of operation discussed in relation to the in-plane velocity vectors in Section 9.4.1. The case with wings demonstrates a significant vertical flux extending throughout the entire projection of the actuator plane. The largest magnitudes are concentrated along the span of the top wing with some smaller regions near the middle wing, consistent with the profile shown in Figure 9.9. Meanwhile, the baseline case does not demonstrate any significant flux, with small magnitudes of positive vertical flux concentrated at the bottom edge of the actuator surface. The baseline case demonstrates minimal lateral flux concentrated in the region beyond the MRS frame at approximately $y/D = -0.7$. Conversely, the flux for the wing case shows a notable component inward towards the actuation surface, consistent with the wake contraction discussed in Section 9.4.1. Beyond the top wing, the flow moves outward following the induced flow of the tip vortex. As in the case with the RANS terms discussed in Section 9.4.4, the fluxes due to turbulence are an order of magnitude lower than the mean flow terms, once again highlighting the driving advective process in the wake recovery.

The distributions of the net normalized flux (sum of mean and turbulent) across the top and side surfaces of the actuator S_1 and S_2 are shown in Figure 9.16. Given the convention shown in Figure 9.15, positive flux on the top surface S_1 indicates movement out of the control volume, whilst a negative flux on the side surface S_2 indicates movement into the control volume. The distributions are shown across all measurement planes, with the dashed and solid lines denoting the baseline and wing cases. The black dashed lines indicate the boundaries of the actuator surface, with the lateral range of S_1 as half of the diameter $0 \leq y/D \leq 0.5$.

About the top surface S_1, the baseline case exhibits low negative magnitudes of flux compared to the wing case. These negative magnitudes likely originate from the intrinsic contraction of the individual rotor wakes, as observed in Chapter 4 and in previous works by [25]. Beyond the edge of the actuator surface at $y/D = 0.9$ the flux becomes positive due to the vorticity shed by the MRS frame, as discussed in Section 9.4.1. Meanwhile, the case with wings demonstrates a significant vertical flux above the actuator plane, induced by the top wing trailing vortex. In the most upstream measurement plane $x/D = 1.0$, there are significant fluctuations in the magnitude as the individual rotor wakes are still coherent and displaced upward through the boundary. When moving downstream, these fluctuations gradually subside as the MRS wake becomes more uniform and transitions to a single wake. Towards $y/D = 0.7$ the fluxes become negative as the center of the top wing vortex is surpassed. For the case $x/D = 2.0$, the flux does not become negative within the measurement domain due to the decrease in induced downwash as the top wing vortex convects upward, as well as the blockage effects of the frame and actuator. In general, the flux decreases when moving from the middle to the actuator surface to the edge.

On the lateral surface S_2, the baseline exhibits low magnitudes of positive flux across all measurement locations. Consistent with the discussion in Section 9.4.4, this is attributed to the ongoing expansion of the wake. As in the upper control surface, the fluctuations are due to the coherence of the individual rotor wakes near the MRS. The case with wings demonstrates a high magnitude of negative flux as flow is injected from the side of the rotor, induced by the trailing vortices. This negative flux persists across the entire height of the MRS, with the highest magnitudes across all measurement planes near the top at $z/D = 0.7$, coinciding with the height of the vertical convecting wing-tip vortex. A local

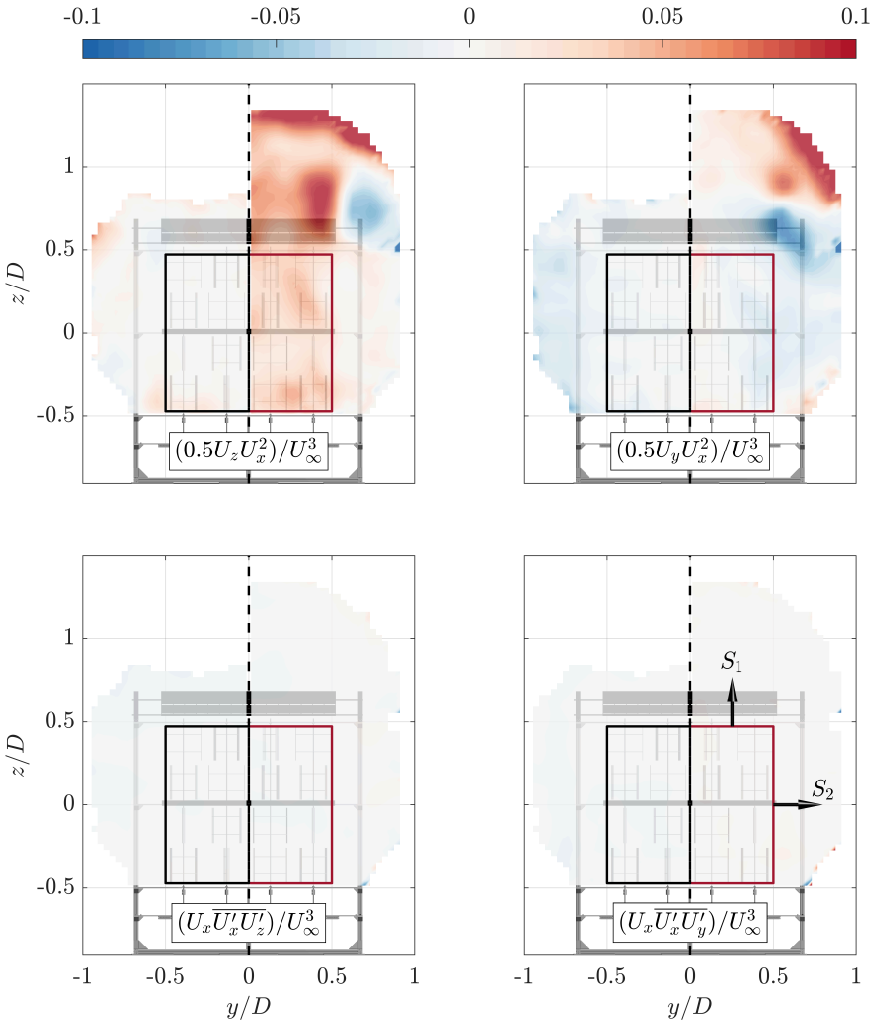


Figure 9.15: Spatial distributions of the mean and Reynolds velocity components' streamwise kinetic and energy fluxes, labeled at the bottom of the MRS. The left and right sides of the plots correspond to the baseline and with wing case, separated by a black dashed line at the symmetry plane $y/D = 0$. The black and red delineated boxes indicate half of the projected area of half of the actuation surface for the baseline and with the wing case. The labels S_1 and S_2 denote the lines across which the fluxes are computed in Figure 9.16 and Figure 9.17.

maximum in flux magnitude is also apparent near $z/D = 0$ at $x/D = 1.0$ and 1.5 due to the induced flux of the middle wing trailing vortex.

The line integral of the flux distribution across S_1 and S_2 is shown for the baseline (black) and wing case (red) as a function of cross-stream location Figure 9.17 is shown in Figure 9.16. The line integral is computed within the domains contained within the black dashed lines indicated in Figure 9.16 and normalized by $L_iU_\infty^3$, where L_i is the length of the

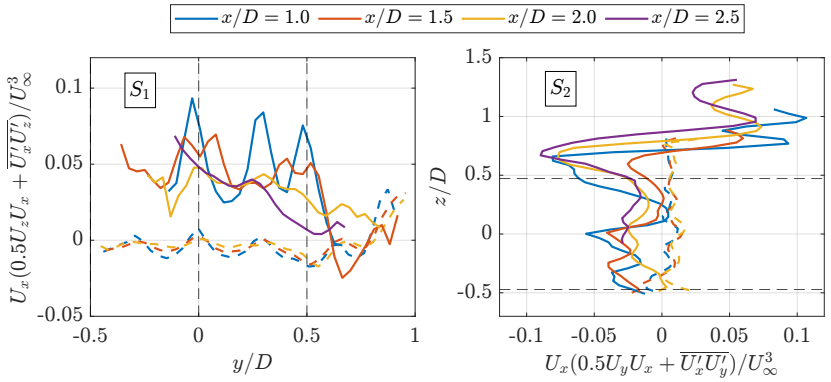


Figure 9.16: Distributions of (left) axial and (right) lateral flux of kinetic energy about the top S_1 and side S_2 surfaces of the actuator plane. The axial flux is evaluated at $z/D = (H/2D)$ and the lateral at $y/D = 0.5$. The dashed and solid lines correspond to the baseline and wing cases. The black dashed lines denote the edges of the domain in which the line integral of the flux is computed, shown in Figure 9.17, corresponding to $0 \leq y/D \leq 0.5$ and $-H/2D \leq z/D \leq H/2D$.

integration domain for surface i. Here, $L_1 = D/2$, and $L_2 = H$. Circular and square markers correspond to fluxes across S_1 and S_2, respectively.

The line-integrated flux across S_1 for the wing case demonstrated the highest magnitudes due to the significant upwash of the wake. The magnitude decreases moving through the wake due to the diffusion and convection of the top wing tip-vortex, with an increase in magnitude by a factor of 10 compared to the baseline case at $x/D = 2.0$. Meanwhile, the factor increase in the integrated flux across S_2 with wings is two compared to the baseline case at $x/D = 2.0$.

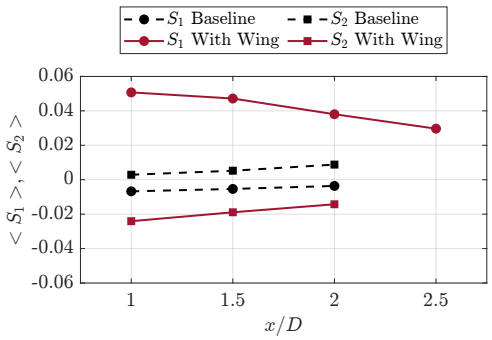


Figure 9.17: Line-integrated fluxes about surfaces S_1 and S_2 for the baseline and with wing case. The values are normalized by $L_iU_\infty^3$, where L_i is the length of the considered domain for $i = 1, 2$ surfaces. In this case, $L_1 = D/2$ within the domain $0 \leq y/D \leq 0.5$ and $L_2 = H$ within the domain $-(H/2D) \leq z/D \leq (H/2D)$.

9.5 Conclusions

The work in this chapter presents the results from the first experimental campaign that measures the near wake of a VAWT-based MRS system. Additionally, the potential of a de-coupled wake recovery and steering strategy through external lift-generating devices has been studied. Wings were designed to maximize the lift given the size limitations imposed by the MRS frame, tunnel dimensions, and low Reynolds number.

As with previous numerical and experimental studies of MRS, the wakes of the individual rotors in the actuation surface were discernible in the near wake. Although the gradual process of them combining into a single wake structure is evident, considering the profiles of streamwise velocity deficit at the most downstream measurement distance of $x/D = 2$ suggests that this state has not yet been reached. Furthermore, pockets of high-speed flow stemming from the gaps between the rotors are evident for both the baseline case and that with wings. The working principle of the wings was verified by considering the streamwise vorticity and the induced upwash in the wake at the symmetry plane, which reached beyond 20% of the freestream velocity near the top wing, decreasing to approximately 10% in the remaining actuator area at $x/D = 2$. Meanwhile, for the baseline case, the upwash does not surpass 3%. The main conclusions are summarized as:

- The available power in the wake for a hypothetical downstream MRS increased by a factor of 1.4 at $x/D = 2$ when using the wings for wake steering.
- The wings increased the thrust force of the actuator by a factor of approximately 2%, whilst increasing the drag of the system as a whole by approximately 40%.
- The circulation of the top wing computed using the load-derived lift coefficient matched within 9% with that derived using the flowfield at $x/D = 2$. Meanwhile, that of the middle wing showed a larger discrepancy with a percentage difference of 25%, likely due to the uncertainties associated with the flowfield-derived circulation of the vortex in the wake of the actuator surface. Nonetheless, the induced upwash of the vortices predicted using a point-vortex model matched well with the experimental distributions at discrete heights in the wake.
- An analysis of the mechanisms driving the momentum exchange and wake recovery was performed using the terms of the streamwise RANS equation. Analogous with the negative pitch cases for the "vortex generator mode" for isolated VAWTS (discussed in Chapters 4 and 8), the dominant wingtip vortices induce a significant upwash of the wake, expelling low momentum flow out from above the rotor, whilst injecting high momentum flow through the sides.
- The flux of kinetic energy through the control surface (defined as the projected frontal area of the rotor actuator plane) demonstrates an increase in magnitude on both the upper and lateral surface across all measurements when using the wings compared to the baseline case. An increase in line integrated flux at $x/D = 2$ by a factor of 10.5 and 1.6 at the top and edge of the actuator plane is found between the baseline and case with wings.

This investigation is the first to explore the potential of external lifting devices to deflect the wake of an MRS. Although the results are very promising, it is important to

consider the limitations and future avenues of research that could lead to improvements and a more complete assessment of the feasibility of this control strategy. A notable limitation to consider in this experiment is the influence of blockage. The blockage ratio when considering the frontal area of the MRS actuator surface (neglecting the support frame and wings) is 0.28. This does not consider the fact that air is free to pass through the rotor system. Nonetheless, the blockage would impact the magnitude and uniformity of the inflow velocity. Furthermore, introducing the wings, which induce a significant upwash, will eventually steer the wake outside the projected frontal area of the OJF outlet. This can be visualized by the smoke visualizations in Figure 9.6. However, this effect is minimized by focusing on the near wake. Measurements of the inflow with and without the MRS combined with numerical simulations would be required to quantify the derived blockage corrections, which would be specific to this geometry, considering the supporting structure and blade designs. Nonetheless, the results presented in this chapter provide a credible proof-of-concept of the novel VAWT-based MRS. As hinted at before, an evaluation of the far wake was not feasible given the scale of the setup. Still, it would be critical to evaluate the full potential of the external lifting wings for wake recovery. Regarding the wake dynamics, several avenues are still open that could contribute to developing a more feasible application of this control strategy, which are discussed in Chapter 10.

V

Conclusions and outlook

10

Conclusion

This chapter concludes this thesis by providing an answer to the following research questions first introduced in Chapter 1:

1. *What is the wake re-energization process of a high-energy density VAWT wind farm and how is it modified when using established wake control strategies?*
2. *What are the driving mechanisms that characterize the wake of the X-Rotor vertical axis wind turbine?*
3. *How does the addition of de-coupled cross-flow generating devices impact the near wake of a VAWT-based multi-rotor system (MRS)?*

Furthermore, recommendations for future work are discussed.

10.1 Key findings

Research Question 1

What is the wake re-energization process of a high-energy density VAWT wind farm and how is it modified when using established wake control strategies?

The wake of a lab-scaled high-density VAWT farm was measured in Chapter 4. The wake topography and kinetic energy replenishment mechanism of the wake were elucidated with and without the passive wake control strategy coined the "vortex generator" mode.

The theory behind the "vortex generator" VAWT wake control strategy using fixed-blade pitch was described, emphasizing the expected wake re-energization modes when blades are pitched in versus out. The wake control strategy's effectiveness was confirmed by the streamwise vortex topology within the farm. Pitching the blades inward energizes upwind vortices, drawing momentum from above and below the rotor while causing significant lateral wake deflection, aligning with thrust measurements of an isolated rotor. Conversely, pitching the blades outward energizes vortices downwind, inducing wake-upwash and injecting high-momentum flow from the rotor's sides. While the wake dynamics for the tested modes of operation resemble those of an isolated rotor tested by [25], the superposition of the wakes in the farm shed light on the cumulative trailing vortex interactions and subsequent re-energization process.

In the baseline case, the second and third rotors generate shorter wake lengths, likely due to their reduced thrust. The streamwise vorticity system of the downwind rotors increasingly resembles that of a bluff body cylinder, with dominant counterclockwise and clockwise rotating structures on the windward and leeward sides, respectively. These structures lead to notable axial contraction and lateral expansion of the wake, as seen in the enhanced advective and turbulent flux of streamwise kinetic energy from above and below the rotor plane.

Under the negative pitch control strategy, a dominant counter-rotating vortex pair forms downwind between the top and bottom of the second and third rotors. This induces significant lateral ejection of the wake from the windward side while drawing high-momentum flow from the leeward side. This effect accumulates within the wake, as evidenced by the increased advective flux of kinetic energy from the leeward side.

Similar to the isolated rotor case, the positive pitch mode generates the highest magnitudes of advective flux in kinetic energy. Consistently observed behind each rotor, the wake is pushed outward from the windward side while high-momentum flow is injected from above and below. Analyzing the surface-integrated kinetic energy flux behind each rotor in the farm reveals a gradual decline in flux through the top and bottom surfaces and along the windward side. Unlike the previous cases, significant lateral wake ejection causes the wakes from neighboring columns to interact with the central measurement column, starting just downwind of the second rotor.

Examining the available power in the wake provides insight into the effectiveness of these control strategies. Across the entire measurement domain, the positive pitch case yields the highest available power, followed by the negative pitch case, with the baseline case performing the lowest. However, due to the ejected wakes from neighboring columns

entering the flow domain, the available power in the positive pitch case is systematically lower behind the third rotor than in previous volumes. While the negative pitch case also deflects the wake laterally, the effect is less pronounced, leading to a more consistent distribution of available power across the rotors. As a result, the disparity between the two “vortex generator” modes narrows in the final measurement volume behind the third rotor. Meanwhile, the baseline case exhibits systematically higher available power behind the second and third rotors, attributed to its shorter wake lengths and the influence of the dominant counter-rotating vortex pair discussed earlier.

Research Question 2

What are the driving mechanisms that characterize the wake of the X-Rotor vertical-axis wind turbine?

The wake within the volume of rotation was measured and discussed in Chapter 5. The wake is concentrated within the projected frontal area of the rotor, following the coned shape. The trailing vorticity stemming from the blade tips varies in a rotational direction depending on the quadrant in which they are generated, consistent with the H-type geometry. The shed vorticity within the volume of rotation follows an extremely elliptical shape due to the coned nature of the X-Rotor blades. The intersection of these curved shed vorticity structures induces cross-flow components of varying magnitude and direction as a function of height.

The near wake measurement ($x/D \leq 1.6$) of the upper blade tips in Chapter 7 demonstrated the interactive process between the upwind and downwind generated trailing vortices, which is intrinsic of VAWTs. Similar to the H-Type, an intrinsic asymmetry in favor of the windward side is evident, with an upward and inward motion of the trailing vortices, causing a local lateral contraction of the wake near the blade tips. The measurements at $x/D = 0.26$ highlighted a spanwise variation in the standard deviation magnitude of the wake following the blade in the windward passage. Given the coned blades and variation in tip-speed ratio along the span, this is likely due to spanwise variations in shed vorticity magnitude.

The full wake measurements in Chapter 8 elucidated further on the change in the overall wake shape up to $x/D = 6$. Near the top and bottom blade tips, the vortex-induced lateral contraction is accompanied by the ejection of the wake from above and below the projected rotor surface. Meanwhile, near the root region, the wake ejects laterally on both the windward and leeward sides. This mode of recovery was confirmed when considering the advective contributions in the lateral and axial direction towards the mean kinetic energy. As with the H-type rotor, the turbulent contributions are concentrated along the wake perimeter.

The "aerodynamic gearbox" concept of the X-Rotor was experimentally tested in Chapter 6. The secondary rotor was designed to achieve a target cycle averaged thrust coefficient based on the balance between the primary rotor torque. The change in primary rotor torque was measured when adding the secondary rotors and compared with the predicted change in torque based on a simplified moment arm induced by the secondary rotors. The values in thrust coefficient had a 3.4% difference, demonstrating the successful implementation of the aerodynamic gearbox concept.

The wake of the secondary rotor was spatially and temporally investigated in Chapter 6. At peak secondary rotor load (when it is perpendicular to the flow), intense turbulent mixing rapidly diffuses the trailing vorticity and is mixed with the vorticity of the secondary rotor blades. As the secondary rotor moves through the upwind windward quadrant, its load decreases while the primary rotor's blade load rises, shedding a more coherent tip vortex. The secondary rotors accelerate the trailing tip-vortex diffusion, reducing in-plane velocity gradients and shifting kinetic energy flux from advective to turbulent contributions. Despite increased vortex diffusion due to the secondary rotors, the circulation of trailing tip vortices remains broadly conserved compared to baseline cases, with a linear increase in vortex strength observed through the upwind windward quadrant.

The available power in the wake for the X-Rotor was evaluated in Chapter 8 up to $x/D = 6$. The positive pitch yields consistently higher available power in the wake, preceded by the negative and then the baseline. Unlike the case with a straight-bladed VAWT, there is an absence of a symmetric counter-rotating vortex pair (assuming no ground and uniform inflow) between the upper and lower blade tips. While the streamwise vorticity system is modified as expected with the passive blade pitch for the upper blades, the lack of an equal and opposite pair from the bottom blade tips and the additional complexity of a root vortex yields a distinctly different wake topology. This is consistent with the flux of streamwise kinetic energy flux through the top and side surfaces of the rotor, which showed minimal contributions from the bottom surface.

Research Question 3

How does the addition of de-coupled cross-flow generating devices impact the near wake of a VAWT-based multi-rotor system (MRS)?

The concept of a de-coupled cross-flow generating device for an accelerated wake recovery of an MRS was investigated in Chapter 9. A lab-scaled novel block-design MRS made of VAWTs was fabricated and tested in TU Delft's OJF, focusing on load and near-wake measurements.

Prandtl's lifting-line theory was used to formulate the working principle for the design of the cross-flow generating devices of the MRS. The objective of maximizing the upwash in the wake translates to a maximization of the circulation of the horseshoe vortex system. In practice, this could be achieved by maximizing the chord length of the devices or the lift coefficient. Given the low operating wind speed of the tunnel (limited to 4 m/s to ensure reasonable tip-speed ratios and thrusts of the VAWT actuator surface), a multi-element wing design was adapted for maximizing the lift force. Furthermore, the overall chord length was kept at a moderate size to minimize the blockage effect in the tunnel and manufacturing cost while keeping modularity. The final design was a 3-element wing with a 504mm chord and lift coefficient of $C_L = 1.97$. A second wing was added to the middle of the MRS to increase the net upwash in the wake. Given the constrained space of the middle wing on the frame, a single-element wing design with a smaller chord of 304mm and a lift coefficient of $C_L = 0.53$.

As the power performance of the MRS system was not measured, a load balance was used to quantify the thrust of the system with and without the cross-flow generating devices.

The thrust coefficient of the overall actuator surface of the MRS increased from $C_T = 0.70$ without wings to $C_T = 0.71$ with wings, presumably due to the ducted effect the wings induce. Taking the frontal area of the VAWTs as an idealized actuator disk, an increase of 1.4% in C_T corresponds to a 0.83% increase in power in C_P. Meanwhile, the overall drag of the system increased by 38.6% when adding the wings. Given the bottom-fixed nature of the setup, the excessive drag did not pose any structural risk. However, this is a critical design parameter to consider for future applications to avoid overturning moments.

Given the low inflow turbulence and uniform inflow, as well as the symmetric operating condition of the MRS, the wake of the baseline MRS and the wings were symmetric about the vertical axis. As in previous numerical and experimental studies of MRS, the wakes of the individual rotors in the actuation surface were discernible in the near wake. Although the gradual process of them combining into a single wake structure is evident, considering the profiles of streamwise velocity suggests that this state has not yet been reached. Furthermore, pockets of high-speed flow stemming from the gaps between the rotors are evident for both the baseline case and that with wings.

The cross-flow generating devices create large-scale streamwise tip-vortices in the wake, which induce a significant upwash, analogous to the negative pitch of the "vortex generator" strategy. The wake contracts laterally whilst being ejected out above the rotor. The flowfield-derived circulations match the load-derived values with a high degree of accuracy, validating the working principle and design process of the wings. Meanwhile, the baseline case does not exhibit any dominant streamwise vortical structures other than the alternative structures stemming from the blade tips of the individual VAWTs, which diffuse before reaching $x/D = 2.0$. At the furthest measurement plane of $x/D = 2.0$, the upwash in the wake reached 20% of the free stream velocity with wings attached, whilst not surpassing 3% for the baseline case.

The available power in the wake increased by a factor of 1.4 at $x/D = 2.0$ when using wings compared to the baseline case. An analysis of the mechanisms driving the momentum exchange in the wake revealed the spatial distribution of sources and sinks for streamwise momentum.

The introduction of cross-flow generating devices significantly increased the advective contribution, both in the injection of high-momentum flow laterally and the expulsion of low-momentum flow vertically. The flux of kinetic energy through the top and side of the projected frontal area of the actuator surface revealed an order of magnitude increase with the wings, with an increase in line-integrated flux at $x/D = 2.0$ by a factor of 10.5 and 1.6 at the top and side, respectively.

10.2 Outlook and recommendations

10.2.1 VAWT wind farms

1. **Inflow conditions**: The wind farm wake measurements in Chapter 4 used uniform and laminar inflow. However, realistic wind farms encounter conditions that stray from these idealized cases, such as turbulent inflow and sheared inflow velocities characteristic of the atmospheric boundary layer. Experimental results for an isolated rotor are still lacking under realistic conditions using the "vortex generator" control mode. A parametric study to evaluate the influence of inflow turbulence, shear

inflow, and passive blade pitch angle on the power performance, structural loads, and wake recovery rate would be valuable to understanding the efficacy of this control strategy under realistic conditions. Scaling up to the farm case would introduce further metrics to consider, such as the impacts of the heavily sheared inflow of downstream rotors imposed by the induced cross-flows of the "vortex generator" mode.

2. **Turbine arrangement**: A grid layout was used in Chapter 4 to mimic the most detrimental case for wake losses and highlight the benefits of the wake control technique. However, the layouts of wind farms can be optimized when considering a wide range of metrics, e.g., cabling costs and meteorological conditions. However, studies have demonstrated significant overall wind farm performance benefits when considering wake control strategies during the layout optimization phase [175], depending on the particular constraints of the optimization. While the benefits of closely spaced VAWTs have been established, understanding the impacts of more organic and staggered layouts on the wake topology of a VAWT farm when using the "vortex generator" mode would be valuable for gaining insight into the efficacy of the technique in more realistic conditions.

3. **Structural implications**: As noted in Chapter 4, applying significant passive pitch adjustments can potentially increase the degree of flow separation and subsequently load fluctuations on the rotor with detrimental effects. This is, in particular, true for positive pitch adjustments, which increase the upwind quadrants more beyond the intrinsic asymmetry. Hence, including metrics such as blade load and torque fluctuations when evaluating the benefits and efficacy of the "vortex generator" control mode would provide a more holistic assessment of its efficacy and suitability for real-world applications.

4. **Active blade pitching**: In relation to the previous comment, the flexibility of active blade pitching could offer a method for amplifying the desired trailing vorticity system of the "vortex generator" mode whilst minimizing the undesired blade load fluctuations.

10.2.2 The X-Rotor VAWT

1. **Numerical validation**: As discussed in Chapter 5 and Chapter 6, the experimental results serve as an experimental database for the development of numerical models. A recent study by [176] applied the free-wake vortex model (CACTUS) to validate the experimental results presented in Chapter 5 and Chapter 7, demonstrating a high degree of similarity within the volume of rotation with no blade pitch applied. However, when using the "vortex generator" strategy, significant deviations from the experimental results were observed, highlighting the need for numerical models to capture the full three-dimensionality of the wake in such operating conditions. While the work of [176] focused on the near wake, other features of the X-Rotor are of particular interest, which have yet to be explored, such as:

    - **Spanwise flow variation**: As hinted in Chapter 5 and Chapter 7, the effective flow conditions and tip-speed ratio vary along the span of the upper and lower

blades of the primary rotor due to the cone angles. As discussed in Chapter 2, the tip-speed ratio is a critical parameter for rotor performance as well as blade-scale unsteady flow phenomena. Hence, a change in spanwise blade loading and subsequent shed vortex strength is expected, which will introduce an additional layer of three-dimensionality to the X-Rotor's wake.

- **The role of the root vortices**: Although the presence of the root vortices was observed in Chapter 8 when evaluating the time-averaged wake, the evolution of these structures and role in the near wake was not captured in Chapter 5. These structures are a byproduct of the difference in loading between the upper and lower blades. As the relative differences evolve during the rotor revolution, so do the strength and direction of the root vortices. However, the importance of these structures on the overall wake topology and mixing process is unknown.

2. **The secondary rotors**: Although the discussion in Chapter 6 shed light on the impact of the secondary rotors on the trailing vorticity and mixing process in the near wake, there are still several aspects of the secondary rotor which remain unanswered. These include:

    - **Aerodynamic coupling**: Although the work by [108] explored the optimal design of the secondary rotors for maximum power conversion between the primary and secondary rotors, the aerodynamic coupling between the primary and secondary rotors was not considered.
    - **The final design**: As highlighted in Chapter 2, the design of the secondary rotor is bound by two main drivers, namely, the allowable tip-speed (to avoid compressibility effects) and the required speed to facilitate direct drive options for the generator. These features dictate several geometric features of the secondary rotor, such as size and number of blades. Although this design space was investigated by [108], a practical design requires more inputs, which would narrow the permissible ranges in allowable tip-speed, which could be attained through higher fidelity simulations that account for coupling. Finally, the design of the mounting for the secondary rotors on the primary rotor and the parasitic drag associated with the structure has not been elucidated in detail and is of particular interest for the operational efficiency and overall efficacy in power conversion of the secondary rotors.

10.2.3 MRS

1. **Flipped lift direction**: In Chapter 9, a downward-directed lifting device was tested, leading to a vertical ejection of the wake. However, simply flipping the wings would flip the lift direction and the subsequent tip-vortex structure, leading to a vertical injection of high-momentum flow whilst the wake is ejected from the sides. The recent study of [177] performed numerical simulations of a small wind farm of MRS with external lifting devices in both configurations, highlighting the different energization mechanisms.

2. **Inflow conditions**: As with conventional wake steering techniques described in Chapter 2, inflow turbulence and velocity profile are critical to wake recovery

performance. Understanding the wake dynamics and efficacy of the wings to induce cross-flow loads with varying turbulent conditions is essential to determine the potential of this concept for offshore wind farm applications. Another important factor to consider is the inflow angle. This has been discussed by [27] in the context of closely packed VAWTs as the actuation surface of the MRS, stating their higher tolerance to varying inflow angles closely aligned to the plane compared to HAWTs. However, adding the lifting wings complicates this as yawed inflow could lead to asymmetric lift distributions and tip-vortex strengths, spanwise flow and separation, and increased drag, to name a few. Hence, depending on the wind resource, it is likely that a yawing system with similar functionality to traditional HAWTs would be required, leading to significant cost considerations in the design process.

3. **Lifting wing design**: Given the wind tunnel imposed limitations of this study, an exaggerated wing size was used to achieve a high lift at the low Reynolds number, which would most likely not be geometrically scaled for full-scale applications. Hence, a comprehensive study of wing design for full-scale applications is critical, considering performance metrics (such as lift, parasitic drag, and induced drag) and material costs, manufacturing, transport, installation, etc. A further consideration is the number of wings, locations, and spans compared to the actuator surface diameter, and relative to their lifting forces.

4. **Structural implications**: This work focused solely on the near-wake aerodynamic considerations of the MRS system with decoupled wake steering devices. The supporting frame was designed to be as stiff as possible to reduce induced vibrations and minimize the blockage. Furthermore, the frame was fixed at several points to a heavy, rigid table. For full-scale applications where even floating applications are considered (as discussed in the preliminary design by [27]), a comprehensive investigation needs to be carried out to assess the impact of the blade loads on the structural soundness of the frame. Lifting forces would have large implications on the floater design, whilst the induced and parasitic drag of the wings will induce significant moments that need to be accounted for. Furthermore, unsteady loads associated with turbulent inflow and vortex shedding are also important when considering the structural soundness and efficacy of the wings.

VI

Appendices

A

In relation to Chapter 4

A.1 Sub-volume size

As discussed in Section 4.3.3, time-resolved particle tracks are spatially and temporally binned on a Cartesian grid. The impact of the selected sub-volume size (in voxels) and the resulting vector grid resolution Δx is presented in Figure A.1. In addition to the selected sub-volume size of 128 voxels used in this paper, the sizes of 52 voxels, 92 voxels, and 152 voxels are presented, with a 75% overlap maintained for all cases. Normalized streamwise velocity U_x/U_∞ and turbulent kinetic energy (TKE) k/U_∞^2 profiles are presented, located at the symmetry plane $z/D = 0$ and at $x/D = 3.5$. Additionally, the root mean square of the differences of the quantities with respect to the 52 voxel case is presented, computed within the presented range of $-1.5 \leq y/D \leq 1.5$.

Overall, the selected sub-volume size has a minimal impact on the governing wake structure. Minor differences can be observed in the region of the maximum wake deficit, likely due to a lack of convergence at the smallest sub-volume size. Meanwhile, the TKE shows a more noticeable difference, especially at the coarsest resolution of 152 voxels. Larger sub-volume sizes will bin together regions with more discernible spatial and temporal fluctuations, mainly concentrated at the shear layer of the wake $y/D = \pm 0.5$. The root mean square of the differences at the selected sub-volume are $U_x/U_\infty = 1.7 \times 10^{-2}$ and $k/U_\infty^2 = 5.0 \times 10^{-3}$. Considering a representative value of $U_x/U_\infty = 0.2$ at the region of maximum difference, there is a relative error of 8.5%. When considering a TKE of $k/U_\infty^2 = 0.05$ in the shear layer, the relative error is on the order of 10%. Choosing a 128-voxel sub-volume with a grid size of $\Delta x = 19.9$mm captures the governing wake shape whilst avoiding convergence issues at small sub-volumes. Given the minimal gains of resolving the turbulence along the shear layer and the relative importance of the advective contributions towards the wake recovery (discussed in Section 4.4.6), the benefits of a smaller sub-volume are outweighed by the required RAM, storage, and computation time, which is 15 times higher with the smallest sub-volume size.

A

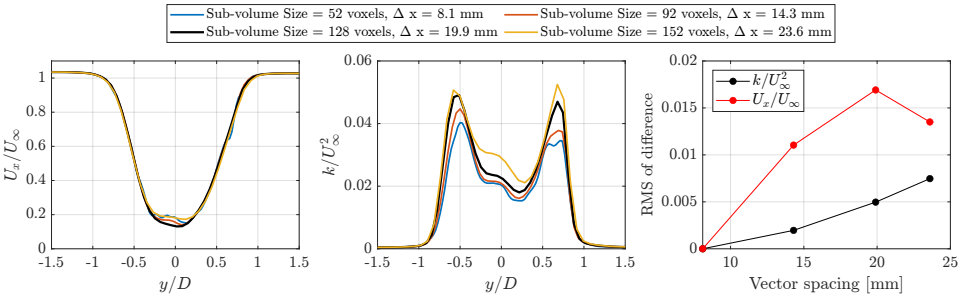


Figure A.1: Profiles of the normalized streamwise velocity U_x/U_∞ and turbulent kinetic energy k/U_∞^2 along the symmetry plane $z/D = 0$ at the cross-stream location $x/D = 3.5$. The root mean square (RMS) of the difference with respect to the sub-volume size of 52 voxels is presented for both metrics.

A.2 Vorticity fields

As described in Section 8.2, the "vortex generator" mode of operation for VAWTs for wake control relies mainly on the modification of the streamwise vorticity ω_x, which has been thoroughly discussed in Section 4.4.2. Nonetheless, for completeness, the other vorticity components, namely the axial ω_y and lateral ω_z, as shown in Figure A.2 and Figure A.3, respectively.

The lateral vorticity components ω_y for the baseline case $\beta = 0^\circ$ show a strong symmetry between the upper and lower halves of the rotor with clockwise and anti-clockwise rotating structures, respectively. Such behavior is also observed by phase-locked measurements of [41] and field experiments of [21]. For the first rotor, the vortex structure transitions from an inboard movement (towards $z/D = 0$) on the leeward half towards an outboard movement on the windward half. A similar trend has been observed by [41]. The subsequent rotors show a similar trend with overall shortened vortex lengths due to the reduction in loads of the rotors. The vortex structure from the leeward side seems to extend further than those on the windward, presumably a product of the reduction in load on the windward side due to the asymmetric wake of the first rotor, as discussed in Section 4.4.3.

For the positive pitch case $\beta = 10^\circ$, the directions of the dominant vortices remain the same as the baseline case. The structures deflect towards the windward side, consistent with the observations and discussion in Section 4.4.2.

The axial vorticity component ω_z is driven by the vortices shed along the span of the blades. For the baseline case, the dominant structure is clockwise and anti-clockwise on the windward and leeward sides, respectively. This is consistent with phase-locked measurements obtained by [41]. As in the aforementioned case, the lengths of these structures are reduced for the subsequent rotors due to the reduction in load. On the windward side, the positive shear layer is also present, concentrated around the upper section of the rotor. This can be attributed to the asymmetric load and wake profile shown in Section 4.4.3, where a switch between the dominant contributor towards curl in the z-direction dU_x/dy would switch twice near the upper windward edge of the wake (given the mushroom-like shape). This would be asymmetric on the bottom half of the rotor, but is absent due to the limited data on the bottom half of the rotor.

For the positive pitch case, the structures deflect laterally. Given the increase in the

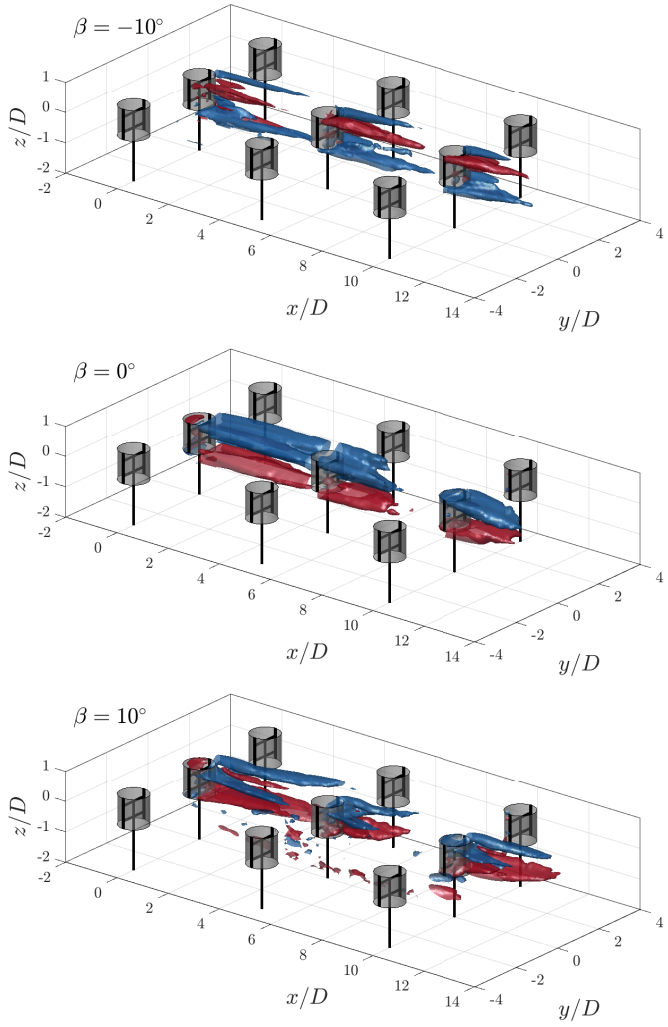


Figure A.2: Iso-surfaces of the lateral vorticity contours at $\omega_y D/U_\infty = \pm 1$ for pitch cases $\beta = \pm 10^\circ$, and $\beta = 0^\circ$. The rotors are shown at a $\theta = 0^\circ$ phase, with the gray-shaded cylinders representing the idealized actuator cylinder load.

severity of the mushroom-like shape compared to the baseline case, the second positive shear layer on the windward side is also present and remains a feature for the subsequent rotors as well, with the asymmetric pair. Finally, for the negative pitch case, the shear layer on the windward side is deflected outwards whilst that on the leeward side is contracted inward towards the core of the rotor as flow is injected more heavily for the subsequent rotors in the farm.

A

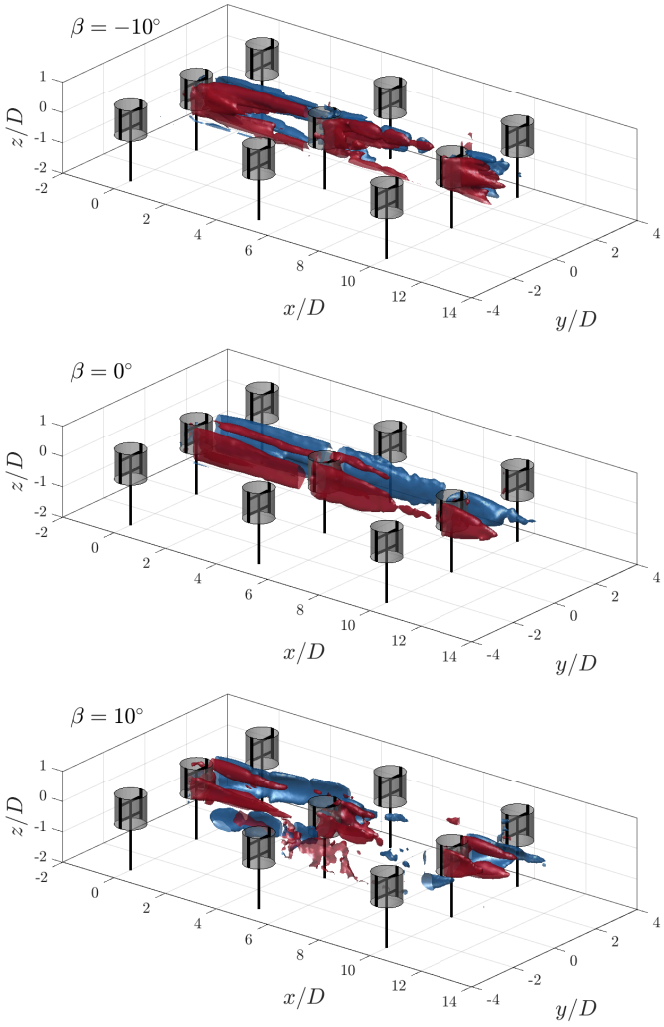


Figure A.3: Iso-surfaces of the axial vorticity contours at $\omega_z D/U_\infty = \pm 1$ for pitch cases $\beta = \pm 10°$, and $\beta = 0°$. The rotors are shown at a $\theta = 0°$ phase, with the gray-shaded cylinders representing the idealized actuator cylinder load.

A.3 Turbulent kinetic energy

As discussed in Section 4.4.6, the turbulent contributions towards the flux of mean kinetic energy within the projected volume of the central rotor column are several orders of magnitude lower than the advective contribution, in particular for the pitched cases. Turbulent inflow is of practical importance for wind farms as it greatly influences rotor performance and blade fatigue, as commented on by [178]. The turbulent kinetic energy (TKE) at discrete cross-stream distances x/D = 2.5, 7.5, and 12.5 is shown in Figure A.4 for the three pitch cases.

Behind the first rotor, the distributions of TKE are qualitatively consistent with the measurements by [25] for an isolated rotor case of the same design, with the turbulence concentrated along the wake perimeter. As commented on by [164], a longer wake perimeter is beneficial for facilitating momentum exchange due to turbulent diffusion along the shear layer. While the TKE remains concentrated within the projected frontal area of the baseline and negatively pitched case, it is ejected laterally outwards for the positive case, following the same trend discussed in Section 4.4.3. Whilst this suggests a reduction in incoming turbulent flow for the rotors in the second row, it also shifts the source of turbulent contributions towards the streamwise momentum recovery away from the projected volume of the central column.

Behind the second and third rotors, the distributions of TKE contract in the axial directions for the baseline case, following the wake shape discussed in Section 4.4.3. Whilst this suggests detrimental effects on the structural integrity of the subsequent rotors, the turbulent contributions towards the streamwise kinetic energy fluxes within the central rotor column would increase, consistent with the increases in the magnitude of Reynolds stress fluxes on S_5 and S_6 behind the second and third rotors, shown in Section 4.4.6. For the negative pitch case, the TKE remains concentrated along the laterally stretching wake on the windward side. Finally, for the positive pitch case, the concentration of TKE is absent within the projected frontal area of the central rotor column within the measurement domain, as the wakes are consistently deflected to the side. However, at $x/D = 7.5$ and $x/D = 12.5$ the regions of high TKE on the leeward side due to ejected wakes of the neighboring column gradually enter the central volume.

A

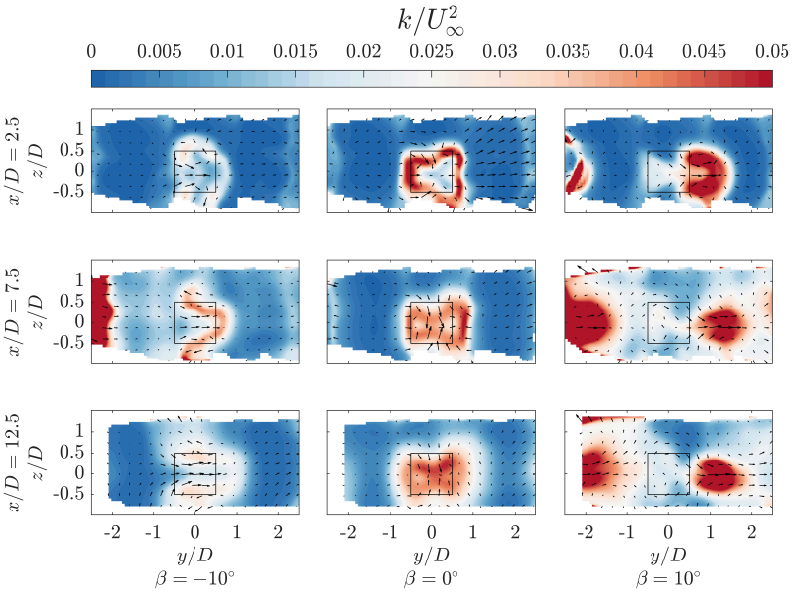


Figure A.4: Normalized turbulent kinetic energy $k = \frac{1}{2}((U_x')^2 + (U_y')^2 + (U_z')^2)$ for the three pitch cases at streamwise locations x/D = 2.5, 7.5, and 12.5. The black outlined square denotes the projected frontal area of the rotor, and the vectors show the in-plane velocity components.

B

In relation to Chapter 7

B.1 Airfoil polar

The XFOIL statically simulated polar for the NACA0021 blade used in the numerical demonstration of the load distribution in Section 7.3.4 is shown in Figure B.1. The tabulated data for the polar is made available in the data repository detailed at the beginning of Chapter 7. In this case, the static stall angle is taken as the point where the linear behavior between the lift and angle of attack ends, at α_{ss} = 9.1°, with C_L =1.02. Beyond this point, the lift continues to increase in a non-linear fashion, reaching a maximum lift of C_L = 1.1 at α_{ss} = 17°.

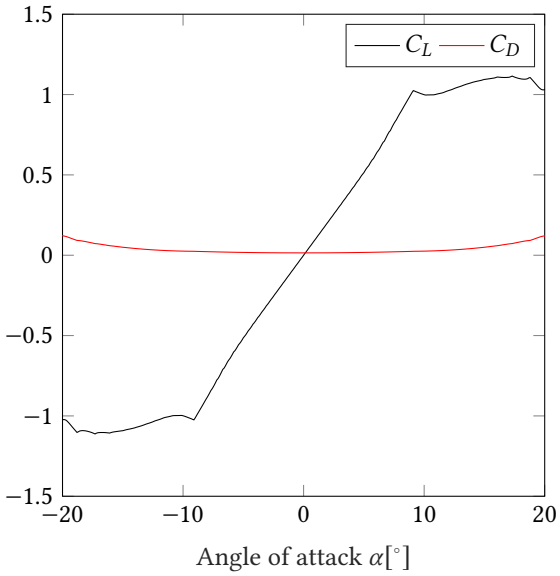


Figure B.1: Simulated NACA0021 polar using XFOIL at a Reynolds Number of 15×10^4. The lift and drag coefficients C_L and C_D, respectively, are presented between angles of attack $-20^\circ \leq \alpha \leq 20^\circ$.

B.2 Isometric view of velocity and vorticity fields

As discussed in Section 7.4.1, an isometric view of the complete set of measured fields in the wake is provided in Figures B.2 to B.4. The frontal area of the rotor is shown with a grey line at azimuth $\theta = 0^\circ$ with a black contour line outlining the wake at $U_x/U_\infty = 0.9$. The cross-stream planes for the pitch case $\beta = 0^\circ$ are x/D = [0.26, 0.4, 0.5, 0.6, 0.7 0.8, 0.9, 1.0, 1.1, 1.2, 1.4,1.6]. The cross-stream planes for the pitch case $\beta = -10^\circ$ are x/D = [0.26, 0.5, 0.6, 0.7, 0.9, 1.0, 1.2, 1.4, 1.6]. The cross-stream planes for the pitch case $\beta = 10^\circ$ are x/D = [0.26, 0.4, 0.5, 0.7, 0.9, 1.0, 1.2, 1.4, 1.6].

The normalized streamwise vorticity fields are shown in Figure B.5. Consistent with the results of [25] and the wake mechanism described in Section 7.2, the streamwise vorticity is dominated by the tip-vortices. Within the rotor's rotation volume ($x/D \leq 0.5$), there is also the presence of shed vorticity of the coned blade, as discussed in Chapter 5. For the $\beta = 0^\circ$ pitch case, coherent vortical structures are evident in the near wake shed from the respective blade and quadrants before mixing and diffusing around $x/D = 1$. The rotation directions of the tip-vortices for the pitched cases are consistent with their induced flows discussed in Section 7.4.1.

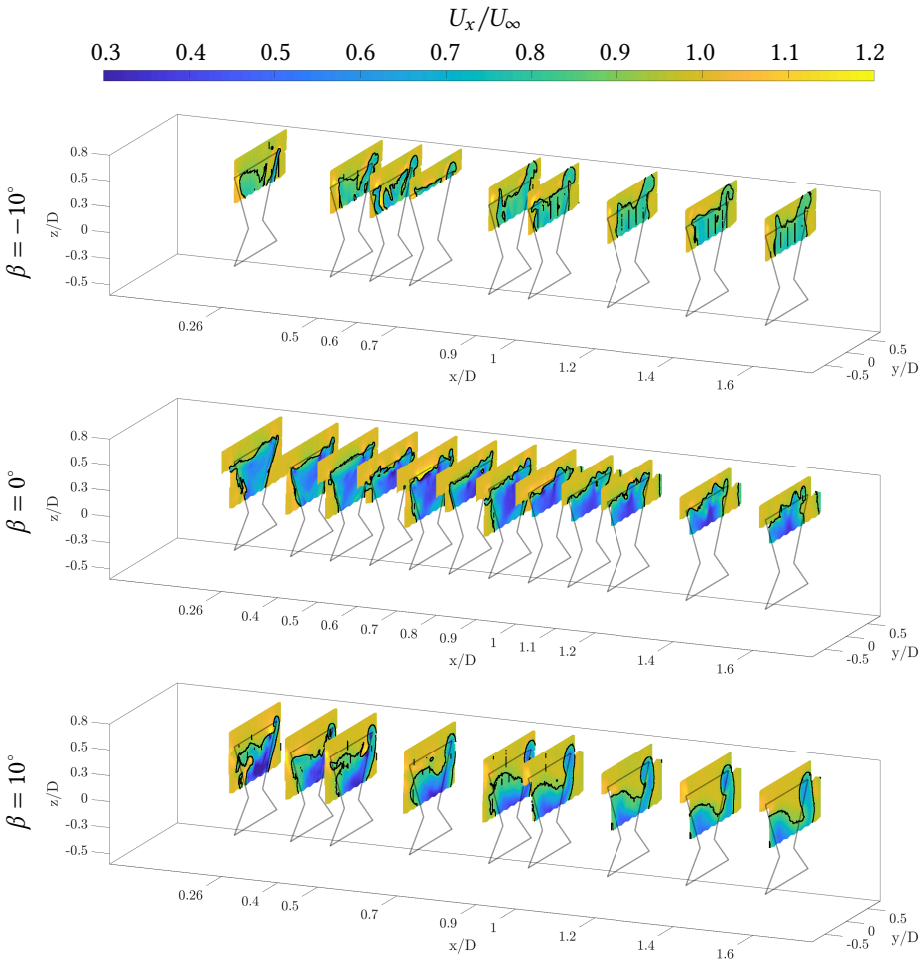


Figure B.2: Normalized streamwise flow (U_x/U_∞) at discrete cross-stream planes. The black solid line shows the frontal area of the rotor at an azimuth of 0° with a black contour line showing where U_x/U_∞ = 0.9. The scale in the streamwise direction is doubled to have the planes more spaced apart for observation.

B

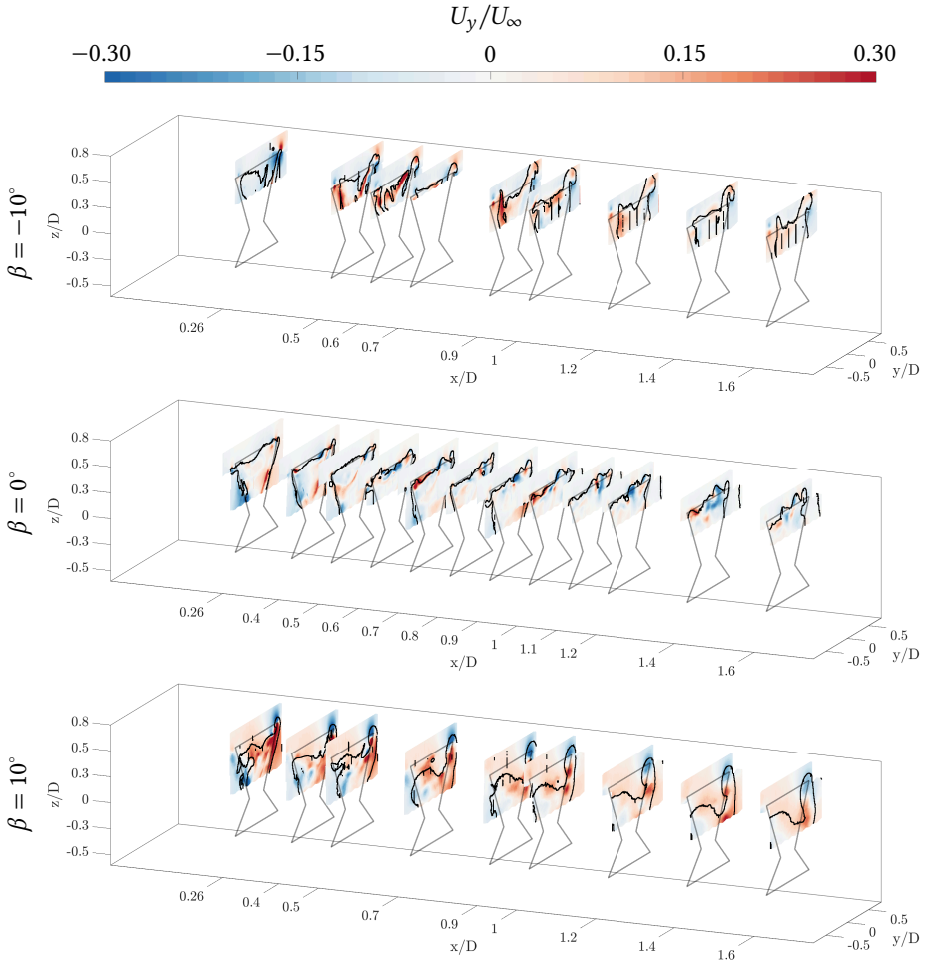


Figure B.3: Normalized lateral flow (U_y/U_∞) at discrete cross-stream planes. The black solid line shows the frontal area of the rotor at an azimuth of 0° with a black contour line showing where U_x/U_∞ = 0.9. The scale in the streamwise direction is doubled to have the planes more spaced apart for observation.

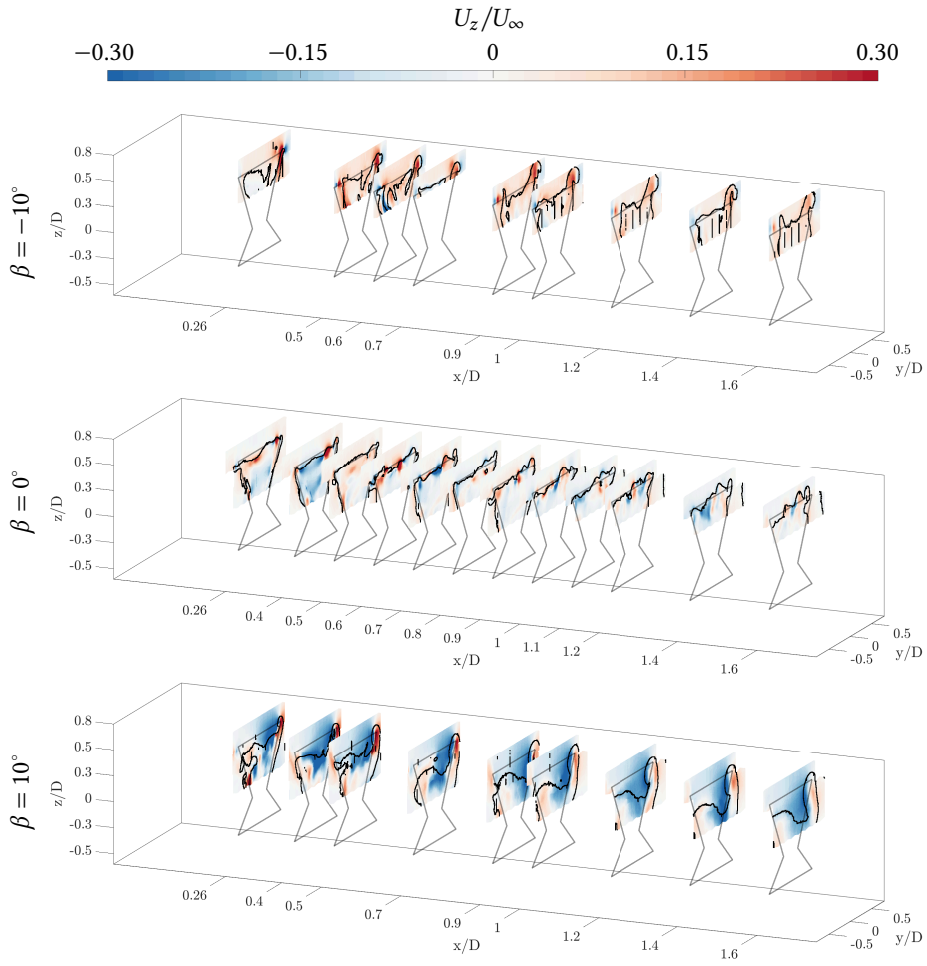


Figure B.4: Normalized axial flow (U_z/U_∞) at discrete cross-stream planes. The black solid line shows the frontal area of the rotor at an azimuth of 0° with a black contour line showing where U_x/U_∞ = 0.9. The scale in the streamwise direction is doubled to have the planes more spaced apart for observation.

B

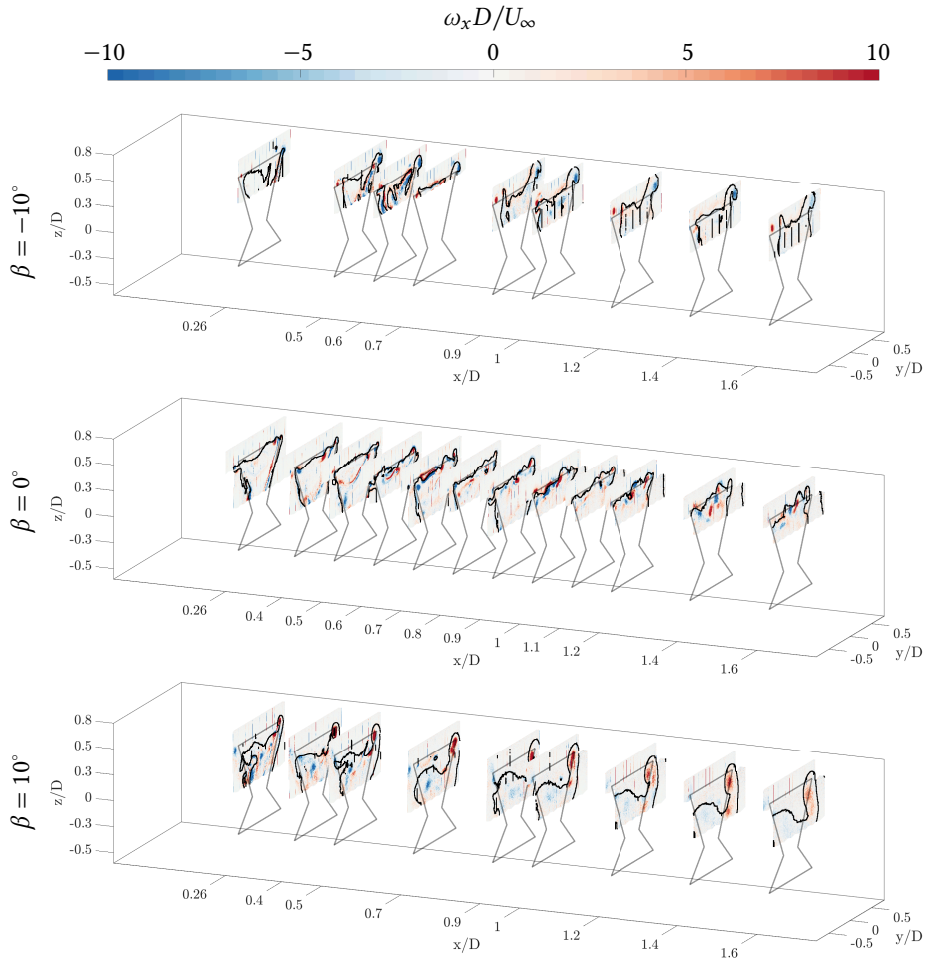


Figure B.5: Normalized streamwise vorticity ($\omega_x D/U_\infty$) at discrete cross-stream planes. The black solid line shows the frontal area of the rotor at an azimuth of 0° with a black contour line showing where U_x/U_∞ = 0.9

C

In relation to Chapter 8

C.1 Curve fitted vorticity distributions

As described in Section 8.4.4, the diffusion length scale parameter η is evaluated by fitting a curve described by Equation (8.8). A comparison between the measured and curve-fitted streamwise vorticity distribution through the vortex core for the UW vortex for the positive pitch case is shown in Figure C.1 at each measurement plane. The solid and dashed lines correspond to the measured and fitted data, respectively. For clarity, the centers of the vortex cores as defined in Figure 8.13 are translated to fall incident at $y/D = 0$. Consistent with the trend shown in Figure C.1, the peak vorticity decreases when progressing downstream in the wake. As it decreases, the size of the vortex structure increases, as evidenced by the increasing width of the curves. This is highlighted by the vertical dashed lines, which correspond to the radial position y from the vortex core where $|\omega_x|$ is 50% of its peak magnitude. Given the decrease in peak magnitude, this radius increases as the wake progresses.

C

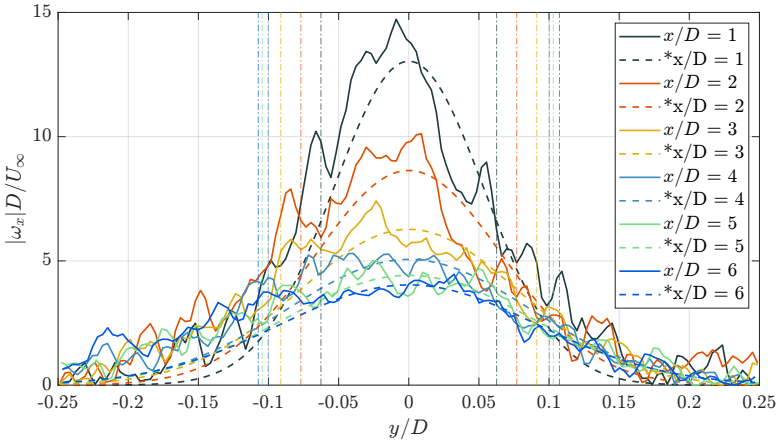


Figure C.1: Normalized streamwise vorticity magnitude $|\omega_x|D/U_\infty$ of the windward vortex of the positive pitch case $\beta = 10^\circ$. The lateral coordinate is normalized such that $y/D = 0$ is the center of the vortex core at each measurement plane. Solid lines are the raw data, and the dashed lines marked with * are the fitted curves using Equation (8.8). The vertical dash-dotted lines indicate lateral coordinate at 50% of the maximum $|\omega_x|D/U_\infty$ of the fitted curve.

D

In relation to Chapter 9

D.1 Wing-tip vortex circulation convergence

The convergence of the trailing tip-vortex circulation within a circular integration area is presented in Figure D.1 for the top and middle wing. The dashed lines indicate the value at which the gradient falls below 1%. As discussed in Section 9.4.2, the top wing circulation converges at $x/D = 2$ given the larger measurement domain near the upper wing tips. Meanwhile, convergence is attainable at all measurement planes for the middle blade, given the larger measurement domain near the middle of the rotor and the smaller structure. As discussed in Section 9.4.2, the circulations have inflection points due to the inclusion of surrounding vortical structures (including the top wing vortex) with a growing integration domain. The converged circulations for the middle wing are tabulated in Table D.1, resulting in a mean value of $\Gamma_{\text{Mid}}/cU_\infty = -0.29 \pm 0.02$.

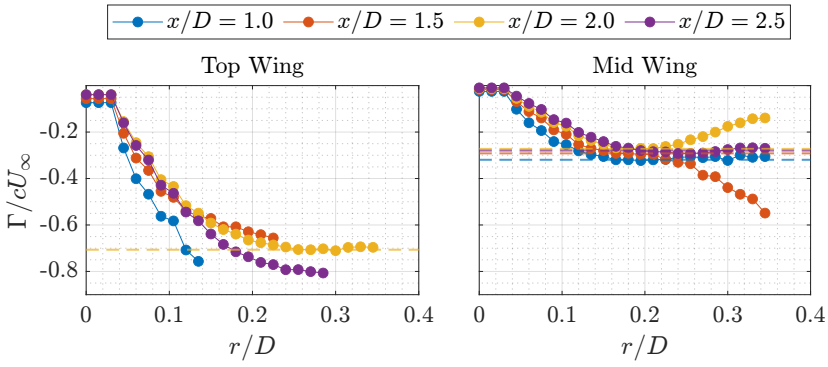


Figure D.1: Convergence of circulation with increasing integration radius for the tip-vortex stemming from the (left) top wing and (right) middle wing as a function of cross-stream measurement plane. The dashed lines indicate the value at which the gradient falls below 1%.

x/D	$\Gamma_{\text{Mid}}/cU_\infty$
1	-0.32
1.5	-0.29
2	-0.27
2.5	-0.28
Mean	-0.29
Standard Deviation	0.02

Table D.1: Converged circulations of the middle wing as a function of measurement plane

D.2 Fitted vortex distribution

As described in Section 9.4.2, the vertical flow component in the wake at $x/D = 2$ is predicted by using a point-vortex approximation, described in Chapter 8. Part of this procedure is determining the viscous length scale variable η, which is a metric for quantifying the diffusion of the wing-tip vortices, as discussed in Chapter 8. To do so, a curve fitting procedure takes the vortex core and flowfield-derived circulations for the wings, as described in Chapter 8. The comparison between the experimental and curve-fitted distribution of vorticity magnitude is shown in Figure D.2.

The experimental distribution of vorticity for the middle wing is less symmetric than that of the top, which can be attributed to the significant stretching imposed by the stronger top-wing vortex as the wake develops, visualized in Figure 9.8. As a result, the fitted distribution of the middle wing matches to a higher degree on the left side of the core ($y/D < 0$). Although the experimental distribution of the top-wing vortex is more symmetric, the fitted curve has a peak vorticity difference of 15.5% compared to the experimental distribution. The curve fitted variable $k(x)$ (m^{-2}) where $k(x) = 1/(4\pi\eta(x)^2)$ for the top and middle wing are $k_{\text{Top}}(x) = 17.5 \pm 3.8$ and $k_{\text{Mid}}(x) = 14.6 \pm 5.6$, respectively, where the range is based on the upper and lower bounds of the 95% confidence interval. Hence, the viscous length scales are $\eta_{\text{Top}}(x) = 0.06\text{m} \pm 0.01\text{m}$ and $\eta_{\text{Mid}}(x) = 0.05\text{m} \pm 0.01\text{m}$. Although the relative uncertainties are high (up to 20%), the impact is minimal for cases where the upwash is evaluated at regions far from the vortex cores, as evidenced by the inverse square-root relationship in Chapter 8. As the upwash in the wake is evaluated at heights below the vortex cores in Section 9.4.2, the impact of the uncertainty in the viscous length scale will be minimal.

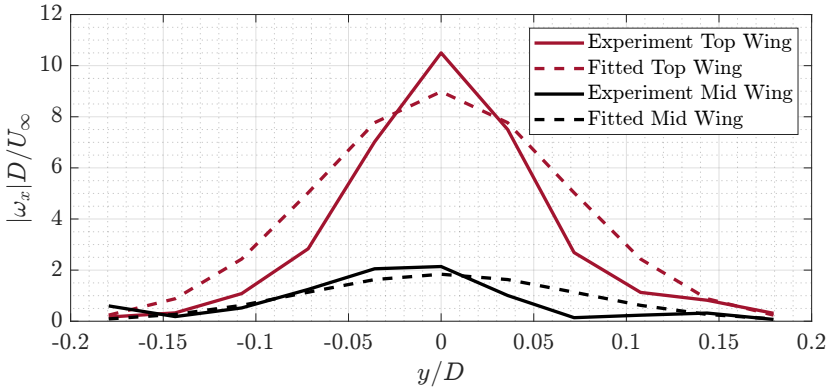


Figure D.2: Normalized streamwise vorticity magnitude of the top and middle wing-tip vortices at $x/D = 2$. The lateral coordinate is normalized such that $y/D = 0$ is at the center of the vortex core, defined in Figure 9.10. Solid and dashed lines correspond to the experimental and curve-fitted distributions receptively.

Bibliography

References

[1] Noah S. Diffenbaugh and Elizabeth A. Barnes. Data-driven predictions of the time remaining until critical global warming thresholds are reached. *Proceedings of the National Academy of Sciences*, 120(6):e2207183120, 2023.

[2] Wind electricity. Technical report, International Energy Agency, 2023.

[3] Rebecca Williams and Feng Zhao. Global offshore wind report 2024. *GWEC: Brussels, Belgium*, 19:90–91, 2024.

[4] M Dolores Esteban, J Javier Diez, Jose S López, and Vicente Negro. Why offshore wind energy? *Renewable energy*, 36(2):444–450, 2011.

[5] Bernd Möller, Lixuan Hong, Reinhard Lonsing, and Frede Hvelplund. Evaluation of offshore wind resources by scale of development. *Energy*, 48(1):314–322, 2012.

[6] Andrew R Henderson, Colin Morgan, Bernie Smith, Hans C Sørensen, Rebecca J Barthelmie, and Bart Boesmans. Offshore wind energy in europe—a review of the state-of-the-art. *Wind Energy: An International Journal for Progress and Applications in Wind Power Conversion Technology*, 6(1):35–52, 2003.

[7] Helena Canet, Pietro Bortolotti, and Carlo L Bottasso. On the scaling of wind turbine rotors. *Wind Energy Science*, 6(3):601–626, 2021.

[8] Mihir Mehta, Michiel Zaaijer, and Dominic von Terzi. Drivers for optimum sizing of wind turbines for offshore wind farms. *Wind Energy Science*, 9(1):141–163, 2024.

[9] Matt Shields, Philipp Beiter, Jake Nunemaker, Aubryn Cooperman, and Patrick Duffy. Impacts of turbine and plant upsizing on the levelized cost of energy for offshore wind. *Applied Energy*, 298:117189, 2021.

[10] Matthias Hofmann and Iver Bakken Sperstad. Will 10 mw wind turbines bring down the operation and maintenance cost of offshore wind farms? *Energy Procedia*, 53:231–238, 2014.

[11] Jens Nørkær Sørensen and Gunner Christian Larsen. A minimalistic prediction model to determine energy production and costs of offshore wind farms. *Energies*, 14(2):448, 2021.

[12] Rebecca Jane Barthelmie, S C Pryor, Sten Tronæs Frandsen, Kurt Schaldemose Hansen, JG Schepers, K Rados, Wolfgang Schlez, Anja Neubert, LE Jensen, and S Neckelmann. Quantifying the impact of wind turbine wakes on power output at

offshore wind farms. *Journal of Atmospheric and Oceanic Technology*, 27(8):1302–1317, 2010.

[13] Rebecca Jane Barthelmie, Sten Tronæs Frandsen, MN Nielsen, SC Pryor, P-E Rethore, and Hans Ejsing Jørgensen. Modelling and measurements of power losses and turbulence intensity in wind turbine wakes at middelgrunden offshore wind farm. *Wind Energy: An International Journal for Progress and Applications in Wind Power Conversion Technology*, 10(6):517–528, 2007.

[14] Peng Hou, Weihao Hu, Mohsen Soltani, Cong Chen, and Zhe Chen. Combined optimization for offshore wind turbine micro siting. *Applied energy*, 189:271–282, 2017.

[15] JN Sørensen, GC Larsen, and A Cazin-Bourguignon. Production and cost assessment of offshore wind power in the north sea. In *Journal of Physics: Conference Series*, volume 1934, page 012019. IOP Publishing, 2021.

[16] Julie K Lundquist, Katharine K DuVivier, Daniel Kaffine, and Jessica M Tomaszewski. Costs and consequences of wind turbine wake effects arising from uncoordinated wind energy development. *Nature Energy*, 4(1):26–34, 2019.

[17] Johannes Schulz-Stellenfleth, Bughsin Djath, and Hereon. Sar observations of offshore windfarm wakes. In *Handbook of Wind Energy Aerodynamics*, pages 1–33. Springer, 2021.

[18] James F Manwell, Jon G McGowan, and Anthony L Rogers. *Wind energy explained: theory, design and application.* John Wiley & Sons, 2010.

[19] VJ Modi and MSUK Fernando. On the performance of the savonius wind turbine. 1989.

[20] Jingna Pan, Carlos Ferreira, and Alexander van Zuijlen. A numerical study on the blade–vortex interaction of a two-dimensional darrieus–savonius combined vertical axis wind turbine. *Physics of Fluids*, 35(12), 2023.

[21] Nathaniel J Wei, Ian D Brownstein, Jennifer L Cardona, Michael F Howland, and John O Dabiri. Near-wake structure of full-scale vertical-axis wind turbines. *Journal of Fluid Mechanics*, 914:A17, 2021.

[22] Antoine Vergaerde, Tim De Troyer, Sara Muggiasca, Ilmas Bayati, Marco Belloli, Joanna Kluczewska-Bordier, Nicolas Parneix, Frederic Silvert, and Mark C Runacres. Experimental characterisation of the wake behind paired vertical-axis wind turbines. *Journal of Wind Engineering and Industrial Aerodynamics*, 206:104353, 2020.

[23] D De Tavernier, Carlos Ferreira, Ang Li, US Paulsen, and HA Madsen. Towards the understanding of vertical-axis wind turbines in double-rotor configuration. In *Journal of Physics: Conference Series*, volume 1037, page 022015. IOP Publishing, 2018.

[24] John O Dabiri. Potential order-of-magnitude enhancement of wind farm power density via counter-rotating vertical-axis wind turbine arrays. *Journal of renewable and sustainable energy*, 3(4), 2011.

[25] Ming Huang, Andrea Sciacchitano, and Carlos Ferreira. On the wake deflection of vertical axis wind turbines by pitched blades. *Wind Energy*, 2023.

[26] Peter Jamieson. *Innovation in wind turbine design*. John Wiley & Sons, 2018.

[27] Peter Jamieson, C Simao Ferreira, Peter Dalhoff, Sven Störtenbecker, Maurizio Collu, Erik Salo, David McMillan, Jade McMorland, Laurence Morgan, and Angus Buck. Development of a multi rotor floating offshore system based on vertical axis wind turbines. In *Journal of Physics: Conference Series*, volume 2257, page 012002. IOP Publishing, 2022.

[28] William Leithead, Arthur Camciuc, Abbas Kazemi Amiri, and James Carroll. The x-rotor offshore wind turbine concept. In *Journal of Physics: Conference Series*, volume 1356, page 012031. IOP Publishing, 2019.

[29] Maarten Paul van der Laan, Søren Juhl Andersen, Néstor Ramos García, Nikolas Angelou, Georg Raimund Pirrung, Søren Ott, Mikael Sjöholm, Kim Hylling Sørensen, Julio Xavier Vianna Neto, Mark Kelly, et al. Power curve and wake analyses of the vestas multi-rotor demonstrator. *Wind Energy Science*, 4(2):251–271, 2019.

[30] Distelbrink L, Fetecau M, Gonzalez L, Jemiol B, Rizk M K, Tapia M P, Porcescu I, Pudans J, Roth J, and Tugtekin M. 30mw multi-rotor turbine block design - design synthesis exercise bsc aerospace engineering. Technical report, Delft University of Technology, 2023.

[31] Lijun Zhang, Junjie Miao, Jiawei Gu, Xiang Li, Kuoliang Hu, Huaibao Zhu, Xuefa Sun, Jing Liu, Yanxin Liu, and Zhiwei Wang. A method of reducing the radial load of the shaft of a vertical axis wind turbine based on movable mass blocks. *Renewable Energy*, 175:952–964, 2021.

[32] D De Tavernier, Carlos Ferreira, A Viré, B LeBlanc, and S Bernardy. Controlling dynamic stall using vortex generators on a wind turbine airfoil. *Renewable Energy*, 172:1194–1211, 2021.

[33] Sébastien Le Fouest and Karen Mulleners. Optimal blade pitch control for enhanced vertical-axis wind turbine performance. *Nature Communications*, 15(1), 2024.

[34] Joshua A Paquette and Matthew Franklin Barone. Innovative offshore vertical-axis wind turbine rotor project. Technical report, Sandia National Lab.(SNL-NM), Albuquerque, NM (United States), 2012.

[35] D. Todd Griffith, Joshua Paquette, Matthew Barone, Andrew J. Goupee, Matthew J. Fowler, Diana Bull, and Brian Owens. A study of rotor and platform design trade-offs for large-scale floating vertical axis wind turbines. *Journal of Physics: Conference Series*, 753(10):102003, sep 2016.

[36] Georgios Sieros, Panagiotis Chaviaropoulos, John Dalsgaard Sørensen, Bernard H Bulder, and Peter Jamieson. Upscaling wind turbines: theoretical and practical aspects and their impact on the cost of energy. *Wind energy*, 15(1):3–17, 2012.

[37] Vincent FC Rolin and Fernando Porté-Agel. Experimental investigation of vertical-axis wind-turbine wakes in boundary layer flow. *Renewable energy*, 118:1–13, 2018.

[38] Matthieu Boudreau and Guy Dumas. Comparison of the wake recovery of the axial-flow and cross-flow turbine concepts. *Journal of Wind Engineering and Industrial Aerodynamics*, 165:137–152, 2017.

[39] Rémi Gosselin, Guy Dumas, and Matthieu Boudreau. Parametric study of h-darrieus vertical-axis turbines using cfd simulations. *Journal of Renewable and Sustainable Energy*, 8(5), 2016.

[40] Delphine De Tavernier, Carlos Ferreira, and Anders Goude. Vertical-axis wind turbine aerodynamics. In *Handbook of Wind Energy Aerodynamics*, pages 1317–1361. Springer, 2022.

[41] Giuseppe Tescione, Daniele Ragni, Chenguang He, Carlos Simao Ferreira, and Gerard G van Bussel. Piv-based analysis of 2d and 3d flow phenomena of vertical axis wind turbine aerodynamics. In *32nd ASME Wind Energy Symposium*, page 1080, 2014.

[42] Victor Mendoza, Peter Bachant, Carlos Ferreira, and Anders Goude. Near-wake flow simulation of a vertical axis turbine using an actuator line model. *Wind Energy*, 22(2):171–188, 2019.

[43] H Aa Madsen, Uwe Schmidt Paulsen, and L Vitae. Analysis of vawt aerodynamics and design using the actuator cylinder flow model. In *Journal of Physics: Conference Series*, volume 555, page 012065. IOP Publishing, 2014.

[44] D De Tavernier, Carlos Ferreira, U Paulsen, and H Madsen. The 3d effects of a vertical-axis wind turbine: rotor and wake induction. In *Journal of Physics: Conference Series*, volume 1618, page 052040. IOP Publishing, 2020.

[45] Lucy Massie, Pablo Ouro, Thorsten Stoesser, and Qianyu Luo. An actuator surface model to simulate vertical axis turbines. *Energies*, 12(24):4741, 2019.

[46] Pablo Ouro, Stefan Runge, Qianyu Luo, and Thorsten Stoesser. Three-dimensionality of the wake recovery behind a vertical axis turbine. *Renewable Energy*, 133:1066–1077, 2019.

[47] Karen Mulleners and Markus Raffel. Dynamic stall development. *Experiments in fluids*, 54:1–9, 2013.

[48] Max Kramer. Increase in the maximum lift of an airplane wing due to a sudden increase in its effective angle of attack resulting from a gust. Technical report, NASA, 1932.

[49] JM Martin, RW Empey, WJ McCroskey, and FX Caradonna. An experimental analysis of dynamic stall on an oscillating airfoil. *Journal of the American Helicopter Society*, 19(1):26–32, 1974.

[50] Norman D Ham and Melvin S Garelick. Dynamic stall considerations in helicopter rotors. *Journal of the American Helicopter Society*, 13(2):49–55, 1968.

[51] Gordon J Leishman. *Principles of helicopter aerodynamics with CD extra*. Cambridge university press, 2006.

[52] A Laneville and P Vittecoq. Dynamic stall: The case of the vertical axis wind turbine. *Journal of Solar Energy Engineering*, 108, 1986.

[53] Carlos Simão Ferreira, Gijs Van Kuik, Gerard Van Bussel, and Fulvio Scarano. Visualization by piv of dynamic stall on a vertical axis wind turbine. *Experiments in fluids*, 46:97–108, 2009.

[54] Sébastien Le Fouest and Karen Mulleners. The dynamic stall dilemma for vertical-axis wind turbines. *Renewable Energy*, 198:505–520, 2022.

[55] Alessandro Zanon, Pietro Giannattasio, and Carlos J Simão Ferreira. Wake modelling of a vawt in dynamic stall: impact on the prediction of flow and induction fields. *Wind Energy*, 18(11):1855–1874, 2015.

[56] Bruce LeBlanc and Carlos Ferreira. Estimation of blade loads for a variable pitch vertical axis wind turbine with strain gage measurements. *Wind Energy*, 25(6):1030–1045, 2022.

[57] Sébastien Le Fouest, Daniel Fernex, and Karen Mulleners. Time scales of dynamic stall development on a vertical-axis wind turbine blade. *Flow*, 3:E11, 2023.

[58] Abdolrahim Rezaeiha, Hamid Montazeri, and Bert Blocken. Towards optimal aerodynamic design of vertical axis wind turbines: Impact of solidity and number of blades. *Energy*, 165:1129–1148, 2018.

[59] Abdolrahim Rezaeiha, Hamid Montazeri, and Bert Blocken. Characterization of aerodynamic performance of vertical axis wind turbines: Impact of operational parameters. *Energy Conversion and Management*, 169:45–77, 2018.

[60] Stefania Zanforlin and Takafumi Nishino. Fluid dynamic mechanisms of enhanced power generation by closely spaced vertical axis wind turbines. *Renewable Energy*, 99:1213–1226, 2016.

[61] Ian D Brownstein, Nathaniel J Wei, and John O Dabiri. Aerodynamically interacting vertical-axis wind turbines: Performance enhancement and three-dimensional flow. *Energies*, 12(14):2724, 2019.

[62] Ayoub Talamalek, Mark C Runacres, and Tim De Troyer. Experimental investigation of the wake replenishment mechanisms of paired counter-rotating vertical-axis wind turbines. *Journal of Wind Engineering and Industrial Aerodynamics*, 252:105830, 2024.

[63] Ayoub Talamalek, Mark C Runacres, and Tim De Troyer. Impact of rotational direction on wake replenishment mechanisms of counter-rotating paired vertical-axis wind turbines. In *Journal of Physics: Conference Series*, volume 2767, page 072005. IOP Publishing, 2024.

[64] Ayoub Talamalek, Mark C Runacres, and Tim De Troyer. Effect of turbulence on the performance of a pair of vertical-axis wind turbines. In *Journal of Physics: Conference Series*, volume 2265, page 022098. IOP Publishing, 2022.

[65] Andreu Carbó Molina, Tim De Troyer, Tommaso Massai, Antoine Vergaerde, Mark C Runacres, and Gianni Bartoli. Effect of turbulence on the performance of vawts: An experimental study in two different wind tunnels. *Journal of Wind Engineering and Industrial Aerodynamics*, 193:103969, 2019.

[66] TC Hohman, L Martinelli, and AJ Smits. The effects of inflow conditions on vertical axis wind turbine wake structure and performance. *Journal of Wind Engineering and Industrial Aerodynamics*, 183:1–18, 2018.

[67] Seyed Hossein Hezaveh and Elie Bou-Zeid. Mean kinetic energy replenishment mechanisms in vertical-axis wind turbine farms. *Physical Review Fluids*, 3(9):094606, 2018.

[68] Matthias Kinzel, Quinn Mulligan, and John O Dabiri. Energy exchange in an array of vertical-axis wind turbines. *Journal of Turbulence*, 13(1):N38, 2012.

[69] Matthias Kinzel, Daniel B Araya, and John O Dabiri. Turbulence in vertical axis wind turbine canopies. *Physics of Fluids*, 27(11), 2015.

[70] Seyed Hossein Hezaveh, Elie Bou-Zeid, John Dabiri, Matthias Kinzel, Gerard Cortina, and Luigi Martinelli. Increasing the power production of vertical-axis wind-turbine farms using synergistic clustering. *Boundary-layer meteorology*, 169:275–296, 2018.

[71] Anna E Craig, John O Dabiri, and Jeffrey R Koseff. A kinematic description of the key flow characteristics in an array of finite-height rotating cylinders. *Journal of Fluids Engineering*, 138(7):070906, 2016.

[72] Anna E Craig, John O Dabiri, and Jeffrey R Koseff. Flow kinematics in variable-height rotating cylinder arrays. *Journal of Fluids Engineering*, 138(11):111203, 2016.

[73] Ming Huang, Yugandhar Vijaykumar Patil, Andrea Sciacchitano, and Carlos Ferreira. Experimental study of the wake interaction between two vertical axis wind turbines. *Wind Energy*, 26(11):1188–1211, 2023.

[74] Jens Nørkær Sørensen. Instability of helical tip vortices in rotor wakes. *Journal of Fluid Mechanics*, 682:1–4, 2011.

[75] Fernando Porté-Agel, Majid Bastankhah, and Sina Shamsoddin. Wind-turbine and wind-farm flows: a review. *Boundary-layer meteorology*, 174(1):1–59, 2020.

[76] LEM Lignarolo, D Ragni, F Scarano, CJ Simão Ferreira, and GJW Van Bussel. Tip-vortex instability and turbulent mixing in wind-turbine wakes. *Journal of Fluid Mechanics*, 781:467–493, 2015.

[77] Richard JAM Stevens and Charles Meneveau. Flow structure and turbulence in wind farms. *Annual review of fluid mechanics*, 49(1):311–339, 2017.

[78] Paul Fleming, Jennifer Annoni, Jigar J Shah, Linpeng Wang, Shreyas Ananthan, Zhijun Zhang, Kyle Hutchings, Peng Wang, Weiguo Chen, and Lin Chen. Field test of wake steering at an offshore wind farm. *Wind Energy Science*, 2(1):229–239, 2017.

[79] Michael F Howland, Sanjiva K Lele, and John O Dabiri. Wind farm power optimization through wake steering. *Proceedings of the National Academy of Sciences*, 116(29):14495–14500, 2019.

[80] Paul Fleming, Jennifer King, Eric Simley, Jason Roadman, Andrew Scholbrock, Patrick Murphy, Julie K Lundquist, Patrick Moriarty, Katherine Fleming, Jeroen van Dam, et al. Continued results from a field campaign of wake steering applied at a commercial wind farm: Part 2. *Wind Energy Science Discussions*, 2020:1–24, 2020.

[81] Eric Simley, David Bensason, Owen Roberts, Paul Fleming, Mithu Debnath, Jennifer King, Christopher Bay, and Rafael Mudafort. Evaluation of the potential for wake steering for us land-based wind power plants. *Journal of Renewable and Sustainable Energy*, 13(NREL/JA-5000-78289), 2021.

[82] Jens H Kasper and Richard JAM Stevens. Effects of wind turbine rotor tilt on large-scale wind farms. In *Journal of Physics: Conference Series*, volume 2767, page 092072. IOP Publishing, 2024.

[83] Carlo Cossu. Evaluation of tilt control for wind-turbine arrays in the atmospheric boundary layer. *Wind Energy Science*, 6(3):663–675, 2021.

[84] Majid Bastankhah and Fernando Porté-Agel. Experimental and theoretical study of wind turbine wakes in yawed conditions. *Journal of Fluid Mechanics*, 806:506–541, 2016.

[85] Juliaan Bossuyt, Ryan Scott, Naseem Ali, and Raúl Bayoán Cal. Quantification of wake shape modulation and deflection for tilt and yaw misaligned wind turbines. *Journal of Fluid Mechanics*, 917:A3, 2021.

[86] Kelsey Shaler, Jason Jonkman, Garrett E Barter, Jasper J Kreeft, and Jelle P Muller. Loads assessment of a fixed-bottom offshore wind farm with wake steering. *Wind Energy*, 25(9):1530–1554, 2022.

[87] Claire VerHulst and Charles Meneveau. Altering kinetic energy entrainment in large eddy simulations of large wind farms using unconventional wind turbine actuator forcing. *Energies*, 8(1):370–386, 2015.

[88] Shujaut H Bader, Venkatesh Inguva, and JB Perot. Improving the efficiency of wind farms via wake manipulation. *Wind Energy*, 21(12):1239–1253, 2018.

[89] Jay P Goit and Johan Meyers. Optimal control of energy extraction in wind-farm boundary layers. *Journal of Fluid Mechanics*, 768:5–50, 2015.

[90] Joeri Alexis Frederik, Robin Weber, Stefano Cacciola, Filippo Campagnolo, Alessandro Croce, Carlo Bottasso, and Jan-Willem van Wingerden. Periodic dynamic induction control of wind farms: proving the potential in simulations and wind tunnel experiments. *Wind Energy Science*, 5(1):245–257, 2020.

[91] Daan Van der Hoek, Joeri Frederik, Ming Huang, Fulvio Scarano, Carlos Simao Ferreira, and Jan-Willem van Wingerden. Experimental analysis of the effect of dynamic induction control on a wind turbine wake. *Wind Energy Science*, 7(3):1305–1320, 2022.

[92] Joeri A Frederik, Bart M Doekemeijer, Sebastiaan P Mulders, and Jan-Willem van Wingerden. The helix approach: Using dynamic individual pitch control to enhance wake mixing in wind farms. *Wind Energy*, 23(8):1739–1751, 2020.

[93] Daan van der Hoek, Bert Van den Abbeele, Carlos Simao Ferreira, and Jan-Willem van Wingerden. Maximizing wind farm power output with the helix approach: Experimental validation and wake analysis using tomographic particle image velocimetry. *Wind Energy*, 2024.

[94] Johan Meyers, Carlo Bottasso, Katherine Dykes, Paul Fleming, Pieter Gebraad, Gregor Giebel, Tuhfe Göçmen, and Jan-Willem Van Wingerden. Wind farm flow control: prospects and challenges. *Wind Energy Science Discussions*, 2022:1–56, 2022.

[95] Jia Guo and Liping Lei. Flow characteristics of a straight-bladed vertical axis wind turbine with inclined pitch axes. *Energies*, 13(23):6281, 2020.

[96] Carlos Simao Ferreira, Kristian Dixon, Claudia Hofemann, Gijs van Kuik, and Gerard van Bussel. Vawt in skew: Stereo-piv and vortex modeling. In *47th AIAA aerospace sciences meeting including the new horizons forum and aerospace exposition*, page 1219, 2009.

[97] Victor Mendoza and Anders Goude. Improving farm efficiency of interacting vertical-axis wind turbines through wake deflection using pitched struts. *Wind Energy*, 22(4):538–546, 2019.

[98] André FP Ribeiro, Carlos S Ferreira, and Damiano Casalino. Vertical axis wind turbine wake steering by pitched struts and blades. In *Journal of Physics: Conference Series*, volume 2767, page 092004. IOP Publishing, 2024.

[99] Abdolrahim Rezaeiha, Ivo Kalkman, and Bert Blocken. Effect of pitch angle on power performance and aerodynamics of a vertical axis wind turbine. *Applied energy*, 197:132–150, 2017.

[100] Carlos Simão Ferreira and Frank Scheurich. Demonstrating that power and instantaneous loads are decoupled in a vertical-axis wind turbine. *Wind Energy*, 17(3):385–396, 2014.

[101] Ming Huang, Andrea Sciacchitano, and Carlos Ferreira. Experimental and numerical study of the wake deflections of scaled vertical axis wind turbine models. *Journal of Physics: Conference Series*, 2505(1):012019, may 2023.

[102] James Carroll, Alasdair McDonald, Iain Dinwoodie, David McMillan, Matthew Revie, and Iraklis Lazakis. Availability, operation and maintenance costs of offshore wind turbines with different drive train configurations. *Wind Energy*, 20(2):361–378, 2017.

[103] Callum Flannigan, James Carroll, and William Leithead. Operations expenditure modelling of the x-rotor offshore wind turbine concept. In *Journal of Physics: Conference Series*, volume 2265, page 032054. IOP Publishing, 2022.

[104] F Devoy McAuliffe, F Anderson, J Carroll, and J Murphy. Modelled cost reductions for the x-rotor offshore wind turbine. In *Journal of Physics: Conference Series*, volume 2875, page 012003. IOP Publishing, 2024.

[105] Laurence Morgan and William Leithead. Aerodynamic modelling of a novel vertical axis wind turbine concept. In *Journal of Physics: Conference Series*, volume 2257, page 012001. IOP Publishing, 2022.

[106] Adhyanth Giri Ajay, Laurence Morgan, Yan Wu, David Bretos, Aurelio Cascales, Oscar Pires, and Carlos Ferreira. Aerodynamic model comparison for an x-shaped vertical-axis wind turbine. *Wind Energy Science Discussions*, 2023:1–25, 2023.

[107] Laurence Boyd Morgan, Abbas Kazemi Amiri, William Leithead, and James Carroll. Effect of blade inclination angle for straight bladed vertical axis wind turbines. *Wind Energy Science Discussions*, 2024:1–26, 2024.

[108] Laurence Morgan, William Leithead, and James Carroll. On the use of secondary rotors for vertical axis wind turbine power take-off. *Wind Energy*, 27(6):569–582, 2024.

[109] L Recalde-Camacho, W Leithead, L Morgan, and A Kazemi Amiri. Controller design for the x-rotor offshore wind turbine concept. In *Journal of Physics: Conference Series*, volume 2767, page 032050. IOP Publishing, 2024.

[110] Jing Dong, Adriana Correia Da Silva, and Michael Muskulus. Pile design for x-rotor offshore wind turbine. In *Journal of Physics: Conference Series*, volume 2626, page 012004. IOP Publishing, 2023.

[111] Adriana Correia Da Silva and Michael Muskulus. Vawt support structure mass sensitivity due to aerodynamic load scaling. 2023.

[112] Reza Yazdanpanah, Seyed Abolfazl Mortazavizadeh, Yang Teng, Olimpo Anaya-Lara, and David Campos-Gaona. An integrated rotary transformer and 3-phase dual-active-bridge converter for high power transfer in novel x-rotor wind turbines. In *2023 IEEE International Magnetic Conference (INTERMAG)*, pages 1–5. IEEE, 2023.

[113] Yang Teng, Olimpo Anaya-Lara, Reza Yazdanpanah, David Campos-Gaona, and Seyed Abolfazl Mortazavizadeh. Design and analysis of a 100kw rotary transformer for xrotor wind generators. In *2023 IEEE Workshop on Electrical Machines Design, Control and Diagnosis (WEMDCD)*, pages 1–5. IEEE, 2023.

[114] Reza Yazdanpanah, Seyed Abolfazl Mortazavizadeh, Mohammad Salehian, David Campos-Gaona, and Olimpo Anaya-Lara. Design optimization of inner and outer-rotor pmsgs for x-rotor wind turbines. *IET Renewable Power Generation*, 18(14):2605–2618, 2024.

[115] Preeti Verma. Multi rotor wind turbine design and cost scaling. 2013.

[116] Petros Chasapogiannis, John M Prospathopoulos, Spyros G Voutsinas, and Takis K Chaviaropoulos. Analysis of the aerodynamic performance of the multi-rotor concept. In *Journal of Physics: Conference Series*, volume 524, page 012084. IOP Publishing, 2014.

[117] Jan Bartl, Idunn Koi, Morten Skoland, Gloria Stenfelt, and Thomas Hansen. Experiments on upstream induction and wake flow for multirotor wind turbines. In *Journal of Physics: Conference Series*, volume 2505, page 012005. IOP Publishing, 2023.

[118] Jessica MI Strickland, Srinidhi N Gadde, and Richard JAM Stevens. Wind farm blockage in a stable atmospheric boundary layer. *Renewable Energy*, 197:50–58, 2022.

[119] Jessica MI Strickland and Richard JAM Stevens. Effect of thrust coefficient on the flow blockage effects in closely-spaced spanwise-infinite turbine arrays. In *Journal of Physics: Conference Series*, volume 1618, page 062069. IOP Publishing, 2020.

[120] Majid Bastankhah and Mahdi Abkar. Multirotor wind turbine wakes. *Physics of Fluids*, 31(8), 2019.

[121] Niranjan S Ghaisas, Aditya S Ghate, and Sanjiva K Lele. Large-eddy simulation study of multi-rotor wind turbines. In *Journal of Physics: Conference Series*, volume 1037, page 072021. IOP Publishing, 2018.

[122] Xue-Lu Xiong, Shujin Laima, and Hui Li. Experimental study of the wake of multi-rotor turbine. *Ocean Engineering*, 269:113594, 2023.

[123] Gustav A Speakman, Mahdi Abkar, Luis A Martínez-Tossas, and Majid Bastankhah. Wake steering of multirotor wind turbines. *Wind Energy*, 24(11):1294–1314, 2021.

[124] Markus Raffel, Christian E Willert, Fulvio Scarano, Christian J Kähler, Steve T Wereley, and Jürgen Kompenhans. *Particle image velocimetry: a practical guide*. Springer, 2018.

[125] Fulvio Scarano. Tomographic piv: principles and practice. *Measurement Science and Technology*, 24(1):012001, 2012.

[126] Daniel Schanz, Sebastian Gesemann, and Andreas Schröder. Shake-the-box: Lagrangian particle tracking at high particle image densities. *Experiments in fluids*, 57:1–27, 2016.

[127] Giuseppe Carlo Alp Caridi, Daniele Ragni, Andrea Sciacchitano, and Fulvio Scarano. Hfsb-seeding for large-scale tomographic piv in wind tunnels. *Experiments in Fluids*, 57:1–13, 2016.

[128] Kevin J Ryan, Filippo Coletti, Christopher J Elkins, John O Dabiri, and John K Eaton. Three-dimensional flow field around and downstream of a subscale model rotating vertical axis wind turbine. *Experiments in Fluids*, 57:1–15, 2016.

[129] D. Bensason, J. Mulay, A. Sciacchitano, and C. Ferreira. Experimental demonstration of regenerative wind farming using a high-density layout of vertical-axis wind turbines. *Wind Energy Science*, 10(7):1499–1528, 2025.

[130] Delphine De Tavernier and Carlos Ferreira. An extended actuator cylinder model: actuator-in-actuator cylinder (ac-squared) model. *Wind Energy*, 22(8):1058–1070, 2019.

[131] Bruce LeBlanc and Carlos Ferreira. Estimation of blade loads for a variable pitch vertical axis wind turbine from particle image velocimetry. *Wind Energy*, 25(2):313–332, 2022.

[132] Edgar Martinez-Ojeda, Francisco Javier Solorio Ordaz, and Mihir Sen. Vertical-axis wind-turbine computations using a 2d hybrid wake actuator-cylinder model. *Wind Energy Science*, 6(4):1061–1077, 2021.

[133] David Bensason, Andrea Sciacchitano, Adhyanth Giri Ajay, and Carlos Simao Ferreira. A study of the near wake deformation of the x-rotor vertical-axis wind turbine with pitched blades. *Wind Energy*, 27(11):1388–1411, 2024.

[134] David Bensason, Andrea Sciacchitano, and Carlos Ferreira. Near wake of the x-rotor vertical-axis wind turbine. In *Journal of Physics: Conference Series*, volume 2505, page 012040. IOP Publishing, 2023.

[135] Ming Huang. *Wake and wind farm aerodynamics of vertical axis wind turbines*. PhD thesis, Delft University of Technology, 2023.

[136] L.E.M. Lignarolo, D. Ragni, C. Krishnaswami, Q. Chen, CJ Simão Ferreira, and GJW Van Bussel. Experimental analysis of the wake of a horizontal-axis wind-turbine model. *Renewable Energy*, 70:31–46, 2014.

[137] David Engler Faleiros, Marthijn Tuinstra, Andrea Sciacchitano, and Fulvio Scarano. Generation and control of helium-filled soap bubbles for piv. *Experiments in Fluids*, 60:1–17, 2019.

[138] D Giaquinta. *The Flow Topology of the Ahmed Body in Cross-Wind*. PhD thesis, MSc Thesis. Delft University of Technology, Department of Aerospace Engineering, 2018.

[139] Bernhard Wieneke. Volume self-calibration for 3d particle image velocimetry. *Experiments in fluids*, 45(4):549–556, 2008.

[140] Nereida Agüera, Gioacchino Cafiero, Tommaso Astarita, and Stefano Discetti. Ensemble 3d ptv for high resolution turbulent statistics. *Measurement Science and Technology*, 27(12):124011, 2016.

[141] Peter Bachant and Martin Wosnik. Effects of reynolds number on the energy conversion and near-wake dynamics of a high solidity vertical-axis cross-flow turbine. *Energies*, 9(2):73, 2016.

[142] Jan FG Schneiders, Giuseppe CA Caridi, Andrea Sciacchitano, and Fulvio Scarano. Large-scale volumetric pressure from tomographic ptv with hfsb tracers. *Experiments in fluids*, 57:1–8, 2016.

[143] Michael F Howland, Juliaan Bossuyt, Luis A Martínez-Tossas, Johan Meyers, and Charles Meneveau. Wake structure in actuator disk models of wind turbines in yaw under uniform inflow conditions. *Journal of Renewable and Sustainable Energy*, 8(4), 2016.

[144] Gerard Cortina, Marc Calaf, and Raúl Bayoán Cal. Distribution of mean kinetic energy around an isolated wind turbine and a characteristic wind turbine of a very large wind farm. *Physical Review Fluids*, 1(7):074402, 2016.

[145] Bruce LeBlanc and Carlos Ferreira. Experimental characterization of h-vawt turbine for development of a digital twin. *Journal of Physics: Conference Series*, 1452(1):012057, jan 2020.

[146] B. LeBlanc and C. Simao Ferreira. Overview and design of pitchvawt: Vertical axis wind turbine with active variable pitch for experimental and numerical comparison. In *2018 Wind Energy Symposium*, page 1243, 2018.

[147] David Bensason, Andrea Sciacchitano, and Carlos Ferreira. Experimental study of the impact of blade-tip mounted rotors on the x-rotor vertical-axis wind turbine. In *Journal of Physics: Conference Series*, volume 2767, page 072016. IOP Publishing, 2024.

[148] A. Giri Ajay, D. Bensason, and C. Ferreira. D2.4 X-Rotor performance and loading evaluation report, December 2022.

[149] K. Koca, M.S. Genç, H.H. Açıkel, and Tuna M. Çağdaş, M.B. Identification of flow phenomena over naca 4412 wind turbine airfoil at low reynolds numbers and role of laminar separation bubble on flow evolution. *Energy*, 144:750–764, 2018.

[150] Thomas Leweke, Stéphane Le Dizès, and Charles HK Williamson. Dynamics and instabilities of vortex pairs. *Annual review of fluid mechanics*, 48(1):507–541, 2016.

[151] Delphine De Tavernier, Carlos Ferreira, and Anders Goude. *Vertical-Axis Wind Turbine Aerodynamics*, pages 1317–1361. Springer International Publishing, Cham, 2022.

[152] Laurent Graftieaux, Marc Michard, and Nathalie Grosjean. Combining piv, pod and vortex identification algorithms for the study of unsteady turbulent swirling flows. *Measurement Science and technology*, 12(9):1422, 2001.

[153] Carlos Simao Ferreira. The near wake of the vawt. *TU Delft, The Netherlands PhD Thesis*, 440, 2009.

[154] Carlos Simao Ferreira, Claudia Hofemann, Kristian Dixon, Gijs Van Kuik, and Gerard Van Bussel. 3-d wake dynamics of the vawt: Experimental and numerical investigation. In *48th AIAA aerospace sciences meeting including the new horizons forum and aerospace exposition*, page 643, 2010.

[155] M Huang, Carlos Ferreira, A Sciacchitano, and F Scarano. Experimental comparison of the wake of a vertical axis wind turbine and planar actuator surfaces. In *Journal of Physics: Conference Series*, volume 1618, page 052063. IOP Publishing, 2020.

[156] Helge Aagaard Madsen. *The Actuator Cylinder–A Flow Model for Vertical Axis Wind Turbines*. PhD thesis, Aalborg University, Denmark, 1983.

[157] Jonathan Murray and Matthew Barone. The Development of CACTUS, a Wind and Marine Turbine Performance Simulation Code. pages 1–21, 2011.

[158] Mark Drela. Xfoil: An analysis and design system for low reynolds number airfoils. In *Low Reynolds Number Aerodynamics: Proceedings of the Conference Notre Dame, Indiana, USA, 5–7 June 1989*, pages 1–12. Springer, 1989.

[159] Andrea Sciacchitano and Bernhard Wieneke. Piv uncertainty propagation. *Measurement Science and Technology*, 27(8):084006, 2016.

[160] Juliaan Bossuyt, Charles Meneveau, and Johan Meyers. Wind farm power fluctuations and spatial sampling of turbulent boundary layers. *Journal of Fluid Mechanics*, 823:329–344, 2017.

[161] D. Bensason, A. Sciacchitano, and C. Ferreira. On the wake re-energization of the x-rotor vertical-axis wind turbine via the vortex-generator strategy. *Wind Energy Science*, 10(10):2137–2159, 2025.

[162] John Anderson. *Fundamentals of Aerodynamics (SI units)*. McGraw hill, 2011.

[163] Juan-José Trujillo, Ferhat Bingöl, Gunner C Larsen, Jakob Mann, and Martin Kühn. Light detection and ranging measurements of wake dynamics. part ii: two-dimensional scanning. *Wind Energy*, 14(1):61–75, 2011.

[164] Ming Huang, Carlos Ferreira, Andrea Sciacchitano, and Fulvio Scarano. Wake scaling of actuator discs in different aspect ratios. *Renewable Energy*, 183:866–876, 2022.

[165] Carl R Shapiro, Dennice F Gayme, and Charles Meneveau. Generation and decay of counter-rotating vortices downstream of yawed wind turbines in the atmospheric boundary layer. *Journal of Fluid Mechanics*, 903:R2, 2020.

[166] Philip G Saffman. *Vortex dynamics*. Cambridge university press, 1995.

[167] Berend G van der Wall and Hugues Richard. Analysis methodology for 3c-piv data of rotary wing vortices. *Experiments in Fluids*, 40:798–812, 2006.

[168] Hiroyuki Kato, S Watanabe, N Kondo, and S Saito. Application of stereoscopic piv to helicopter rotor blade tip vortices. In *20th International Congress on Instrumentation in Aerospace Simulation Facilities, 2003. ICIASF'03.*, pages 179–189. IEEE, 2003.

[169] TJ Broertjes, D Bensason, A Sciacchitano, and C Ferreira. Lift-induced wake re-energization for a vawt-based multi-rotor system. In *Journal of Physics: Conference Series*, volume 2767, page 072012. IOP Publishing, 2024.

[170] Hai-Chau Chang and Lih-Chung Wang. A simple proof of thue's theorem on circle packing. *arXiv preprint arXiv:1009.4322*, 2010.

[171] T.J. Broertjes. Lift-induced wake re-energization for a vawt-based multi-rotor system. Master's thesis, TU Delft, Netherlands, 2024.

[172] Apollo Milton Olin Smith. High-lift aerodynamics. *Journal of Aircraft*, 12(6):501–530, 1975.

[173] M.S. Selig, J.J. Guglielmo, A.P. Broeren, and P. Giguere. Summary of low-speed airfoil data, 1995.

[174] W Terra, A Sciacchitano, and YH Shah. Aerodynamic drag determination of a full-scale cyclist mannequin from large-scale ptv measurements. *Experiments in Fluids*, 60:1–11, 2019.

[175] Paul A Fleming, Andrew Ning, Pieter MO Gebraad, and Katherine Dykes. Wind plant system engineering through optimization of layout and yaw control. *Wind Energy*, 19(2):329–344, 2016.

[176] A. Giri Ajay, D. Bensason, and D. De Tavernier. Validation of the near-wake of a scaled x-rotor vertical-axis wind turbine predicted by a free-wake vortex model. *Wind Energy Science Discussions*, 2025:1–28, 2025.

[177] YuanTso Li, Wei Yu, Andrea Sciacchitano, and Carlos Ferreira. Numerical investigation of regenerative wind farms featuring enhanced vertical energy entrainment. *Wind Energy Science*, 10(4):631–659, 2025.

[178] Sang Lee, Matthew Churchfield, Patrick Moriarty, Jason Jonkman, and John Michalakes. Atmospheric and wake turbulence impacts on wind turbine fatigue loadings. In *50th AIAA Aerospace Sciences Meeting including the New Horizons Forum and Aerospace Exposition*, page 540, 2012.

Curriculum Vitæ

David Yefim Bensason



21/02/1999 Born in Houston (TX), United States of America

Education

2015 – 2017	International Baccalaureate Zurich International School, Switzerland
2017 – 2021	MEng in Mechanical Engineering University of Bath, United Kingdom
2021 – 2025	PhD in Aerospace Engineering Delft University of Technology, Netherlands

List of Publications

Journal Papers

Ajay A., **Bensason D.**, Tavernier D. Validation of the near-wake of a scaled X-Rotor vertical-axis wind turbine predicted by a free-wake vortex model, *Wind Energy Science*. 2025. DOI: Link.

Bensason D., Sciacchitano A., Simao Ferreira C. On the wake re-energization of the X-Rotor vertical-axis wind turbine via the vortex-generator strategy, *Wind Energy Science*. 2025. DOI: Link.

Bensason D., Mulay J., Sciacchitano A., Simao Ferreira C. Experimental demonstration of regenerative wind farming using a high-density layout of VAWTs, *Wind Energy Science*. 2024. DOI: Link.

Bensason D., Sciacchitano A., Ajay A., Simao Ferreira C. A Study of the Near Wake Deformation of the X-Rotor Vertical-Axis Wind Turbine With Pitched Blades, *Wind Energy*. 2024. DOI: Link.

Bensason D., Le Fouest S.,Young A., Mulleners K. Greenberg's Force Prediction for Vertical-Axis Wind Turbine Blades, *AIAA Journal*. 2022. DOI: Link.

Bensason D., Simley E., Roberts O., Fleming P., et al. Evaluation of the potential for wake steering for U.S. land-based wind power plants, *Journal of Renewable and Sustainable Energy*. 2021. DOI: Link.

Conference Papers

Bensason D., Sciacchitano A.,Simao Ferreira C. Experimental study of the impact of blade-tip mounted rotors on the X-Rotor vertical-axis wind turbine, *Journal of Physics: Conf. Series*. 2024. DOI: Link.

Simao Ferreira C., **Bensason D.**, et al. Enhancing Wind Farm Efficiency Through Active Control of the Atmospheric Boundary Layer's Vertical Entrainment of Momentum, *Journal of Physics: Conf. Series*. 2024. DOI: Link.

Broertjes T., **Bensason D.**, Sciacchitano A., Simao Ferreira C. Lift-Induced Wake Re-Energization for a VAWT-Based Multi-Rotor System, *Journal of Physics: Conf. Series*. 2024. DOI: Link.

Bensason D., Sciacchitano A.,Simao Ferreira C. Near wake of the X-Rotor vertical-axis wind turbine, *Journal of Physics: Conf. Series*. 2023. DOI: Link.

Le Fouest S., **Bensason D.**, Mulleners K. Asymmetry of timescales, loads, and flow structures for a vertical-axis wind turbine blade, *AIAA Forum*. 2022. DOI: Link.

Bensason D., Le Fouest S.,Young A., Mulleners K. Strategy for diagnosing the degree of dynamic stall on a vertical-axis wind turbine blade, *AIAA Forum*. 2022. DOI: Link.

Open-source Datasets

Bensason D., Sciacchitano A., Simao Ferreira C. Supporting data belonging to publication: "Near wake of the X-Rotor vertical-axis wind turbine", *4TU.ResearchData.* 2025. DOI: Link.

Bensason D., Broertjes T., Sciacchitano A.,Simao Ferreira C. Supporting data belonging to publication: "Lift-Induced Wake Re-Energization for a VAWT-Based Multi-Rotor System", *4TU.ResearchData.* 2025. DOI: Link.

Bensason D., Sciacchitano A.,Simao Ferreira C. Supporting data belonging to publication: "Experimental study of the impact of blade-tip mounted rotors on the X-Rotor vertical-axis wind turbine", *4TU.ResearchData.* 2025. DOI: Link.

Bensason D., Mulay J., Sciacchitano A.,Simao Ferreira C. Supporting data belonging to publication: "Experimental demonstration of regenerative wind farming using a high-density layout of VAWTs", *4TU.ResearchData.* 2025. DOI: Link.

Bensason D., Sciacchitano A.,Simao Ferreira C. Supporting data belonging to publication: "On the wake re-energization of the X-Rotor vertical-axis wind turbine via the vortex-generator strategy", *4TU.ResearchData.* 2025. DOI: Link.

Bensason D., Sciacchitano A., Ajay A., Simao Ferreira C. Supporting data belonging to publication: "A study of the near wake deformation of the X-Rotor vertical-axis wind turbine with pitched blades", *4TU.ResearchData.* 2024. DOI: Link.

